

Aus dem
Universitätsklinikum Düsseldorf
Institut für Diagnostische und Interventionelle Radiologie
(Direktor: Univ.-Prof. Dr. med. Gerald Antoch)

Implementierung und klinische Anwendung des PET/MRT

Habilitationsschrift zur Erlangung der venia legendi für
das Fach Radiologie des Fachbereichs Medizin
der Heinrich-Heine-Universität Düsseldorf
vorgelegt von

Dr. med. Nils-Martin Bruckmann

2023

Inhaltsverzeichnis

KURZE ZUSAMMENFASSUNG	5
LITERATURANGABEN DER ZUGRUNDE LIEGENDEN FORSCHUNGSArBEITEN	10
AUSFÜHRLICHE ZUSAMMENFASSUNG UND DISKUSSION.....	12
EINLEITUNG	12
HYBRIDE BILDGEBUNGSVERFAHREN.....	14
<i>PET und PET/CT</i>	14
<i>PET/MRT</i>	17
UNTERSUCHUNGEN UND ERGEBNISSE	19
DISKUSSION	45
AUSBLICK	53
LITERATURVERZEICHNIS.....	56
DANKSAGUNG.....	80
ZUGRUNDE LIEGENDE FORSCHUNGSArBEITEN	82

Abkürzungen

AC	Attenuation Correction
ADC	Apparent Diffusion Coefficient
bDMARDs	Biological Disease Modifying Antirheumatic Drugs
CT	Computertomographie
DOTA	1,4,7,10-Tetraazacyclo-dodecan-1,4,7,10-Tetraacetic acid
DOTATOC	DOTA-Phel-Tyr3-Octreotid
DWI	Diffusion Weighted Imaging / Diffusionsbildgebung
ESMO	European Society For Medical Oncology
¹⁸ F	Fluor-18
FDG	Fluorodesoxyglucose
⁶⁸ Ga	Gallium-68
GK	Ganzkörper
GRE	Gradientenecho
HASTE	Half-Fourier Acquired Turbo Spin Echo
keV	Kiloelektronenvolt
LAC	Linearer Abschwächungskoeffizient
LSO	Lutetium Oxyorthosilicat
MRT	Magnetresonanztomographie
Na[¹⁸ F]F	¹⁸ F-Natriumfluorid
NEC	Neuroendokrines Karzinom
NEN	Neuroendokrine Neoplasie
NET	Neuroendokriner Tumor
NSAID	Nichtsteroidales Antirheumatikum

NSCLC	Non-Small Cell Lung Cancer / Nicht-kleinzelliges Bronchialkarzinom
NPV	Negativ Prädiktiver Wert
OR	Odds Ratio
PET	Positronen-Emissions-Tomographie
PMT	Photomultiplier
PSMA	Prostata-Membran Spezifisches Antigen
PPV	Positiv Prädiktiver Wert
ROI	Region Of Interest
SpA	Spondyloarthritis
SUV	Standardized Uptake Value
TNFi	Tumornekrosefaktor-Inhibitor
T1w	T1-gewichtete Sequenz
T2w	T1-gewichtete Sequenz
UICC	Union for International Cancer Control / Internationale Vereinigung gegen Krebs
VIBE	Volumetric Interpolated Breath-hold Examination
VOI	Volume Of Interest

Kurze Zusammenfassung

Die Anwendung hybrider Bildgebungsverfahren, also die Fusion morphologischer und funktioneller Bilddatensätze zur Erlangung komplementärer Informationen, ist seit vielen Jahren mit großem Erfolg Teil der klinischen Routine. Seit Beginn dieses Jahrtausends ist die PET/CT, also die Kombination aus Positronenemissionstomographie und Computertomographie, bereits ein etabliertes Verfahren und in vielen Leitlinien als Diagnostikum verankert. Seit 2010 steht auch die PET/MRT zur Verfügung und stellt damit die bis dato neueste der hybriden Bildgebungsmodalitäten dar. Sie kombiniert funktionelle sowie morphologisch hochauflösende Daten aus der Magnetresonanztomographie mit Stoffwechselinformationen aus der PET.

Insbesondere in der Onkologie ist die PET/MRT ein vielversprechendes bildgebendes Verfahren mit vielfältigen Anwendungsmöglichkeiten. Seit ihrer Einführung haben sich eine große Anzahl an Studien mit dieser Modalität beschäftigt und ihren hohen diagnostischen Wert für das Staging von Tumorerkrankungen herausgestellt.

Beispielsweise wird erwartet, dass die gleichzeitige Erfassung von metabolischen PET- und morphologischen sowie funktionellen MRT-Daten einen großen Einfluss auf die Bildgebung des Mammakarzinoms haben könnte, da die MRT im Vergleich zur CT eine bessere Auflösung des Brustgewebes bietet. Neben den molekularen Markern sind Fernmetastasen und der Befall der axillären Lymphknoten die wichtigsten Prädiktoren für das Gesamtüberleben und die Rezidivwahrscheinlichkeit bei Patientinnen mit Mammakarzinom.

Analog hierzu beschäftigten sich die *Arbeiten 1, 2 und 3* mit dem Vergleich des diagnostischen Potentials von Knochenszintigraphie, Computertomographie, Ganzkörper-MRT und Ganzkörper [¹⁸F]FDG PET/MRT Untersuchungen für das lokoregionäre (N-Staging) und Ganzkörperstaging (M-Staging) bei Patientinnen mit neu diagnostiziertem, histologisch gesichertem Mammakarzinom. In *Arbeit 1* wurde

die diagnostische Wertigkeit vom MRT allein mit dem [¹⁸F]FDG PET/MRT verglichen. In der Studie konnten beide Modalitäten sehr gute diagnostische Ergebnisse erzielen, wobei die [¹⁸F]FDG PET/MRT sowohl beim N- als auch beim M-Staging eine Überlegenheit gegenüber der alleinigen MRT-Untersuchung bot. In *Arbeit 2* erfolgte der Vergleich der derzeit in der Leitlinie als Goldstandard festgelegten kontrastverstärkten Computertomographie mit der [¹⁸F]FDG PET/MRT Untersuchung. Auch hier konnte die [¹⁸F]FDG PET/MRT eine diagnostische Überlegenheit zeigen, sodass trotz der offensichtlichen Vorteile der Computertomographie wie Verfügbarkeit, geringerer Kosten oder schnellerer Akquisitionsgeschwindigkeit der Aufnahmen die [¹⁸F]FDG PET/MRT als potentielle Alternative beim primären Staging des Mammakarzinoms in Zukunft als Alternative in Betracht gezogen werden muss.

Trotz der Fortschritte bei der Behandlung des Mammakarzinoms entwickeln immer noch bis zu 30 % der Patientinnen im Laufe der Erkrankung Fernmetastasen. Hierbei ist das Skelettsystem mit etwa 50-70 % aller Metastasen am häufigsten betroffen. Dies kann zu verschiedenen Komplikationen wie Schmerzen, pathologischen Frakturen oder Hyperkalzämie führen, was oft einen großen Einfluss auf die Morbidität und Mortalität der Patientinnen hat. Aufgrund der Relevanz von ossären Metastasen beschäftigte sich *Arbeit 3* mit der diagnostischen Wertigkeit von [¹⁸F]FDG PET/MRT, dem MRT allein, der Computertomographie und der Knochenszintigraphie in Bezug auf die Detektion von ossären Metastasen im Rahmen des primären Stagings bei Patientinnen mit primärem Mammakarzinom. In dieser Studie konnte gezeigt werden, dass sowohl die MRT als auch die [¹⁸F]FDG PET/MRT in der Detektion von Knochenmetastasen beim Mammakarzinom der CT und insbesondere der Knochenszintigraphie deutlich überlegen sind. Die MRT allein und das [¹⁸F]FDG PET/MRT erreichten hierbei gleich gute Ergebnisse, sodass auch in Anbetracht des häufig jungen Patientenalters und der therapeutischen Bedeutung von ossären

Metastasen die strahlenfreie Ganzkörper-MRT als Diagnostikum der Wahl beim primären Staging von Brustkrebspatientinnen dienen könnte.

Diesen Ergebnissen entsprechend hat die Ganzkörper-MRT zunehmend an Bedeutung gewonnen und wird heute in internationalen Leitlinien für verschiedene Tumorentitäten (z.B. multiples Myelom, Prostatakarzinom und auch Mammakarzinom) empfohlen. Eine wesentliche Einschränkung ist allerdings weiterhin die Anfälligkeit für Atem- und Herzbewegungen, was zu einer deutlich geringeren Beurteilbarkeit des Lungenparenchyms und eingeschränkten Erkennbarkeit von Lungenmetastasen im Vergleich zum CT-Thorax führt. In *Arbeit 4* wurde daher das diagnostische Potential einer radial akquirierten *Stack of Stars* T1-gewichteten Gradientenecho (GRE) 3D-VIBE-Sequenz (StarVIBE), bei der keine Atempausen nötig sind, mit den konventionellen, standardmäßig verwendeten T1- und T2- gewichteten MRT-Sequenzen und der Computertomographie als Referenzstandard in Hinblick auf die Erkennung von Lungenrundherden in der kontrastverstärkten Ganzkörper-[18F]FDG PET/MRT Untersuchung verglichen. Hier war die StarVIBE-Sequenz bei der Erkennung zentral gelegener Lungenrundherde im Vergleich zu den übrigen Sequenzen besonders vorteilhaft, allerdings waren alle MRT-Sequenzen der Computertomographie als Referenzstandard insgesamt weiterhin unterlegen.

Die PET/MRT bietet neben mindestens gleichwertigen diagnostischen Ergebnissen im Vergleich zu den konventionellen Bildgebungsmodalitäten zusätzlich Informationen über Metabolismus mittels PET sowie die Tumorzellularität mittels funktioneller Bildgebung wie beispielsweise den diffusionsgewichteten Sequenzen (DWI). Ziel verschiedener Studien ist es, mittels Kombination einzelner Tumorparameter eine Vorhersage über Tumoraggressivität und -differenzierung zu ermöglichen und damit den Krankheitsverlauf und die Prognose abschätzen und frühzeitig eine gezielte Therapie einzuleiten zu können. Dies ist besonders wichtig bei Tumoren, die eine hohe

Letalität besitzen oder durch ihre Heterogenität eine frühzeitige Auswahl einer geeigneten Therapie erschweren.

Ein Beispiel hierfür ist das Lungenkarzinom, welches die weltweit am häufigsten diagnostizierte Tumorentität und mit etwa 18% die mit Abstand häufigste krebsbedingte Todesursache darstellt. Ziel der *Arbeit 5* war es, mit Hilfe einer [18F]FDG PET/MRT Untersuchung einen unabhängigen, möglichst präzisen Marker für das Langzeitüberleben von Patienten mit fortgeschrittenem NSCLC (*non small cell lung cancer*) zu finden. Die Studie unterstreicht den Wert des SUVmax als unabhängigen prognostischen Marker für das Gesamtüberleben bei NSCLC-Patienten, die Bestimmung des ADC-Wertes brachte in dieser Studie jedoch keinen zusätzlichen Nutzen.

Auch *Arbeit 6* beschäftigte sich mit der Kombination verschiedener Daten aus dem PET/MRT, um möglichst frühzeitig Aussagen zu Tumorparametern treffen zu können. In dieser Studie wurde der Einfluss der Kontrastmittelanreicherung, der Diffusionsstörungen und des SUV-Wertes auf das Tumorgrading bei therapienaiven Patienten mit neuroendokrinem Tumor mittels [⁶⁸Ga]DOTATOC-PET/MRT untersucht und gezeigt, dass diese Parameter eine Vorhersage des Gradings und der Tumoraggressivität bei neuroendokrinen Tumoren ermöglichen.

Um möglichst exakte quantitative Ergebnisse aus der PET-Untersuchung zu erhalten, ist auch im PET/MRT eine Schwächungskorrektur notwendig, die umgebendes Körpergewebe und Hardwarekomponenten des Gerätes berücksichtigt. In der PET/MRT ist die Erstellung dieser Schwächungskorrektur besonders schwierig. In der Regel wird ein Segmentierungsansatz verwendet, bei dem umgebendes Gewebe einzelnen Gewebeklassen zugeordnet wird (Luft, Lunge, Fett, Weichgewebe, Knochen). Ziel vieler Studien in den letzten Jahren war es daher, diese Schwächungskorrektur stetig zu verbessern um möglichst exakte quantitative Werte

zu erreichen. In *Arbeit 7* wurde der Einfluss einer Kontrastmittelgabe während der Untersuchung auf die Schwächungskorrektur in den neuesten verwendeten Dixon-Sequenzen untersucht und festgestellt, dass die Kontrastmittelgabe die Schwächungskorrektur teils erheblich beeinflussen kann und quantitative Daten wie SUV-Werte verfälscht werden. Neue PET/MRT Protokolle müssen daher für eine optimale Vergleichbarkeit der gewonnenen Daten so erstellt werden, dass die Schwächungskorrektur immer vor der Kontrastmittelgabe erfolgt.

Das zunehmende Verständnis von Stoffwechselprozessen und der Pathogenese verschiedener Erkrankungen hat in den letzten Jahren zur Entwicklung einer ganzen Reihe neuer, spezifischer Radiotracer geführt. Ein Beispiel hierfür ist der osteoblastenspezifische Radiotracer ^{18}F -Natriumfluorid ($\text{Na}[^{18}\text{F}]F$), der die Visualisierung lokaler osteoblastischer Aktivität in entzündlichen und strukturellen Läsionen des Skeletts ermöglicht. In *Arbeit 8* wurde mit Hilfe dieses Radiotracers die Wirkung einer Therapie mit TNF-Inhibitoren auf die osteoblastische Aktivität mittels eines $\text{Na}[^{18}\text{F}]F$ PET/MRT bei Patienten mit röntgenologischer axialer Spondyloarthritis untersucht und festgestellt, dass die TNF-Inhibitoren neben der entzündungshemmenden auch eine positive, antiosteoblastische Wirkung besitzen und damit eine Rückbildung der radiologischen Progression dieser Erkrankung zur Folge haben können. Außerdem ist eine möglichst frühzeitige Einleitung der Therapie für den Krankheitsverlauf entscheidend.

Literaturangaben der zugrunde liegenden Forschungsarbeiten

1. **Bruckmann NM**, Sawicki LM, Kirchner J, Martin O, Umutlu L, Herrmann K, Fendler W, Bittner AK, Hoffmann O, Mohrmann S, Dietzel F, Ingenwerth M, Schaarschmidt BM, Li Y, Kowall B, Stang A, Antoch G, Buchbender C (2020). *Prospective evaluation of whole-body MRI and [¹⁸F]FDG PET/MRI in N and M staging of primary breast cancer patients.* Eur J Nucl Med Mol Imaging.

Impact Factor (IF): 9,236

2. **Bruckmann NM**, Kirchner J, Morawitz J, Umutlu L, Herrmann K, Bittner AK, Hoffmann O, Mohrmann S, Ingenwerth M, Schaarschmidt BM, Li Y, Stang A, Antoch G, Sawicki LM, Buchbender C (2021). *Prospective comparison of CT and [¹⁸F]FDG PET/MRI in N and M staging of primary breast cancer patients: Initial results.* PLoS One.

Impact Factor (IF): 3,752

3. **Bruckmann NM**, Kirchner J, Umutlu L, Fendler WP, Seifert R, Herrmann K, Bittner AK, Hoffmann O, Mohrmann S, Antke C, Schimmöller L, Ingenwerth M, Breuckmann K, Stang A, Buchbender C, Antoch G, Sawicki LM (2021). *Prospective comparison of the diagnostic accuracy of [¹⁸F]FDG PET/MRI, MRI, CT and bone scintigraphy for the detection of bone metastases in the initial staging of primary breast cancer patients.* Eur Radiol.

Impact Factor (IF): 7,034

4. **Bruckmann NM**, Kirchner J, Morawitz J, Umutlu L, Fendler WP, Herrmann K, Bittner AK, Hoffmann O, Fehm T, Lindemann ME, Buchbender C, Antoch G,

Sawicki LM (2022). *Free-breathing 3D Stack of Stars GRE (StarVIBE) sequence for detecting pulmonary nodules in [¹⁸F]FDG PET/MRI*. Eur J Nucl Med Mol Imaging Phys.

Impact Factor (IF): 4,20

5. **Bruckmann NM**, Kirchner J, Grueneisen J, Li Y, McCutcheon A, Aigner C, Rischpler C, Sawicki LM, Herrmann K, Umutlu L, Schaarschmidt BM (2021). *Correlation of the apparent diffusion coefficient (ADC) and standardized uptake values (SUV) with overall survival in patients with primary non-small cell lung cancer (NSCLC) using [¹⁸F]FDG PET/MRI*. Eur J Radiol.

Impact Factor (IF): 4,531

6. **Bruckmann NM**, Rischpler C, Kirchner J, Umutlu L, Herrmann K, Ingenwerth M, Theurer S, Lahner H, Antoch G, Sawicki LM (2021). *Correlation between contrast enhancement, standardized uptake value (SUV), and diffusion restriction (ADC) with tumor grading in patients with therapy-naive neuroendocrine neoplasms using hybrid ⁶⁸Ga-DOTATOC PET/MRI*. Eur J Radiol.

Impact Factor (IF): 4,531

7. **Bruckmann NM**, Lindemann ME, Grueneisen J, Grafe H, Li Y, Sawicki LM, Rischpler C, Herrmann K, Umutlu L, Quick HH, Schaarschmidt BM (2021). *Comparison of pre- and post-contrast-enhanced attenuation correction using a CAIPI-accelerated T1-weighted Dixon 3D-VIBE sequence in ⁶⁸Ga-DOTATOC PET/MRI*. Eur J Radiol.

Impact Factor (IF): 4,531

8. Bruckmann NM, Rischpler C, Tsiami S, Kirchner J, Abrar DB, Bartel T, Theysohn J, Umutlu L, Herrmann K, Fendler WP, Buchbender C, Antoch G, Sawicki LM, Tsobanelis A, Braun J, Baraliakos X (2022). *Effects of anti-TNF-therapy on inflammatory, structural and osteoblastic activity lesions in radiographic axial spondyloarthritis - a prospective proof-of-concept study using PET/MRI of SIJ and spine.* *Arthritis Rheumatol.*

Impact Factor (IF): 15,483

Ausführliche Zusammenfassung und Diskussion

Einleitung

Der hybriden Bildgebung liegt die Idee zugrunde, klinische Radiologie, die Pathologien aufgrund der morphologischen oder funktionellen Gewebeveränderungen mittels Computertomographie (CT) und Magnetresonanztomographie (MRT) detektiert, mit der Nuklearmedizin, welche durch die Injektion radioaktiv markierter Stoffe (Tracer) metabolische Veränderungen mittels Positronenemissionstomographie (PET) darstellen kann, zu kombinieren. Ziel ist es, durch die Aufhebung einer strikten Trennung zwischen morphologischen und metabolischen Verfahren eine möglichst exakte Bildgebung zu erhalten, mit der Krankheiten frühzeitig und genau klassifiziert oder verlaufskontrolliert werden können (1).

Seit 2011 stehen hierfür auch Ganzkörper-PET/MRT Scanner zur Verfügung, die neben einer Reduzierung der ionisierenden Strahlung durch den Wegfall der CT-

Untersuchung zusätzlich einen hohen Weichteilkontrast und funktionelle Informationen aus Diffusions- und Perfusionsbildgebung liefern (2,3).

Ein großer Stellenwert wird den hybriden Verfahren in der Onkologie beigemessen, da hier vor allem eine exakte und sichere initiale bildgebende Ausbreitungsdiagnostik für die stadienadaptierte Behandlung eine wesentliche Rolle spielt und somit die Prognose entscheidend mit beeinflussen kann. Einen großen Vorteil bietet die PET/MRT dabei bei primären Staginguntersuchungen, welche die Akquisition mehrerer MRT erfordern, beispielsweise von Kopf und Mamma beim Mammakarzinom, da diese in einer Untersuchung erfolgen können und so der Zeitaufwand verringert und der Patientenkomfort erhöht wird.

Darüber hinaus lassen sich das Therapieansprechen kontrollieren und insbesondere beim PET/MRT durch die Vielzahl an gewonnenen Informationen Prognosefaktoren beispielsweise für das Gesamtüberleben oder verschiedene Tumoreigenschaften ableiten (4–7).

In den letzten Jahren wurden darüber hinaus immer neue und präzisere Anwendungsmöglichkeiten für hybride Bildgebungsverfahren erschlossen. Aus dem wachsenden Verständnis von Stoffwechselprozessen und der Pathogenese von Krankheiten sind eine ganze Reihe neuer Tracer entstanden, beispielsweise die Verwendung spezieller Radiopharmaka bei der Alzheimererkrankung oder bei entzündlichen Erkrankungen wie der rheumatoïden Arthritis oder der axialen Spondyloarthritis (8–10). Letztlich kann durch die Anwendung von PET/MRT eine höhere Sensitivität und Spezifität in der Diagnostik und Verlaufskontrolle verschiedener Erkrankungen erreicht werden und somit möglicherweise eine frühere und präzisere Therapieeinleitung erfolgen.

Hybride Bildgebungsverfahren

PET und PET/CT

Ähnlich wie bei der Szintigraphie werden bei der Positronen-Emissions-Tomographie Radiopharmaka verwendet. Hierbei handelt es sich um Medikamente, die entweder alleine aus einer radioaktiven Substanz bestehen oder mit einem Radionuklid markiert sind und am gewöhnlichen Stoffwechsel des Organismus teilnehmen, diesen aber nicht quantitativ beeinflussen. Bei der PET nutzt man Radionuklide, die dem β^+ -Zerfall unterliegen. Beim β^+ -Zerfall erfolgt die Umwandlung eines Kernprotons in ein Neutron (n), wobei ein Neutrino und ein Positron (e^+) ausgesendet werden. Das emittierte Positron tritt in unmittelbare Wechselwirkung mit einem Elektron des angrenzenden Gewebes. Bei diesem Vorgang entsteht eine sekundäre Vernichtungsstrahlung (Annihilation), bei der zwei Gammaquanten (Photonen) mit einer Energie von 511 keV erzeugt werden, die sich in entgegengesetzte Richtungen bewegen. Diese im 180°-Winkel emittierten Photonen können dann koinzident von gegenüberliegenden Detektoren erfasst werden. In der Klinik werden hierfür Ringdetektoren verwendet, die um die Patientenliege angeordnet sind. In den heute gängigen PET-Scannern werden hierfür Szintillationsdetektoren verwendet. Bei der Wechselwirkung von anorganischen Szintillationskristallen mit den auftreffenden hochenergetischen Photonen wird sichtbares bzw. nahultraviolette Licht ausgesendet, das wiederum von Photodetektoren erkannt und gemessen werden kann. Aus der zeitlichen und räumlichen Verteilung der registrierten Zerfallsereignisse kann nun auf die räumliche Verteilung des Radiopharmakons im Organismus geschlossen werden. Die Detektoren sind zylindrisch in mehreren Ringen um den Patienten angeordnet. Die räumliche Auflösung wird durch die Größe der einzelnen Detektorkristalle definiert. Das Volumen innerhalb des Ringkomplexes wird als das field-of-view (FOV)

bezeichnet, das meist einen Durchmesser von 70 cm und eine axiale Länge von 16 bis 25 cm (1 Bettposition) besitzt. Die Dauer einer Messung in einer Bettposition kann je nach Untersuchung variieren und wird zunehmend verkürzt, liegt aber in der Regel bei 2-3 Minuten. Da die Bettpositionen überlappend akquiriert werden, können für eine Ganzkörperuntersuchung bis zu 15 Bettpositionen nötig sein. Während der Erfassung der PET Daten werden die Photonen durch das umgebende Körpergewebe und die Hardwarekomponenten des Scanners abgeschwächt, bevor der PET-Detektor erreicht wird (2). Diese Photonenabschwächung führt zu Ungenauigkeiten bei der Tracer-Quantifizierung, da beispielsweise bei adipösen Patienten eine stärkere Abschwächung stattfindet. Folglich erfordert die PET-Datenrekonstruktion eine Abschwächungskorrektur, die korrekte quantitative Ergebnisse liefert. Bei reinen PET-Scannern wird dies mithilfe eines Transmissionsscans erreicht. Hierbei rotiert eine externe Positronenquelle um den Patienten und berechnet die Abschwächung der ausgesendeten Photonen (11).

In der onkologischen Bildgebung ist immer noch die [¹⁸F]-2-Fluoro-2-desoxy-D-glucose (FDG) das am häufigsten verwendete Radiopharmakon, auch wenn es sich hierbei um einen sehr unspezifischen Tracer handelt. Tumorzellen weisen im Vergleich zu gesunden Zellen einen erhöhten Glukosemetabolismus auf und lassen sich daher durch diesen Tracer sehr gut detektieren (12). Ein großes Problem der alleinigen PET-Bildgebung ist die geringe Ortsauflösung, die eine anatomische Zuordnung von Traceranreicherungen erschwert (11).

Dieses Problem sollte mit der gleichzeitigen Akquisition von PET- und CT-Daten in einer Untersuchung behoben werden (1). Denn mit der Computertomographie lassen sich überlagerungsfreie Darstellungen der Körperanatomie erreichen. Hierbei werden Röntgenstrahlen von einer Röntgenquelle ausgesendet, die das abzubildende Objekt

durchleuchten und von einem gegenüberliegenden Detektorelement erfasst werden. Durch Rotationsbewegungen des Scanners werden Absorptionsprofile des Objekts aus unterschiedlichen Richtungen erstellt und hieraus die Volumenstruktur des durchstrahlten Körpers rekonstruiert. Durch computergestützte Bildrekonstruktion, heute meist mittels iterativer Rekonstruktion, können Transversalschnitte durch das Untersuchungsobjekt berechnet werden (13,14).

Die direkte Kombination von PET- und CT-Messungen bietet technische Vorteile gegenüber der retrospektiven Fusion, da der CT-Datensatz direkt für die Schwächungskorrektur verwendet werden kann und somit ein zusätzlicher Transmissionsscan entfällt. Außerdem erfolgt die Aufnahme des CT-Scans deutlich schneller als der früher nötige Transmissionsscan, sodass sich zusätzlich eine deutliche Verkürzung der Aufnahmedauer von bis zu 40 % ergibt (15,16). Da es zwischen PET und CT kaum Störsignale gibt, können die beiden Systeme direkt ringförmig hintereinander angeordnet werden. Es wird also zu Beginn eine CT-Untersuchung der entsprechenden Körperregion angefertigt, die sowohl als diagnostisches full-dose CT mit Kontrastmittel oder als low-dose CT ohne Kontrastmittel zur Schwächungskorrektur durchgeführt werden kann.

Die Kombination der beiden Modalitäten führt zu einer höheren Genauigkeit bei der Diagnose und der Stadieneinteilung in der onkologischen Bildgebung als bei der alleinigen Anwendung von CT, MRT oder PET (17–20), sodass die PET/CT schnell als Diagnostikum der Wahl in viele Leitlinien etabliert wurde.

Trotz des hohen diagnostischen Nutzens offenbart die Modalität Schwächen. So ist die Strahlenexposition durch PET- und CT-Untersuchung höher als bei den Einzeluntersuchungen und sollte daher gerade bei pädiatrischen Patienten und/oder rezidivierenden Erkrankungen kritisch hinterfragt werden (21,22). Außerdem ist bei der kontrastmittelgestützten CT der Weichteilkontrast für die Beurteilung vieler

Erkrankungen nicht ausreichend, beispielsweise für Läsionen in der Brust, gynäkologische Beckentumore oder Kopf-Hals-Tumoren (23–26).

PET/MRT

Seit 2010 ist die PET/MRT in der klinischen Anwendung verfügbar und stellt damit das neueste der hybriden Bildgebungsverfahren dar. Es liefert sowohl die funktionellen und morphologischen Informationen aus der MRT als auch die Stoffwechselinformationen der PET Bildgebung. Insbesondere in der Onkologie ist die PET/MRT ein vielversprechendes bildgebendes Verfahren mit diversen Anwendungsmöglichkeiten. Vor allem bei Indikationen, in denen die morphologische Bildgebung mittels MRT der CT-Untersuchung überlegen ist, aber auch durch die Verwendung der funktionellen Informationen aus der MRT-Untersuchung erhofft man sich einen zusätzlichen Nutzen (27–29).

Ein großes Problem bei der Entwicklung eines solchen PET/MRT-Scanners war die Anfälligkeit der vorhandenen PET-Detektoren (Photomultiplier / Szintillationskristalle) für das statische Hauptmagnetfeld des MR-Tomographen sowie die variierenden Gradientenfelder und Radiofrequenzimpulse, die für die Bildakquisition benötigt werden. Hierdurch kam es zu geometrischen Verzerrungen der PET-Daten (30). Erst die Entwicklung einer Kombination aus Lutetium Oxyorthosilicat (LSO)-Szintillatoren und Avalanche Photodioden schaffte 2006 die nötigen Voraussetzungen (30,31). Ein weiterer Vorteil dieser Technologie ist die Möglichkeit, breitere Detektoren einzusetzen als beim PET/CT, wodurch sich die Anzahl der Bettpositionen verringern lässt.

Eine Herausforderung für die Integration des PET/MRT war die Entwicklung einer zuverlässigen Schwächungskorrektur.

Die PET/CT-Untersuchung nutzt die CT-Bildgebung, um Informationen über die Elektronendichte von Geweben und die geometrische Darstellung von

photonenschwächenden Organen im Körper zu liefern. Durch die Umwandlung der im CT gemessenen Hounsfield-Einheiten (HU) in lineare Abschwächungskoeffizienten (LACs) auf dem PET-Emissionsenergieniveau von 511 keV können diese Daten für die CT-basierte Abschwächungskorrektur genutzt werden. Bei der MRT hingegen kann nur die Photonendichte und die Relaxationszeiten bestimmt werden und ein linearer Zusammenhang zur Gewebedichte liegt nicht vor (32–34).

In der klinischen Anwendung von PET/MRT Scannern wird heutzutage ein Segmentierungsansatz verwendet, bei dem die MR-Bilder mit Hilfe einer MR-Dixon-VIBE Sequenz in die vier Gewebeklassen Luft, Lunge, Fett und Weichgewebe unterteilt werden. Jeder dieser Klassen werden vordefinierte Abschwächungskoeffizienten zugeordnet und eine Abschwächungskarte erstellt. Eine weitere Verbesserung erfolgte durch das Hinzufügen von Knochenmodellen und Trunkierungskorrekturen der Arme, sodass die Unterschiede zur CT-basierten Schwächungskorrektur in Studien keinen relevanten Einfluss auf die klinische Aussagekraft haben (35,36). Die Optimierung der Schwächungskorrektur ist weiterhin Gegenstand aktueller Forschung. So wird beispielsweise an Alternativen zur Dixon-VIBE-Sequenz gearbeitet, um die Auflösung der resultierenden Schwächungskarten weiter zu verbessern.

Seit der Einführung der PET/MRT gibt es bereits eine Vielzahl an Studien, die einen hohen diagnostischen Wert dieser Untersuchung zeigen, beispielsweise bei Ganzkörperstaginguntersuchungen. Grundsätzlich legen die Studien eine gleichwertige Bildgebungsqualität für die Läsionsdetektion von PET/CT und PET/MRT nahe, wobei die PET/MRT durch den besseren Weichteilkontrast und der funktionellen Bildgebung bei der Detektion von Leber-, Hirn- und Knochenmetastasen überlegen ist, während sich in der PET/CT Lungenrundherde besser beurteilen lassen (37–41).

Untersuchungen und Ergebnisse

1. Arbeit: Bruckmann NM, Sawicki LM, Kirchner J, Martin O, Umutlu L, Herrmann K, Fendler W, Bittner AK, Hoffmann O, Mohrmann S, Dietzel F, Ingenwerth M, Schaarschmidt BM, Li Y, Kowall B, Stang A, Antoch G, Buchbender C (2020). *Prospective evaluation of whole-body MRI and ¹⁸F-FDG PET/MRI in N and M staging of primary breast cancer patients.* Eur J Nucl Med Mol Imaging.

Brustkrebs ist mit ungefähr 2,1 Millionen neuen Erkrankungsfällen jedes Jahr die häufigste solide Neoplasie bei Frauen weltweit (42). Wie bei den meisten Tumorerkrankungen korreliert die Mortalität mit der individuellen Tumorlast und Prognose als auch Therapiemanagement sind maßgeblich vom initialen Tumorstadium abhängig. Ein präzises Staging ist daher für die optimale Behandlung essentiell (43). Entscheidend ist beim Staging die korrekte Detektion von lokoregionären Lymphknotenmetastasen oder Fernmetastasen, denn bei Nachweis einer Fernmetastasierung kann das Therapiekonzept von kurativ zu palliativ wechseln (44).

Der aktuelle diagnostische Algorithmus zur Evaluation der lokalen Tumorausdehnung umfasst die Mammographie, die Sonographie sowie in ausgewählten Fällen die Magnetresonanztomographie (45,46). Insbesondere die Nachfrage nach dezidierten Brust-MRT hat in den letzten Jahren deutlich zugenommen (47). Entsprechend der Leitlinie wird bei entsprechendem Risikoprofil aktuell zur Suche von Fernmetastasen eine thorakoabdominelle Computertomographie sowie eine Knochenszintigraphie empfohlen (45,48). Trotz der Vorteile des MRT bei der Evaluation von parenchymatösen Organen und der Möglichkeit einer Kombination mit einem dezidierten Brust-MRT wird eine Ganzkörper-MRT Untersuchung zur Metastasensuche hingegen aktuell nur selten durchgeführt (37,38,49). In Bezug auf

die hybriden Bildgebungsverfahren hat die ^{18}F -FDG PET/CT in Studien sehr gute Ergebnisse bei der Diagnostik von Fernmetastasen ergeben, sodass diese in der Leitlinie als alternatives Stagingtool geführt wird (50–52). Auch die ^{18}F -FDG PET/MRT hat in einigen kleineren Studien vielversprechende Ergebnisse als alternatives Stagingtool bei primär an Brustkrebs erkrankten Patientinnen (53,54) und Patientinnen mit einem Tumorrezidiv (55–57) geliefert.

Ziel dieser Studie war daher zum einen die Evaluation der diagnostischen Aussagekraft einer Ganzkörper-MRT Untersuchung im Vergleich zu einer Ganzkörper ^{18}F -FDG PET/MRT Untersuchung für das initiale N- und M-Stadium in einer großen Kohorte mit therapienaiven Patientinnen mit primär diagnostiziertem Mammakarzinom. Zum anderen sollte die ^{18}F -FDG PET/MRT als potentielles „All-in-one“ Stagingtool für die Routinediagnostik eingeführt werden, das neben der Ganzkörperdiagnostik ein dezidiertes MRT der Mamma sowie ein MRT des Schädelns umfasst.

Insgesamt wurden 104 Patientinnen (durchschnittliches Alter $53,4 \pm 12,5$ Jahre) mit neu diagnostiziertem, histopathologisch gesichertem Brustkrebs in diese prospektive Studie eingeschlossen. Alle Patientinnen erhielten eine Ganzkörper ^{18}F -FDG PET/MRT Untersuchung und die Datensätze für MRT und PET/MRT wurden getrennt hinsichtlich der Läsionszahl, der Läsionslokalisation, der Läsionscharakterisierung (maligne/benigne) und der diagnostischen Sicherheit ausgewertet. Als Referenzstandard diente in der Mehrzahl der Läsionen die Histopathologie, die übrigen Läsionen wurden durch Bildgebung und klinische Untersuchungen weiterverfolgt. Die Sensitivität und Spezifität für nodal-positive und nodal-negative Patientinnen wurde mittels McNemar-Chi-Quadrat-Test ausgewertet. Unterschiede in der diagnostischen Sicherheit wurden mittels Wilcoxon-Vorzeichen-Rang-Test ermittelt.

Die MRT bestimmte das N-Stadium bei 78 von 104 (75 %) Patientinnen korrekt mit einer Sensitivität von 62,3 % (95 % CI: 0,48-0,75), einer Spezifität von 88,2 % (95 %

CI: 0,76-0,96), einem PPV (positiver prädiktiver Wert) von 84,6 % (95 % CI: 69,5-0,94) und einem NPV (negativer prädiktiver Wert) von 69,2 % (95 % CI: 0,57-0,8). Die entsprechenden Ergebnisse für die ¹⁸F-FDG PET/MRT waren 87/104 (83,7 %), 75,5 % (95 % CI: 0,62-0,86) , 92,2 % (0,81-0,98), 90 % (0,78-0,97) und 78,3 % (0,66-0,88), was eine signifikant bessere Sensitivität der ¹⁸F-FDG PET/MRT bei der Bestimmung maligner Lymphknoten zeigt ($p = 0,008$). Das M-Stadium wurde im MRT und im ¹⁸F-FDG PET/MRT bei 100 von 104 Patientinnen (96,2 %) korrekt erkannt. Bei allen 7 Patientinnen mit Fernmetastasen wurde das Stadium mit beiden Methoden korrekt bestimmt, wobei es bei 4 Patientinnen mit jeder Methode zu falsch-positiven Befunden kam (3,8 %). In einer läsionsbasierten Analyse zeigte die ¹⁸F-FDG PET/MRT signifikant bessere Ergebnisse bei der korrekten Bestimmung maligner Läsionen (85,8 % vs. 67,1 %, Differenz 18,7 % (95 % CI: 0,13-0,26), $p < 0,0001$) und bot eine höhere Diagnosesicherheit im Vergleich zur MRT allein ($4,1 \pm 0,7$ vs. $3,4 \pm 0,7$, $p < 0,0001$). Zusammenfassend zeigt die Studie eine bessere diagnostische Genauigkeit des ¹⁸F-FDG PET/MRT gegenüber dem MRT allein für das N-Staging bei primären Brustkrebspatientinnen und bietet eine höhere diagnostische Sicherheit bei der Läsionscharakterisierung als das MRT allein. Beide Methoden bergen jedoch das Risiko falsch-positiver Befunde für das M-Stadium.

2. Arbeit: Bruckmann NM, Kirchner J, Morawitz J, Umutlu L, Herrmann K, Bittner AK, Hoffmann O, Mohrmann S, Ingenwerth M, Schaarschmidt BM, Li Y, Stang A, Antoch G, Sawicki LM, Buchbender C (2021).

Prospective comparison of CT and ¹⁸F-FDG PET MRI in N and M staging of primary breast cancer patients: Initial results. PLoS One.

Bei Patientinnen mit neu diagnostiziertem Mammakarzinom spielt ein möglichst genaues bildgebendes Staging eine entscheidende Rolle, um ein optimales Behandlungsmanagement zu bestimmen und potenziell schädliche chirurgische Eingriffe und umfangreiche systemische Therapien zu minimieren (44).

Wesentliche Punkte für das initiale Staging sind der Nachweis von Tumormanifestationen in der kontralateralen Brust, die Beurteilung der lokoregionalen Lymphknoten und der Nachweis von Fernmetastasen (43). In Abhängigkeit von der Größe des Primärtumors und des lokoregionalen Lymphknotenstatus kann die Operation von einer brusterhaltenden Therapie bis hin zu einer kompletten Mastektomie und ipsilateraler Axilladissektion reichen. Bei gesicherten Fernmetastasen geht das Behandlungskonzept zu einer umfangreichen systemischen und meist palliativen Therapie über (44).

Gemäß den Leitlinien der Europäischen Gesellschaft für Medizinische Onkologie (ESMO) von 2020 und des National Comprehensive Cancer Network (NCCN) von 2021 wird ein Staging mit kontrastverstärkter thorako-abdominaler CT sowie eine Knochenszintigraphie (45,58) erwogen bei Patientinnen mit fortgeschrittenem Brustkrebs (UICC III/IV) und Patientinnen mit UICC-Stadium II in Kombination mit zusätzlichen Risikofaktoren wie klinisch positiven axillären Lymphknoten, großer Tumorgröße, aggressiver Tumorbiologie (HER2neu-Überexpression, triple-negativer Tumor) oder klinischen Zeichen/Laborwerten, die auf das Vorhandensein von Metastasen hindeuten. Da asymptomatische Fernmetastasen in frühen Tumorstadien sehr selten sind, profitieren symptomlose Patientinnen im Frühstadium der Erkrankung nicht von einem Ganzkörper-Staging, sodass hier die lokoregionäre Metastasensuche im Fokus steht (43,45,55).

Neuere Studien haben gezeigt, dass hybride Bildgebungsverfahren bei der Erkennung von Fernmetastasen und der korrekten Einstufung maligner Läsionen bei

Brustkrebspatientinnen überlegen sind (55,59,60). Daher wurden hybride Bildgebungsverfahren in den letzten Jahren zunehmend in internationale Leitlinien aufgenommen. Hier wird mittlerweile eine ¹⁸F-FDG PET/CT Untersuchung empfohlen, wenn konventionelle Methoden keine eindeutigen Ergebnisse liefern, bei Hochrisikopatientinnen oder bei Patientinnen mit neu diagnostiziertem Mammakarzinom im Stadium III (45,61). Zusätzlich wurde in Studien die Überlegenheit der ¹⁸F-FDG PET/MRT im Vergleich zur ¹⁸F-FDG PET/CT bei der Erkennung von Brustkrebsmetastasen nachgewiesen (62). Insbesondere in Kombination mit einer speziellen Brust-(PET/)MRT kann sie eine wertvolle Alternative für das primäre Staging von Brustkrebspatientinnen darstellen (53,63–67).

Ziel dieser Studie war es daher, das diagnostische Potenzial der CT, die dem derzeitigen klinischen Standard entspricht, im Vergleich zur ¹⁸F-FDG PET/MRT für das initiale N- und M-Staging von Patientinnen mit primärem Brustkrebs zu bewerten. Hierzu wurden insgesamt 80 Frauen mit neu diagnostiziertem und histopathologisch gesichertem Mammakarzinom in diese prospektive Studie aufgenommen. Folgende Einschlusskriterien mussten erfüllt sein: (1) Neu diagnostizierter, therapienaiver T2-Tumor oder höheres T-Stadium oder (2) neu diagnostizierter, therapienaiver triple-negativer Tumor jeder Größe oder (3) neu diagnostizierter, therapienaiver Tumor mit molekularem Hochrisiko (T1c, Ki67 >14%, HER2neu-Überexpression, G3). Bei allen Patientinnen wurde ein thorako-abdominales CeCT und ein Ganzkörper ¹⁸F-FDG PET/MRT durchgeführt. Alle Datensätze wurden hinsichtlich der Anzahl der suspekten Läsionen, der Lokalisation, der Kategorisierung und der diagnostischen Sicherheit ausgewertet. Histopathologische Ergebnisse und Follow-Up Untersuchungen dienten als Referenzstandard. Die Unterschiede in der Genauigkeit der Stadieneinteilung wurden mittels McNemar-Chi-Quadrat-Test ermittelt.

Die Computertomographie bewertete das N-Stadium bei 64 von 80 (80 %, 95 % CI: 70,0-87,3 %) Patientinnen richtig mit einer Sensitivität von 61,5 % (CI: 45,9-75,1 %), einer Spezifität von 97,6 % (CI: 87,4-99,6 %), einem PPV von 96 % (CI: 80,5-99,3 %) und einem NPV von 72,7 % (CI: 59,8-82,7 %). Im Vergleich dazu bestimmte die ¹⁸F-FDG PET/MRT das N-Stadium bei 71 von 80 (88,75 %, CI: 80,0-94,0 %) Patientinnen korrekt mit einer Sensitivität von 82,1 % (CI: 67,3-91,0 %), einer Spezifität von 95,1 % (CI: 83,9-98,7 %), einem PPV von 94,1 % (CI: 80,9-98,4 %) und einem NPV von 84,8 % (CI: 71,8-92,4 %). Die Unterschiede in der Sensitivität waren statistisch signifikant (Differenz 20,6 %, CI: -0,02-40,9 %; p = 0,008). Fernmetastasen waren bei 7/80 Patientinnen (8,75 %) vorhanden. In der ¹⁸F-FDG PET/MRT wurden alle histopathologisch nachgewiesenen Metastasen ohne falsch-positive Befunde nachgewiesen, während 3 Patientinnen mit Knochenmetastasen im CT übersehen wurden (Sensitivität 57,1 %, Spezifität 95,9 %). Außerdem zeigte die CT bei 3 Patientinnen falsch-positive Befunde.

Zusammenfassend zeigt die vorliegende Studie, dass die ¹⁸F-FDG PET/MRT ein hohes diagnostisches Potenzial besitzt und der CT bei der Beurteilung des N- und M-Stadiums bei Patientinnen mit primärem Mammkarzinom überlegen ist. Trotz der Vorteile der CT, wie z.B. Verfügbarkeit, geringere Kosten oder Akquisitionsgeschwindigkeit sollte diese Studie zusammen mit den aktuellen Daten Anlass zur Diskussion über die Empfehlungen für das primäre Staging in den Leitlinien für das Mammakarzinom geben.

- 3. Arbeit:** Bruckmann NM, Kirchner J, Umutlu L, Fendler WP, Seifert R, Herrmann K, Bittner AK, Hoffmann O, Mohrmann S, Antke C, Schimmöller L, Ingenwerth M, Breuckmann K, Stang A, Buchbender C, Antoch G, Sawicki LM (2021). *Prospective comparison of the diagnostic accuracy of 18-FDG PET MRI, MRI,*

CT and bone scintigraphy for the detection of bone metastases in the initial staging of primary breast cancer patients. Eur Radiol.

Beim Mammakarzinom ist neben der Beurteilung der Ausdehnung des Primärtumors in der Brust und des lokoregionären Lymphknotenbefalls der Nachweis von Fernmetastasen entscheidend, da dies zu einer Erweiterung des Bestrahlungsfeldes oder einer Anpassung der Chemotherapie und schließlich zu einem Wechsel zu einem palliativen Therapiekonzept führen kann (68). Daher spielt das bildgebende Ganzkörper-Staging eine zentrale Rolle in der Primärdiagnostik von Brustkrebspatientinnen mit einem hohen Risiko für das Vorhandensein von Fernmetastasen. Trotz der Fortschritte bei der Behandlung des Mammakarzinoms entwickeln immer noch bis zu 30 % der Patientinnen im Laufe der Erkrankung Fernmetastasen (68). Dabei ist das Skelett die häufigste Lokalisation und macht etwa 50-70 % aller Metastasen aus (68–72). Der Befall des Knochens kann zu verschiedenen Komplikationen wie Schmerzen, pathologischen Frakturen, Rückenmarkskompression und Hyperkalzämie führen, die oft einen großen Einfluss auf die Morbidität und Mortalität der Patientinnen haben (73–75). Eine frühzeitige Erkennung kann dazu beitragen, die Krankheit besser zu kontrollieren, Komplikationen zu minimieren und somit eine bessere Lebensqualität zu erreichen (74).

Aktuell gilt die Knochenszintigraphie in Kombination mit der Computertomographie weithin als Goldstandard für den Nachweis von Knochenmetastasen und wird auch in aktuellen Leitlinien als Methode der Wahl empfohlen (45,46,76). Sofern verfügbar, kann auch eine PET/CT-Untersuchung für das primäre Staging eingesetzt werden, wurde aber aufgrund der geringen Verfügbarkeit und der höheren Kosten bisher nur selten angewendet. Frühere Studien haben jedoch gezeigt, dass die MRT im Vergleich zur Knochenszintigrafie Vorteile bei der Erkennung von Knochenläsionen bietet und

die CT als vorteilhafteste Ganzkörper-Staging-Untersuchung ablösen könnte (74,77). Dementsprechend wurde die MRT als alternatives Staging-Instrument für Mammakarzinompatientinnen diskutiert und in den Leitlinien der Europäischen Gesellschaft für Medizinische Onkologie (ESMO) für 2018 und 2020 bereits als Methode der Wahl bei Patientinnen mit neurologischen Symptomen und Anzeichen, die auf eine mögliche Rückenmarkskompression hindeuten, aufgenommen (45,78). Auch die Anwendung von hybriden Bildgebungsverfahren hat sich in diesem Zusammenhang als nützlich erwiesen (79–82). Die Bedeutung einer [¹⁸F]FDG PET/MRT-Untersuchung für die Erkennung von Knochenmetastasen bei primären Brustkrebspatientinnen ist jedoch bisher kaum untersucht worden (83–85). Ziel dieser Studie war es daher, den diagnostischen Wert von [¹⁸F]FDG PET/MRT, dem alleinigen MRT, CT und Knochenszintigraphie für den Nachweis von Knochenmetastasen bei der Erstdiagnose von Brustkrebspatientinnen zu untersuchen und zu vergleichen.

154 Patientinnen mit neu diagnostiziertem, therapienavivem, histopathologisch gesichertem Mammakarzinom wurden prospektiv in diese Studie aufgenommen. Alle Patientinnen unterzogen sich vor der Therapie einer Ganzkörper [¹⁸F]FDG PET/MRT, einer Computertomographie (CT) und einer Knochenszintigraphie. Alle Datensätze wurden hinsichtlich des Vorhandenseins von Knochenmetastasen ausgewertet. Der McNemar-Chi-Quadrat-Test wurde angewendet, um die Sensitivität und Spezifität zwischen den Modalitäten zu vergleichen.

Es konnten insgesamt 41 Knochenmetastasen in 7 von 154 Patientinnen nachgewiesen werden (4,5 %). Sowohl die [¹⁸F]FDG PET/MRT als auch die MRT allein waren in der Lage, alle Patientinnen mit histopathologisch gesichertem Knochenmetastasen zu erkennen (Sensitivität 100 %; Spezifität 100 %) und es wurde keine der 41 Metastasen übersehen. Die CT entdeckte 5/7 Patientinnen (Sensitivität

71,4 %; Spezifität 98,6 %) und 23/41 Läsionen (Sensitivität 56,1 %), während die Knochenszintigraphie nur bei 2/7 Patientinnen (Sensitivität 28,6 %) und 15/41 Läsionen (Sensitivität 36,6 %) eine Metastasierung nachweisen konnte. Darüber hinaus führten CT und Knochenszintigraphie bei 2 bzw. 1 Patientin zu falsch-positiven Befunden von Knochenmetastasen. Die Sensitivität der [18F]FDG PET/MRT und MRT allein war signifikant besser als die der CT ($p<0,01$, Differenz 43,9 %) und Knochenszintigraphie ($p<0,01$, Differenz 63,4 %).

Zusammenfassend waren sowohl die [18F]FDG PET/MRT als auch die MRT allein in der läsionsbasierten Analyse bei der Erkennung von Knochenmetastasen bei Patientinnen mit neu diagnostiziertem Mammakarzinom der CT und der Knochenszintigrafie deutlich überlegen. Die [18F]FDG PET/MRT und die alleinige MRT lieferten hierbei identische Ergebnisse. In Anbetracht der relativ geringen Prävalenz von Knochenmetastasen bei der Erstdiagnose, der hohen Zahl von Patientinnen in relativ jungem Alter, die sich dem klinischen Staging-Algorithmus unterziehen, und der therapeutischen Bedeutung von Knochenmetastasen könnte die strahlenfreie Ganzkörper-MRT daher als Mittel der Wahl dienen. Im Gegensatz dazu erscheint der Einsatz der derzeit empfohlenen CT und Knochenszintigraphie zum Nachweis von Knochenmetastasen fraglich.

4. Arbeit: Bruckmann NM, Kirchner J, Morawitz J, Umutlu L, Fendler WP, Herrmann K, Bittner AK, Hoffmann O, Fehm T, Lindemann ME, Buchbender C, Antoch G, Sawicki LM (2022).

Free-breathing 3D Stack of Stars GRE (StarVIBE) sequence for detecting pulmonary nodules in ¹⁸F-FDG PET/MRI. Eur J Nucl Med Mol Imaging Phys.

Die Magnetresonanztomographie (MRT) hat in den letzten Jahrzehnten enorme Fortschritte gemacht, angetrieben durch neue Entwicklungen in der Sequenztechnik, welche die Gesamtuntersuchungszeit verkürzen und die Bildqualität verbessern.

In der onkologischen Bildgebung hat die Ganzkörper-MRT als Methode für das Staging und die Nachsorge von Krebserkrankungen zunehmend an Bedeutung gewonnen und wird heute in internationalen Leitlinien für verschiedene Tumorentitäten (z. B. multiples Myelom, Prostatakrebs, Brustkrebs) empfohlen (46,86,87). Da die MRT eine strahlungsfreie Bildgebungsmethode ist, stellt sie insbesondere bei jüngeren Patienten eine wertvolle Alternative zur Computertomographie dar. Eine wesentliche Einschränkung ist die Anfälligkeit für Atem- und Herzbewegungen, was im Vergleich zur Thorax-CT zu einer deutlich reduzierten Beurteilbarkeit des Lungenparenchyms und einer eingeschränkten Erkennbarkeit potenzieller Lungenmetastasen führt. Die konventionelle MR-Bildgebung unter Atemstillstand ist derzeit eine gängige Methode, um eine gute Bildqualität zu gewährleisten (88). Dazu ist eine strikte Immobilität und die Einhaltung von Atemanweisungen erforderlich, was im klinischen Alltag manchmal schwierig sein kann, insbesondere bei der Untersuchung von Kindern oder multimorbid älteren Patienten. Zusätzlich ist die Verwendung schneller MR-Sequenzen erforderlich, die mit einem Verlust an räumlicher Bildauflösung verbunden sind (89).

Die hohe Bewegungsanfälligkeit konventioneller MR-Bilder resultiert aus der zeilenweisen Erfassung (kartesisches Sampling) des Datenraums (k-Raum). Selbst kleine Bewegungen während der Untersuchung verursachen Störungen im Phasenkodierungsschema und führen zu Phasenverschiebungen in Richtung der Bewegung, was Inkonsistenzen im k-Raum zur Folge hat. Hierdurch entstehen Artefakte in der Phasenkodierungsrichtung (90,91) in konventionellen MR-Sequenzen wie der T2-gewichteten HASTE-Sequenz (Half Fourier Acquisition Single shot Turbo

spin Echo) und der T1-gewichteten, fettgesättigten VIBE-Sequenz (Volume Interpolated Breath-Hold Examination), die aktuell die gängigsten Sequenzen für die Erkennung von Lungenrundherden in der MRT darstellen. Diese Sequenzen werden für die Thoraxbildgebung verwendet, da sie schnell akquiriert und zwischen den Atemzügen Schicht für Schicht aufgenommen werden können. Die Geschwindigkeit resultiert aus einer unvollständigen Füllung oder Abtastung des k-Raums, was diese Sequenzen sehr anfällig für Bewegungsartefakte macht (92). Eine mögliche Lösung zur Verringerung des Bewegungseinflusses besteht darin, die Art der k-Raum-Akquisition zu ändern.

Ein neueres Beispiel ist die radial akquirierte Stack of Stars T1-gewichtete Gradientenecho (GRE) 3D-VIBE-Sequenz (StarVIBE), bei der keine Atempausen nötig sind (89,93). Bei der StarVIBE-Sequenz werden die Daten entlang einzelner radialer Speichen aufgenommen. Aufgrund der Überlappung der Speichen in der Mitte können Phasenkodierfehler durch Mittelung niederfrequenter Komponenten reduziert werden. Diese Überlappung hat einen bewegungsausgleichenden Effekt, sodass Bilder während der freien Atmung akquiriert werden können, was nicht nur Artefakte reduziert, sondern auch den Vorteil einer höheren räumlichen Auflösung bietet, da die Akquisitionszeit nicht auf die Dauer einer Atempause begrenzt ist (92).

Der geringere Bewegungseinfluss bei der MRT des Thorax ist insbesondere für die Beurteilung von Lungenkarzinomen und Lungenmetastasen interessant, da die MRT aus den bereits genannten Gründen immer noch große Nachteile gegenüber der CT aufweist. Ob diese Technologie Vorteile bei der Erkennung von Lungenrundherden im Vergleich zu konventionellen MRT-Sequenzen bietet, ist bisher noch nicht untersucht worden.

Ziel dieser Studie war daher der Vergleich des diagnostischen Potenzials der StarVIBE-Sequenz mit der konventionellen T1-gewichteten, fettgesättigten

Postkontrast-VIBE-Sequenz, der T2-gewichteten, fettunterdrückten HASTE-Sequenz und der Computertomographie als Referenzstandard zur Erkennung von Lungenrundherden in der kontrastverstärkten Ganzkörper [¹⁸F]FDG PET/MRT Untersuchung.

88 Patientinnen mit neu diagnostiziertem Mammakarzinom wurden sowohl einer kontrastverstärkten Ganzkörper-PET/MRT mit [¹⁸F]FDG als auch einer Computertomographie unterzogen. Der Thorax der Patientinnen wurde sowohl mit der CT als auch mit der StarVIBE und konventionellen T1-gewichteten VIBE- und T2-gewichteten HASTE-MR-Sequenzen untersucht, wobei die Computertomographie als Referenzstandard diente. Vorhandensein, Größe und Lage aller nachweisbaren Lungenrundherde wurden bewertet. Zum Vergleich wurde der Wilcoxon-Vorzeichen-Rang-Test angewandt und es wurden Pearson's und Spearman's Korrelationskoeffizienten berechnet.

Von 65 Lungenrundherden, die bei 36 Patienten mit der CT ($3,7 \pm 1,4$ mm) entdeckt wurden, konnten mit der StarVIBE 31 (47,7 %), mit der VIBE 26 (40 %) bzw. mit der HASTE 11 (16,8 %) entdeckt werden. Insgesamt zeigte die CT eine signifikant höhere Detektionsrate als alle MRT-Sequenzen zusammen (65 vs. 36, Differenz 44,6 %, $p < 0,001$). Die VIBE wies eine signifikant bessere Detektionsrate auf als die HASTE (23,1 %, $p = 0,001$). Die Detektionsraten zwischen StarVIBE und VIBE unterschieden sich nicht signifikant (7,7 %, $p = 0,27$), wobei die StarVIBE aber einen signifikanten Vorteil bei der Detektion zentral gelegener Lungenrundherde zeigen konnte (66,7 % vs. 16,7 %, $p = 0,031$). Es bestand eine starke Korrelation der Größe der Rundherde zwischen CT- und MRT-Sequenzen (HASTE: $p = 0,80$, $p = 0,003$; VIBE: $p = 0,77$, $p < 0,001$; StarVIBE: $p = 0,78$, $p < 0,001$). Die mittlere Bildqualität wurde sowohl für die Computertomographie als auch für die MRT-Sequenzen als sehr gut bis ausgezeichnet bewertet.

Zusammenfassend hat diese Studie gezeigt, dass die Erkennung von Lungenrundherden mit der T1-gewichteten 3D Stack of Stars GRE (StarVIBE) MR-Sequenz als Teil eines Ganzkörper [¹⁸F]FDG PET/MRT Tumorstaging-Protokolls nicht signifikant besser war als mit der herkömmlichen T1-gewichteten VIBE-Sequenz mit Atemstillstand, aber signifikant besser als mit der T2-gewichteten HASTE-Sequenz. Die StarVIBE-Sequenz scheint besonders vorteilhaft bei der Erkennung zentral gelegener Lungenrundherde zu sein. Allerdings ist die Sensitivität der [¹⁸F]FDG PET/MRT bei der Erkennung von Lungenrundherden im Vergleich zur CT immer noch deutlich eingeschränkt, sodass diese ein Risiko birgt, kleine Lungenmetastasen bei onkologischen Patienten zu übersehen.

5. Arbeit: Bruckmann NM, Kirchner J, Grueneisen J, Li Y, McCutcheon A, Aigner C, Rischpler C, Sawicki LM, Herrmann K, Umutlu L, Schaarschmidt BM (2021). *Correlation of the apparent diffusion coefficient (ADC) and standardized uptake values (SUV) with overall survival in patients with primary non-small cell lung cancer (NSCLC) using 18F-FDG PET/MRI. Eur J Radiol.*

Das Lungenkarzinom ist die zweithäufigste diagnostizierte Krebserkrankung weltweit und mit 18 % der Hauptgrund für krebsbedingte Todesfälle. Etwa 83 % der Erkrankungen sind dabei auf das nicht-kleinzelige Lungenkarzinom (NSCLC) zurückzuführen (94–96). Für die effektive Tumorbehandlung ist ein möglichst exaktes primäres Tumorstaging unabdingbar. Daher spielt die diagnostische Bildgebung eine entscheidende Rolle. Die [¹⁸F]FDG PET/CT hat sich bereits als unverzichtbares Instrument für das initiale Tumor-Staging und die Erkennung von Rezidiven erwiesen, insbesondere aufgrund ihrer hohen Genauigkeit bei der Erkennung des Primarius sowie lokoregionaler und Fernmetastasen (18,97–99). Daher wurde die Hybrid-

Bildgebung in alle wichtigen Leitlinien für das Staging des primären Lungenkarzinoms aufgenommen (96,100). Mit der $[^{18}\text{F}]$ FDG PET/MRT steht darüber hinaus eine Bildgebung zu Verfügung, die neben vergleichbaren diagnostischen Ergebnissen (101–103) zusätzlich Informationen über Metabolismus mittels PET und Tumorzellularität mittels funktioneller Bildgebung wie den diffusionsgewichteten Sequenzen (DWI) geben kann (104–108).

Die Rolle des SUVmax als nützlicher prognostischer Marker für das Gesamtüberleben bei Tumorpatienten wurde schon in diversen Studien und Tumorentitäten untersucht, beispielweise beim kolorektalen Karzinom und beim Mammakarzinom. Ein hoher SUVmax des Primarius scheint hierbei mit dem Risiko eines Tumorrezidivs zu korrelieren und ist mit einer schlechten Prognose assoziiert. Speziell beim NSCLC sind die bisherigen Studienergebnisse jedoch nicht eindeutig (4,5,109–111).

Eine positive Korrelation zwischen dem Diffusionskoeffizienten (ADC), der als quantitativer Biomarker aus der DWI abgeleitet werden kann, und prognostischen Faktoren wurde bereits bei anderen Tumorentitäten beschrieben, z. B. beim Prostatakarzinom (6). Das prognostische Potential beim Lungenkarzinom ist jedoch bisher nicht untersucht worden. Dennoch weisen einige Studien auf das Potenzial von ADC-Werten bei der Vorhersage eines Tumoransprechens im Vergleich zur PET/CT hin (112,113). Daher könnte die DWI mit ADC-Wert-Messung ein weiterer prognostischer Marker für das Gesamtüberleben bei Patienten mit NSCLC sein.

Ziel unserer Studie war es, ADC- und SUV-Werte aus $[^{18}\text{F}]$ FDG PET/MRT Untersuchungen mit dem Gesamtüberleben zu korrelieren, um einen unabhängigen oder kombinierten Marker für das Langzeitergebnis von Patienten mit fortgeschrittenem NSCLC zu ermitteln.

Insgesamt erhielten 92 Patientinnen mit neu diagnostiziertem, histopathologisch gesichertem NSCLC (44 Frauen, 48 Männer, mittleres Alter $63,1 \pm 9,9$ Jahre) eine

dezidierte thorakale [¹⁸F]FDG PET/MRT Untersuchung. Es wurde eine region of interest (ROI) manuell in den fusionierten PET/MRT-Bildern um den Primarius festgelegt, um die maximalen und mittleren SUV-Werte zu ermitteln (SUVmax, SUVmean). Gleichzeitig wurden die mittleren und minimalen ADC-Werte bestimmt (ADCmean, ADCmin). Der Einfluss der Parameter auf das Gesamtüberleben wurde mittels Hazard Ratios (HR) getestet sowie Abhängigkeiten zwischen den Werten berechnet.

Bei der Auswertung aller 92 Patienten (n=59 verstorben zum Zeitpunkt der retrospektiven Datenerfassung, mittlere Zeit bis zum Tod: 19 ± 16 Monate, mittlere Zeit bis zur letzten Nachuntersuchung: 56 ± 22 Monate) ergab sich für den SUVmax als unabhängiger Prädiktor für das Gesamtüberleben eine Hazard Ratio von 2,37 (95% CI: 1,23-4,59, p = 0,008), für den SUVmean von 1,85 (95% CI: 1,05-3,26, p = 0,03), während der ADCmin eine HR von 0,95 (95% CI: 0,57-1,59, p = 0,842) und der ADCmean eine HR von 2,01 (95% CI: 1,2-3,38, p = 0,007) aufwies. Darüber hinaus ergab eine kombinierte Analyse für SUVmax/ADCmean, SUVmax/ADCmin und SUVmean/ADCmean eine HR von 2,01 (95% CI: 1,10-3,67, p = 0,02), 1,75 (95% CI: 0,97-3,15, p = 0,058) und 1,78 (95% CI: 1,02-3,10, p = 0,04).

Zusammenfassend unterstreicht diese Studie den Wert von SUVmax und SUVmean als unabhängige prognostische Marker für das Gesamtüberleben bei Patienten mit NSCLC, während der ADC-Wert als alleiniger Marker keinen diagnostischen Nutzen zeigt. Auch die kombinierte Analyse des Glukosestoffwechsels und der Tumorzellularität durch die Bildung von Hazard Ratios kann keine Verbesserung in der Vorhersage des Gesamtüberlebens erreichen. Daher müssen wir zum jetzigen Zeitpunkt schlussfolgern, dass die multiparametrische Auswertung von NSCLC-Patienten mittels [¹⁸F]FDG PET/MRT durch eine kombinierte Analyse von SUV und

ADC gegenüber der alleinigen SUVmax-Messung bei der Vorhersage des Gesamtüberlebens keine Vorteile bietet.

6. Arbeit: Bruckmann NM, Rischpler C, Kirchner J, Umutlu L, Herrmann K, Ingenwerth M, Theurer S, Lahner H, Antoch G, Sawicki LM.

Correlation between contrast enhancement, standardized uptake value (SUV), and diffusion restriction (ADC) with tumor grading in patients with therapy-naïve neuroendocrine neoplasms using hybrid ⁶⁸Ga-DOTATOC PET/MRI. Eur J Radiol.

Neuroendokrine Neoplasien gelten als sehr seltene Tumorentität, die mit etwa 7/100000 Fällen im Jahr weltweit nur etwa 1 % der Neoplasien ausmacht (114). Insgesamt hat die Inzidenz aber aufgrund neuer Detektionsmöglichkeiten in den letzten Jahren erheblich zugenommen (115). Es handelt sich bei NEN um eine heterogene Gruppe von Tumoren, die von allen endokrinen Systemen der Körpers ausgehen können und sich grundlegend in ihrer Histologie, der hormonellen Aktivität, der molekularen Signatur oder in ihrem Aggressivitätsgrad unterscheiden können (116). Auch regional gibt es Unterschiede bei den NEN. Während in westlichen Populationen die Erstmanifestation häufig im Dünndarm lokalisiert ist, gehen in Asien die NEN meist vom Rektum aus. Weitere häufige Lokalisationen sind das Pankreas, die Lungen und der Magen (115,117,118). Aufgrund dieser Heterogenität kann sowohl die Therapie als auch das Ansprechen auf eine Behandlung und damit die Prognose variieren (117). Entsprechend der aktuellen Klassifikation der Weltgesundheitsorganisation (WHO) von 2017 lassen sich die neuroendokrinen

Neoplasien in einen gut und einen schlecht differenzierten Typ unterscheiden. Bei den gut differenzierten neuroendokrinen Tumoren (NET) erfolgt zusätzlich anhand der Mitoserate und des Ki-67-Index eine Unterteilung in niedriggradig (G1, Ki67 < 3%), mittelgradig (G2, Ki67 3-20 %) oder hochgradig (G3, Ki-67 >20 %). Schlecht differenzierte Neoplasien vom groß- oder kleinzelligen Typ werden hingegen als neuroendokrine Karzinome (NEC) bezeichnet und ebenfalls als Grad 3 (G3) klassifiziert (117,119,120). Durch die Anwendung von hochgradig Somatostatinrezeptor (SSTR)-aviden ^{68}Ga -markierten 1,4,7,10-Tetraazacyclododecan-1,4,7,10-Tetraacidsäure (DOTA)-Peptiden, wie beispielsweise ^{68}Ga -DOTA-Phel-Tyr3-Octreotid (DOTATOC) für die Positronen-Emissions-Tomographie (PET) in Kombination mit der Computertomographie (CT) oder der Magnetresonanztomographie im Rahmen der Hybridbildgebung hat sich die Erkennungsrate auch sehr kleiner Läsionen in den letzten Jahren deutlich verbessert. Aus diesem Grund hat sich die ^{68}Ga -DOTA-Peptid-basierte PET/CT- oder PET/MRT zum bildgebenden Goldstandard in der NEN Diagnostik entwickelt. Die PET/MRT bietet hierbei aufgrund des besseren Weichteilkontrasts und der Verwendung von funktionellen Bildgebungssequenzen wie der diffusionsgewichteten Bildgebung (DWI) im Vergleich zum PET/CT einen zusätzlichen Vorteil (50–53). Mit der gleichzeitigen Erfassung von morphologischen und funktionellen MR-Sequenzen und PET-Bildern kann die ^{68}Ga -DOTATOC PET/MRT Vorteile bei der Vorhersage des Tumorgrades und der Aggressivität von NEN (126–132) bieten. Beispielsweise stellt die DWI aus der MRT einen Surrogatparameter für die Tumorzelldichte dar und ist durch den Diffusionskoeffizienten quantifizierbar (126). Eine Korrelationsanalyse zwischen ADC und dem Tumorgrading kann daher einen Zusammenhang zwischen diesen Merkmalen aufzeigen und eine nicht-invasive Bewertung der Tumoraggressivität ermöglichen (55–58). Es wurde auch festgestellt, dass die zunehmende

Entdifferenzierung von NEN zu einer Abnahme der SSTR-Expression und damit des SUV bei der DOTATOC-Bildgebung führt. Neben der DOTATOC-Expression galt lange auch die intensive arterielle und venöse Anreicherung zu den charakteristischen bildgebenden Merkmalen von NEN (130). Neuere Studien zeigen jedoch, dass ein großer Teil der Tumoren auch eine geringere Perfusion aufweisen kann, insbesondere bei G2/G3-Tumoren (131,132). Da die Behandlung in hohem Maße vom Grad des Tumors abhängt, ist eine bildbasierte Charakterisierung der Histopathologie von NEN und die Auswahl geeigneter Biopsiestellen äußerst wünschenswert (129).

Ziel dieser Studie war es daher, das Ausmaß der Kontrastmittelanreicherung, die Diffusionsrestriktion und den SUV unter Verwendung eines ⁶⁸Ga-DOTATOC PET/MRT mit dem Tumorgrading bei therapienaiven NEN-Patienten zu korrelieren.

Insgesamt wurden 26 Patienten mit neu diagnostizierter, therapienaiver neuroendokriner Neoplasie in diese prospektive Studie aufgenommen und mittels eines ⁶⁸Ga-DOTATOC PET/MRT untersucht. Die Bilder wurden hinsichtlich der Anzahl und Lage der NEN-Läsionen, der vorherrschenden Tumorsignalintensität auf nativen T1w- und T2w-Bildern und auf T1w-Bildern in der arteriellen und portalvenösen Phase untersucht. Außerdem wurde jeweils der ADC-Wert und der SUVmax der Läsionen erfasst. Das histopathologische Tumorgrading wurde anschließend mittels des Pearson-Korrelationskoeffizienten und des exakten Fisher-t-Test mit den PET/MRT-Merkmalen korreliert. Es wurde eine binäre logistische Regressionsanalyse durchgeführt und Odds Ratios (OR) berechnet, um einen möglichen Zusammengang mit einer aggressiven Tumobiologie zu bewerten.

In der Auswertung ergab sich eine moderate negative Korrelation zwischen arterieller Kontrastmittelanreicherung und Tumorgrading ($r=-0,35$, $p=0,005$), während die portalvenöse Anreicherung eine schwache positive Korrelation mit dem Ki-67-Index ($r=0,28$, $p=0,008$) und eine nicht-signifikante positive Korrelation mit dem

Tumorgrading ($r=0,19$, $p=0,063$) zeigte. Merkmale, die signifikant mit einer aggressiven Tumoriologie assoziiert waren, waren das Vorhandensein von Lebermetastasen (OR 2,6, $p=0,042$), eine T1w-Hyperintensität im Vergleich zum Muskel (OR 12,7, $p=0,0001$), eine Hyperintensität in der arteriellen Phase (OR 1,4, $p=0,001$), eine Diffusionseinschränkung (OR 2,8, $p=0,02$) und ein SUVmax oberhalb des Leberniveaus (OR 7,0, $p=0,001$).

Zusammenfassend zeigt diese Studie, dass die aus der ^{68}Ga -DOTATOC PET/MRT gewonnenen Merkmale wie die arterielle und portalvenöse Kontrastmittelanreicherung, die Diffusionsbildgebung und der SUVmax mit dem Tumorgrading assoziiert sind und zur Vorhersage des NEN-Gradings und der Aggressivität des Tumors verwendet werden können.

7. Arbeit: Bruckmann NM, Lindemann ME, Grueneisen J, Grafe H, Li Y, Sawicki LM, Rischpler C, Herrmann K, Umutlu L, Quick HH, Schaarschmidt BM (2021). *Comparison of pre- and post-contrast-enhanced attenuation correction using a CAIPI-accelerated T1-weighted Dixon 3D-VIBE sequence in ^{68}Ga -DOTATOC PET/MRI.* Eur J Radiol.

Während der PET-Datenerfassung werden die Photonen durch das umgebende Körpergewebe und die Hardwarekomponenten abgeschwächt, bevor sie den PET-Detektor erreichen (133). Diese Schwächung der Photonen führt letztlich zu einer systematischen Verzerrung bei der PET-basierten Tracer-Quantifizierung und folglich erfordert die PET-Datenrekonstruktion genaue Mittel zur Schwächungskorrektur (AC), um korrekte quantitative Ergebnisse zu liefern.

Bei der PET/CT liefert die CT-Bildgebung nützliche Informationen über die Elektronendichte der einzelnen Gewebe und über die geometrische Darstellung der

photonenschwächenden Organe im Körper. Diese Daten können direkt umgewandelt werden, indem die im CT gemessenen Hounsfield-Einheiten (HU) jedes Gewebes in lineare Abschwächungskoeffizienten (LACs) auf dem PET-Emissionsenergieniveau von 511 keV umgerechnet werden. Auf diese Weise können die CT-Daten für die CT-basierte Abschwächungskorrektur (CTAC) verwendet werden, die eine bewährte Methode in der PET/CT ist (33,34,133).

Bei der PET/MRT gestaltet sich die Erstellung einer Schwächungskorrektur schwieriger. Das MR-Signal steht in keinem Zusammenhang mit der Elektronendichte des untersuchten Gewebes und kann nicht direkt für eine MR-Schwächungskorrektur (MRAC) verwendet werden (134). In der klinischen Anwendung von PET/MRT-Scannern ist die heute am häufigsten verwendete Methode für die MRAC ein Segmentierungsansatz, der auf einer MR-Dixon-VIBE-Sequenz (*Volume interpolated breath-hold examination*) basiert (134,135). Die MR-Bilder werden in vier Gewebeklassen (Luft, Lunge, Fett, Weichgewebe) segmentiert und jeder segmentierten Gewebeklasse wird ein vordefinierter Abschwächungskoeffizient zugewiesen, um eine aus vier Kompartimenten bestehende Abschwächungskarte, die so genannte μ map, zu erstellen (2,134,136). In den letzten Jahren wurden solche MRAC-Methoden weiter verfeinert und die anfänglichen Einschränkungen im Vergleich zu CTAC wurden durch die Hinzufügen von Knochenmodellen als weitere Gewebeklasse und durch das Hinzufügen einer Trunkierungskorrektur für die Arme zur μ map verringert (137,138). Darüber hinaus wurde kürzlich eine CAIPIRINHA-beschleunigte (Controlled aliasing in parallel imaging results in higher acceleration) Dixon 3D-VIBE (MRACaipi) eingeführt, um die räumliche Auflösung der resultierenden μ maps im Vergleich zu den ursprünglichen Dixon-VIBE-Sequenzen weiter zu verbessern (139,140).

Im Allgemeinen empfehlen die Hersteller von PET/MRT-Systemen die Akquisition einer nicht kontrastverstärkten Dixon-MRAC-Sequenz für die μ map-Rekonstruktion, um eine optimale Gewebeklassifizierung zu gewährleisten (141). Dementsprechend muss die Dixon-MRAC-Sequenz zu Beginn der Ganzkörper-PET/MRT Untersuchung und damit vor einer möglichen Verabreichung von intravenösem Kontrastmittel durchgeführt werden. Im klinischen Umfeld bestehen PET/MRT-Protokolle für ^{68}Ga -Tracer-basierte Untersuchungen jedoch häufig aus zwei Schritten: erstens einer Ganzkörper-Bildgebung, und zweitens einer speziellen Bildgebung einzelner Organe, wie z. B. bei ^{68}Ga -PSMA für die Prostata oder ^{68}Ga -DOTATOC für die Bildgebung bei gastrointestinalen Tumoren. Bei solchen Protokollen könnte die Verabreichung von Kontrastmitteln während der Akquisition von Ganzkörpersequenzen zu einer μ map-Rekonstruktion mit kontrastverstärkten Dixon-MRAC-Sequenzen für die gezielte Organbildgebung führen oder umgekehrt. Da Gadolinium-basierte Kontrastmittel zu einer Verringerung der T1-Relaxation von Blut und Gewebe führen, kann die Gewebesegmentierung in der μ map durch die Kontrastmittelgabe beeinflusst werden und folglich die PET-Tracer-Quantifizierung in der Ganzkörper-PET/MRT verfälschen, wie in früheren Studien für eine ältere Version der Dixon MRAC-Sequenz gezeigt wurde (142).

Entsprechend diesen praktischen Anforderungen des klinischen Arbeitsablaufs bei ausgewählten PET/MRT-Anwendungen war der Zweck dieser retrospektiven Studie die Bewertung eines möglichen Einflusses der Gadolinium-Kontrastmittelverabreichung auf die MR-basierte Schwächungskorrektur unter Verwendung einer modernen CAIPI-beschleunigten Dixon-basierten Sequenz mit hoher räumlicher Auflösung, einer Knochenkorrektur und einer MR-basierten Trunkierungskorrektur bei ^{68}Ga -DOTATOC PET/MRT Untersuchungen. Das übergeordnete Ziel dieser Studie war es, zu prüfen, ob die neueste Version der Dixon-

MRAC-Sequenz und ihr Segmentierungsalgorithmus vor und nach der Kontrastmittelverabreichung in einem klinischen Umfeld identische Ergebnisse liefern, da dies eine höhere Flexibilität für die Planung komplexer klinischer PET/MRT-Protokolle bieten würde.

51 Patienten mit neuroendokrinen Tumoren unterzogen sich einer ^{68}Ga -DOTATOC PET/MRT-Ganzkörperuntersuchung zum Tumor-Staging. Für jeden Patienten wurden erfolgreich zwei μ maps (vor und nach Gadolinium KM-Gabe) aufgenommen und zwei PET-Datensätze pro Patient rekonstruiert, die als Grundlage für die weitere quantitative Auswertung dienten. Die SUV-Werte von 21 definierten *volume of interest* (VOI) wurden in beiden PET-Datensätzen pro Patient erhoben. Ein Student's t-Test für gepaarte Stichproben wurde durchgeführt, um mögliche Unterschiede zwischen den beiden AC-Karten und den beiden rekonstruierten PET-Datensätzen zu ermitteln. Es wurde eine Bonferroni-Korrektur durchgeführt, um eine Akkumulation von α -Fehlern zu verhindern. Bei einem p-Wert von $p<0,0024$ wurden die Daten als statistisch signifikant betrachtet.

Bereits die visuelle Auswertung der μ maps zeigte deutliche Unterschiede in der relativen Abschwächung in den Postkontrast-AC-Maps, insbesondere in der Lunge bei 46/51 der Patienten (90,2 %) mit Nachweis einer zusätzlichen perihilären Weichteilsegmentierung sowie auch im Fettgewebe aller Patienten. In den Postkontrast- μ maps wurde beobachtet, dass das Fettgewebe bei allen Patienten teilweise mit einem zusätzlichen Kompartiment segmentiert war. Diesem zweiten Kompartiment im Fettgewebe wurde automatisch eine LAC von $0,0927 \text{ cm}^{-1}$ zugewiesen, die zwischen der LAC von Weichgewebe ($0,1 \text{ cm}^{-1}$) und Fett ($0,0854 \text{ cm}^{-1}$) liegt. Bei 27,5 % (14/51 Patienten) konnte auch zusätzliches Weichteilgewebe im Knochenmark nachgewiesen werden. Darüber hinaus war bei 3,9 % (2/51) der Patienten ein fehlendes Signal der Schädelbasis bzw. ein fehlendes Signal von Teilen

des Achsenknochens in der Nachkontrast-AC-Karte erkennbar. Bei 5,9 % (3/51) war ein kleiner Offset des Achsenknochens nachweisbar. Daher wurde die LAC des Knochens in diesen drei Fällen mit der LAC des Weichteilgewebes gleichgesetzt. Dies führte zu einer leichten systematischen Unterschätzung der PET-Daten in diesen Knochenregionen. Bei einem Patienten (1/51) konnte eine vollständige Fehlklassifizierung der inneren Organe und ein "Swap" von Fett- und Weichgewebe beobachtet werden. Signifikante quantitative Unterschiede zwischen den SUVmax-Werten wurden im perirenalen Fett ($19,65 \pm 48,03\%$, $p<0,0001$), im axillären Fett ($17,46 \pm 63,67\%$, $p<0,0001$) und im dorsalen subkutanen Fett auf Höhe des Lendenwirbelkörpers L4 ($10,26 \pm 25,29\%$, $p<0,0001$) festgestellt. Signifikante Unterschiede zeigten sich auch in der Lunge apikal ($5,80 \pm 10,53\%$, $p<0,0001$), dorsal auf Höhe des Lungenstamms ($15,04 \pm 19,09\%$, $p<0,0001$) und dorsal in der Basallunge ($51,27 \pm 147,61\%$, $p<0,0001$).

Die Ergebnisse dieser Studie deuten darauf hin, dass die Verabreichung von Gadolinium-Kontrastmittel einen potenziellen Einfluss auf die MR-basierte Schwächungskorrektur in bestimmten Gewebekompartimenten wie Fett und Lunge haben und erhebliche interindividuelle Abweichungen in mehreren Organen verursachen kann, insbesondere bei Verwendung einer CAIPI-beschleunigten Dixon-basierten Sequenz im ^{68}Ga -DOTATOC-PET/MRT. Daher sollte die MR-basierte Abschwächungskorrektur bei der PET/MRT vor der Kontrastmittelgabe durchgeführt werden. Komplexe hybride Bildgebungsprotokolle, die sowohl Ganzkörperuntersuchungen als auch spezielle Untersuchungen bestimmter Organe wie Prostata oder gastrointestinale Tumorbildgebung umfassen, sollten entsprechend angepasst werden.

8. Arbeit: Bruckmann NM, Rischpler C, Tsiami S, Kirchner J, Abrar DB, Bartel T, Theysohn J, Umutlu L, Herrmann K, Fendler WP, Buchbender C, Antoch G, Sawicki LM, Tsobanelis A, Braun J, Baraliakos X (2022).

Effects of anti-TNF-therapy on inflammatory, structural and osteoblastic activity lesions in radiographic axial spondyloarthritis - a prospective proof-of-concept study using PET/MRI of SIJ and spine. Arthritis Rheumatol.

Die röntgenologische axiale Spondyloarthritis (SpA), auch bekannt als ankylosierende Spondylitis (AS) (143), ist eine chronisch-entzündliche rheumatische Erkrankung, die die am weitesten fortgeschrittene Form der axialen Spondylarthritiden beschreibt (144). In der Frühphase ist die Erkrankung durch eine chronische Entzündung lumbal und in den Iliosakralgelenken (SI) gekennzeichnet (145). Bei Fortschreiten kann sich die Entzündung auf die Wirbelsäule ausweiten und zu einer vollständigen Versteifung des Achsenskeletts und zu entsprechenden Haltungsschäden führen, die mit schweren körperlichen Behinderungen und eingeschränkter Lebensqualität einhergehen (146,147).

Die Behandlung umfasst nicht-pharmakologische und pharmakologische Maßnahmen, wobei letztere in erster Linie nicht-steroidale anti-inflammatorische Medikamente (NSAIDs) umfassen. Bei Patienten, die nicht auf eine NSAID-Behandlung ansprechen, können biologische Antirheumatika (bDMARDs) wie z. B. Antikörper gegen den Tumornekrosefaktor (TNFi) oder Interleukin-17 eingesetzt werden (148).

Die Bildgebung spielt eine wesentliche Rolle bei der Diagnose und Behandlung der axialen Spondyloarthritis und kann auch zur Beurteilung des Therapieansprechens verwendet werden (149,150). Der derzeitige diagnostische Goldstandard bei der axialen Spondyloarthritis ist die MRT, da sie entzündliche Veränderungen wie

Knochenmarködeme als auch strukturelle Schäden wie Fettläsionen, Erosionen, Sklerose und Ankylose (149,151,152) unterscheiden kann.

Die Einführung von hybriden Bildgebungsverfahren wie Positronen-Emissions Tomographie/Computertomographie (PET/CT) und PET/MRT ermöglicht zusätzliche Einblicke in die Pathogenese und die Stoffwechselaktivität der röntgenologischen axialen Spondyloarthritis (9). Daher wird der osteoblastenspezifische Radiotracer ¹⁸F-NaF zur Visualisierung der lokalen Osteoblastenaktivität in entzündlichen und strukturellen Läsionen bei röntgenologischer axialer Spondyloarthritis zunehmend in Studien angewendet (9,153,154). Viele dieser Studien bestätigen, dass das Niveau der Osteoblastenaktivität an Stellen besonders hoch war, an denen ein Knochenmarködem und fetthaltige Läsionen im MRT nachgewiesen wurden, und dass Knochenmarködeme und Fettläsionen mit der Entwicklung von Syndesmophyten und neuer Knochenbildung korrelieren (155). Dies steht im Einklang mit den Ergebnissen neuerer Biopsiestudien bei Patienten mit röntgenologischer axialer Spondyloarthritis (156).

Eine kontinuierliche Behandlung mit TNFi über ≥4 Jahre führte nachweislich zu geringeren Raten einer radiologischen Progression als die Behandlung mit Nicht-bDMARDs (149,157–159). Dies ist sehr wahrscheinlich auf die positive Wirkung von bDMARDs auf frühe inflammatorische Veränderungen der Wirbelsäule zurückzuführen. Eine direkte Wirkung von bDMARDs auf die osteoblastische Aktivität konnte jedoch bisher nicht nachgewiesen werden. Ziel dieser prospektiven Studie war es daher, mittels eines ¹⁸F-NaF PET/MRT die Wirkung von TNFi auf die osteoblastische Aktivität in krankheitsspezifischen Läsionen zu analysieren.

Hierzu wurden 16 Patienten mit klinisch aktiver röntgenologischer axialer Spondyloarthritis in die Studie eingeschlossen. Die Patienten erhielten eine ¹⁸F-NaF PET/MRT-Untersuchung der Iliosakralgelenke und der Wirbelsäule nach initialer TNFi

Therapie sowie erneut etwa 3-6 Monate nach Beginn der Behandlung. Die Bilder wurden auf das Vorhandensein von Knochenmarködemen, strukturellen Läsionen (d. h. Fettläsionen, Sklerose, Erosionen und Ankylose) und ¹⁸F-NaF-Uptake in den Quadranten der Sakroiliakgelenke und den Wirbelkörpern untersucht.

Insgesamt wurden 11 männliche und 5 weibliche Patienten (Durchschnittsalter \pm SD 38,6 \pm 12,0 Jahre) über einen Zeitraum von 4,6 Monaten untersucht. Die ¹⁸F-NaF PET/MRT-Untersuchung wurde bei 16 Patienten an den SI-Gelenken und bei 10 Patienten an der Wirbelsäule durchgeführt. Zu beiden Zeitpunkten wurden 128 SI-Gelenkquadranten und 920 Wirbelkörperquadranten analysiert. Zu Beginn der Untersuchung wurde eine ¹⁸F-NaF-Aufnahme in 96,0 % der SI-Gelenkquadranten mit Knochenmarködem, bei 94,2 % mit Sklerose und bei 88,3 % mit Fettläsionen nachgewiesen. In der Follow-Up Untersuchung waren bei 65,3 % der SI-Gelenk-Quadranten mit Knochenmarködem ($P < 0,001$), bei 33,8 % mit Sklerose ($p = 0,23$) und bei 24,5 % mit Fettläsionen ($p = 0,01$) eine geringere ¹⁸F-NaF Aufnahme im Vergleich zum Ausgangswert nachweisbar. Bei den Wirbelkörperquadranten war die ¹⁸F-NaF-Aufnahme zu Studienbeginn bei 81,5 % der Ränder mit Sklerose, bei 41,9 % mit Fettläsionen und 33,7 % mit Knochenmarködemen zu finden. Bei der Nachuntersuchung zeigten 73,5 % der VCs mit Knochenmarködem ($P = 0,01$), 53,3 % mit Fettläsionen ($P = 0,03$) und 55,6 % mit Sklerose ($P = 0,16$) eine geringere ¹⁸F-NaF-Aufnahme im Vergleich zum Ausgangswert.

Die Ergebnisse dieser Studie deuten darauf hin, dass eine frühzeitige Einleitung einer entzündungshemmenden Therapie mit TNFi eine positive, antiosteoblastische Wirkung haben könnte, die zu einer Rückbildung der radiologischen Progression bei Patienten mit aktiver radiologischer axialer Spondylarthritis führt. Weitere Untersuchungen mit größeren Patientenkollektiven sind erforderlich, um diese Ergebnisse zu bestätigen. Es wird auch interessant sein zu sehen, ob die Behandlung

mit anderen bDMARDs, wie Interleukin-17-Inhibitoren oder mit kleinen Molekülen wie JAK-Inhibitoren zu ähnlichen Ergebnissen führen wird.

Diskussion

Die besondere Stärke hybrider Bildgebungsverfahren liegt in ihrer Möglichkeit, sowohl morphologische als auch metabolische Veränderungen im Körper darzustellen. Die PET/MRT ist die neueste der hybriden Bildgebungsverfahren und wurde in den letzten Jahren immer häufiger auch in der klinischen Praxis eingesetzt. Durch das hierbei eingesetzte MRT lassen sich auch die Informationen aus der funktionellen MRT-Bildgebung nutzen. Die Entwicklung neuer Radiopharmaka, die spezifisch an bestimmte biochemische Prozesse im Körper binden, kann zusätzliche Anwendungsmöglichkeiten für die PET/MRT bei vielen entzündlichen und onkologischen Erkrankungen zur Früherkennung oder Verlaufskontrolle schaffen (160,161). In den hier vorgestellten Arbeiten wurden unterschiedlichen klinische Anwendungsmöglichkeiten, das diagnostische Potential und mögliche Fehlerquellen einer PET/MRT untersucht und Vorteile, Limitationen und zukünftige Entwicklungen diskutiert.

Seit ihrer Einführung haben eine Vielzahl von Studien den diagnostischen Wert der PET/MRT für das Staging von Tumorerkrankungen belegt (162). Das Mammakarzinom ist die häufigste Tumorerkrankung und hat die zweithöchste krebsbedingte Morbidität bei Frauen weltweit (163). Neben einer molekularen Subtypisierung und der pathologischen Diagnose ist das Stadium entscheidend für das Überleben von Brustkrebspatientinnen. Aus diesem Grund hat eine möglichst exakte Bildgebung einen hohen Stellenwert in der Diagnostik und Nachsorge von Brustkrebspatientinnen. Die PET/MRT bietet hier durch den Einsatz des MRT

zusätzlich den Vorteil einer besseren Auflösung des Brustgewebes und kann bei der Diagnostik des Primärtumors helfen.

Entsprechend der aktuellen Leitlinien der Europäischen Gesellschaft für Medizinische Onkologie (ESMO) von 2020 und des National Comprehensive Cancer Network (NCCN) von 2021 ist bei Patientinnen mit fortgeschrittenem Mammakarzinom aktuell eine thorakoabdominelle Computertomographie sowie eine Knochenszintigraphie empfohlen (45,58). Einzelne Studien zeigen aber auch Vorteile einer Ganzkörper-Staging-Untersuchung mittels MRT, insbesondere bei der Detektion von Knochenmetastasen und bei Patientinnen mit Anzeichen einer möglichen Rückenmarkskompression (75,164). In den *Arbeiten 1 und 2* konnte jedoch gezeigt werden, dass die PET/MRT die höchstmögliche diagnostische Genauigkeit bietet und sowohl CT als auch MRT in der Beurteilung des N- und M-Stadiums bei Patientinnen mit primärem Brustkrebs überlegen ist. Die Studienergebnisse bestätigen die Resultate aus vorherigen Studien von Sawicki et al. (165), Botsikas et al. (166) und Heusner et al. (167), die ebenfalls eine verbesserte Genauigkeit und Reduktion falsch positiver Werte zeigen konnten. Der Vorteil dieser Studie im Gegensatz zu früheren Arbeiten ist die große, prospektiv erfasste Patientenkohorte, die sich neben dem PET/MRT beim Primärstaging den aktuellen ESMO-Leitlinien unterzieht und somit die klinische Routine widerspiegelt.

Insbesondere die frühzeitige Detektion von Fernmetastasen ist für die Wahl des richtigen Therapieregimes relevant und kann einen großen Einfluss auf Mortalität und Morbidität haben. Im Rahmen der Erkrankung entwickeln etwa 30 % der betroffenen Frauen Fernmetastasen und hiervon fallen wiederum 50-70 % auf das Skelettsystem (68–72). In *Arbeit 3* konnte nun gezeigt werden, dass sowohl die [18F]FDG-PET/MRT als auch die Ganzkörper MRT allein dem derzeitigen Goldstandard aus CT und Skelettszintigraphie in der Detektion von Knochenmetastasen deutlich überlegen sind.

Dies bestätigt bereits frühere Ergebnisse über die diagnostische Aussagekraft von 18F-FDG PET/CT, MRT und Skelettszintigraphie (74,77,81,82). Korrelierend zu älteren Studien, beispielsweise der Arbeit von Bristol et al. (168) sollte aufgrund der auch in dieser Studie nachgewiesenen Überlegenheit der CT gegenüber der Knochenszintigraphie die Sinnhaftigkeit der Knochenszintigraphie beim Primärstaging hinterfragt (83,169) und die Ganzkörper-MRT als Diagnostikum der Wahl diskutiert werden, da sie durch die Fähigkeit, metastatisches Knochenmark frühzeitig nachzuweisen, der CT insbesondere in der Detektion osteolytischer Metastasen deutlich überlegen ist (170,171). Entsprechend der aktuellen Datenlage bieten hybriden Bildgebungsverfahren keine höhere Sensitivität (172–174), können aber die diagnostische Sicherheit des Untersuchers in der Differenzierung zwischen benigne und maligne durch die Visualisierung eines pathologischen Glukosemetabolismus erhöhen (175).

Diverse Studien belegen außerdem eine höhere Sensitivität der PET/MRT Untersuchung gegenüber der PET/CT in der Detektion von Metastasen beim Mammakarzinom (56,57,176,177). In einer Studie von Pinker et al. (178) ließ sich darüber hinaus die Anzahl der unnötigen Biopsien mittels PET/MRT in einem Kollektiv von 78 suspekten Läsionen um die Hälfte verringern. Insgesamt sind die diagnostischen, bildgebenden Methoden jedoch weit davon entfernt, eine gleichwertige Alternative zur Biopsie darzustellen (179,180). Daher wird beispielsweise die Sentinel-Lymphknoten-Biopsie weiterhin als Methode der Wahl bei suspekten Lymphknoten großzügig angewendet (181–184). In Zukunft erhofft man sich durch die Einführung neuer, selektiver Radiotracer die Sensitivität in der Diagnostik weiter verbessern zu können. In der Mammadiagnostik wird beispielsweise der Tracer ⁶⁸Ga-FAPI-46 zunehmend angewendet. Das Molekül lagert sich an das Fibroblasten-Aktivierungsprotein (FAP) an, welches als Marker für invasive

Mammakarzinome gilt. In ersten Studien konnte durch die selektivere Anreicherung eine bessere Diagnostik unklarer Läsionen erreicht werden. Auch ist eine Reduktion falsch positiver Befunde möglich, beispielsweise durch die bessere Differenzierung von reaktiv anreichernden Läsionen nach Biopsie (185,186).

Eine wesentliche Einschränkung eines Ganzkörper-Stagings mittels PET/MRT bei diversen Tumorerkrankungen ist weiterhin die Anfälligkeit der MRT-Bildgebung für Atem- und Herzbewegungen, wodurch es zu einer reduzierten Beurteilbarkeit des Lungenparenchyms kommen kann. Daher gilt die CT-Thorax immer noch als Methode der Wahl zur Diagnostik potentieller Lungenmetastasen. Insbesondere kleinere Lungenrundherde sind in der MRT hierdurch teils nur schwer zu detektieren (187,188). Gerade in der Magnetresonanztomographie hat es in den letzten Jahren neue Entwicklungen gegeben, die mehrheitlich darauf abzielen, die Untersuchungszeit zu verkürzen und die Bildqualität zu verbessern. Ein Beispiel für die Lunge ist die radial akquirierte Stack of Stars T1-gewichtete Gradientenecho (GRE) 3D-VIBE-Sequenz (StarVIBE). Das besondere bei dieser Sequenz ist, dass die Daten entlang radialer Speichen aufgenommen werden, dadurch Atempausen nicht mehr nötig sind und Phasenkodierfehler aufgrund von Atmung und Herzschlag durch Mittelung reduziert werden. Da die Akquisitionszeit nicht auf die Atempausen begrenzt ist, lässt sich auch die räumliche Auflösung verbessern (89,92,93). In *Arbeit 4* wurde diese Sequenz in der Bewertung von Lungenrundherden beim Mammakarzinom analysiert und festgestellt, dass die Anwendung insbesondere bei der Erkennung von zentral gelegenen, durch die Bewegung besonders beeinflussten Lungenrundherden vorteilhaft sein kann. Insgesamt zeigte sich jedoch weiterhin eine deutlich reduzierte Sensitivität im Vergleich zur Computertomographie insbesondere in der Detektion sehr kleiner Lungenrundherde < 4 mm. Die Interpretation dieser kleinen Lungenrundherde stellt generell ein Problem in der radiologischen Diagnostik dar, da viele der in der CT

detektieren Rundherde benigne sind und unnötig kontrolliert werden. So wird in verschiedenen Studien postuliert, dass Lungenrundherde < 10 mm in onkologischen Patienten in den meisten Fällen benigne sind und häufig post-entzündlicher oder indurativer Genese (37,189). So zeigte sich trotz der geringeren Sensitivität der MRT in der Studie von Jannusch et al. kein Nachteil einer MRT-basierten Lungendiagnostik für das Primärstaging bei Mammakarzinompatientinnen (190) unter Anwendung von schnellen VIBE- und HASTE-Sequenzen (92). Die Anwendung radial akquirierter Sequenzen kann helfen, die Detektionsrate kleiner Lungenrundherde zusätzlich zu erhöhen und eine stetige hohe Qualität der Lungenaufnahmen zu gewährleisten.

Um möglichst frühzeitig gezielte Therapien bei onkologischen Erkrankungen einleiten oder Krankheitsverlauf und Prognose abschätzen zu können, werden zunehmend Informationen über die Tumobiologie gesammelt. Gerade bei Tumoren mit einer hohen Letalität und Heterogenität wie dem Lungenkarzinom ist dies von besonderer Bedeutung. Die PET/MRT bietet hier neben der konventionellen Bildgebung Informationen über Metabolismus mittels PET sowie über die Tumorzellularität mittels funktioneller Bildgebung aus der MRT. Am häufigsten Anwendung finden hier der SUV- und der ADC-Wert in der klinischen Routine, die in *Arbeit 5* hinsichtlich ihres diagnostischen Potentials zur Prognoseabschätzung im kleinzelligen Lungenkarzinom untersucht wurden. Der SUVmax Wert ist bereits ein etablierter Parameter in der hybriden bildgebenden Diagnostik, vor allem aufgrund der guten Reproduzierbarkeit und Verfügbarkeit. Dennoch sind die Ergebnisse als prognostischer Marker in Studien nicht eindeutig. Korrelierend zu unseren Ergebnissen konnte in Studien zum prognostischen Wert von SUVmax beim Frühstadium des NSCLC ein Zusammenhang zwischen hohen SUVmax Werten und einem erhöhten Rezidivrisiko sowie einer schlechten Prognose gezeigt werden (191,192). Auch in einer Metaanalyse von Dong

et al. ließen sich die SUV-Werte aus einer 18F-FDG PET/CT Untersuchung als gute prognostische Marker für NSCLC im Frühstadium nutzen (192). Die Studien von Sharma et al. und Burdick et al. konnten diese Ergebnisse jedoch nicht bestätigen (193,194). Einige Studien konnten darüber hinaus auf das Potential des ADC-Wertes für die Vorhersage des Tumoransprechens und das Therapiemonitorings beim NSCLC hinweisen (112,113). So beobachteten Weiss et al. in einer Kohorte von zehn NSCLC-Patienten einen signifikanten Anstieg der ADC-Werte im Verlauf ihrer Radiochemotherapie (113). Unsere Ergebnisse bestätigen, dass auch der ADC-Wert prognostische Bedeutung hat, aber einer Kombination beider Parameter die diagnostische Aussagekraft des SUV-Wertes nicht zusätzlich steigern kann.

Ebenso wie das Lungenkarzinom sind auch die neuroendokrinen Neoplasien eine heterogene Gruppe von Tumoren, bei denen sich die richtige Therapie und damit die Prognose aufgrund der Diversität in Tumorbiologie, hormoneller Aktivität oder Aggressivität ihres Wachstumsverhaltens nur schwer bestimmen lassen (116,117). In diesem Zusammenhang hat sich das Tumorgrading als hilfreicher Prädiktor für das klinische Outcome von NEN-Patienten erwiesen und spielt daher bei der Wahl des Therapieregimes eine entscheidende Rolle (195). Aufgrund ihrer Fähigkeit, auch sehr kleine Läsionen zu detektieren, haben sich die beiden hybriden Bildgebungsverfahren PET/CT und PET/MRT unter Anwendung hochgradig Somatostatinrezeptor-avider Peptide wie beispielsweise 68Ga-markiertes DOTATOC in den letzten Jahren zum Goldstandard in der NEN Diagnostik entwickelt. *Arbeit 6* konnte nun zeigen, dass die 68Ga-DOTATOC-PET/MRT neben der reinen Tumordetektion den Vorteil bietet, dass durch die gleichzeitige Erfassung von Kontrastmittelphasen, funktioneller MRT-Sequenzen wie DWI und dem SUVmax-Wert Aussagen über das Tumorgrading möglich sind und diese Daten zur Vorhersage des NEN-Grades sowie der

Aggressivität verwendet werden könnten. Korrelierend zu den Ergebnissen der Studien von Jang et al. und Guo et al. zeigte sich vor allem bei den G1-Tumoren ein arterielles Hyperenhancement, während sich dies bei G2/G3 Tumoren deutlich seltener nachweisen ließ (196,197). Eine Diffusionsrestriktion war in unserer Studie bei aggressiven Tumorgraden 2,8-mal häufiger, was frühere Studien von De Robertis et al. und Canellas et al. unterstützt (119,198). Eine signifikante negative Korrelation zwischen ADC-Werten und Tumorgrad, wie von Kim et al. (199) und Pereira et al. (127) beschrieben, konnte in unserer Studie hingegen nicht gefunden werden. Ein verlässlicher Parameter für die Vorhersage des Tumorgradings ist der SUVmax-Wert, der in unserer Studie bei Werten über dem Leberniveau bei aggressiven Tumorgraden siebenmal häufiger war. Dies korreliert mit diversen Studien, beispielsweise von Kayani et al., der in seiner Studie mit 38 Patienten unter Verwendung von ⁶⁸Ga-DOTATATE und ¹⁸F-FDG im kombinierten PET/CT sogar eine signifikante Korrelation mit dem Tumorgrading feststellen konnte (200).

Wie beim PET/CT ist es auch im PET/MRT notwendig, eine Schwächungskorrektur zu erstellen, die umgebendes Körpergewebe und Hardwarekomponenten berücksichtigt, um möglichst exakte quantitative Werte zu erhalten. In den letzten Jahren wurde diese Schwächungskorrektur zunehmend verbessert, beispielsweise durch die Anwendung von Knochenmodellen oder einer Trunkierungskorrektur für die Arme (137,138). In *Arbeit 7* wurde nun der Einfluss einer Kontrastmittelgabe während der Untersuchung auf die Schwächungskorrektur unter Anwendung neuester Dixon-MRAC-Sequenzen untersucht und festgestellt, dass die Kontrastmittelgabe die Schwächungskorrektur teils erheblich beeinflussen kann und quantitative Daten wie SUV-Werte an bestimmten Stellen des Körpers verfälscht werden können. Der Einfluss von Artefakten auf die Schwächungskorrektur wurde bereits ausführlich mit älteren

Versionen der Dixon-basierten umap untersucht. Beispielsweise zeigte sich in den Studien von Keller et al. [26] und Brendle et al. [27] ein erheblicher Einfluss von Bewegung, Metallartefakten und falscher Gewebeklassifizierung auf die Schwächungskorrektur, wobei keine dieser Veränderungen eine Änderung der Diagnose durch Verfälschung der SUV-Werte zur Folge hatte. Passend zu den Ergebnissen unserer Studie ließen sich bei Ruhlmann et al. [19] in einer Ganzkörper PET/MRT-Studie nach der Applikation von gadoliniumhaltigen Kontrastmitteln Einflüsse auf die Fett/Wasser-Trennung an der Bettposition des Kopfes beobachten, wodurch die SUV-Werte erheblich verfälscht wurden. Während dort Fett/Wasser-Vertauschungen bei 12 von 30 Patienten nachweisbar waren, ließ sich in *Arbeit 7* lediglich bei 1 von 51 Patienten eine Fehlklassifizierung der inneren Organe nach Kontrastmittelgabe nachweisen, was auf eine verbesserte Rekonstruktion der Schwächungskorrektur unter Verwendung von CAIPI-akzelerierten Dixon-VIBE Sequenzen mit verbesserter räumlicher Auflösung und einem robusteren Gewebesegmentierungsalgorithmus zurückgeführt wird. Entscheidend ist hierbei aber der relevante Einfluss des Kontrastmittels auf die Schwächungskorrektur. Auch ein direkter Schwächungseffekt des gadolinium-haltigen Kontrastmittels auf die PET-Photonen wurde beispielsweise durch Lois et al. untersucht. Aufgrund der geringen Mengen (<20 ml) wurde dieser Effekt aber als vernachlässigbar eingestuft [19, 29]. Letztlich suggerieren die Ergebnisse aus *Arbeit 7*, dass PET/MRT-spezifische Protokollanpassungen vorgenommen werden sollten, um die Verwendung von Post-KM-umaps zu verhindern oder aber die umaps im Befundungsprozess berücksichtigt werden sollten.

Durch die Entwicklung neuer, spezifischer Radiotracer, die beispielsweise Pathomechanismen bestimmter Erkrankungen zum Ziel haben, ist das Anwendungsgebiet der hybriden Bildgebung über onkologische Fragestellungen

erweitert worden. In *Arbeit 8* konnte nun unter Anwendung des osteoblastenspezifischen Radiotracers ^{18}F -Natriumfluorid ($\text{Na}[^{18}\text{F}]F$) zum ersten Mal herausgefunden werden, dass die TNF-Inhibitoren bei der axialen Spondyloarthritis neben der entzündungshemmenden auch eine positive, antiosteoblastische Wirkung besitzen und damit eine Rückbildung der radiologischen Progression dieser Erkrankung zur Folge haben können. Insgesamt stützen diese Daten frühere Beobachtungen wonach Inflammation und Knochenneubildung einen reparativen Prozess darstellen, der über Fettmetaplasie, Erosion und Sklerose verläuft und in einer Ankylose endet [25]. Außerdem ist eine möglichst frühzeitige Einleitung der Therapie für den Krankheitsverlauf entscheidend. Auch wenn bei allen Patienten die Quantifizierung der osteoblastischen Aktivität entweder rückläufig oder gleich blieb, konnten nicht alle einen Status geringerer Krankheitsaktivität erreichen, sodass letztlich das Ausmaß des Behandlungseffektes auf struktureller Ebene, wie er in der Bildgebung beurteilt wird, nicht das Ausmaß des Behandlungsergebnisses widerspiegelt. Eine mögliche Erklärung ist der in *Arbeit 8* gewählte Untersuchungszeitraum von nur 4-6 Monaten. In Studien werden durch die bDMARDs auch langfristige klinische Behandlungswirkungen beschrieben, die sich in dieser Studie nicht abbilden ließen [30, 31]. Der Umstand, dass in *Arbeit 8* besonders an Stellen erhöhter Entzündungsaktivität und weniger bei chronischen Veränderungen ein Rückgang der osteoblastischen Aktivität beobachtet werden konnte, lässt auf eine Übertragbarkeit der Daten auch für die Auswirkungen von Behandlungen bei Patienten mit nicht-radiographischer axialer Spondyloarthritis schließen [32].

Ausblick

Die im Rahmen dieser kumulativen Habilitationsschrift vorgestellten Arbeiten beschäftigen sich mit der Implementierung und Verbesserung der PET/MRT in der

klinischen Routine-Diagnostik sowie dem Erschließen neuer Anwendungsmöglichkeiten.

Seit nunmehr über 10 Jahren steht dem Gebiet der hybriden Bildgebung die PET/MRT zur Verfügung und stellt damit bis dato die neueste der hybriden Bildgebungsmodalitäten dar. Der große Durchbruch, der dieser Modalität seit Beginn an prophezeit wird, ist dem PET/MRT aber bisher nicht gelungen. Das PET/CT ist aufgrund der exzellenten Ergebnisse mittlerweile der Goldstandard in vielen onkologischen Fragestellungen, an dem sich andere bildgebende Verfahren messen müssen. Auch in großen Kohortenstudien zeigte sich im Vergleich von PET/MRT und PET/CT bisher meist eine Gleichwertigkeit oder nur leichte Vorteile des PET/MRT (201).

Einerseits ist das Ziel aktueller Studien in der hybriden Bildgebung, die Vorteile der MRT-Komponente beim PET/MRT herauszustellen und hierdurch universale Staging-Lösungen anzubieten, beispielsweise beim Mammakarzinom oder beim Prostatakarzinom. Hier lassen sich zum Ganzkörperstaging dedizierte Untersuchungsprotokolle einer Körperregion wie Mamma oder Prostata ergänzen, sodass in Zukunft bei ausreichender Verfügbarkeit das Staging mittels unterschiedlicher Modalitäten abgelöst werden kann.

Andererseits lassen sich durch die Entwicklung neuer, hochspezifischer Radiotracer zunehmend präzisere Anwendungsmöglichkeiten erschließen, beispielsweise bei entzündlichen Erkrankungen oder der rheumatoïden Arthritis, sodass hier der Stellenwert dieser Modalität zur Beurteilung oder sogar Voraussage einer Therapie vielversprechend ist und die potentiellen Möglichkeiten zahlreich sind.

Ein weiterer vielversprechender Ansatz ist die Integration von künstlicher Intelligenz und hier speziell dem maschinellen Lernen. Hier erhofft man sich in Zukunft, durch die

systematische Auswertung der vielen insbesondere in der PET/MRT gewonnenen Informationen die Bildinterpretation zu verbessern und frühzeitig Prognosefaktoren oder sogar Tumoreigenschaften abschätzen und eine zunehmend individualisierte, zielgerichtete Therapie anbieten zu können.

Zusammenfassend wird die hybride Bildgebung auch in Zukunft eine wichtige Rolle in der Diagnostik und Therapie von Krankheiten spielen und dazu beitragen, die Patientenversorgung zu verbessern und die Gesundheitsversorgung zu optimieren.

Literaturverzeichnis

1. Townsend DW. Combined positron emission tomography-computed tomography: the historical perspective. *Semin Ultrasound CT MR.* 2008;29:232-235.
2. Quick HH. Integrated PET/MR. *J Magn Reson Imaging.* 2014;39:243-58.
3. Kirchner J. Onkologische Diagnosik mittels hybrider Bildgebung.; 2020.
4. Kitajima K, Yamano T, Miyoshi Y, Katsuura T, Enoki T, Yamakado K. Prognostic value of 18 F-FDG PET/CT prior to breast cancer treatment. Comparison with magnetic resonance spectroscopy and diffusion weighted imaging. *Hell J Nucl Med.* 2019;22:25-35.
5. Hwang JP, Lim I, Byun BH, Kim B II, Choi CW, Lim SM. Prognostic value of SUVmax measured by pretreatment 18F-FDG PET/CT in patients with primary gastric lymphoma. *Nucl Med Commun.* 2016;37:1267-1272.
6. Chung MP, Margolis D, Mesko S, Wang J, Kupelian P, Kamrava M. Correlation of quantitative diffusion-weighted and dynamic contrast-enhanced MRI parameters with prognostic factors in prostate cancer. *J Med Imaging Radiat Oncol.* 2014;58:588-94.
7. Nakamura K, Joja I, Kodama J, Hongo A, Hiramatsu Y. Measurement of SUVmax plus ADCmin of the primary tumour is a predictor of prognosis in patients with cervical cancer. *Eur J Nucl Med Mol Imaging.* 2012.
8. Gao F. Integrated Positron Emission Tomography/Magnetic Resonance Imaging in clinical diagnosis of Alzheimer's disease. *Eur J Radiol.* 2021;145:110017.
9. Buchbender C, Ostendorf B, Ruhlmann V, et al. Hybrid 18f-labeled fluoride positron emission tomography/Magnetic Resonance (MR) imaging of the sacroiliac joints and the spine in patients with axial spondyloarthritis: A pilot study exploring the link of MR bone pathologies and increased osteoblastic ac. *J*

Rheumatol. 2015;42:1631-7.

10. Kogan F, Fan AP, Gold GE. Potential of PET-MRI for imaging of non-oncologic musculoskeletal disease. *Quant Imaging Med Surg.* 2016;6:756-771.
11. Moses WW. Fundamental Limits of Spatial Resolution in PET. *Nucl instruments methods Phys Res Sect A, Accel/ spectrometers, Detect Assoc Equip.* 2011;648 Supple:S236-S240.
12. Beyer T, Townsend DW, Brun T, et al. A combined PET/CT scanner for clinical oncology. *J Nucl Med.* 2000;41:1369-1379.
13. Kalender WA. Computertomographie. Grundlagen, Gerätetechnologie, Bildqualität, Anwendungen. 2. überarb. Erlangen: Publicis Corporate Publishing; 2006.
14. Alkadhi H, Leschka S, Stolzmann P, Scheffel H. Wie funktioniert CT? Springer Medizin Verlag Heidelberg; 2011.
15. Kinahan PE, Townsend DW, Beyer T, Sashin D. Attenuation correction for a combined 3D PET/CT scanner. *Med Phys.* 1998;25:2046-2053.
16. Kinahan PE, Hasegawa BH, Beyer T. X-ray-based attenuation correction for positron emission tomography/computed tomography scanners. *Semin Nucl Med.* 2003.
17. Antoch G, Stattaus J, Nemat AT, et al. Non-Small Cell Lung Cancer: Dual-Modality PET/CT in Preoperative Staging. *Radiology.* 2003.
18. Antoch G, Vogt FM, Freudenberg LS, et al. Whole-Body Dual-Modality PET/CT and Whole-Body MRI for Tumor Staging in Oncology. *J Am Med Assoc.* 2003;290:3199-206.
19. Bar-Shalom R, Yefremov N, Guralnik L, et al. Clinical performance of PET/CT in evaluation of cancer: additional value for diagnostic imaging and patient management. *J Nucl Med.* 2003;44:1200-1209.

20. Lardinois D, Weder W, Hany TF, et al. Staging of non-small-cell lung cancer with integrated positron-emission tomography and computed tomography. *N Engl J Med.* 2003;348:2500-2507.
21. Hahn K, Pfluger T. Is PET/CT necessary in paediatric oncology? Against. *Eur J Nucl Med Mol Imaging.* 2006;33:966-968.
22. Brix G, Nosske D, Lechel U. Radiation exposure of patients undergoing whole-body FDG-PET/CT examinations: an update pursuant to the new ICRP recommendations. *Nuklearmedizin.* 2014;53:217-220.
23. Magometschnigg HF, Baltzer PA, Fueger B, et al. Diagnostic accuracy of (18)F-FDG PET/CT compared with that of contrast-enhanced MRI of the breast at 3 T. *Eur J Nucl Med Mol Imaging.* 2015;42:1656-1665.
24. Fukui MB, Blodgett TM, Snyderman CH, et al. Combined PET-CT in the head and neck: part 2. Diagnostic uses and pitfalls of oncologic imaging. *Radiogr a Rev Publ Radiol Soc North Am Inc.* 2005;25:913-930.
25. Gu P, Pan L-L, Wu S-Q, Sun L, Huang G. CA 125, PET alone, PET-CT, CT and MRI in diagnosing recurrent ovarian carcinoma: a systematic review and meta-analysis. *Eur J Radiol.* 2009;71:164-174.
26. Khalil HI, Patterson SA, Panicek DM. Hepatic lesions deemed too small to characterize at CT: prevalence and importance in women with breast cancer. *Radiology.* 2005;235:872-878.
27. Buchbender C, Heusner TA, Lauenstein TC, Bockisch A, Antoch G. Oncologic PET/MRI, part 2: Bone tumors, soft-tissue tumors, melanoma, and lymphoma. *J Nucl Med.* 2012;53:1244-52.
28. Buchbender C, Heusner TA, Lauenstein TC, Bockisch A, Antoch G. Oncologic PET/MRI, part 1: Tumors of the brain, head and neck, chest, abdomen, and pelvis. *J Nucl Med.* 2012;53:928-938.

29. Antoch G, Bockisch A. Combined PET/MRI: A new dimension in whole-body oncology imaging? *Eur J Nucl Med Mol Imaging*. 2009.
30. Catana C, Wu Y, Judenhofer MS, Qi J, Pichler BJ, Cherry SR. Simultaneous acquisition of multislice PET and MR images: initial results with a MR-compatible PET scanner. *J Nucl Med*. 2006;47:1968-1976.
31. Pichler BJ, Judenhofer MS, Catana C, et al. Performance test of an LSO-APD detector in a 7-T MRI scanner for simultaneous PET/MRI. *J Nucl Med*. 2006;47:639-647.
32. Quick HH. Integrated PET/MR. *J Magn Reson Imaging*. 2014;39:243-258.
33. Visvikis D, Costa DC, Croasdale I, et al. CT-based attenuation correction in the calculation of semi-quantitative indices of [18F]FDG uptake in PET. *Eur J Nucl Med Mol Imaging*. 2003;30:344-53.
34. Carney JPJ, Townsend DW, Rappoport V, Bendriem B. Method for transforming CT images for attenuation correction in PET/CT imaging. *Med Phys*. 2006;38:2948-56.
35. Kim JH, Lee JS, Song I-C, Lee DS. Comparison of segmentation-based attenuation correction methods for PET/MRI: evaluation of bone and liver standardized uptake value with oncologic PET/CT data. *J Nucl Med*. 2012;53:1878-1882.
36. Heusch P, Buchbender C, Beiderwellen K, et al. Standardized uptake values for [18F] FDG in normal organ tissues: Comparison of whole-body PET/CT and PET/MRI. *Eur J Radiol*. 2013;82:870-6.
37. Sawicki LM, Grueneisen J, Buchbender C, et al. Evaluation of the Outcome of Lung Nodules Missed on 18F-FDG PET/MRI Compared with 18F-FDG PET/CT in Patients with Known Malignancies. *J Nucl Med*. 2016;57:15-20.
38. Sawicki LM, Grueneisen J, Buchbender C, et al. Comparative Performance of

- 18F-FDG PET/MRI and 18F-FDG PET/CT in Detection and Characterization of Pulmonary Lesions in 121 Oncologic Patients. *J Nucl Med.* 2016;57:582-586.
39. Beiderwellen K, Gomez B, Buchbender C, et al. Depiction and characterization of liver lesions in whole body [(1)(8)F]-FDG PET/MRI. *Eur J Radiol.* 2013;82:e669-75.
40. Krüger S, Mottaghy FM, Buck AK, et al. Brain metastasis in lung cancer. Comparison of cerebral MRI and 18F-FDG-PET/CT for diagnosis in the initial staging. *Nuklearmedizin.* 2011;50:101-106.
41. Beiderwellen K, Huebner M, Heusch P, et al. Whole-body [¹⁸F]FDG PET/MRI vs. PET/CT in the assessment of bone lesions in oncological patients: initial results. *Eur Radiol.* 2014;24:2023-2030.
42. Bray F, Ferlay J, Soerjomataram I, Siegel RL, Torre LA, Jemal A. Global cancer statistics 2018: GLOBOCAN estimates of incidence and mortality worldwide for 36 cancers in 185 countries. *CA Cancer J Clin.* 2018;68:394-424.
43. Michaelson JS, Chen LL, Silverstein MJ, et al. How cancer at the primary site and in the lymph nodes contributes to the risk of cancer death. *Cancer.* 2009;115:5095-5107.
44. Wockel A, Festl J, Stuber T, et al. Interdisciplinary Screening, Diagnosis, Therapy and Follow-up of Breast Cancer. Guideline of the DGGG and the DKG (S3-Level, AWMF Registry Number 032/045OL, December 2017) - Part 2 with Recommendations for the Therapy of Primary, Recurrent and Advanced Br. *Geburtshilfe Frauenheilkd.* 2018;78:1056-1088.
45. Cardoso F, Paluch-Shimon S, Senkus E, et al. 5th ESO-ESMO international consensus guidelines for advanced breast cancer (ABC 5). *Ann Oncol.* 2020;31:1623-1649.
46. Gradishar WJ, Anderson BO, Balassanian R, et al. Breast Cancer, Version

4.2017, NCCN Clinical Practice Guidelines in Oncology. *J Natl Compr Cancer Netw.* 2018;16:310-320.

47. Menezes GL, Knuttel FM, Stehouwer BL, Pijnappel RM, van den Bosch MA. Magnetic resonance imaging in breast cancer: A literature review and future perspectives. *World J Clin Oncol.* 2014;5:61-70.
48. Senkus E, Kyriakides S, Ohno S, et al. Primary breast cancer: ESMO Clinical Practice Guidelines for diagnosis, treatment and follow-up. *Ann Oncol Off J Eur Soc Med Oncol.* 2015;26 Suppl 5:v8-30.
49. Hausmann D, Kern C, Schröder M. Ganzkörper-MRT in der präoperativen Diagnostik des Mammakarzinoms – ein Vergleich mit den Staging- methoden in der S 3-Leitlinie Whole-Body MRI in Preoperative Diagnostics of Breast Cancer – a Comparison of. *Fortschritte Röntgenstrahlen.* 2011;183:1130-1137.
50. Tatsumi M, Cohade C, Mourtzikos KA, Fishman EK, Wahl RL. Initial experience with FDG-PET/CT in the evaluation of breast cancer. *Eur J Nucl Med Mol Imaging.* 2006.
51. Ulaner GA. PET/CT for Patients With Breast Cancer: Where Is the Clinical Impact? *Am J Roentgenol.* 2019:1-12.
52. Ulaner GA, Castillo R, Goldman DA, et al. 18F-FDG-PET/CT for systemic staging of newly diagnosed triple-negative breast cancer. *Eur J Nucl Med Mol Imaging.* 2016;43:1937-44.
53. Botsikas D, Bagetakos I, Picarra M, et al. What is the diagnostic performance of 18-FDG-PET/MR compared to PET/CT for the N- and M- staging of breast cancer? *Eur Radiol.* 2019;29:1787-1798.
54. Grueneisen J, Nagarajah J, Buchbender C, et al. Positron Emission Tomography/Magnetic Resonance Imaging for Local Tumor Staging in Patients with Primary Breast Cancer: A Comparison with Positron Emission

Tomography/Computed Tomography and Magnetic Resonance Imaging. *Invest Radiol.* 2015;50:505-13.

55. Sawicki LM, Grueneisen J, Schaarschmidt BM, et al. Evaluation of 18F-FDG PET/MRI, 18F-FDG PET/CT, MRI, and CT in whole-body staging of recurrent breast cancer. *Eur J Radiol.* 2016;85:459-465.
56. Grueneisen J, Sawicki LM, Wetter A, et al. Evaluation of PET and MR datasets in integrated 18F-FDG PET/MRI: A comparison of different MR sequences for whole-body restaging of breast cancer patients. *Eur J Radiol.* 2017;89:14-19.
57. Melsaether AN, Raad RA, Pujara AC, et al. Comparison of Whole-Body 18 F FDG PET/MR Imaging and Whole-Body 18 F FDG PET/CT in Terms of Lesion Detection and Radiation Dose in Patients with Breast Cancer. *Radiology.* 2016;281:193-202.
58. Gradishar WJ, Moran MS, Abraham J, et al. NCCN Guidelines® Insights: Breast Cancer, Version 4.2021. *J Natl Compr Canc Netw.* 2021;19:484-493.
59. Kanda T, Kitajima K, Suenaga Y, et al. Value of retrospective image fusion of 18F-FDG PET and MRI for preoperative staging of head and neck cancer: Comparison with PET/CT and contrast-enhanced neck MRI. *Eur J Radiol.* 2013.
60. Anderson WF, Reiner AS, Matsuno RK, Pfeiffer RM. Shifting breast cancer trends in the United States. *J Clin Oncol.* 2007;25:3923-9.
61. Telli ML, Gradishar WJ, Ward JH. NCCN Guidelines Updates: Breast Cancer. *J Natl Compr Canc Netw.* 2019;17:552-555.
62. Kirchner J, Sawicki LM, Deuschl C, et al. 18 F-FDG PET/MR imaging in patients with suspected liver lesions: Value of liver-specific contrast agent Gadobenate dimeglumine. *PLoS One.* 2017;12:1-14.
63. Beiderwellen K, Grueneisen J, Ruhlmann V, et al. [(18)F]FDG PET/MRI vs. PET/CT for whole-body staging in patients with recurrent malignancies of the

- female pelvis: initial results. *Eur J Nucl Med Mol Imaging*. 2015;42:56-65.
64. Heusch P, Buchbender C, Köhler J, et al. Thoracic staging in lung cancer: Prospective comparison of 18F-FDG PET/MR imaging and 18F-FDG PET/CT. *J Nucl Med*. 2014;55:373-8.
65. Bruckmann NM, Kirchner J, Umutlu L, et al. Prospective comparison of the diagnostic accuracy of 18F-FDG PET/MRI, MRI, CT, and bone scintigraphy for the detection of bone metastases in the initial staging of primary breast cancer patients. *Eur Radiol*. 2021;31:8714-8724.
66. Tabouret-Viaud C, Botsikas D, Delattre BMA, et al. PET/MR in Breast Cancer. *Semin Nucl Med*. 2015;45:304-321.
67. Kirchner J, Grueneisen J, Martin O, et al. Local and whole-body staging in patients with primary breast cancer: a comparison of one-step to two-step staging utilizing 18F-FDG-PET/MRI. *Eur J Nucl Med Mol Imaging*. 2018;45:2328-2337.
68. Parkes A, Clifton K, Al-Awadhi A, et al. Characterization of bone only metastasis patients with respect to tumor subtypes. *npj Breast Cancer*. 2018;4:2.
69. Coleman RE, Rubens RD. The clinical course of bone metastases from breast cancer. *Br J Cancer*. 1987;55:61-66.
70. Liede A, Jerzak KJ, Hernandez RK, Wade SW, Sun P, Narod SA. The incidence of bone metastasis after early-stage breast cancer in Canada. *Breast Cancer Res Treat*. 2016;156:587-595.
71. Brockton NT, Gill SJ, Laborge SL, et al. The Breast Cancer to Bone (B2B) Metastases Research Program: A multi-disciplinary investigation of bone metastases from breast cancer. *BMC Cancer*. 2015;15:512.
72. Jung SY, Rosenzweig M, Sereika SM, Linkov F, Brufsky A, Weissfeld JL. Factors associated with mortality after breast cancer metastasis. *Cancer Causes Control*.

2012;23:103-112.

73. Hortobagyi GN, Theriault RL, Lipton A, et al. Long-term prevention of skeletal complications of metastatic breast cancer with pamidronate. *J Clin Oncol*. 1998;16:2038-44.
74. Liu T, Cheng T, Xu W, Yan WL, Liu J, Yang HL. A meta-analysis of 18FDG-PET, MRI and bone scintigraphy for diagnosis of bone metastases in patients with breast cancer. *Skeletal Radiol*. 2011;40:523-31.
75. Rossi L, Longhitano C, Kola F, Del Grande M. State of art and advances on the treatment of bone metastases from breast cancer: a concise review. *Chinese Clin Oncol*. 2020;9:18.
76. Cardoso F, Senkus E, Costa A, et al. 4th ESO-ESMO international consensus guidelines for advanced breast cancer (ABC 4). *Ann Oncol*. 2018.
77. Ohlmann-Knafo S, Pickuth D, Kirschbaum M, Fenzl G. Diagnostic value of whole-body MRI and bone scintigraphy in the detection of osseous metastases in patients with breast cancer - A prospective double-blinded study at two hospital centers. *RoFo Fortschritte auf dem Gebiet der Rontgenstrahlen und der Bildgeb Verfahren*. 2009;181:255-63.
78. Cardoso F, Senkus E, Costa A, et al. 4th ESO-ESMO International Consensus Guidelines for Advanced Breast Cancer (ABC 4)dagger. *Ann Oncol Off J Eur Soc Med Oncol*. 2018;29:1634-1657.
79. Hildebrandt MG, Gerke O, Baun C, et al. [18F] Fluorodeoxyglucose (FDG)-Positron emission tomography (PET)/computed tomography (CT) in suspected recurrent breast cancer: A prospective comparative study of dual-time-point FDG-PET/CT, contrast-enhanced CT, and bone scintigraphy. *J Clin Oncol*. 2016;34:1889-1897.
80. Bitencourt AGV, Andrade WP, Cunha RR da, et al. Detection of distant

metastases in patients with locally advanced breast cancer: role of 18F-fluorodeoxyglucose positron emission tomography/computed tomography and conventional imaging with computed tomography scans. *Radiool Bras.* 2017;50:211-215.

81. Park S, Yoon JK, Jin Lee S, Kang SY, Yim H, An YS. Prognostic utility of FDG PET/CT and bone scintigraphy in breast cancer patients with bone-only metastasis. *Med (United States)*. 2017;96:e8985.
82. Hahn S, Heusner T, Kümmel S, et al. Comparison of FDG-PET/CT and bone scintigraphy for detection of bone metastases in breast cancer. *Acta radiol*. 2011;52:1009-14.
83. Heindel W, Gübitz R, Vieth V, Weckesser M, Schober O, Schäfers M. The diagnostic imaging of bone metastases. *Dtsch Arztebl Int*. 2014;111:741-747.
84. Catalano OA, Nicolai E, Rosen BR, et al. Comparison of CE-FDG-PET/CT with CE-FDG-PET/MR in the evaluation of osseous metastases in breast cancer patients. *Br J Cancer*. 2015;112:1452-1460.
85. Sonni I, Minamimoto R, Baratto L, et al. Simultaneous PET/MRI in the Evaluation of Breast and Prostate Cancer Using Combined Na[18F] F and [18F]FDG: a Focus on Skeletal Lesions. *Mol Imaging Biol*. 2020;22:397-406.
86. Kumar SK, Callander NS, Hillengass J, et al. NCCN Guidelines Insights: Multiple Myeloma, Version 1.2020. *J Natl Compr Cancer Netw*. 2019;17:1154-1165.
87. Mottet N, Bellmunt J, Bolla M, et al. EAU-ESTRO-SIOG Guidelines on Prostate Cancer. Part 1: Screening, Diagnosis, and Local Treatment with Curative Intent. *Eur Urol*. 2017;71:618-629.
88. Schafer JF, Vollmar J, Schick F, et al. [Detection of pulmonary nodules with breath-hold magnetic resonance imaging in comparison with computed tomography]. *Rofo*. 2005;177:41-49.

89. Block KT, Chandarana H, Milla S, et al. Towards Routine Clinical Use of Radial Stack-of-Stars 3D Gradient-Echo Sequences for Reducing Motion Sensitivity. *J Korean Soc Magn Reson Med.* 2014;18:87.
90. Kumar S, Rai R, Stemmer A, et al. Feasibility of free breathing Lung MRI for Radiotherapy using non-Cartesian k-space acquisition schemes. *Br J Radiol.* 2017;90:20170037.
91. McRobbie DW, Moore EA, Graves MJ, Prince MR. MRI from Picture to Proton. Third Edit. Cambridge university press; 2017.
92. Block KT, Chandarana H, Fatterpekar G, et al. Improving the Robustness of Clinical T1-Weighted MRI Using Radial VIBE. *Magnetom Flash.* 2013;6-11.
93. Azevedo RM, De Campos ROP, Ramalho M, Herédia V, Dale BM, Semelka RC. Free-breathing 3D T1-weighted gradient-echo sequence with radial data sampling in abdominal MRI: Preliminary observations. *Am J Roentgenol.* 2011;197:650-7.
94. Sung H, Ferlay J, Siegel RL, et al. Global Cancer Statistics 2020: GLOBOCAN Estimates of Incidence and Mortality Worldwide for 36 Cancers in 185 Countries. *CA Cancer J Clin.* 2021;71:209-249.
95. Torre LA, Siegel RL, Jemal A. Lung cancer statistics. *Adv Exp Med Biol.* 2016;893:1-19.
96. Ettinger DS, Aisner DL, Wood DE, et al. NCCN Guidelines Insights: Non-Small Cell Lung Cancer, Version 5.2018. *J Natl Compr Cancer Netw.* 2018;16:807-821.
97. Bunyaviroch T, Coleman RE. PET evaluation of lung cancer. *J Nucl Med.* 2006;47:451-69.
98. Goeckenjan G, Sitter H, Thomas M, et al. Prevention, diagnosis, therapy, and follow-up of lung cancer: Interdisciplinary guideline of the German respiratory society and the German cancer society. *Pneumologie.* 2011;65:e51-75.

99. Choi SH, Kim YT, Kim SK, et al. Positron emission tomography-computed tomography for postoperative surveillance in non-small cell lung cancer. *Ann Thorac Surg.* 2011;92:1826-32.
100. Postmus PE, Kerr KM, Oudkerk M, et al. Early and locally advanced non-small-cell lung cancer (NSCLC): ESMO Clinical Practice Guidelines for diagnosis, treatment and follow-up. *Ann Oncol.* 2017;28:iv1-iv21.
101. Heusch P, Buchbender C, Kohler J, et al. Thoracic staging in lung cancer: prospective comparison of 18F-FDG PET/MR imaging and 18F-FDG PET/CT. *J Nucl Med.* 2014;55:373-378.
102. Schaarschmidt BM, Grueneisen J, Metzenmacher M, et al. Thoracic staging with (18)F-FDG PET/MR in non-small cell lung cancer - does it change therapeutic decisions in comparison to (18)F-FDG PET/CT? *Eur Radiol.* 2017;27:681-688.
103. Kirchner J, Sawicki LM, Nensa F, et al. Prospective comparison of 18 F-FDG PET/MRI and 18 F-FDG PET/CT for thoracic staging of non-small cell lung cancer. *Eur J Nucl Med Mol Imaging.* 2019;46:437-445.
104. Heusch P, Buchbender C, Köhler J, et al. Correlation of the apparent diffusion coefficient (ADC) with the standardized uptake value (SUV) in hybrid 18F-FDG PET/MRI in non-small cell lung cancer (NSCLC) lesions: Initial results. *Fortschritte auf dem Gebiet der Röntgenstrahlen und der Bildgeb Verfahren.* 2013;185:1056-62.
105. Regier M, Derlin T, Schwarz D, et al. Diffusion weighted MRI and 18F-FDG PET/CT in non-small cell lung cancer (NSCLC): Does the apparent diffusion coefficient (ADC) correlate with tracer uptake (SUV)? *Eur J Radiol.* 2012;81:2913-8.
106. Rakheja R, Chandarana H, DeMello L, et al. Correlation between standardized uptake value and apparent diffusion coefficient of neoplastic lesions evaluated

- with whole-body simultaneous hybrid PET/MRI. *Am J Roentgenol.* 2013;201:1115-9.
107. Schaarschmidt BM, Buchbender C, Nensa F, et al. Correlation of the apparent diffusion coefficient (ADC) with the standardized uptake value (SUV) in lymph node metastases of non-small cell lung cancer (NSCLC) patients using hybrid 8F-FDG PET/MRI. *PLoS One.* 2015;10:1-14.
 108. Zhong J, Gore JC. Studies of restricted diffusion in heterogeneous media containing variations in susceptibility. *Magn Reson Med.* 1991;19:276-84.
 109. Shi D, Cai G, Peng J, et al. The preoperative SUVmax for 18 F-FDG uptake predicts survival in patients with colorectal cancer. *BMC Cancer.* 15:991.
 110. Song B II, Kim HW, Won KS, Ryu SW, Sohn SS, Kang YN. Preoperative standardized uptake value of metastatic lymph nodes measured by 18F-FDG PET/CT improves the prediction of prognosis in gastric cancer. *Med (United States).* 2015;94:e1037.
 111. Diao W, Tian F, Jia Z. The prognostic value of SUVmax measuring on primary lesion and ALN by 18F-FDG PET or PET/CT in patients with breast cancer. *Eur J Radiol.* 2018;105:1-7.
 112. Ohno Y, Koyama H, Yoshikawa T, et al. Diffusion-weighted MRI versus 18F-FDG PET/CT: Performance as predictors of tumor treatment response and patient survival in patients with non-small cell lung cancer receiving chemoradiotherapy. *Am J Roentgenol.* 2012;198:75-82.
 113. Weiss E, Ford JC, Olsen KM, et al. Apparent diffusion coefficient (ADC) change on repeated diffusion-weighted magnetic resonance imaging during radiochemotherapy for non-small cell lung cancer: A pilot study. *Lung Cancer.* 2016;96:113-119.
 114. Taal BG, Visser O. Epidemiology of neuroendocrine tumours.

Neuroendocrinology. 2004;80 Suppl 1:3-7.

115. Yao JC, Hassan M, Phan A, et al. One hundred years after "carcinoid": Epidemiology of and prognostic factors for neuroendocrine tumors in 35,825 cases in the United States. *J Clin Oncol*. 2008;26:3063-3072.
116. Klimstra DS, Beltran H, Lilenbaum R, Bergsland E. The Spectrum of Neuroendocrine Tumors: Histologic Classification, Unique Features and Areas of Overlap. *Am Soc Clin Oncol Educ B*. 2015:92-103.
117. Chai SM, Brown IS, Kumarasinghe MP. Gastroenteropancreatic neuroendocrine neoplasms: selected pathology review and molecular updates. *Histopathology*. 2018;72:153-167.
118. Kunz PL. Carcinoid and neuroendocrine tumors: Building on success. *J Clin Oncol*. 2015.
119. Canellas R, Lo G, Bhowmik S, Ferrone C, Sahani D. Pancreatic neuroendocrine tumor: Correlations between MRI features, tumor biology, and clinical outcome after surgery. *J Magn Reson Imaging*. 2018.
120. Singhi AD, Klimstra DS. Well-differentiated pancreatic neuroendocrine tumours (PanNETs) and poorly differentiated pancreatic neuroendocrine carcinomas (PanNECs): concepts, issues and a practical diagnostic approach to high-grade (G3) cases. *Histopathology*. 2018;72:168-177.
121. Hofman MS, Eddie Lau WF, Hicks RJ. Somatostatin receptor imaging with⁶⁸Ga DOTATATE PET/CT: Clinical utility, normal patterns, pearls, and pitfalls in interpretation. *Radiographics*. 2015;35:500-16.
122. Hope TA, Pampaloni MH, Nakakura E, et al. Simultaneous ⁶⁸Ga-DOTA-TOC PET/MRI with gadoxetate disodium in patients with neuroendocrine tumor. *Abdom Imaging*. 2015;40:1432-40.
123. Treglia G, Castaldi P, Rindi G, Giordano A, Rufini V. Diagnostic performance of

Gallium-68 somatostatin receptor PET and PET/CT in patients with thoracic and gastroenteropancreatic neuroendocrine tumours: A meta-analysis. *Endocrine*. 2012;42:80-7.

124. Beiderwellen KJ, Poeppel TD, Hartung-Knemeyer V, et al. Simultaneous 68Ga-DOTATOC PET/MRI in patients with gastroenteropancreatic neuroendocrine tumors: Initial results. *Invest Radiol*. 2013;48:273-9.
125. Sawicki LM, Deuschl C, Beiderwellen K, et al. Evaluation of 68Ga-DOTATOC PET/MRI for whole-body staging of neuroendocrine tumours in comparison with 68Ga-DOTATOC PET/CT. *Eur Radiol*. 2017;27:4091-4099.
126. Schmid-Tannwald C, Oto A, Reiser MF, Zech CJ. Diffusion-weighted MRI of the abdomen: Current value in clinical routine. *J Magn Reson Imaging*. 2013;37:35-37.
127. Pereira JAS, Rosado E, Bali M, Metens T, Chao SL. Pancreatic neuroendocrine tumors: correlation between histogram analysis of apparent diffusion coefficient maps and tumor grade. *Abdom Imaging*. 2015;40:3122-8.
128. Lotfalizadeh E, Ronot M, Wagner M, et al. Prediction of pancreatic neuroendocrine tumour grade with MR imaging features: added value of diffusion-weighted imaging. *Eur Radiol*. 2017;27:1748-1759.
129. Öksüz MÖ, Winter L, Pfannenberg C, et al. Peptide receptor radionuclide therapy of neuroendocrine tumors with 90Y-DOTATOC: Is treatment response predictable by pre-therapeutic uptake of 68Ga-DOTATOC? *Diagn Interv Imaging*. 2014;jnumed.119.
130. Rha SE, Jung SE, Lee KH, Ku YM, Byun JY, Lee JM. CT and MR imaging findings of endocrine tumor of the pancreas according to WHO classification. *Eur J Radiol*. 2007;62:371-7.
131. Humphrey PE, Alessandrino F, Bellizzi AM, Mortele KJ. Non-hyperfunctioning

- pancreatic endocrine tumors: multimodality imaging features with histopathological correlation. *Abdom Imaging*. 2015;40:2398-4010.
132. Manfredi R, Bonatti M, Mantovani W, et al. Non-hyperfunctioning neuroendocrine tumours of the pancreas: MR imaging appearance and correlation with their biological behaviour. *Eur Radiol*. 2013.
 133. Quick HH. Integrated PET/MR. *J Magn Reson Imaging*. 2014.
 134. Martinez-Moller A, Souvatzoglou M, Delso G, et al. Tissue classification as a potential approach for attenuation correction in whole-body PET/MRI: Evaluation with PET/CT data. *J Nucl Med*. 2009;50:520-6.
 135. Beyer T, Lassen ML, Boellaard R, et al. Investigating the state-of-the-art in whole-body MR-based attenuation correction: an intra-individual, inter-system, inventory study on three clinical PET/MR systems. *Magn Reson Mater Physics, Biol Med*. 2016;29:75-87.
 136. Seith F, Gatidis S, Schmidt H, et al. Comparison of Positron Emission Tomography Quantification Using Magnetic Resonance- and Computed Tomography-Based Attenuation Correction in Physiological Tissues and Lesions. *Invest Radiol*. 2016;51:66-71.
 137. Blumhagen JO, Ladebeck R, Fenchel M, Scheffler K. MR-based field-of-view extension in MR/PET: B0 homogenization using gradient enhancement (HUGE). *Magn Reson Med*. 2013;70:1047-57.
 138. Lindemann ME, Oehmigen M, Blumhagen JO, Gratz M, Quick HH. MR-based truncation and attenuation correction in integrated PET/MR hybrid imaging using HUGE with continuous table motion: *Med Phys*. 2017;44:4559-4572.
 139. Breuer F, Blaimer M, Griswold M, Jakob P. Controlled Aliasing in Parallel Imaging Results in Higher Acceleration (CAIPIRINHA). *Magnetom Flash*. 2012.
 140. Freitag MT, Fenchel M, Bäumer P, et al. Improved clinical workflow for

- simultaneous whole-body PET/MRI using high-resolution CAIPIRINHA-accelerated MR-based attenuation correction. *Eur J Radiol*. 2017;96:12-20.
141. Quick HH, Von Gall C, Zeilinger M, et al. Integrated whole-body PET/MR hybrid imaging: Clinical experience. *Invest Radiol*. 2013;48:280-9.
 142. Ruhlmann V, Heusch P, Kühl H, et al. Potential influence of Gadolinium contrast on image segmentation in MR-based attenuation correction with Dixon sequences in whole-body 18F-FDG PET/MR. *Magn Reson Mater Physics, Biol Med*. 2016;29:301-8.
 143. Boel A, Molto A, van der Heijde D, et al. Do patients with axial spondyloarthritis with radiographic sacroiliitis fulfil both the modified New York criteria and the ASAS axial spondyloarthritis criteria? Results from eight cohorts. *Ann Rheum Dis*. 2019;78:1545-1549.
 144. Rudwaleit M, Van Der Heijde D, Landewé R, et al. The Assessment of SpondyloArthritis international Society classification criteria for peripheral spondyloarthritis and for spondyloarthritis in general. *Ann Rheum Dis*. 2011;70:25-31.
 145. Sieper J, Rudwaleit M, Baraliakos X, et al. The Assessment of SpondyloArthritis international Society (ASAS) handbook: a guide to assess spondyloarthritis. *Ann Rheum Dis*. 2009;68 Suppl 2:ii1-44.
 146. Kiltz U, Baraliakos X, Braun J. Ankylosing spondylitis. In: Comorbidity in Rheumatic Diseases. ; 2017:125-143.
 147. Kiltz U, Baraliakos X, Regel A, Bühring B, Braun J. Causes of pain in patients with axial spondyloarthritis. *Clin Exp Rheumatol*. 2017;35 Suppl 1:102-107.
 148. Van Der Heijde D, Ramiro S, Landewé R, et al. 2016 update of the ASAS-EULAR management recommendations for axial spondyloarthritis. *Ann Rheum Dis*. 2017;76:978-991.

149. Baraliakos X, Listing J, Rudwaleit M, Sieper J, Braun J. The relationship between inflammation and new bone formation in patients with ankylosing spondylitis. *Arthritis Res Ther*. 2008;10:R104.
150. Baraliakos X, Fruth M, Kiltz U, Braun J. Inflammatory spinal diseases: axial spondyloarthritis: Central importance of imaging. *Inflamm spinal Dis axial spondyloarthritis Cent importance imaging*. 2017;76:149-162.
151. Krohn M, Braum LS, Sieper J, et al. Erosions and fatty lesions of sacroiliac joints in patients with axial spondyloarthritis: Evaluation of different MRI techniques and two scoring methods. *J Rheumatol*. 2014;41:473-80.
152. Maksymowych WP, Chiowchanwisawakit P, Clare T, Pedersen SJ, Østergaard M, Lambert RGW. Inflammatory lesions of the spine on magnetic resonance imaging predict the development of new syndesmophytes in ankylosing spondylitis evidence of a relationship between inflammation and new bone formation. *Arthritis Rheum*. 2009;60:93-102.
153. Hawkins RA, Choi Y, Huang SC, et al. Evaluation of the skeletal kinetics of fluorine-18-fluoride ion with PET. *J Nucl Med*. 1992;33:633-42.
154. Fischer DR, Pfirrmann CWA, Zubler V, et al. High bone turnover assessed by 18F-fluoride PET/CT in the spine and sacroiliac joints of patients with ankylosing spondylitis: Comparison with inflammatory lesions detected by whole body MRI. *EJNMMI Res*. 2012;2:38.
155. Sawicki LM, Lütje S, Baraliakos X, et al. Dual-phase hybrid 18F-Fluoride Positron emission tomography/MRI in ankylosing spondylitis: Investigating the link between MRI bone changes, regional hyperaemia and increased osteoblastic activity. *J Med Imaging Radiat Oncol*. 2018;62:313-319.
156. Baraliakos X, Boehm H, Bahrami R, et al. What constitutes the fat signal detected by MRI in the spine of patients with ankylosing spondylitis? A

- prospective study based on biopsies obtained during planned spinal osteotomy to correct hyperkyphosis or spinal stenosis. *Ann Rheum Dis.* 2019;78:1220-1225.
157. Baraliakos X, Haibel H, Listing J, Sieper J, Braun J. Continuous long-term anti-TNF therapy does not lead to an increase in the rate of new bone formation over 8 years in patients with ankylosing spondylitis. *Ann Rheum Dis.* 2014;73:710-5.
158. Haroon N, Inman RD, Learch TJ, et al. The impact of tumor necrosis factor α inhibitors on radiographic progression in ankylosing spondylitis. *Arthritis Rheum.* 2013;65:2645-2654.
159. Molnar C, Scherer A, Baraliakos X, et al. TNF blockers inhibit spinal radiographic progression in ankylosing spondylitis by reducing disease activity: Results from the Swiss Clinical Quality Management cohort. *Ann Rheum Dis.* 2018;77:63-69.
160. Schuler MK, Platzek I, Beuthien-Baumann B, Fenchel M, Ehninger G, van den Hoff J. (18)F-FDG PET/MRI for therapy response assessment in sarcoma: comparison of PET and MR imaging results. *Clin Imaging.* 2015;39:866-870.
161. Tian J, Fu L, Yin D, et al. Does the novel integrated PET/MRI offer the same diagnostic performance as PET/CT for oncological indications? *PLoS One.* 2014;9:e90844.
162. Kwon HW, Becker A-K, Goo JM, Cheon GJ. FDG Whole-Body PET/MRI in Oncology: a Systematic Review. *Nucl Med Mol Imaging (2010).* 2017;51:22-31.
163. Siegel RL, Miller KD, Jemal A. Cancer statistics, 2018. *CA Cancer J Clin.* 2018;68:7-30.
164. Zugni F, Ruju F, Pricolo P, et al. The added value of whole-body magnetic resonance imaging in the management of patients with advanced breast cancer. *PLoS One.* 2018;13:e0205251.
165. Sawicki LM, Grueneisen J, Schaarschmidt BM, et al. Evaluation of 18F-FDG PET/MRI, 18F-FDG PET/CT, MRI, and CT in whole-body staging of recurrent

- breast cancer. *Eur J Radiol*. 2016;85:459-465.
166. Botsikas D, Kalovidouri A, Becker M, et al. Clinical utility of 18F-FDG-PET/MR for preoperative breast cancer staging. *Eur Radiol*. 2016;26:2297-2307.
167. Heusner TA, Hahn S, Jonkmanns C, et al. Diagnostic accuracy of fused positron emission tomography/magnetic resonance mammography: initial results. *Br J Radiol*. 2011;84:126-135.
168. Bristow AR, Agrawal A, Evans AJ, et al. Can computerised tomography replace bone scintigraphy in detecting bone metastases from breast cancer? A prospective study. *Breast*. 2008;17:98-103.
169. Muindi J, Coombes RC, Golding S, Powles TJ, Khan O, Husband J. The role of computed tomography in the detection of bone metastases in breast cancer patients. *Br J Radiol*. 1983;56:233-6.
170. Avrahami E, Tadmor R, Dally O, Hadar H. Early MR demonstration of spinal metastases in patients with normal radiographs and CT and radionuclide bone scans. *J Comput Assist Tomogr*. 1989;13:598-602.
171. Steinborn M, Tiling R, Heuck A, Brügel M, Stäbler A, Reiser M. Diagnosis of bone marrow metastases with MRI | Diagnostik der Metastasierung im Knochenmark mittels MRT. *Radiologe*. 2000;40:826-34.
172. Heusner T, Gölitz P, Hamami M, et al. "One-stop-shop" staging: Should we prefer FDG-PET/CT or MRI for the detection of bone metastases? *Eur J Radiol*. 2011;78:430-5.
173. Jambor I, Kuisma A, Ramadan S, et al. Prospective evaluation of planar bone scintigraphy, SPECT, SPECT/CT, 18F-NaF PET/CT and whole body 1.5T MRI, including DWI, for the detection of bone metastases in high risk breast and prostate cancer patients: SKELETA clinical trial. *Acta Oncol (Madr)*. 2016;55:59-67.

174. Löfgren J, Mortensen J, Rasmussen SH, et al. A prospective study comparing ^{99m}Tc-hydroxyethylene-diphosphonate planar bone scintigraphy and whole-body SPECT/CT with ¹⁸F-fluoride PET/CT and ¹⁸F-fluoride PET/MRI for diagnosing bone metastases. *J Nucl Med*. 2017;58:1778-1785.
175. Sawicki LM, Kirchner J, Umutlu L, et al. Comparison of ¹⁸F-FDG PET/MRI and MRI alone for whole-body staging and potential impact on therapeutic management of women with suspected recurrent pelvic cancer: a follow-up study. *Eur J Nucl Med Mol Imaging*. 2017;45:622-629.
176. Bitencourt AG V, Lima ENP, Chojniak R, et al. Multiparametric evaluation of breast lesions using PET-MRI: initial results and future perspectives. *Medicine (Baltimore)*. 2014;93:e115.
177. van Nijnatten TJA, Goorts B, Vöö S, et al. Added value of dedicated axillary hybrid ¹⁸F-FDG PET/MRI for improved axillary nodal staging in clinically node-positive breast cancer patients: a feasibility study. *Eur J Nucl Med Mol Imaging*. 2018;45:179-186.
178. Pinker K, Bogner W, Baltzer P, et al. Improved differentiation of benign and malignant breast tumors with multiparametric ¹⁸fluorodeoxyglucose positron emission tomography magnetic resonance imaging: a feasibility study. *Clin cancer Res an Off J Am Assoc Cancer Res*. 2014;20:3540-3549.
179. Morawitz J, Bruckmann N-M, Dietzel F, et al. Comparison of nodal staging between CT, MRI, and [(¹⁸F)]-FDG PET/MRI in patients with newly diagnosed breast cancer. *Eur J Nucl Med Mol Imaging*. 2021;49:992-1001.
180. Morawitz J, Bruckmann N-M, Dietzel F, et al. Determining the axillary nodal status with four current imaging modalities including (¹⁸F)-FDG PET/MRI in newly diagnosed breast cancer: A comparative study using histopathology as reference standard. *J Nucl Med*. 2021;62:1677-1683.

181. Lee B, Lim AK, Krell J, et al. The efficacy of axillary ultrasound in the detection of nodal metastasis in breast cancer. *Am J Roentgenol.* 2013;200:W314-20.
182. Valente SA, Levine GM, Silverstein MJ, et al. Accuracy of predicting axillary lymph node positivity by physical examination, mammography, ultrasonography, and magnetic resonance imaging. *Ann Surg Oncol.* 2012;19:1825-30.
183. Panda SK, Goel A, Nayak V, Shaik Basha S, Pande PK, Kumar K. Can Preoperative Ultrasonography and MRI Replace Sentinel Lymph Node Biopsy in Management of Axilla in Early Breast Cancer—a Prospective Study from a Tertiary Cancer Center. *Indian J Surg Oncol.* 2019;10:483-488.
184. Shin CH, Kim JI, Lee JY. The role of radiologic evaluation for detection of axillary lymph node metastasis in early breast cancer. *Eur J Cancer.* 2016;57:143-144.
185. Dendl K, Koerber SA, Kratochwil C, et al. FAP and FAPI-PET/CT in Malignant and Non-Malignant Diseases: A Perfect Symbiosis? *Cancers (Basel).* 2021;13:4946.
186. Backhaus P, Burg MC, Roll W, et al. Simultaneous FAPI PET/MRI Targeting the Fibroblast-Activation Protein for Breast Cancer. *Radiology.* 2022;302:39-47.
187. Rauscher I, Eiber M, Fürst S, et al. PET/MR imaging in the detection and characterization of pulmonary lesions: Technical and diagnostic evaluation in comparison to PET/CT. *J Nucl Med.* 2014;55:724-9.
188. Wielpütz MO. MRI of Pulmonary Nodules: Closing the Gap on CT. *Radiology.* November 2021;212516.
189. Benjamin MS, Drucker EA, McLoud TC, Shepard JAO. Small pulmonary nodules: Detection at chest CT and outcome. *Radiology.* 2003;226:489-493.
190. Jannusch K, Bruckmann NM, Geuting CJ, et al. Lung Nodules Missed in Initial Staging of Breast Cancer Patients in PET/MRI-Clinically Relevant? *Cancers (Basel).* 2022;14.

191. Horne ZD, Clump DA, Vargo JA, et al. Pretreatment SUVmax predicts progression-free survival in early-stage non-small cell lung cancer treated with stereotactic body radiation therapy. *Radiat Oncol.* 2014;9:41.
192. Liu J, Dong M, Sun X, Li W, Xing L, Yu J. Prognostic value of 18F-FDG PET/CT in surgical non-small cell lung cancer: A meta-analysis. *PLoS One.* 2016;11:e0146195.
193. Sharma A, Mohan A, Bhalla AS, et al. Role of Various Metabolic Parameters Derived from Baseline 18 F-FDG PET/CT as Prognostic Markers in Non-Small Cell Lung Cancer Patients Undergoing Platinum-Based Chemotherapy. *Clin Nucl Med.* 2018;43:e8-e17.
194. Burdick MJ, Stephans KL, Reddy CA, Djemil T, Srinivas SM, Videtic GMM. Maximum standardized uptake value from staging FDG-PET/CT does not predict treatment outcome for early-stage non-small-cell lung cancer treated with stereotactic body radiotherapy. *Int J Radiat Oncol Biol Phys.* 2010;78:1033-9.
195. Martin-Perez E, Capdevila J, Castellano D, et al. Prognostic factors and long-term outcome of pancreatic neuroendocrine neoplasms: Ki-67 index shows a greater impact on survival than disease stage. the large experience of the spanish national tumor registry (RGETNE). *Neuroendocrinology.* 2013;98:156-68.
196. Guo C, Chen X, Xiao W, Wang Q, Sun K, Wang Z. Pancreatic neuroendocrine neoplasms at magnetic resonance imaging: Comparison between grade 3 and grade 1/2 tumors. *Onco Targets Ther.* 2017;10:1465-1474.
197. Jang KM, Kim SH, Lee SJ, Choi D. The value of gadoxetic acid-enhanced and diffusion-weighted MRI for prediction of grading of pancreatic neuroendocrine tumors. *Acta radiol.* 2014;55:140-8.
198. De Robertis R, Cingarlini S, Martini PT, et al. Pancreatic neuroendocrine

- neoplasms: Magnetic resonance imaging features according to grade and stage. *World J Gastroenterol.* 2017;23:275-285.
199. Kim M, Kang TW, Kim YK, et al. Pancreatic neuroendocrine tumour: Correlation of apparent diffusion coefficient or WHO classification with recurrence-free survival. *Eur J Radiol.* 2016;85:680-7.
200. Kayani I, Bomanji JB, Groves A, et al. Functional imaging of neuroendocrine tumors with combined PET/CT using 68Ga-DOTATATE (Dota-DPhe1, Tyr3-octreotate) and 18F-FDG. *Cancer.* 2008;112:2447-55.
201. Spick C, Herrmann K, Czernin J. 18F-FDG PET/CT and PET/MRI Perform Equally Well in Cancer: Evidence from Studies on More Than 2,300 Patients. *J Nucl Med.* 2016.

Danksagung

Als erstes möchte mich bei Herrn Univ.-Prof. Dr. med. Gerald Antoch bedanken, der mich sowohl bei meinen Forschungsarbeiten als auch meiner klinischen Ausbildung jederzeit uneingeschränkt unterstützt und gefördert hat.

Bedanken möchte ich mich auch bei Frau Prof. Dr. med. Lale Umutlu und Herrn Prof. Dr. med. Benedikt Schaarschmidt für die enge und freundschaftliche Zusammenarbeit während meiner Forschungszeit am Universitätsklinikum Essen und für die Unterstützung bei der Erarbeitung neuer Forschungsthemen.

Mein Dank gilt auch Herrn Univ.-Prof. Dr. med. Michael Forsting und Univ.-Prof. Dr. med. Ken Herrmann und den Mitarbeitern des Institutes für Diagnostische und Interventionelle Radiologie und Neuroradiologie und der Klinik für Nuklearmedizin des Universitätsklinikums Essen für die gute Zusammenarbeit.

Außerdem möchte ich mich bei allen klinischen Kooperationspartnern für die gute Zusammenarbeit und Unterstützung bei der Umsetzung der wissenschaftlichen Projekte bedanken.

Mein ganz besonderer Dank gilt Herrn Priv.-Doz. Dr. med. Lino Sawicki und Herrn Priv.-Doz. Dr. med. Julian Kirchner, die früh mein Interesse an der onkologisch-hybridnen Bildgebung geweckt haben und mich mit großer Freude an diesem Thema arbeiten ließen. Mit seiner positiven und optimistischen Art ist Julian ein Motivator, der seinesgleichen sucht. Seine Begeisterung für das Thema und die Forschung, aber auch die stets freundschaftliche und überaus kollegiale und gute Zusammenarbeit in der Arbeitsgruppe mit Frau Dr. med. Janna Morawitz und Herrn Dr. med. Kai Jannusch sind maßgeblich für den Erfolg und den Abschluss dieser Arbeit verantwortlich. Diese

Umstände werden mich immer sehr positiv, mit Freude und Dankbarkeit an diese Zeit zurückdenken lassen.

Auch bedanken möchte ich mich bei meinen Mitarbeitern des Institutes für Diagnostische und Interventionelle Radiologie am Universitätsklinikum Düsseldorf für die kollegiale und gute Zusammenarbeit im klinischen Alltag und die Unterstützung bei meinen wissenschaftlichen Projekten.

Mein abschließender Dank gilt meinen guten Freunden, deren Rat und Beistand ich in vielen Lebenslagen gerne angenommen habe, meiner Familie, deren Herzlichkeit und Hilfe keine Grenzen kennt und meiner lieben Frau Charlotte, die mir fortwährend den Rücken freigehalten hat. Ohne ihre bedingungslose Unterstützung und liebevolle Hilfe wäre diese Arbeit nicht möglich gewesen.

Zugrunde liegende Forschungsarbeiten

Die Sonderdrucke erfolgen im Rahmen der Autorenrechte.



Prospective evaluation of whole-body MRI and ^{18}F -FDG PET/MRI in N and M staging of primary breast cancer patients

Nils Martin Bruckmann¹ · Lino M. Sawicki¹ · Julian Kirchner¹ · Ole Martin¹ · Lale Umutlu² · Ken Herrmann³ · Wolfgang Fendler³ · Ann-Kathrin Bittner⁴ · Oliver Hoffmann⁴ · Svetlana Mohrmann⁵ · Frederic Dietzel¹ · Marc Ingenwerth⁶ · Benedikt M. Schaarschmidt² · Yan Li² · Bernd Kowall⁷ · Andreas Stang⁷ · Gerald Antoch¹ · Christian Buchbender¹

Received: 26 January 2020 / Accepted: 30 March 2020 / Published online: 24 April 2020
© The Author(s) 2020

Abstract

Objectives To evaluate and compare the diagnostic potential of whole-body MRI and whole-body ^{18}F -FDG PET/MRI for N and M staging in newly diagnosed, histopathologically proven breast cancer.

Material and methods A total of 104 patients (age 53.4 ± 12.5) with newly diagnosed, histopathologically proven breast cancer were enrolled in this study prospectively. All patients underwent a whole-body ^{18}F -FDG PET/MRI. MRI and ^{18}F -FDG PET/MRI datasets were evaluated separately regarding lesion count, lesion localization, and lesion characterization (malignant/benign) as well as the diagnostic confidence (5-point ordinal scale, 1–5). The N and M stages were assessed according to the eighth edition of the American Joint Committee on Cancer staging manual in MRI datasets alone and in ^{18}F -FDG PET/MRI datasets, respectively. In the majority of lesions histopathology served as the reference standard. The remaining lesions were followed-up by imaging and clinical examination. Separately for nodal-positive and nodal-negative women, a McNemar chi² test was performed to compare sensitivity and specificity of the N and M stages between ^{18}F -FDG PET/MRI and MRI. Differences in diagnostic confidence scores were assessed by Wilcoxon signed rank test.

Results MRI determined the N stage correctly in 78 of 104 (75%) patients with a sensitivity of 62.3% (95% CI: 0.48–0.75), a specificity of 88.2% (95% CI: 0.76–0.96), a PPV (positive predictive value) of 84.6% (95% CI: 69.5–0.94), and a NPV (negative predictive value) of 69.2% (95% CI: 0.57–0.8). Corresponding results for ^{18}F -FDG PET/MRI were 87/104 (83.7%), 75.5% (95% CI: 0.62–0.86), 92.2% (0.81–0.98), 90% (0.78–0.97), and 78.3% (0.66–0.88), showing a significantly better sensitivity of ^{18}F -FDG PET/MRI determining malignant lymph nodes ($p = 0.008$). The M stage was identified correctly in MRI and ^{18}F -FDG PET/MRI in 100 of 104 patients (96.2%). Both modalities correctly staged all 7 patients with distant metastases, leading to false-positive findings in 4 patients in each modality (3.8%). In a lesion-based analysis, ^{18}F -FDG PET/MRI showed a significantly better performance in correctly determining malignant lesions (85.8% vs. 67.1%, difference 18.7% (95% CI: 0.13–0.26), $p < 0.0001$) and offered a superior diagnostic confidence compared with MRI alone (4.1 ± 0.7 vs. 3.4 ± 0.7 , $p < 0.0001$).

Nils Martin Bruckmann and Lino M. Sawicki contributed equally to this work.

This article is part of the Topical Collection on Oncology - Chest

✉ Julian Kirchner
Julian.Kirchner@med.uni-duesseldorf.de

¹ Medical Faculty, Department of Diagnostic and Interventional Radiology, University Dusseldorf, Dusseldorf, Germany

² Department of Diagnostic and Interventional Radiology and Neuroradiology, University Hospital Essen, University of Duisburg-Essen, Essen, Germany

³ Department of Nuclear Medicine, University Hospital Essen, University of Duisburg-Essen, Essen, Germany

⁴ Department Gynecology and Obstetrics, University Hospital Essen, University of Duisburg-Essen, Essen, Germany

⁵ Department of Gynecology, Medical Faculty, University Dusseldorf, Dusseldorf, Germany

⁶ Institute of Pathology, University Hospital Essen, West German Cancer Center, University Duisburg-Essen and the German Cancer Consortium (DKTK), Essen, Germany

⁷ Institute of Medical Informatics, Biometry and Epidemiology, University Hospital of Essen, Essen, Germany

Conclusion ^{18}F -FDG PET/MRI has a better diagnostic accuracy for N staging in primary breast cancer patients and provides a significantly higher diagnostic confidence in lesion characterization than MRI alone. But both modalities bear the risk to overestimate the M stage.

Keywords PET/MRI · MRI · Breast cancer staging

Introduction

Breast cancer is the most common cancer in women worldwide with approximately 2.1 million new cases every year [1]. As in most malignancies, breast cancer mortality increases with the individual tumor burden, while management and prognosis depend heavily on the initial tumor stage [2]. Therefore, for optimal treatment and better survival, precise initial staging plays a pivotal role. Herein, the correct determination of the lymph node status and the detection of distant metastases are of utmost importance. Treatment of breast cancer patients without distant metastases usually includes surgery and chemotherapy, alongside irradiation or further drug therapy before and after surgery [3]. Depending on primary tumor size and locoregional metastases, the surgical procedure of choice can go from breast-preserving resection to complete mastectomy and dissection of the ipsilateral axillary and sub-clavian lymph nodes. In patients with proven distant metastases a palliative concept is intended, including extensive systemic therapy [4].

The current diagnostic algorithm comprises plain mammography, ultrasound, and in some cases magnetic resonance imaging (MRI) of the breast to evaluate the local tumor extent [3, 5]. Especially the demand for dedicated breast MRI has heavily increased over the last few years [6]. Due to a growing understanding of the importance of an accurate initial staging of breast cancer patients, whole-body imaging with computed tomography (CT) has recently been established in addition to bone scintigraphy for the detection of locoregional and distant metastases [3, 7]. However, whole-body MRI is rarely used for initial staging of breast cancer [8], despite the option of combining dedicated breast MRI with a whole-body examination and its well-known advantages when imaging parenchymal organs [9, 10]. When it comes to PET recent studies have reported a high diagnostic accuracy of ^{18}F -fluorodeoxyglucose-positron emission tomography/CT (^{18}F -FDG PET/CT) in distant breast cancer metastases [11–13]. Consequently, hybrid ^{18}F -FDG PET/MRI might serve as a comprehensive “all-in-one” breast cancer staging tool, providing precise local and whole-body staging in one procedure. In smaller cohorts, ^{18}F -FDG PET/MRI has already shown promising results as an alternative modality in primary breast cancer staging [14–18] and in recurrent disease [19–22].

Therefore, the purpose of this prospective study was to evaluate the diagnostic accuracy of whole-body MRI compared with whole-body ^{18}F -FDG PET/MRI for the initial N and M staging in a large cohort of therapy-naïve breast cancer patients.

Material and methods

Patients

This prospective, multi-center study was approved by the institutional review board of the University Duisburg-Essen (study number 17-7396-BO) and Düsseldorf (study number 6040R), and all patients signed a written informed consent form prior to enrolment. Between August 2017 and June 2019, a total of 104 female patients (53.4 ± 12.5 , range 29–84 years, Table 1) with newly diagnosed breast cancer were included if they met the following inclusion criteria: [1] Newly diagnosed, treatment-naïve T2-tumor or higher T-stage or [2] newly diagnosed, treatment-naïve triple-negative tumor of every size or [3] newly diagnosed, treatment-naïve tumor with molecular high risk (T1c, Ki67 > 14%, HER2-new over-expression, G3). Exclusion criteria were former malignancies in the last 5 years, contraindications to MRI or MRI contrast agents and pregnancy or breast-feeding. All enrolled patients underwent ^{18}F -FDG PET/MRI.

PET/MRI

The ^{18}F -FDG PET/MRI examinations were performed on an integrated 3.0-Tesla Biograph mMR scanner (Siemens Healthcare GmbH, Erlangen, Germany). To ensure blood glucose levels below 150 mg/dl, blood samples were obtained prior to the injection of a body-weight adapted dose of ^{18}F -FDG (4 MBq/kg bodyweight), resulting in a mean activity of 253.8 ± 42.6 MBq. All patients underwent whole-body ^{18}F -FDG PET/MRI in supine position from head to the mid-thigh using a dedicated 16-channel head-and neck radiofrequency (RF) coil, a 24-channel spine-array RF coil and referring to the patients height three to five flexible 6-channel body array RF coils. PET images were performed simultaneously with the MRI data acquisition and with an acquisition time of 3 min per bed position in four or five positions, depending on the patients’ height (axial FOV 25.8 cm, matrix size 344×344).

Table 1 Patients demographics

		N (%)
Total patients		104(100)
Menopause status	Pre	43
	Peri	11
	Post	50
Family risk profile	Positive	11
	Negative	93
BRCA-1	Positive	1
	Negative	27
	Unknown	76
BRCA-2	Positive	2
	Negative	26
	Unknown	76
Ki 67	Positive (> 14%)	88
	Negative (< 14%)	16
PR status	Positive	74
	Negative	30
ER status	Positive	77
	Negative	27
HER2-neu expression	0	42
	1+	33
	2+	11
	3+	18
Subtype	Luminal a	12
	Luminal b	74
	HER2-enriched	2
	Basal-like	16
Tumor Grade	G1	2
	G2	60
	G3	42
Histology	Ductal invasive/NST	97
	Lobular invasive	5
	Mucinous invasive	1
	Mixed type	1

Mean duration time according to manufacturer's specifications is set at 40 min for the whole-body examination. PET data sets were reconstructed utilizing an iterative ordered-subset expectation maximization (OSEM) algorithm with three iterations and 21 subsets.

For MR-based PET attenuation correction, a two-point (fat, water) coronal 3D-Dixon-VIBE sequence was acquired to generate a four-compartment model (background air, lungs, fat, muscle).

The dedicated ¹⁸F- FDG PET/MRI protocol consisted of the following sequences:

1. A transverse T2-weighted (T2w) fat-suppressed half Fourier acquisition single shot turbo spin echo (HASTE)

sequence in respiratory medium position and a slice thickness of 7 mm.

2. A transverse diffusion-weighted echo-planar imaging (EPI DWI) sequence (*b* values 0, 500, 1000) in respiratory medium position with a slice thickness of 5 mm.
3. A transversal T1-weighted (T1w) fat saturated post-contrast volume-interpolated breath-hold examination (VIBE) sequence after intravenous injection of a gadolinium-based contrast agent (0.2 mmol/kg body weight, Dotarem, Guerbet GmbH, Germany) with a slice thickness of 3 mm.

As part of the ¹⁸F- FDG PET/MRI examination, a dedicated breast PET/MRI in head-first prone position was performed in all patients prior to whole-body imaging. The presented analysis is based on data of a larger prospective study. Therefore, in consideration of the focus of the presented study, these dedicated breast MRI sequences were not included in evaluation.

Image analysis

MRI and ¹⁸F-FDG PET/MRI images were analyzed separately by two experienced radiologists in hybrid imaging and MR imaging with a reading gap of at least 4 weeks to avoid recognition bias. The datasets were evaluated on a dedicated OsiriX workstation (Osirix MD v.9.0.2, Pixmeo, SARL, Bernex, Switzerland). The readers were aware of the diagnosis but blinded to results of N and M stages and results from prior imaging (e.g., sonography). For every patient, the number of lesions, the lesion type (malignant / benign), location, and size as well as the diagnostic confidence of lesion type ratings (5-point ordinal scale, 1 = very low confidence, 2 = low confidence, 3 = indeterminate confidence, 4 = high confidence, 5 = very high confidence) were determined in MRI alone and ¹⁸F-FDG PET/MRI. Discrepant interpretations were resolved by consensus decision-making in a separate session between the two readers. Lymph nodes were classified as malignant based on morphological and metabolic criteria, comprising short-axis diameter > 10 mm, spherical configuration, shape (smooth vs. irregular), increased contrast enhancement, diffusion restriction, and focally increased FDG uptake [22, 23]. In accordance with previous publications, findings were considered to be malignant for the evaluation of distant metastases when showing an invasive growth pattern, central necrosis, and typically malignant MR signal characteristics like pathological contrast enhancement and diffusion restriction. On ¹⁸F-FDG PET/MRI a visually detectable focal uptake of FDG above background signal counted as a sign of malignancy. The standardized uptake value (SUVmax) was measured in every lesion with a focal FDG uptake by placing a manually drawn polygonal volume of interest (VOI) over each

lesion on attenuation-corrected PET images. In all lesions, the maximum diameter was measured.

Reference standard

The 104 patients enrolled in this study had a total of 298 lesions, excluding the primary tumor mass. In 98 patients, 204 out of 298 lesions were confirmed histopathologically. A surrogate reference standard was applied to the remaining 94 lesions containing follow-up imaging and clinical examinations. A decrease in size of suspicious lesions after therapy was regarded as a sign of malignancy. Forty-five lesions were followed-up by CT and 19 lesions by MRI (mean interval 8 ± 5 months). The remaining 30 lesions were followed-up with sonography and clinical examination.

Statistical analysis

Statistical analysis was performed using SPSS Statistics 22 (IBM Inc., Armonk, NY, USA) and GraphPad Prism 7 (GraphPad Software, La Jolla, CA, USA). All data are presented as mean \pm standard deviation. The data were analyzed calculating sensitivity, specificity, positive and negative predictive values (PPV, NPV) on a per-patient basis, and a per-lesion basis. Separately for nodal-positive and nodal-negative patients, a McNemar chi² test was performed to compare sensitivity and specificity between MRI alone and ¹⁸F-FDG PET/MRI. We used a Wilcoxon signed rank test to compare the diagnostic confidence of lesion nature assessments (benign/malignant). A *p* value of less than 0.05 was set as indicating a statistical significance.

Results

Patient-based analysis

When differentiating between nodal-positive and nodal-negative patients, MRI rated 78/104 (75%, 95% CI 65.5–83.0) of the patients correctly, leading to a sensitivity of 62.3% (95% CI: 47.9–75.2), a specificity of 88.2% (95% CI 76.1–95.6), a PPV of 84.6% (95% CI 69.5–94.1), and a NPV of 69.2% (95% CI 56.6–80.1) (see Table 2). The exact N stage (i.e., N0, N1, N2, N3) was determined correctly by MRI in 74 of 104 patients (71.2%, 95% CI 61.5–79.6). The specific distribution of lymph nodes is shown in Fig. 1.

With ¹⁸F-FDG PET/MRI differentiation between nodal-positive and nodal-negative patients was rated correctly in 87/104 (83.7%, 95% CI 75.1–90.2) with a sensitivity of 75.5% (95% CI 61.7–86.2), a specificity of 92.2% (95% CI 81.1–97.8), a PPV 90.9% (95% CI 78.3–97.5), and a NPV of 78.3% (95% CI 65.8–87.9). The exact N stage was determined correctly in 86/104 (82.7%, 95% CI 74.0–89.4) of the patients (Fig. 1). A total of 20/53 (37.7%, 95% CI 24.8–52.1)

Table 2 N staging on a patient-based analysis. Distribution of N staging for MRI alone and ¹⁸F-FDG PET/MRI and comparison with the reference standard

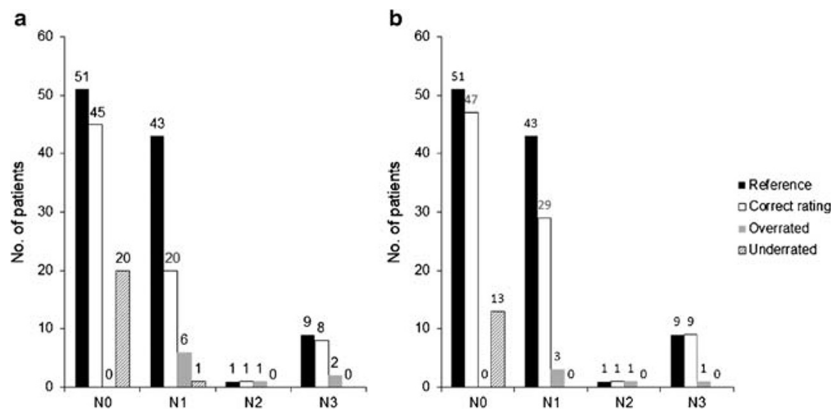
N stage MRI	Standard of reference		
	Nodal negative	Nodal positive	Total
Nodal negative	45	20	65
Nodal positive	6	33	39
Total	51	53	
Correct N ratings			78 (75.0%)
N stage PET/MRI			
Nodal negative	47	13	60
Nodal positive	4	40	44
Total	51	53	
Correct N ratings			87 (83.7%)

nodal-positive patients were missed by MRI, while only 13/53 (24.5%, 95% CI 13.8–38.3) nodal-positive patients were missed with ¹⁸F-FDG PET/MRI (Fig. 4). There were 6 (11.8%, 95% CI 4.4–23.9) false-positive lymph node findings in MRI and 4 (7.8%, 95% CI 2.2–18.9) in PET/MRI.

For nodal-positive women, the exact McNemar chi² test indicated that nodes were more often found by ¹⁸F-FDG PET/MRI than by MRI alone (test statistic = 7.0, *p* = 0.002). The corresponding difference in sensitivities was 13.2% (95% CI –4.2–30.7). For nodal-negative women, the test statistic of the exact McNemar chi² test was 2.0 (*p* = 0.50). The corresponding difference in specificities was 3.9% (95% CI –7.6–15.4%). Table 2 gives a detailed overview of N stage performance with MRI and ¹⁸F-FDG PET/MRI.

According to the reference standard distant metastases were present in 7/104 patients (6.7%, Table 3, Figs. 2 and 3). The M stage was defined correctly with MRI and ¹⁸F-FDG PET/MRI in 100 of 104 patients. As both modalities correctly detected all patients with proven distant metastases, there were false-positive findings in 4 patients (3.8%, 95% CI 1.1–9.6) in each modality, resulting in a sensitivity of 100% (95% CI 59.0–100.0), a specificity of 95.9% (95% CI 90.4–98.9), a NPV of 100% (95% CI 96.3–100.0), and a PPV of 63.7% (95% CI 30.8–89.1). Three of the false-positive ratings were identical in both modalities, comprising one patient with a focal pericarditis showing a normal follow-up MRI after 12 months, one patient with two suspicious lung lesions that were followed-up by CT after 2 months without any sign of malignancy and one patient with multiple enlarged abdominal lymph nodes, which turned out benign in a histopathological examination and on follow-up MRI after 1 year. Additionally, ¹⁸F-FDG PET/MRI identified one patient with a suspicious liver lesion and MRI determined a pararenal and a subcutaneous mass in another patient. Both these lesions were non-malignant according to follow-up imaging (Fig. 4).

Fig. 1 Determination of the lymph node stage with MRI alone (a) and ^{18}F -FDG PET/MRI (b)



Lesion-based analysis

In accordance with the reference standard, a total of 298 lesions, containing 155 malignant (52%) and 143 benign lesions (48%), were included in the final analysis (see Table 4, Fig. 3). ^{18}F -FDG PET/MRI showed a higher diagnostic accuracy in the lesion-based analysis than MRI alone with 258 vs. 224 correct lesion nature ratings (86.6% vs. 75.2%, difference: 11.4% (95% CI 5.1–17.7)). Furthermore, the McNemar chi² test indicated a significant difference for correct malignant lesion rating between MRI alone and ^{18}F -FDG PET/MRI (104 vs. 133 correct lesion nature ratings, 67.1% vs. 85.8%, difference 18.7% (95% CI 9.5–27.9), $p < 0.0001$) and an equivalent result in detecting benign lesions (120 vs. 125 correct lesion nature ratings, 83.9% vs. 87.4%, difference 3.5% (95% CI –4.6–11.6), $p = 0.063$) (see Table 5). In detail, ^{18}F -FDG PET/MRI had 22/155 (14.2%, 95% CI 9.1–20.7) false-negative ratings of axillary and subclavian lymph nodes, due to small lesion size and weak FDG uptake, while MRI alone misinterpreted a total of 38/155 (24.5%, 95% CI 18.0–32.1) of the malignant lesions as not malignant. ^{18}F -FDG PET/MRI correctly identified all of the 31 distant metastases and did not miss any of the malignant lesions while MRI failed to detect 5 bone metastases in one patient and one malignant hilar lymph node as well as seven non-enlarged lymph node metastases in clavicular and mammalian position. Moreover, there were 19

and 18 histopathologically proven false-positive findings in MRI and ^{18}F -FDG PET/MRI, respectively, due to elevated size, suspicious shape, or increased FDG uptake.

Diagnostic confidence

^{18}F -FDG PET/MRI showed a significantly higher overall diagnostic confidence than MRI alone (4.1 ± 0.7 vs. 3.4 ± 0.7 , $p < 0.0001$). Comparing the diagnostic confidence regarding malignant lesions only, containing locoregional and distant metastatic lesions, ^{18}F -FDG PET/MRI was also significantly superior to MRI alone (4.3 ± 0.7 vs. 3.4 ± 0.7 , $p < 0.0001$). Comparing the diagnostic confidence regarding benign lesions only, significant differences in favor of ^{18}F -FDG PET/MRI were observed (3.8 ± 0.7 vs. 3.3 ± 0.7 , $p < 0.001$).

Discussion

This study shows that both the whole-body ^{18}F -FDG PET/MRI and whole-body MRI are valuable diagnostic tools for staging breast cancer patients. ^{18}F -FDG PET/MRI outperforms the accuracy of MRI alone when assessing the N stage, and the diagnostic confidence is significantly higher with ^{18}F -FDG PET/MRI.

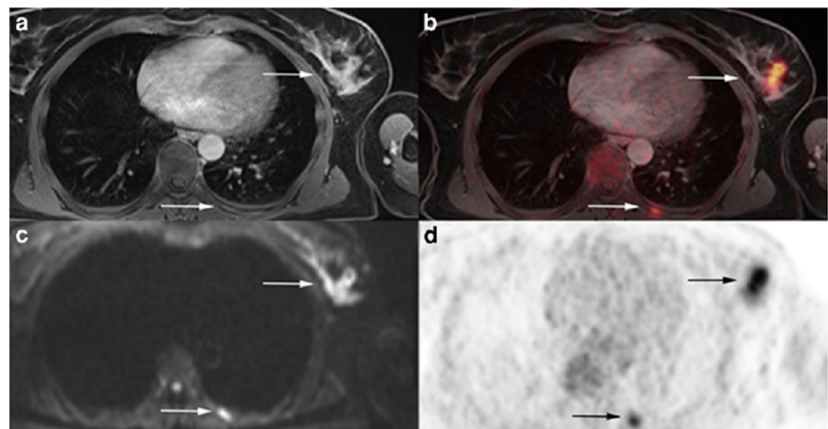
Due to a growing understanding of the importance of an accurate initial staging, new staging modalities, primarily the CT, have been established and integrated into breast cancer guidelines [4, 7]. The demand for dedicated breast MRI has heavily increased over the last few years, and based on the growing usage of breast MRI, a subsequent implementation of a whole-body MRI is also conceivable.

In regard to the application of hybrid imaging modalities, the 2015 European Society For Medical Oncology (ESMO) and the 2016 National Comprehensive Cancer Network (NCCN) guidelines consider systemic staging with ^{18}F -FDG PET/CT only for patients with inconclusive results in conventional imaging, in high-risk patients [7] or in patients with newly diagnosed stage III breast cancer, except for operable

Table 3 M staging on a patient-based analysis. Distribution of M staging for MRI and ^{18}F -FDG PET/MRI and comparison to the reference standard. This table is identical for both modalities

M stage MRI and PET/MRI	Standard of reference		
	Negative	Positive	Total
Negative	93	0	93
Positive	4	7	11
Total	97	7	
Correct N and M in MRI			72 (69.2%)
Correct N and M in PET/MRI			84 (80.8%)

Fig. 2 A 57-year old woman with diagnosis of primary breast cancer. Primary tumor located in the left breast and visible bone metastasis in a left rib with contrast enhancement on T1w fs VIBE (a), corresponding diffusion restriction (c), and pathological FDG uptake on PET (d) and fused ¹⁸F-FDG PET/MRI (b)



IIIA breast cancer [24]. However, recent studies showed that ¹⁸F-FDG PET/CT detects unsuspected distant metastases in up to 15% of patients compared to the traditional staging algorithm in patients with initial stage IIB breast cancer [13, 25, 26]. Since its introduction in 2011, there has been a large quantity of studies indicating a high diagnostic value of PET/MRI for whole-body cancer staging [27]. Several trials have already noted a superiority of PET/MRI compared with MRI alone in primary and recurrent cancer staging, for example in women with pelvic cancer [23, 28]. Furthermore, some initial studies showed similar results for the superiority of hybrid imaging modalities in detecting malignant lymph nodes and distant metastases in breast cancer [19, 29, 30].

Furthermore, it has been shown that ¹⁸F-FDG PET/MRI is superior to ¹⁸F-FDG PET/CT in the detection of breast cancer metastases [19]. This applies to axillary lymph node metastases, to liver and bone metastases, and to the total tumor stage [21, 31, 32]. It was emphasized in former studies that in combination with a dedicated breast PET/MRI protocol, ¹⁸F-FDG PET/MRI has the appealing potential of a one-stop-shop solution for patients with primary breast cancer [33, 34]. The results of our study reveal a significantly better accuracy for determining the correct N stage with ¹⁸F-FDG PET/MRI than with MRI alone. Both modalities showed similarly strong

results in specificity on a patient-based analysis for the N and M rating. The lesion-based analysis confirmed these results discovering a significant higher diagnostic accuracy of ¹⁸F-FDG PET/MRI especially in detecting malignant lesions with lower false-negative ratings, especially in malignant lymph nodes.

Regarding the detection of locoregional lymph node metastases, Grueneisen et al. described a higher sensitivity of PET-based imaging, comparing ¹⁸F-FDG PET/CT, ¹⁸F-FDG PET/MRI, and MRI alone in a study cohort of 49 primary breast cancer patients with sensitivities of 78%, 78%, and 67% and specificities of 94%, 90%, and 87%, supporting the results of our trial [32]. Ergul et al. also showed a higher performance of PET-based imaging for axillary metastases with a sensitivity of 67% and a specificity of 89% with ¹⁸F-FDG PET/CT, compared with 47% and 78% for MRI [35]. The sentinel lymph node biopsy is still the clinical standard for determining nodal-positive patients. In clinical routine, nodal-positive patients undergo axillary lymph node dissection (ALND) in a second surgical intervention. The traditional staging algorithm with clinical examination, sonography, conventional mammography, and breast MRI is a useful but still inadequate predictor of axillary lymph node involvement and is far away from serving as a potential alternative to invasive

Fig. 3 A 47-year old woman with primary breast cancer on the left side. Visible enlarged axillary lymph node with contrast enhancement in T1w fs VIBE (a) and corresponding diffusion restriction (c) as well as a pathological FDG uptake on PET (d) and fused ¹⁸F-FDG PET/MRI (b), rated as an axillary lymph node metastasis

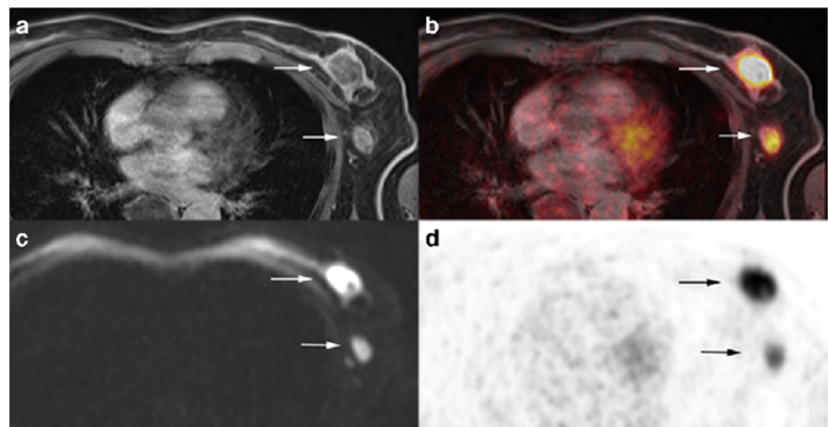
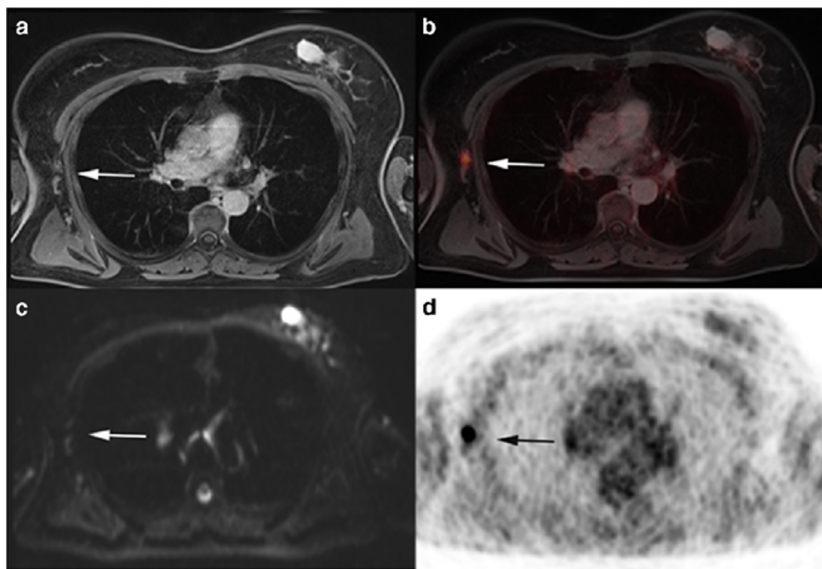


Fig. 4 A 61-year old woman with diagnosis of primary breast cancer. Not enlarged, ovoid axillary lymph nodes in T1w fs VIBE without contrast enhancement and with visible fatty hilum (**a**). No evidence of a clear diffusion restriction (**c**). However, a pathological FDG uptake on PET (**d**) and fused ¹⁸F-FDG PET/MRI (**b**) is visible, indicating an axillary lymph node metastasis. Accordingly, histopathology confirmed malignancy



procedures [36, 37]. Thus, according to previous results and the results of our study, PET/MRI and PET/CT are imaging techniques with a more reliable selection of patients in nodal-positive and nodal-negative and could help to reduce surgical intervention, for example, identifying patients who should be treated with ALND immediately, avoiding a prior lymph node biopsy.

In our study, there was no difference between ¹⁸F-FDG PET/MRI and MRI alone when assessing the M stage. Both modalities were able to detect all of the seven patients with distant metastases but bear the risk of overestimating the M stage, rating four patients as false positive. In the study of Sawicki et al. [19], whole-body ¹⁸F-FDG PET/MRI reported superiority regarding detection of distant malignant lesions compared to whole-body MRI in recurrent breast cancer patients. Catalano et al. [38] compared whole-body ¹⁸F-FDG PET/MRI with whole-body DWI MRI in a smaller cohort study, yielding an insignificantly

better performance of PET/MRI in predicting the initial whole-body tumor stage of breast cancer.

Other studies explored the expected high diagnostic potential of ¹⁸F-FDG PET/MRI and revealed a higher sensitivity of ¹⁸F-FDG PET/MRI over ¹⁸F-FDG PET/CT in the diagnosis of locoregional and distant metastases in breast cancer, especially regarding liver and bone metastases, the most common locations of distant breast cancer spread [19, 21, 39]. For instance, Catalano et al. [40] described a significantly higher identification of bone metastases in breast cancer by ¹⁸F-FDG PET/MRI compared with ¹⁸F-FDG PET/CT (141 vs. 90, $p < 0.001$) in 25 patients. In the study of Pace et al. [41], ¹⁸F-FDG PET/MRI showed equivalent performance to ¹⁸F-FDG PET/CT in terms of qualitative lesion detection. Only the overall detection and characterization of lung lesions remains inferior with ¹⁸F-FDG PET/CT, caused by the limited ability of MRI to detect small lung lesions [9, 10]. In view of our own results and results of the aforementioned previous studies, it can be summarized that

Table 4 Location of all 155 malignant lesions according to the standard of reference

	Location	Number	Percentage
Distant	Bone metastases	28	18.1
	Lung metastases	2	1.3
	Hilar lymph node	1	0.6
Locoregional	Lymph node metastases	124	80
	Axillary	102	
	Clavicular	12	
	Subpectoral	2	
	Cervical	1	
	Internal mammary artery	7	
Total		155	100

Table 5 Lesion-based analysis. Correct ratings, false ratings and missed lesions on MRI alone and ¹⁸F-FDG PET/MRI in relation to the total number of malignant and benign according to the reference standard

	MRI	PET/MRI	Malignant lesions	Benign lesions
MRI	Correct ratings	104 (67.1%)	120 (83.9%)	
	False ratings	38 (24.5%)	19 (13.3%)	
	Missed lesions	13 (8.4%)	4 (2.8%)	
	Total	155 (100%)	143 (100%)	
PET/MRI	Correct ratings	133 (85.8%)	125 (87.4%)	
	False ratings	22 (14.2%)	18 (12.6%)	
	Missed lesions	0 (0%)	0 (0%)	
	Total	155 (100%)	143 (100%)	

regarding distant metastases detection ^{18}F -FDG PET/MRI appears to have a high sensitivity but bears the risk of false-positive findings. From a clinical perspective, a final histopathological confirmation of suspicious lesions is still required.

Besides, the mere detection of potential lesions, in daily routine diagnostic or interpretation confidence, is also a matter of high interest, and the level of confidence might vary between imaging modalities. In our study, we assessed the practical confidence of the reading radiologists in ^{18}F -FDG PET/MRI and MRI. We found that hybrid PET/MRI imaging has great advantages with regard to the confidence of the final diagnosis that was assigned to a suspicious lesion. We believe that this is before all other reasons based on its ability to visualize pathologically increased glucose metabolism of malignant lesions, thereby, minimizing the uncertainty in the dichotomization between benign and malignant lesion nature compared with conventional imaging techniques [23].

This study has some limitations. First of all, a general limitation of PET/MRI still remains the long acquisition time, reducing the patients comfort during examination [42]. Secondly, since biopsy, especially in patients with advanced tumor stages, was not necessarily required in all lesions according to guideline-based management and ethical standards, a modified reference standard had to be applied including follow-up imaging and clinical examinations. This procedure was in accordance with former studies [15, 19, 28]. Another relative limitation of our study is the fact, that we used the MRI images of the ^{18}F -FDG PET/MRI protocol, as some authors prefer a dedicated MRI. However, a comprehensive MRI protocol was established as part of the ^{18}F -FDG PET/MRI scan, and, based on this protocol, MRI image quality was not limited compared with a stand-alone MRI.

In conclusion, this prospective study demonstrates a high value of ^{18}F -FDG PET/MRI for the N and M staging in patients with primary breast cancer. ^{18}F -FDG PET/MRI has a superior diagnostic performance on a per-patient and a per-lesion basis compared with MRI alone when determining the N-stage. Although MRI alone and ^{18}F -FDG PET/MRI detected all patients with histopathological proven distant metastases, both modalities bear a certain risk to overestimate the M stage. Nevertheless, ^{18}F -FDG PET/MRI should be considered as a useful alternative for systematic staging of breast cancer patients at time of diagnosis.

Data availability statement The corresponding author had full access to all data in the study and had all responsibility for the decision to submit for publication.

Funding information Open Access funding provided by Projekt DEAL. The study is funded by the Deutsche Forschungsgemeinschaft (DFG), the German Research Foundation (BU3075/2-1).

Compliance with ethical standards

Conflict of interest The authors declare that they have no conflict of interest.

Ethical approval All procedures performed were in accordance with the ethical standards of the institutional research committee of the University Duisburg-Essen (study number 17-7396-BO) and Düsseldorf (study number 6040R) and with the principles of the 1964 Declaration of Helsinki and its later amendments.

Informed consent Informed consent was obtained from all individual participants included in the study.

Gratitude to Deutsche Forschungsgemeinschaft (DFG) for financially promoting this research project.

Disclaimer The funding foundation was not involved in trial design, patient recruitment, data collection, analysis, interpretation or presentation, writing or editing of the reports, or the decision to submit for publication.

Open Access This article is licensed under a Creative Commons Attribution 4.0 International License, which permits use, sharing, adaptation, distribution and reproduction in any medium or format, as long as you give appropriate credit to the original author(s) and the source, provide a link to the Creative Commons licence, and indicate if changes were made. The images or other third party material in this article are included in the article's Creative Commons licence, unless indicated otherwise in a credit line to the material. If material is not included in the article's Creative Commons licence and your intended use is not permitted by statutory regulation or exceeds the permitted use, you will need to obtain permission directly from the copyright holder. To view a copy of this licence, visit <http://creativecommons.org/licenses/by/4.0/>.

References

1. The Global Cancer Observatory G. Breast Cancer. Source: Globocan 2018. World Heal Organ. 2018;876:2018–9.
2. Michaelson JS, Chen LL, Silverstein MJ, Mihm MCJ, Sober AJ, Tanabe KK, et al. How cancer at the primary site and in the lymph nodes contributes to the risk of cancer death. *Cancer*. 2009;115(21):5095–107.
3. Cardoso F, Senkus E, Costa A, Papadopoulos E, Aapro M, André F, et al. 4th ESO-ESMO international consensus guidelines for advanced breast cancer (ABC 4). *Ann Oncol*. 2018;29(8):1634–57.
4. Wockel A, Festl J, Stuber T, Brust K, Krockenberger M, Heuschmann PU, et al. Interdisciplinary screening, diagnosis, therapy and follow-up of breast cancer. Guideline of the DGGG and the DKG (S3-level, AWMF registry number 032/045OL, December 2017) - part 2 with recommendations for the therapy of primary, recurrent and advanced Br. Geburtshilfe Frauenheilkd. 2018 Nov;78(11):1056–88.
5. NCCN. NCCN clinical practice guidelines in oncology breast cancer, Version 2.2016. NCCN.org, 2016
6. Menezes GL, Knutel FM, Stehouwer BL, Pijnappel RM, van den Bosch MA. Magnetic resonance imaging in breast cancer: a literature review and future perspectives. *World J Clin Oncol*. 2014;5(2):61–70.
7. Senkus E, Kyriakides S, Ohno S, Penault-Llorca F, Poortmans P, Rutgers E, et al. Primary breast cancer: ESMO clinical practice guidelines for diagnosis, treatment and follow-up. *Ann Oncol Off J Eur Soc Med Oncol*. 2015;26(Suppl 5):v8–30.

8. Hausmann D, Kern C, Schröder M. Ganzkörper-MRT in der präoperativen Diagnostik des Mammakarzinoms – ein Vergleich mit den Staging- methoden in der S 3-Leitlinie whole-body MRI in preoperative diagnostics of breast cancer – a comparison of. Fortschritte Röntgenstrahlen. 2011;183:1130–7.
9. Sawicki LM, Grueneisen J, Buchbender C, Schaarschmidt BM, Gomez B, Ruhlmann V, et al. Comparative performance of 18F-FDG PET/MRI and 18F-FDG PET/CT in detection and characterization of pulmonary lesions in 121 oncologic patients. J Nucl Med. 2016;57(4):582–6.
10. Sawicki LM, Grueneisen J, Buchbender C, Schaarschmidt BM, Gomez B, Ruhlmann V, et al. Evaluation of the outcome of lung nodules missed on 18F-FDG PET/MRI compared with 18F-FDG PET/CT in patients with known malignancies. J Nucl Med. 2016 Jan;57(1):15–20.
11. Tatsumi M, Cohade C, Mountzikos KA, Fishman EK, Wahl RL. Initial experience with FDG-PET/CT in the evaluation of breast cancer. Eur J Nucl Med Mol Imaging. 2006;33(3):254–62.
12. Ulaner GA. PET/CT for patients with breast cancer: where is the clinical impact? Am J Roentgenol. 2019;213(2):254–65.
13. Ulaner GA, Castillo R, Goldman DA, Wills J, Riedl CC, Pinker-Domenig K, et al. 18F-FDG-PET/CT for systemic staging of newly diagnosed triple-negative breast cancer. Eur J Nucl Med Mol Imaging. 2016;43(11):1937–44.
14. Beiderwellen K, Grueneisen J, Ruhlmann V, Buderath P, Aktas B, Heusch P, et al. [(18)F]FDG PET/MRI vs. PET/CT for whole-body staging in patients with recurrent malignancies of the female pelvis: initial results. Eur J Nucl Med Mol Imaging. 2015 Jan;42(1):56–65.
15. Beiderwellen K, Gomez B, Buchbender C, Hartung V, Poeppl TD, Nensa F, et al. Depiction and characterization of liver lesions in whole body [(18)F]-FDG PET/MRI. Eur J Radiol. 2013;82(11):e669–75.
16. Heusch P, Buchbender C, Kohler J, Nensa F, Gaufer T, Gomez B, et al. Thoracic staging in lung cancer: prospective comparison of 18F-FDG PET/MR imaging and 18F-FDG PET/CT. J Nucl Med. 2014;55(3):373–8.
17. Kirchner J, Sawicki LM, Nensa F, Schaarschmidt BM, Reis H, Ingenwerth M, et al. Prospective comparison of 18 F-FDG PET/ MRI and 18 F-FDG PET/CT for thoracic staging of non-small cell lung cancer. Eur J Nucl Med Mol Imaging. 2019;46(2):437–45.
18. Botsikas D, Bagetakos I, Picarra M, Da Cunha Afonso Barisits AC, Boudabbous S, Montet X, et al. What is the diagnostic performance of 18-FDG-PET/MR compared to PET/CT for the N- and M- staging of breast cancer? Eur Radiol. 2019;29(4):1787–98.
19. Sawicki LM, Grueneisen J, Schaarschmidt BM, Buchbender C, Nagarajah J, Umutlu L, et al. Evaluation of 18F-FDG PET/MRI, 18F-FDG PET/CT, MRI, and CT in whole-body staging of recurrent breast cancer. Eur J Radiol. 2016;85(2):459–65.
20. Grueneisen J, Sawicki LM, Wetter A, Kirchner J, Kinner S, Aktas B, et al. Evaluation of PET and MR datasets in integrated 18F-FDG PET/MRI: a comparison of different MR sequences for whole-body restaging of breast cancer patients. Eur J Radiol. 2017 Apr;89:14–9.
21. Melsaether AN, Raad RA, Pujara AC, Ponzo FD, Pysarenko KM, Jhaveri K, et al. Comparison of whole-body ¹⁸F FDG PET/MR imaging and whole-body ¹⁸F FDG PET/CT in terms of lesion detection and radiation dose in patients with breast cancer. Radiology. 2016;281(1):193–202.
22. Grueneisen J, Nagarajah J, Buchbender C, Hoffmann O, Schaarschmidt BM, Poeppel T, et al. Positron emission tomography / magnetic resonance imaging for local tumor staging in patients with primary breast cancer. Investig Radiol. 2015;50(8):1–9.
23. Sawicki LM, Kirchner J, Umutlu L, Forsting M, Schaarschmidt BM, Ruhlmann V, et al. Comparison of 18F-FDG PET/MRI and MRI alone for whole-body staging and potential impact on therapeutic management of women with suspected recurrent pelvic cancer: a follow-up study. Eur J Nucl Med Mol Imaging. 2017;45(4):622–9.
24. Gradishar WJ, Anderson BO, Balassanian R, Blair SL, Burstein HJ, Cyr A, et al. Invasive breast cancer version 1.2016, NCCN Clinical Practice Guidelines in Oncology. J Natl Compr Cancer Netw. 2016;14(3):324–54.
25. Ulaner GA, Castillo R, Wills J, Gönen M, Goldman DA. 18F-FDG-PET/CT for systemic staging of patients with newly diagnosed ER-positive and HER2-positive breast cancer. Eur J Nucl Med Mol Imaging. 2017;44(9):1420–27.
26. Riedl CC, Slobod E, Jochelson M, Morrow M, Goldman DA, Gonen M, et al. Retrospective analysis of 18F-FDG PET/CT for staging asymptomatic breast cancer patients younger than 40 years. J Nucl Med. 2014;55(10):1578–83.
27. Spick C, Herrmann K, Czernin J. 18F-FDG PET/CT and PET/MRI perform equally well in cancer: evidence from studies on more than 2,300 patients. J Nucl Med. 2016.
28. Grueneisen J, Beiderwellen K, Heusch P, Gratz M, Schulze-Hagen A, Heubner M, et al. Simultaneous positron emission tomography/magnetic resonance imaging for whole-body staging in patients with recurrent gynecological malignancies of the pelvis: a comparison to whole-body magnetic resonance imaging alone. Invest Radiol. 2014.
29. Kanda T, Kitajima K, Suenaga Y, Konishi J, Sasaki R, Morimoto K, et al. Value of retrospective image fusion of 18F-FDG PET and MRI for preoperative staging of head and neck cancer: comparison with PET/CT and contrast-enhanced neck MRI. Eur J Radiol. 2013;82(11):2005–10.
30. Anderson WF, Reiner AS, Matsuno RK, Pfeiffer RM. Shifting breast cancer trends in the United States. J Clin Oncol. 2007;25(25):3923–9.
31. van Nijnatten TJA, Goorts B, Vöö S, de Boer M, Kooreman LFS, Heuts EM, et al. Added value of dedicated axillary hybrid 18F-FDG PET/MRI for improved axillary nodal staging in clinically node-positive breast cancer patients: a feasibility study. Eur J Nucl Med Mol Imaging. 2018;45(2):179–186.
32. Grueneisen J, Nagarajah J, Buchbender C, Hoffmann O, Schaarschmidt BM, Poeppel T, et al. Positron emission tomography/magnetic resonance imaging for local tumor staging in patients with primary breast cancer: a comparison with positron emission tomography/computed tomography and magnetic resonance imaging. Invest Radiol. 2015;50(8):505–13.
33. Tabouret-Viaud C, Botsikas D, Delattre BMA, Mainta I, Amzalag G, Rager O, et al. PET/MR in breast cancer. Semin Nucl Med. 2015;45(4):304–21.
34. Kirchner J, Grueneisen J, Martin O, Oehmigen M, Quick HH, Bittner AK, et al. Local and whole-body staging in patients with primary breast cancer: a comparison of one-step to two-step staging utilizing 18F-FDG-PET/MRI. Eur J Nucl Med Mol Imaging. 2018;45(13):2328–37.
35. Ergul N, Kadioglu H, Yildiz S, Yucel SB, Gucin Z, Erdogan EB, et al. Assessment of multifocality and axillary nodal involvement in early-stage breast cancer patients using 18F-FDG PET/CT compared to contrast-enhanced and diffusion-weighted magnetic resonance imaging and sentinel node biopsy. Acta Radiol. 2015;56(8):917–23.
36. Lee B, Lim AK, Krell J, Satchithananda K, Coombes RC, Lewis JS, et al. The efficacy of axillary ultrasound in the detection of nodal metastasis in breast cancer. Am J Roentgenol. 2013;200(3):w314–20.
37. Valente SA, Levine GM, Silverstein MJ, Rayhanabad JA, Weng-Grumley JG, Ji L, et al. Accuracy of predicting axillary lymph node positivity by physical examination, mammography, ultrasonography, and magnetic resonance imaging. Ann Surg Oncol. 2012;19(6):1825–30.
38. Catalano OA, Daye D, Signore A, Iannace C, Vangel M, Luongo A, et al. Staging performance of whole-body DWI, PET/CT and PET/

- MRI in invasive ductal carcinoma of the breast. *Int J Oncol.* 2017;51(1):281–8.
- 39. Plecha DM, Faulhaber P. European Journal of Radiology: PET/MRI of the breast; 2017.
 - 40. Catalano OA, Nicolai E, Rosen BR, Luongo A, Catalano M, Iannace C, et al. Comparison of CE-FDG-PET/CT with CE-FDG-PET/MR in the evaluation of osseous metastases in breast cancer patients. *Br J Cancer.* 2015;112(9):1452–60.
 - 41. Pace L, Nicolai E, Luongo A, Aiello M, Catalano OA, Soricelli A, et al. Comparison of whole-body PET/CT and PET/MRI in breast cancer patients: lesion detection and quantitation of 18F-deoxyglucose uptake in lesions and in normal organ tissues. *Eur J Radiol.* 2014;83(2):289–96.
 - 42. Gückel B, Gatidis S, Enck P, Schäfer J, Bisdas S, Pfannenberg C, et al. Patient comfort during positron emission tomography/magnetic resonance and positron emission tomography/computed tomography examinations: subjective assessments with visual analog scales. *Investig Radiol.* 2015;50(10):726–32.

Publisher's note Springer Nature remains neutral with regard to jurisdictional claims in published maps and institutional affiliations.

RESEARCH ARTICLE

Prospective comparison of CT and ^{18}F -FDG PET/MRI in N and M staging of primary breast cancer patients: Initial results

Nils Martin Bruckmann¹, Julian Kirchner^{1*}, Janna Morawitz¹, Lale Umutlu², Ken Herrmann³, Ann-Kathrin Bittner⁴, Oliver Hoffmann⁴, Svjetlana Mohrmann⁵, Marc Ingenwerth⁶, Benedikt M. Schaarschmidt², Yan Li², Andreas Stang⁷, Gerald Antoch¹, Lino M. Sawicki¹, Christian Buchbender¹

1 Department of Diagnostic and Interventional Radiology, Medical Faculty, University Dusseldorf, Dusseldorf, Germany, **2** Department of Diagnostic and Interventional Radiology and Neuroradiology, University Hospital Essen, University of Duisburg-Essen, Essen, Germany, **3** Department of Nuclear Medicine, University Hospital Essen, University of Duisburg-Essen, Essen, Germany, **4** Department Gynecology and Obstetrics, University Hospital Essen, University of Duisburg-Essen, Essen, Germany, **5** Department of Gynecology, Medical Faculty, University Dusseldorf, Dusseldorf, Germany, **6** Institute of Pathology, West German Cancer Center, University Hospital Essen, University Duisburg-Essen and the German Cancer Consortium (DKTK), Essen, Germany, **7** Institute of Medical Informatics, Biometry and Epidemiology, University Hospital of Essen, Essen, Germany

* Julian.Kirchner@med.uni-duesseldorf.de



OPEN ACCESS

Citation: Bruckmann NM, Kirchner J, Morawitz J, Umutlu L, Herrmann K, Bittner A-K, et al. (2021) Prospective comparison of CT and ^{18}F -FDG PET/MRI in N and M staging of primary breast cancer patients: Initial results. PLoS ONE 16(12): e0260804. <https://doi.org/10.1371/journal.pone.0260804>

Editor: Pascal A. T. Baltzer, Medical University of Vienna, AUSTRIA

Received: July 26, 2021

Accepted: November 18, 2021

Published: December 2, 2021

Copyright: © 2021 Bruckmann et al. This is an open access article distributed under the terms of the [Creative Commons Attribution License](#), which permits unrestricted use, distribution, and reproduction in any medium, provided the original author and source are credited.

Data Availability Statement: Data cannot be shared publicly because as this would allow identification of the patients. This is not possible for data protection reasons. Data are available from the Ethics Committee of the University of Essen and Düsseldorf, Germany (ethikkommission@uk-essen.de; ethikkommission@med.uni-duesseldorf.de) for researchers who meet the criteria for access to confidential data.

Abstract

Objectives

To compare the diagnostic accuracy of contrast-enhanced thoraco-abdominal computed tomography and whole-body ^{18}F -FDG PET/MRI in N and M staging in newly diagnosed, histopathological proven breast cancer.

Material and methods

A total of 80 consecutive women with newly diagnosed and histopathologically confirmed breast cancer were enrolled in this prospective study. Following inclusion criteria had to be fulfilled: (1) newly diagnosed, treatment-naïve T2-tumor or higher T-stage or (2) newly diagnosed, treatment-naïve triple-negative tumor of every size or (3) newly diagnosed, treatment-naïve tumor with molecular high risk (T1c, Ki67 >14%, HER2neu over-expression, G3). All patients underwent a thoraco-abdominal ceCT and a whole-body ^{18}F -FDG PET/MRI. All datasets were evaluated by two experienced radiologists in hybrid imaging regarding suspect lesion count, localization, categorization and diagnostic confidence. Images were interpreted in random order with a reading gap of at least 4 weeks to avoid recognition bias. Histopathological results as well as follow-up imaging served as reference standard. Differences in staging accuracy were assessed using Mc Nemars chi² test.

Results

CT rated the N stage correctly in 64 of 80 (80%, 95% CI:70.0–87.3) patients with a sensitivity of 61.5% (CI:45.9–75.1), a specificity of 97.6% (CI:87.4–99.6), a PPV of 96% (CI:80.5–

Funding: The study is funded by Deutsche Forschungsgemeinschaft (DFG), the German Research Foundation (BU3075/2-1). The funding foundation was not involved in trial design, patient recruitment, data collection, analysis, interpretation or presentation, writing or editing of the reports, or the decision to submit for publication. The corresponding author had full access to all data in the study and had all responsibility for the decision to submit for publication. Christian Buchbender was the main recipient.

Competing interests: The authors have declared that no competing interests exist.

Abbreviations: AC, Attenuation correction; ALND, Axillary lymph node dissection; CI, Confidence interval; CT, Computed tomography; DWI, Diffusion-weighted imaging; EPI, Echo-planar imaging; ESMO, European Society For Medical Oncology; FDG, Fluorodeoxyglucose; FOV, Field of view; FWHM, Full-width at half maximum; HASTE, Half Fourier acquisition single shot turbo spin echo; HER2, Human epidermal growth factor receptor 2; MRI, Magnetic resonance imaging; NCCN, National Comprehensive Cancer Network; OSEM, Ordered-subset expectation maximization; PET, Positron emission tomography; RF, Radiofrequency; VIBE, Volume interpolated breath-hold examination; WHO, World Health Organization.

99.3), and a NPV of 72.7% (CI:59.8–82.7). Compared to this, ^{18}F -FDG PET/MRI determined the N stage correctly in 71 of 80 (88.75%, CI:80.0–94.0) patients with a sensitivity of 82.1% (CI:67.3–91.0), a specificity of 95.1% (CI:83.9–98.7), a PPV of 94.1% (CI:80.9–98.4) and a NPV of 84.8% (CI:71.8–92.4). Differences in sensitivities were statistically significant (difference 20.6%, CI:-0.02–40.9; $p = 0.008$). Distant metastases were present in 7/80 patients (8.75%). ^{18}F -FDG PET/MRI detected all of the histopathological proven metastases without any false-positive findings, while 3 patients with bone metastases were missed in CT (sensitivity 57.1%, specificity 95.9%). Additionally, CT presented false-positive findings in 3 patients.

Conclusion

^{18}F -FDG PET/MRI has a high diagnostic potential and outperforms CT in assessing the N and M stage in patients with primary breast cancer.

Introduction

Accounting for approximately 12% of new cancer diagnoses every year, breast cancer is considered to be the most frequent cancer in women worldwide and the leading cause of cancer-related death [1]. Treatment concepts and consecutively the survival rate heavily depend on the initial cancer staging. Therefore, accurate imaging-based staging of patients with newly diagnosed breast cancer is playing a pivotal role to determine the optimal treatment management and to minimize potential harmful surgical interventions and extensive systemic therapy [2].

Key points for the initial staging are the detection of tumor manifestations in the contralateral breast, evaluation of locoregional lymph nodes and the detection of distant metastases [3]. Depending on the primary tumor size and the locoregional lymph node status, surgery can extent from a breast-conserving therapy to a complete mastectomy and ipsilateral axillary dissection. In case of validated distant metastases the treatment concept switches to an extensive systemic and most likely palliative therapy [2].

According to the 2018 European Society For Medical Oncology (ESMO) and the 2016 National Comprehensive Cancer Network (NCCN) guidelines a staging, including contrast-enhanced thoraco-abdominal CT and bone scintigraphy [2, 4], is considered in patients with advanced breast cancer (UICC III/IV) and patients with UICC stage II combined with additional risk factors like clinically positive axillary lymph nodes, large tumor size, aggressive biology (HER2neu over-expression, triple negative tumor) or clinical signs/laboratory values suggesting the presence of metastases. Staging in early breast cancer is directed at locoregional disease as patients do not benefit from a whole-body staging, since asymptomatic distant metastases are very rare in early tumor stages [2, 4–6].

Recent studies revealed a superiority of hybrid imaging modalities in detection of distant metastases and in correct malignant lesion rating for breast cancer patients [7–9]. Thus, dual imaging methods have been implemented in international guidelines recommending a ^{18}F -FDG PET/CT when conventional methods are inconclusive, in high-risk patients or in patients with newly diagnosed stage III breast cancer [4, 6]. Nevertheless, recent studies demonstrated the superiority of ^{18}F -FDG PET/MRI compared to ^{18}F -FDG PET/CT in the detection of breast cancer metastases [10]. Especially in combination with a dedicated breast (PET/)

MRI may serve as a valuable one-stop-shop alternative for primary staging of breast cancer patients [11–17].

Thus, the purpose of our study was to evaluate the diagnostic potential of CT resembling the current clinical standard compared to ^{18}F -FDG PET/MRI for the initial N and M staging of primary breast cancer patients.

Material and methods

Patients

This study was approved by the institutional review board of the University Duisburg-Essen (study number 17-7396-BO) and Düsseldorf (study number 6040R) and performed in conformance with the Declaration of Helsinki [18]. All enrolled patients underwent an ^{18}F -FDG PET/MRI and contrast-enhanced thoraco-abdominal computed tomography after written informed consent form was obtained. A total of 80 women (mean age: 52.9 ± 11.9 , range: 29–79 years) with newly diagnosed breast cancer were enrolled in this prospective study between August 2017 and October 2019. Following inclusion criteria had to be fulfilled: (1) newly diagnosed, treatment-naïve T2-tumor or higher T-stage or (2) newly diagnosed, treatment-naïve triple-negative tumor of every size or (3) newly diagnosed, treatment-naïve tumor with molecular high risk (T1c, Ki67 >14%, HER2neu over-expression, G3). Exclusion criteria were former malignancies in the last 5 years, contraindications to MRI or MRI contrast agents and pregnancy or breast-feeding.

CT

Thoraco-abdominal multi-slice contrast-enhanced CT were performed in two different CT scanners (Definition Edge and Definition Flash, Siemens Healthineers). The examination was performed in supine position with the arms above the head. Automated tube current modulation and automated tube voltage selection (CareDose 4D and CareKV, Siemens Healthineers) were applied in all examinations. All CT were acquired after intravenous administration of body-weight adapted non-ionic contrast agent with a time delay commonly used in portal venous phase imaging.

PET/MRI

All ^{18}F -FDG PET/MRI examinations were performed on an integrated 3.0-Tesla PET/MRI scanner (Magnetom Biograph mMR, Siemens Healthcare GmbH, Germany) with a mean delay of 67 ± 16 min after ^{18}F -FDG injection. Blood samples of all patients were obtained prior to injection of a body-weight adapted dosage of ^{18}F -FDG (4 MBq/kg, mean activity 255 ± 45 MBq) to ensure blood glucose levels below 150 mg/dl.

The field of view (FOV) contained the body volume from head to the mid-thigh using a dedicated 16-channel head-and-neck radiofrequency (RF) coil, a 24-channel spine-array RF coil and up to five 6-channel flex body coils. The examination was performed in supine position with head first and arms next to the body. PET acquisition time was 3 minutes per bed position in four or five positions (axial FOV: 25.8 cm, matrix size 344 x 344) and the PET images were performed concurrently with the MRI. The iterative algorithm OSEM (ordered-subset expectation maximization) was utilized for reconstruction of PET images with 3 iterations and 21 subsets and a Gaussian filter with 4-mm full width at half maximum.

For MR-based attenuation correction a coronal 3D-Dixon-VIBE sequence (repetition time (TR) 3.6 ms, echo time 1 (TE1) 1.23 ms, TE2 2.46 ms, slice thickness 3.12 mm, FOV 500×328 mm, matrix size 192×121) was acquired to create a four-compartment model attenuation map

(μ -map), calculated from fat-only and water-only data sets. Subsequently, the following MRI sequences were performed:

1. A transverse T2-weighted (T2w) fat-suppressed half Fourier acquisition single shot turbo spin echo (HASTE) sequence in respiratory medium position and a slice thickness of 7 mm.
2. A transverse diffusion-weighted echo-planar imaging (EPI DWI) sequence (b values 0, 500, 1000) in respiratory medium position with a slice thickness of 5 mm.
3. A transversal T1-weighted (T1w) fat saturated post-contrast Volume-Interpolated Breath-hold Examination (VIBE) sequence after intravenous injection of a gadolinium-based contrast agent (0.2 mmol/kg body weight, Dotarem, Guerbet GmbH, Germany) with a slice thickness of 3 mm.

Image analysis

All images were interpreted by two experienced radiologists in hybrid imaging in consensus and in random order with a reading gap of at least 4 weeks to avoid recognition bias. CT and ^{18}F -FDG PET/MRI images were read in separate sessions. A picture archiving and communication system (Centricity; General Electric Medical Systems, Milwaukee, WI, USA) and a dedicated OsiriX workstation (Pixmeo, SARL, Bernex, Switzerland) were used for image analysis. Lesion count, lesion localization, lesion characterization (benign or malignant) and size as well as the diagnostic confidence of every lesion were assessed (5-point ordinal scale, 1 = very low confidence, 2 = low confidence, 3 = indeterminate confidence, 4 = high confidence, 5 = very high confidence). The malignancy criteria for evaluating the lymph nodes were established based on previous studies, comprising both morphological and metabolic criteria. Following criteria were applied to determine suspicious lymph nodes: a short-axis diameter >10 mm, increased contrast enhancement, spherical configuration, irregular shape, diffusion restriction and focally increased FDG-uptake. At least two of these criteria had to be fulfilled to rate a lymph node as malignant [19, 20]. Criteria for distant metastases were a local invasive growth, central necrosis, contrast enhancement and a typically malignant MR signal like diffusion restriction. In addition, on ^{18}F -FDG PET/MRI a visually detectable focal FDG-uptake above background signal was considered as a sign of malignancy. The maximum standardized uptake value (SUVmax) and the maximum diameter were measured in all suspected lesions.

Reference standard

Due to clinical and ethical standards a histological confirmation of all detected malignant lesions was not applicable and a surrogate reference standard was applied taking into account all follow-up imaging. 148 out of 236 lesions were confirmed histopathologically. 55 lesions were followed-up by CT and 25 lesions by MRI (4 ± 3 months). The remaining 8 lesions were followed-up with sonography and clinical examination, consisting of five benign axillary lymph nodes, two liver cysts and one liver haemangioma.

Statistical analysis

SPSS Statistics 22 was used for data analysis (IBM Inc., Armonk, NY, USA). All data are presented as mean \pm standard deviation. Data were analyzed on a per-patient and a per-lesions basis, calculating sensitivity, specificity, positive and negative predictive values. To investigate statistically significant differences between CT and ^{18}F -FDG PET/MRI the McNemar chi² test was performed. A Wilcoxon test was used to assess differences between CT and ^{18}F -FDG PET/

MRI regarding the diagnostic confidence. A p-value of less than 0.05 designated a statistical significance.

Results

Patient-based analysis

Lymph nodes. CT and ¹⁸F-FDG PET/MRI were concordant for N and M stage in 56 of 80 patients (70%). CT determined the exact N stage correctly in 59/80 (73.75%, 95% CI:63.2–82.1) of the patients (Table 1). The distinction between nodal-positive and nodal-negative patients was rated correctly in 64 of 80 (80%, CI:70.0–87.3) patients by CT. This results in a sensitivity of 61.5% (CI:45.9–75.1), a specificity of 97.6% (CI: 87.4–99.6), a PPV of 96% (CI: 80.5–99.3) and a NPV of 72.7% (CI: 59.8–82.7) (Table 2). In comparison to this the exact N stage was determined correctly by ¹⁸F-FDG PET/MRI in 70/80 (87.5%, CI: 78.5–93.1) of the patients. PET/MRI yielded a correct classification in nodal-positive and nodal-negative patients in 71/80 (88.75%, CI: 80.0–94.0) of the cases. This results in a sensitivity of 82.1% (CI: 67.3–91.0), a specificity of 95.1% (CI: 83.9–98.7), a PPV of 94.1% (CI: 80.9–98.4) and a NPV of 84.8% (CI: 71.8–92.4). In total, 39 of the patients (48.75%) had a nodal-positive status. 15/39 (38.5%, CI: 24.9–54.1) nodal-positive patients were missed by CT, while ¹⁸F-FDG PET/MRI missed 7/39 (17.5%, CI: 9.0–32.7) patients. In detail, all missed lymph nodes were stage N1 in

Table 1. N and M staging on a patient-based analysis.

	CT	PET/MRI	Standard of reference
N stage			
0	40	39	41
1	15	24	32
2	0	1	1
3	4	6	6
Total correct N ratings	59 (73.75%)	70 (87.5%)	80 (100%)
M Stage			
0	70	73	73
1	4	7	7
Total correct M ratings	74 (92.5%)	80 (100%)	80 (100%)

Distribution of N and M staging for CT alone and ¹⁸F-FDG PET/MRI and comparison to the reference standard.

<https://doi.org/10.1371/journal.pone.0260804.t001>

Table 2. Diagnostic performance of CT and PET/MRI on a patient-based analysis.

	Locoregional metastases		Distant metastases	
	CT	PET/MRI	CT	PET/MRI
True positive (n)	24	32	3	7
True negative (n)	40	39	71	73
False positive (n)	1	2	3	0
False negative (n)	15	7	3	0
Sensitivity (%)	61.5	82.1	57.1	100
Specificity (%)	97.6	95.1	95.9	100
Positive predictive value (%)	96.0	94.1	57.1	100
Negative predictive value (%)	72.7	84.8	95.9	100
Accuracy (%)	80	88.75	57.1	100

<https://doi.org/10.1371/journal.pone.0260804.t002>

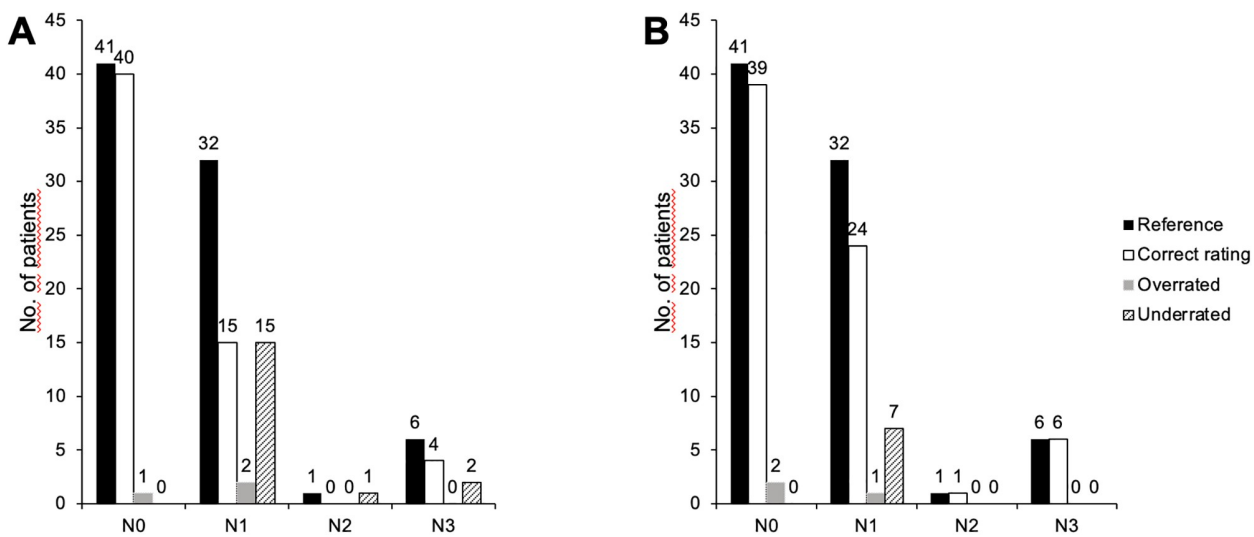


Fig 1. Determination of the lymph node stage in CT (A) and ^{18}F -FDG PET/MRI (B).

<https://doi.org/10.1371/journal.pone.0260804.g001>

both modalities. However, CT underrated two patients with N3 stage according to the reference standard as N1, while PET/MRI was able to detect all of the six patients with N3 stage. Practically, this led to a change of therapy in two patients with expansion of the radiation field after surgery (Fig 1). The McNemars chi² test yielded a significant difference in favor of ^{18}F -FDG PET/MRI over CT for determining nodal-positive patients (test statistic = 13.7, p = 0.008) with a corresponding difference in sensitivities of 20.6% (CI: -0.02-40.9). The corresponding difference in specificities did not reach statistical significance (difference 2.4%, CI: -0.06-12.6; test statistic = 0.05, p = 1.0).

Distant metastases. According to the reference standard distant metastases were detected in 7/80 (8.75%) patients. By CT the M stage was defined correctly in 74 of 80 patients (92.5%, CI: 84.6–96.5). In 3 patients, all with bone metastases, CT showed false-negative results (missing 42.9% of the patients with distant metastases). In 2 of these patients the osseous lesions were not visible and in one patient the visible lesions were misinterpreted as simple sclerosis (Fig 2). Furthermore, there were false-positive ratings in 3 patients (4.1%, CI: 1.4–11.4) due to misinterpreted bone degeneration (checked by histopathology), non-specific indurations (checked by CT after 3 month) and several liver hemangiomas (checked by liver-specific MRI). This results in a sensitivity of 57.1% (CI: 25.0–84.2), a specificity of 95.9% (CI: 88.6–98.6), a PPV 57.1% (CI: 25.0–84.2) and a NPV of 95.9% (CI: 88.6–98.6) for the detection of distant metastasis. In comparison to that, ^{18}F -FDG PET/MRI was able to detect all malignant lesions without any false-positive findings.

Lesion-based analysis

A total of 236 lesions were included in the final evaluation, comprising 126 (53.4%) malignant and 110 (46.6%) benign lesions. Table 3 shows the localizations of all malignant lesions, consisting of 90 lymph node metastases and 36 distant metastases. CT detected 192 of 236 lesions (94.5% vs. 81.4%, difference 13.1%, CI: 7.3–18.8), while ^{18}F -FDG PET/MRI detected 223 of the 236 lesions.

CT failed to detect 36 malignant lesions, comprising 19 bone metastases, 2 liver metastases and 1 hilar lymph node metastases as well as 14 locoregional lymph node metastases in axillary

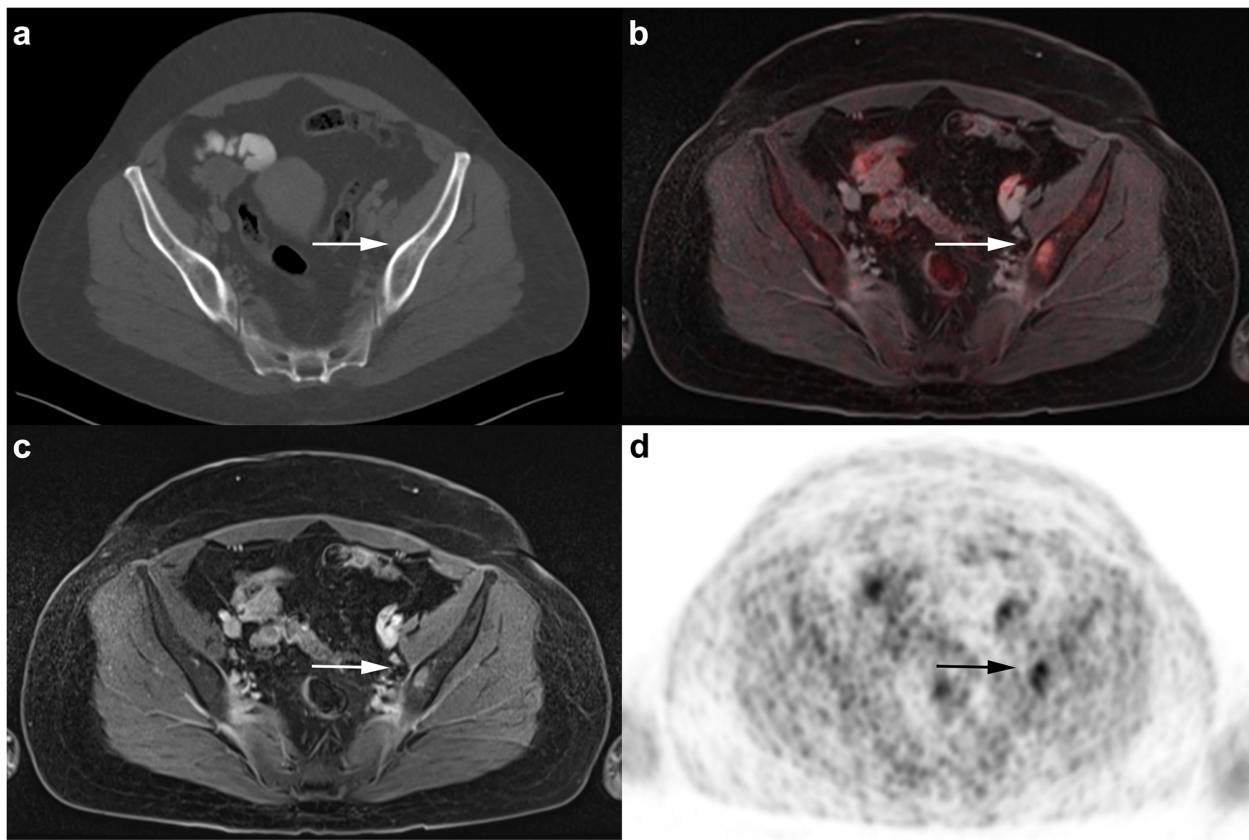


Fig 2. A 45-year old woman with diagnosis of primary breast cancer. No distant metastases were detected in the CT scan (a). The subsequently performed ¹⁸F-FDG PET/MRI shows a bone metastasis in the left iliac bone with contrast enhancement on T1w fs VIBE (c) and pathological FDG uptake on PET (d) and fused ¹⁸F-FDG PET/MRI (b).

<https://doi.org/10.1371/journal.pone.0260804.g002>

(5), mammarian (4), subpectoral (2) and clavicular (3) position (Figs 3 and 4). Furthermore, CT had 27 false-negative ratings, including 23 lymph nodes, which were morphologically unsuspicious and 4 bone metastases, which were evaluated as unspecific sclerosis (Fig 2). There were 12 false-positive findings in CT: 3 bone subsidences, 3 lung indurations, 3 liver

Table 3. Location of all 126 malignant lesions according to the standard of reference.

	Location	Number (n)	Percentage (%)
Distant	Bone metastases	27	21.4
	Lung metastases	4	3.2
	Liver metastases	4	3.2
	Hilar lymph node	1	0.8
Locoregional	Lymph node metastases	90	71.4
	Axillary	77	
	Clavicular	7	
	Subpectoral	2	
	Internal mammary artery	4	
Total		126	100

<https://doi.org/10.1371/journal.pone.0260804.t003>

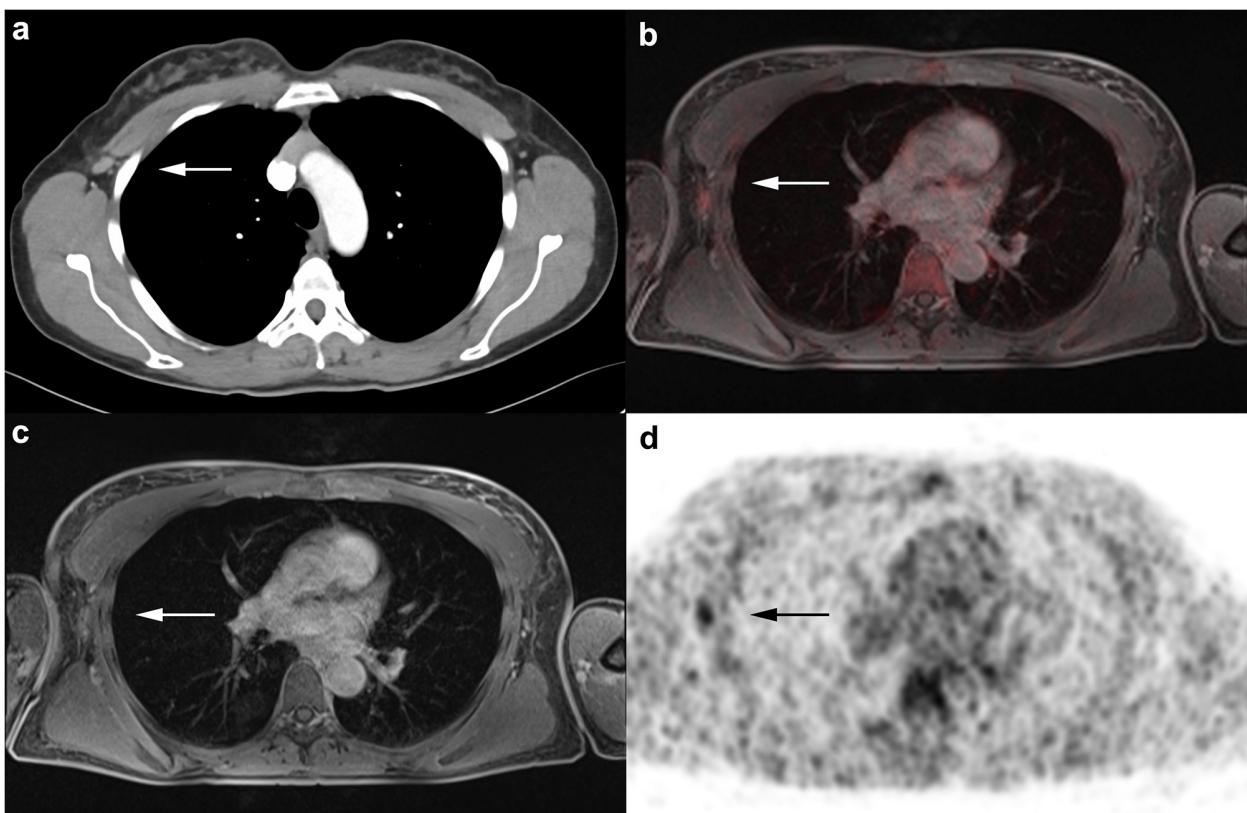


Fig 3. A 48-year old woman with diagnosis of primary breast cancer. Morphologically unsuspicious right axillary lymph node rated as not malignant in the CT scan (a). The ^{18}F -FDG PET/MRI shows a slight FDG uptake (b-d), indicating malignancy. Histopathology proved a tumor infestation.

<https://doi.org/10.1371/journal.pone.0260804.g003>

haemangiomas as well as a swelling in the contralateral breast and a single axillary and mammary lymph node were rated as malignant. All these lesions turned out to be benign in histopathology and follow-up examination. All in all CT correctly rated 63/126 of the malignant lesions, resulting in a sensitivity of 50% (CI: 41.4–58.6), a specificity of 88.2% (CI: 80.6–93.1), a PPV of 84% (CI: 74.1–90.6) and a NPV of 76.9% (CI: 68.5–83.6) (Table 4). In contrast to that ^{18}F -FDG PET/MRI did not miss any of the 126 malignant lesions. ^{18}F -FDG PET/MRI correctly rated 115/126 of the malignant lesions, resulting in a sensitivity of 91.3% (CI: 85.0–95.1), a specificity of 97.9% (CI: 92.8–99.4), a PPV of 98.3% (CI: 94.0–99.5), and a NPV of 89.6% (CI: 82.4–94.1) (Table 4). False-negative ratings were due to axillary lymph nodes with small lesion size and weak FDG-uptake. There were two false-positive findings in ^{18}F -FDG PET/MRI, because two axillary lymph nodes demonstrated an increased suspicious FDG-uptake. There was a significant difference for correct rating of lesions as malignant between CT and ^{18}F -FDG PET/MRI (63 vs. 115 out of 126 lesions, 50% vs. 91.3%, difference 41.3%, CI: 30.7–50.6; test statistic = 12.1, $p < 0.0001$). The exact division between locoregional lymph node metastases and distant metastases can be seen in Table 4.

Diagnostic confidence

The diagnostic confidence for distinguishing between benign and malignant lesions was significantly higher in ^{18}F -FDG PET/MRI than in CT (3.9 ± 0.7 vs. 3.2 ± 0.7 , $p < 0.0001$). Comparing the diagnostic confidence regarding malignant lesions only, containing distant and

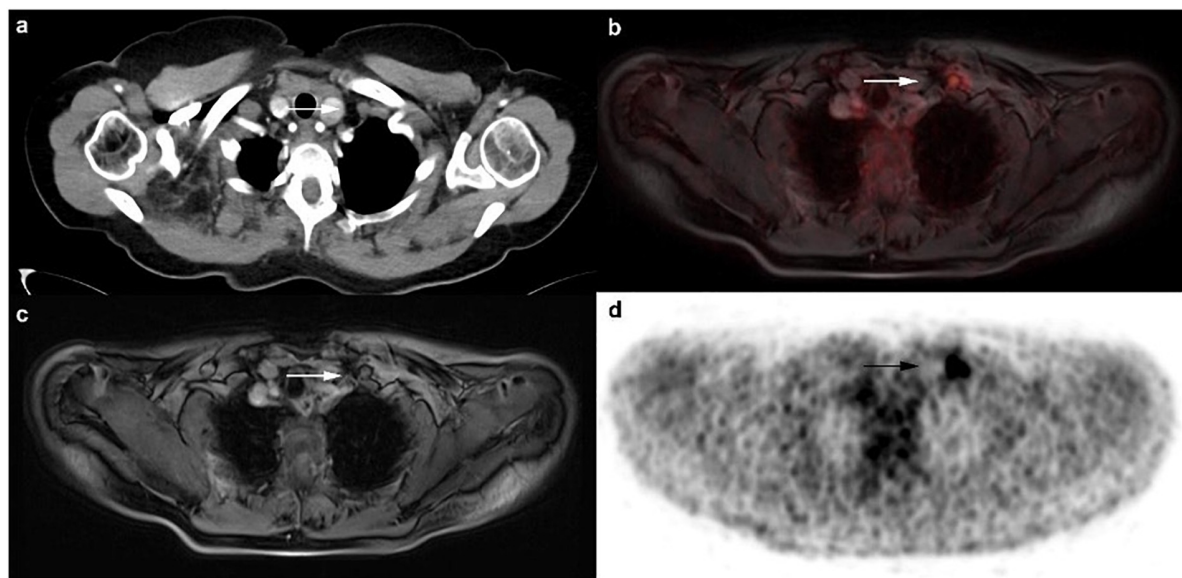


Fig 4. A 72-year old woman with diagnosis of primary breast cancer and lymph node metastases. The reading radiologist did not detect the morphologically inconspicuous left clavicular lymph node in CT scan (a). In ¹⁸F-FDG PET/MRI a clear FDG uptake is visible (b-d). Histopathology confirmed malignancy.

<https://doi.org/10.1371/journal.pone.0260804.g004>

locoregional metastatic lesions, differences between the two modalities were even higher (4.1 ± 0.7 vs. 3.3 ± 0.7 , $p < 0.0001$).

Discussion

The present study shows the superiority of ¹⁸F-FDG PET/MRI for the primary N and M staging of breast cancer patients compared to ce-CT. Due to an increasing attention to reach accurate staging prior to therapy, the diagnostic algorithm of breast cancer has changed in recent times. The basic staging with chest x-ray and abdominal sonography has been replaced by thoraco-abdominal CT and bone scintigraphy [2, 4]. Therefore, the current international guidelines recommend a generalized thoraco-abdominal staging with CT and scintigraphy in

Table 4. Diagnostic performance of CT and PET/MRI on a lesion-based analysis.

	All lesions		Locoregional metastases		Distant metastases	
	126/236		90/147		36/89	
	CT	PET/MRI	CT	PET/MRI	CT	PET/MRI
True positive (n)	63	115	53	79	10	36
True negative (n)	90	95	49	54	41	41
False positive (n)	12	2	2	2	10	0
False negative (n)	27	11	23	11	4	0
Missed benign (n)	8	13	6	1	2	12
Missed malignant (n)	36	0	14	0	22	0
Sensitivity (%)	50	91.3	69.7	87.8	27.8	100
Specificity (%)	88.2	97.9	96.1	96.4	80.4	100
PPV (%)	84	98.3	96.4	97.5	50	100
NPV (%)	76.9	89.6	68.1	83.1	91.1	100
Accuracy (%)	64.8	89	69.4	90.5	57.3	86.5

<https://doi.org/10.1371/journal.pone.0260804.t004>

patients with advanced breast cancer (UICC III/IV) and patients with additional risk factors, since the likelihood of distant metastases is increased with positive lymph node findings and an aggressive tumor biology [5, 21, 22]. This amendment to international guidelines [5, 21] is not based on studies designed specifically for this purpose, but was determined with an expert consensus based on the sensitivities and specificities for lesion detection of each modality. The aim is to improve the detection of distant metastases, since the presence of metastases leads to a completely different therapy regime.

CT is the simplest and most cost-effective alternative for a thoraco-abdominal staging, but in accordance with the current state of science, the sentinel lymph node biopsy and histological work-up is still the clinical standard of choice for determining a lymph node involvement and prove distant metastases. Patients confirmed as nodal-positive are surgically treated undergoing an axillary lymph node dissection (ALND) in a further intervention. A preselection of which patients receive a sentinel lymph node biopsy is currently carried out by clinical examination, sonography, conventional mammography and breast MRI. However, these methods are far from serving as a real alternative to biopsy. So the sentinel lymph node biopsy is very generously performed in patients with the slightest suspicion of a lymph node involvement [23–26].

Hybrid imaging modalities have proven to be advantageous in cancer staging in comparison to conventional imaging techniques [27–29], but these also cannot compete with the biopsy according to the current state of research [26]. However, a better preselection of nodal-positive patients may result in fewer surgeries, avoiding prior lymph node biopsy before ALND. Nevertheless, a general recommendation for the use of hybrid imaging modalities is not given, based on the 2015 and the 2018 European Society For Medical Oncology (ESMO) and the 2018 National Comprehensive Cancer Network (NCCN) guidelines. However, a systemic staging with ¹⁸F-FDG PET/CT is considered for patients with inconclusive results in conventional imaging and in high risk patients [4–6].

With regard to the correct determination of the N stage, there were huge differences between CT and ¹⁸F-FDG PET/MRI visible in this study in favor of the ¹⁸F-FDG PET/MRI. ¹⁸F-FDG PET/MRI showed a significantly higher sensitivity on a patient-based and a lesion-based analysis and thus demonstrated a higher accuracy of detecting the N stage. In addition, especially the undervaluation of lymph node stage in CT had a direct impact on treatment in two patients, since radiation field had to be expanded after ¹⁸F-FDG PET/MRI was done.

Although, CT represents the standard in primary breast cancer staging according to the guidelines, this is the first study comparing the diagnostic potential with ¹⁸F-FDG PET/MRI. However, many studies have already compared ¹⁸F-FDG PET/CT with conventional imaging techniques. In terms of locoregional lymph node involvement, many authors describe a clear added benefit of ¹⁸F-FDG PET/CT. Bitencourt et al. emphasize a significant superiority of ¹⁸F-FDG PET/CT in comparison to conventional imaging especially in providing information on extra-axillary and not enlarged lymph nodes [27, 30–32]. These statements are in line with the results of our study, in which the CT failed to detect 4 not enlarged axillary lymph node metastases and 12 lymph node metastases in mammalian, subpectoral and subclavian position (Fig 4). Mahner et al. [33] also described a clear advantage of hybrid imaging, indicating the sensitivity of CT for the determination of axillary, supraclavicular and mediastinal lymph nodes with 53%, 40% and 31%, compared to PET with 86%, 84% and 96%. In accordance with our results, these studies show that the number of biopsies can be reduced in the future by considerably improving the sensitivity in the detection of lymph node metastases, even if biopsy still remains the gold standard. The more accurate assessment of N stage can ultimately also directly influence therapy, for example in the adaption of the radiation field.

In the assessment of the M stage, our study determined a clear superiority of ¹⁸F-FDG PET/MRI in comparison to CT. While the CT missed metastasis in 3 patients and also provided false-positive findings in 3 other patients, the ¹⁸F-FDG PET/MRI was able to detect all of the seven patients with distant metastases without any false-positive findings. These results are consistent with the results from earlier studies. For example, Hildebrandt et al. compared the diagnostic value of ¹⁸F-FDG PET/CT, contrast-enhanced CT and bone scintigraphy in 100 women with suspected recurrence of breast cancer. The study suggests that PET/CT has a greater accuracy than conventional imaging techniques in this patient group [29, 34]. These results are also supported by a study of Gajjala et al., rating PET/CT as more accurate than conventional imaging techniques for staging locally advanced breast cancer in a cohort of 61 patients. A direct comparison of ¹⁸F-FDG PET/MRI and CT in recurrent breast cancer is also provided by the study of Sawicki et al. [7]. In this study with 21 patients with suspected breast cancer recurrence ¹⁸F-FDG PET/MRI offered the highest diagnostic performance and outperformed both CT and PET/CT. Especially the CT alone scored poorly in this study, missing about 30% of malignant lesions (PET/CT: 3.4%; PET/MRI: 0%). On the other hand, there are also studies that have not explored any advantage of hybrid imaging in primary breast cancer patients. In the study of Monzawa et al. with 50 patients suffering from invasive breast cancer no superiority in diagnostic performance of ¹⁸F-FDG PET/CT in comparison to ultrasonography and contrast-enhanced CT could be determined [35]. Furthermore, it has been confirmed by a whole series of studies that ¹⁸F-FDG PET/MRI is superior to ¹⁸F-FDG PET/CT in the detection of breast cancer metastases [20, 36, 37]. Only in the overall detection and characterization of lung lesions ¹⁸F-FDG PET/MRI gives worse results so far, caused by the limited ability of MRI to detect small lung lesions [38, 39]. However, a superiority of CT over ¹⁸F-FDG PET/MRI in terms of detection of pulmonary lesions could not be determined in our study. Summarizing, with regard to distant metastases, the performance of PET/MRI can thus have a fundamental influence on the therapy regime for some patients and has to be considered as a helpful diagnostic tool, due to the high sensitivity in distant lesion detection. Taking into account the results of former studies, however, a histological confirmation is still necessary to ensure tumor infestation.

In addition to the direct detection of suspicious lesions, the diagnostic or interpretation confidence of the modalities, with which a lesion can be classified as benign or malignant, is of great interest. This study confirms, that ¹⁸F-FDG PET/MRI has a great advantage in comparison to CT in the definitive assessment of a suspicious lesion, facilitating the final diagnosis for the reading radiologist. This advantage is primarily due to the glucose uptake of tumorous lesions, which can thus be assessed as malignant and therefore reduce the uncertainty of the radiologist in comparison to conventional imaging techniques [40].

An additional benefit of using PET/MRI is a potential reduction of ionizing radiation, when compared to CT or even PET/CT. This is particularly relevant in the primary staging of breast cancer, since the tumor tends to occur more often in younger patients compared to other cancer entities [41, 42]. In addition, with PET/MRI an imaging of the head is directly acquired. In our study, however, this did not result in any advantage since no relevant findings were discovered.

This study has some limitations. In conformity with previous studies, a modified reference standard had to be applied, based on follow-up imaging for lesions without a histological sampling, since management of advanced tumor stages does not necessarily require a histological sampling of all detected malignant lesions [7, 11, 43].

Conclusion

In conclusion, the present study shows that ¹⁸F-FDG PET/MRI has a high diagnostic potential and outperforms CT in assessing the N and M stage in patients with primary breast cancer. Despite the advantages of CT such as availability, costs or acquisition speed, this study together with present data should provide cause of discussion, regarding the current recommendations for primary staging in breast cancer guidelines.

Author Contributions

Conceptualization: Julian Kirchner, Janna Morawitz, Oliver Hoffmann, Christian Buchbender.

Data curation: Nils Martin Bruckmann, Janna Morawitz, Ann-Kathrin Bittner, Oliver Hoffmann, Svjetlana Mohrmann, Marc Ingenwerth.

Formal analysis: Nils Martin Bruckmann.

Funding acquisition: Christian Buchbender.

Investigation: Christian Buchbender.

Methodology: Christian Buchbender.

Project administration: Christian Buchbender.

Resources: Lale Umutlu, Ken Herrmann, Gerald Antoch.

Software: Nils Martin Bruckmann.

Supervision: Julian Kirchner, Lale Umutlu, Ken Herrmann, Benedikt M. Schaarschmidt, Yan Li, Gerald Antoch, Lino M. Sawicki.

Validation: Nils Martin Bruckmann, Julian Kirchner, Janna Morawitz, Andreas Stang, Lino M. Sawicki.

Visualization: Nils Martin Bruckmann, Lino M. Sawicki.

Writing – original draft: Nils Martin Bruckmann.

Writing – review & editing: Julian Kirchner, Janna Morawitz, Lale Umutlu, Ken Herrmann, Ann-Kathrin Bittner, Oliver Hoffmann, Svjetlana Mohrmann, Benedikt M. Schaarschmidt, Yan Li, Andreas Stang, Gerald Antoch, Lino M. Sawicki.

References

1. The Global Cancer Observatory G. Breast Cancer. Source: Globocan 2018. World Heal Organ. 2018; 876: 2018–2019.
2. Wockel A, Festl J, Stuber T, Brust K, Krockenberger M, Heuschmann PU, et al. Interdisciplinary Screening, Diagnosis, Therapy and Follow-up of Breast Cancer. Guideline of the DGGG and the DKG (S3-Level, AWMF Registry Number 032/045OL, December 2017)—Part 2 with Recommendations for the Therapy of Primary, Recurrent and Advanced Br. Geburtshilfe Frauenheilkd. 2018; 78: 1056–1088. <https://doi.org/10.1055/a-0646-4630> PMID: 30581198
3. Michaelson JS, Chen LL, Silverstein MJ, Mihm MCJ, Sober AJ, Tanabe KK, et al. How cancer at the primary site and in the lymph nodes contributes to the risk of cancer death. Cancer. 2009; 115: 5095–5107. <https://doi.org/10.1002/cncr.24592> PMID: 19670458
4. Senkus E, Kyriakides S, Ohno S, Penault-Llorca F, Poortmans P, Rutgers E, et al. Primary breast cancer: ESMO Clinical Practice Guidelines for diagnosis, treatment and follow-up. Ann Oncol Off J Eur Soc Med Oncol. 2015; 26 Suppl 5: v8–30. <https://doi.org/10.1093/annonc/mdv298> PMID: 26314782

5. Cardoso F, Senkus E, Costa A, Papadopoulos E, Aapro M, Andre F, et al. 4th ESO-ESMO International Consensus Guidelines for Advanced Breast Cancer (ABC 4)dagger. Ann Oncol Off J Eur Soc Med Oncol. 2018; 29: 1634–1657. <https://doi.org/10.1093/annonc/mdy192> PMID: 30032243
6. Gradishar WJ, Anderson BO, Balassanian R, Blair SL, Burstein HJ, Cyr A, et al. Breast Cancer, Version 4.2017, NCCN Clinical Practice Guidelines in Oncology. J Natl Compr Cancer Netw. 2018; 16: 310–320. <https://doi.org/10.6004/jnccn.2018.0012> PMID: 29523670
7. Sawicki LM, Grueneisen J, Schaarschmidt BM, Buchbender C, Nagarajah J, Umutlu L, et al. Evaluation of ¹⁸F-FDG PET/MRI, ¹⁸F-FDG PET/CT, MRI, and CT in whole-body staging of recurrent breast cancer. Eur J Radiol. 2016; 85: 459–465. <https://doi.org/10.1016/j.ejrad.2015.12.010> PMID: 26781152
8. Kanda T, Kitajima K, Suenaga Y, Konishi J, Sasaki R, Morimoto K, et al. Value of retrospective image fusion of ¹⁸F-FDG PET and MRI for preoperative staging of head and neck cancer: Comparison with PET/CT and contrast-enhanced neck MRI. Eur J Radiol. 2013; 82: 2005–2010. <https://doi.org/10.1016/j.ejrad.2013.06.025> PMID: 23891295
9. Anderson WF, Reiner AS, Matsuno RK, Pfeiffer RM. Shifting breast cancer trends in the United States. J Clin Oncol. 2007; 25: 3923–9. <https://doi.org/10.1200/JCO.2007.11.6079> PMID: 17679726
10. Kirchner J, Sawicki LM, Deuschl C, Grüneisen J, Beiderwellen K, Lauenstein TC, et al. ¹⁸F-FDG PET/ MR imaging in patients with suspected liver lesions: Value of liver-specific contrast agent Gadobenate dimeglumine. PLoS One. 2017; 12: 1–14. <https://doi.org/10.1371/journal.pone.0180349> PMID: 28683109
11. Beiderwellen K, Grueneisen J, Ruhmann V, Buderath P, Aktas B, Heusch P, et al. [(18)F]FDG PET/ MRI vs. PET/CT for whole-body staging in patients with recurrent malignancies of the female pelvis: initial results. Eur J Nucl Med Mol Imaging. 2015; 42: 56–65. <https://doi.org/10.1007/s00259-014-2902-8> PMID: 25223420
12. Beiderwellen K, Gomez B, Buchbender C, Hartung V, Poeppel TD, Nensa F, et al. Depiction and characterization of liver lesions in whole body [(18)F]-FDG PET/MRI. Eur J Radiol. 2013; 82: e669–75. <https://doi.org/10.1016/j.ejrad.2013.07.027> PMID: 24011443
13. Heusch P, Buchbender C, Kohler J, Nensa F, Gauler T, Gomez B, et al. Thoracic staging in lung cancer: prospective comparison of ¹⁸F-FDG PET/MR imaging and ¹⁸F-FDG PET/CT. J Nucl Med. 2014; 55: 373–378. <https://doi.org/10.2967/jnumed.113.129825> PMID: 24504054
14. Kirchner J, Sawicki LM, Nensa F, Schaarschmidt BM, Reis H, Ingenwerth M, et al. Prospective comparison of ¹⁸F-FDG PET/MRI and ¹⁸F-FDG PET/CT for thoracic staging of non-small cell lung cancer. Eur J Nucl Med Mol Imaging. 2019; 46: 437–445. <https://doi.org/10.1007/s00259-018-4109-x> PMID: 30074073
15. Botsikas D, Bagetakos I, Picarra M, Da Cunha Afonso Barisits AC, Boudabbous S, Montet X, et al. What is the diagnostic performance of ¹⁸-FDG-PET/MR compared to PET/CT for the N- and M- staging of breast cancer? Eur Radiol. 2019; 29: 1787–1798. <https://doi.org/10.1007/s00330-018-5720-8> PMID: 30267154
16. Tabouret-Viaud C, Botsikas D, Delattre BMA, Mainta I, Amzalag G, Rager O, et al. PET/MR in Breast Cancer. Semin Nucl Med. 2015; 45: 304–321. <https://doi.org/10.1053/j.semnuclmed.2015.03.003> PMID: 26050658
17. Kirchner J, Grueneisen J, Martin O, Oehmigen M, Quick HH, Bittner AK, et al. Local and whole-body staging in patients with primary breast cancer: a comparison of one-step to two-step staging utilizing ¹⁸F-FDG-PET/MRI. Eur J Nucl Med Mol Imaging. 2018; 45: 2328–2337. <https://doi.org/10.1007/s00259-018-4102-4> PMID: 30056547
18. World Medical Association Declaration of Helsinki: ethical principles for medical research involving human subjects. JAMA. 2013; 310: 2191–2194. <https://doi.org/10.1001/jama.2013.281053> PMID: 24141714
19. Grueneisen J, Sawicki LM, Wetter A, Kirchner J, Kinner S, Aktas B, et al. Evaluation of PET and MR datasets in integrated ¹⁸F-FDG PET/MRI: A comparison of different MR sequences for whole-body restaging of breast cancer patients. Eur J Radiol. 2017; 89: 14–19. <https://doi.org/10.1016/j.ejrad.2016.12.019> PMID: 28267530
20. Grueneisen J, Nagarajah J, Buchbender C, Hoffmann O, Schaarschmidt BM, Poeppel T, et al. Positron Emission Tomography/Magnetic Resonance Imaging for Local Tumor Staging in Patients with Primary Breast Cancer: A Comparison with Positron Emission Tomography/Computed Tomography and Magnetic Resonance Imaging. Invest Radiol. 2015; 50: 505–13. <https://doi.org/10.1097/RLI.0000000000000197> PMID: 26115367
21. National Institute for Health and Care Excellence. Early and locally advanced breast cancer: diagnosis and treatment | 1-Guidance | Guidance and guidelines | NICE. In: NICE Guidance. 2018.
22. Brennan M, Houssami N. Newly diagnosed early breast cancer—an update on pre-operative assessment and staging. Aust Fam Physician. 2012; 41: 871–874. PMID: 23145418

23. Lee B, Lim AK, Krell J, Satchithananda K, Coombes RC, Lewis JS, et al. The efficacy of axillary ultrasound in the detection of nodal metastasis in breast cancer. *Am J Roentgenol.* 2013; 200: W314–20. <https://doi.org/10.2214/AJR.12.9032> PMID: 23436877
24. Valente SA, Levine GM, Silverstein MJ, Rayhanabad JA, Weng-Grumley JG, Ji L, et al. Accuracy of predicting axillary lymph node positivity by physical examination, mammography, ultrasonography, and magnetic resonance imaging. *Ann Surg Oncol.* 2012; 19: 1825–30. <https://doi.org/10.1245/s10434-011-2200-7> PMID: 22227922
25. Panda SK, Goel A, Nayak V, Shaik Basha S, Pande PK, Kumar K. Can Preoperative Ultrasonography and MRI Replace Sentinel Lymph Node Biopsy in Management of Axilla in Early Breast Cancer—a Prospective Study from a Tertiary Cancer Center. *Indian J Surg Oncol.* 2019; 10: 483–488. <https://doi.org/10.1007/s13193-019-00924-7> PMID: 31496596
26. Shin CH, Kim JI, Lee JY. The role of radiologic evaluation for detection of axillary lymph node metastasis in early breast cancer. *Eur J Cancer.* 2016; 57: 143–144.
27. Bitencourt AGV, Andrade WP, da Cunha RR, de Conrado JLF A, Lima ENP, Barbosa PNVP, et al. Detection of distant metastases in patients with locally advanced breast cancer: role of ¹⁸F-fluorodeoxyglucose positron emission tomography/computed tomography and conventional imaging with computed tomography scans. *Radiol Bras.* 2017; 50: 211–215. <https://doi.org/10.1590/0100-3984.2015-0232> PMID: 28894327
28. Choi SH, Kim YT, Kim SK, Kang KW, Goo JM, Kang CH, et al. Positron emission tomography-computed tomography for postoperative surveillance in non-small cell lung cancer. *Ann Thorac Surg.* 2011; 92: 1826–32. <https://doi.org/10.1016/j.athoracsur.2011.07.005> PMID: 22051278
29. Hildebrandt MG, Gerke O, Baun C, Falch K, Hansen JA, Farahani ZA, et al. [18F] Fluorodeoxyglucose (FDG)-Positron emission tomography (PET)/computed tomography (CT) in suspected recurrent breast cancer: A prospective comparative study of dual-time-point FDG-PET/CT, contrast-enhanced CT, and bone scintigraphy. *J Clin Oncol.* 2016; 34: 1889–1897. <https://doi.org/10.1200/JCO.2015.63.5185> PMID: 27001573
30. Choi YJ, Shin YD, Kang YH, Lee MS, Lee MK, Cho BS, et al. The effects of preoperative ¹⁸F-FDG PET/CT in breast cancer patients in comparison to the conventional imaging study. *J Breast Cancer.* 2012; 15: 441–8. <https://doi.org/10.4048/jbc.2012.15.4.441> PMID: 23346174
31. Fuster D, Duch J, Paredes P, Velasco M, Muñoz M, Santamaría G, et al. Preoperative staging of large primary breast cancer with [18F]fluorodeoxyglucose positron emission tomography/computed tomography compared with conventional imaging procedures. *J Clin Oncol.* 2008; 26: 4746–51. <https://doi.org/10.1200/JCO.2008.17.1496> PMID: 18695254
32. Groheux D, Moretti JL, Baillet G, Espie M, Giacchetti S, Hindie E, et al. Effect of ¹⁸F-FDG PET/CT Imaging in Patients With Clinical Stage II and III Breast Cancer. *Int J Radiat Oncol Biol Phys.* 2008; 71: 695–704. <https://doi.org/10.1016/j.ijrobp.2008.02.056> PMID: 18436392
33. Mahner S, Schirrmacher S, Brenner W, Jenicke L, Habermann CR, Avril N, et al. Comparison between positron emission tomography using 2-[fluorine-18]fluoro-2-deoxy-D-glucose, conventional imaging and computed tomography for staging of breast cancer. *Ann Oncol.* 2008; 19: 1249–1254. <https://doi.org/10.1093/annonc/mdn057> PMID: 18356138
34. Hildebrandt M, Falch K, Baun C, Ansholm J, Gerke O, Alavi A. Imaging of bone metastases in suspected recurrent breast cancer. *J Nucl Med.* 2015; 56: 570.
35. Monzawa S, Adachi S, Suzuki K, Hirokaga K, Takao S, Sakuma T, et al. Diagnostic performance of fluorodeoxyglucose-positron emission tomography/computed tomography of breast cancer in detecting axillary lymph node metastasis: Comparison with ultrasonography and contrast-enhanced CT. *Ann Nucl Med.* 2009; 23: 855–861. <https://doi.org/10.1007/s12149-009-0314-9> PMID: 19876704
36. Melsaether AN, Raad RA, Pujara AC, Ponzo FD, Pysarenko KM, Jhaveri K, et al. Comparison of Whole-Body ¹⁸F FDG PET/MR Imaging and Whole-Body ¹⁸F FDG PET/CT in Terms of Lesion Detection and Radiation Dose in Patients with Breast Cancer. *Radiology.* 2016; 281: 193–202. <https://doi.org/10.1148/radiol.2016151155> PMID: 27023002
37. van Nijnatten TJA, Goorts B, Vöö S, de Boer M, Kooreman LFS, Heuts EM, et al. Added value of dedicated axillary hybrid ¹⁸F-FDG PET/MRI for improved axillary nodal staging in clinically node-positive breast cancer patients: a feasibility study. *Eur J Nucl Med Mol Imaging.* 2018; 45: 179–186. <https://doi.org/10.1007/s00259-017-3823-0> PMID: 28905091
38. Sawicki LM, Grueneisen J, Buchbender C, Schaarschmidt BM, Gomez B, Ruhlmann V, et al. Comparative Performance of ¹⁸F-FDG PET/MRI and ¹⁸F-FDG PET/CT in Detection and Characterization of Pulmonary Lesions in 121 Oncologic Patients. *J Nucl Med.* 2016; 57: 582–586. <https://doi.org/10.2967/jnumed.115.167486> PMID: 26742715
39. Sawicki LM, Grueneisen J, Buchbender C, Schaarschmidt BM, Gomez B, Ruhlmann V, et al. Evaluation of the Outcome of Lung Nodules Missed on ¹⁸F-FDG PET/MRI Compared with ¹⁸F-FDG PET/CT in

- Patients with Known Malignancies. *J Nucl Med.* 2016; 57: 15–20. <https://doi.org/10.2967/jnumed.115.162966> PMID: 26514173
40. Sawicki LM, Kirchner J, Umutlu L, Forsting M, Schaarschmidt BM, Ruhlmann V, et al. Comparison of ¹⁸F-FDG PET/MRI and MRI alone for whole-body staging and potential impact on therapeutic management of women with suspected recurrent pelvic cancer: a follow-up study. *Eur J Nucl Med Mol Imaging.* 2017; 45: 622–629. <https://doi.org/10.1007/s00259-017-3881-3> PMID: 29164299
41. DeSantis CE, Ma J, Gaudet MM, Newman LA, Miller KD, Goding Sauer A, et al. Breast cancer statistics, 2019. *CA Cancer J Clin.* 2019; 69: 438–451. <https://doi.org/10.3322/caac.21583> PMID: 31577379
42. Bidoli E, Virdone S, Hamdi-Cherif M, Toffolutti F, Taborelli M, Panato C, et al. Worldwide Age at Onset of Female Breast Cancer: A 25-Year Population-Based Cancer Registry Study. *Sci Rep.* 2019; 9: 14111. <https://doi.org/10.1038/s41598-019-50680-5> PMID: 31575963
43. Grueneisen J, Nagarajah J, Buchbender C, Hoffmann O, Schaarschmidt BM, Poeppel T, et al. Positron Emission Tomography / Magnetic Resonance Imaging for Local Tumor Staging in Patients With Primary Breast Cancer. *Invest Radiol.* 2015; 50: 1–9.



Prospective comparison of the diagnostic accuracy of ¹⁸F-FDG PET/MRI, MRI, CT, and bone scintigraphy for the detection of bone metastases in the initial staging of primary breast cancer patients

Nils Martin Bruckmann¹ · Julian Kirchner¹ · Lale Umutlu² · Wolfgang Peter Fendler³ · Robert Seifert³ · Ken Herrmann³ · Ann-Kathrin Bittner⁴ · Oliver Hoffmann⁴ · Svjetlana Mohrmann⁵ · Christina Antke⁶ · Lars Schimmöller¹ · Marc Ingenwerth⁷ · Katharina Breuckmann² · Andreas Stang⁸ · Christian Buchbender¹ · Gerald Antoch¹ · Lino M. Sawicki¹

Received: 25 January 2021 / Revised: 15 March 2021 / Accepted: 26 March 2021 / Published online: 28 April 2021
© The Author(s) 2021

Abstract

Objectives To compare the diagnostic performance of [¹⁸F]FDG PET/MRI, MRI, CT, and bone scintigraphy for the detection of bone metastases in the initial staging of primary breast cancer patients.

Material and methods A cohort of 154 therapy-naïve patients with newly diagnosed, histopathologically proven breast cancer was enrolled in this study prospectively. All patients underwent a whole-body [¹⁸F]FDG PET/MRI, computed tomography (CT) scan, and a bone scintigraphy prior to therapy. All datasets were evaluated regarding the presence of bone metastases. McNemar χ^2 test was performed to compare sensitivity and specificity between the modalities.

Results Forty-one bone metastases were present in 7/154 patients (4.5%). Both [¹⁸F]FDG PET/MRI and MRI alone were able to detect all of the patients with histopathologically proven bone metastases (sensitivity 100%; specificity 100%) and did not miss any of the 41 malignant lesions (sensitivity 100%). CT detected 5/7 patients (sensitivity 71.4%; specificity 98.6%) and 23/41 lesions (sensitivity 56.1%). Bone scintigraphy detected only 2/7 patients (sensitivity 28.6%) and 15/41 lesions (sensitivity 36.6%). Furthermore, CT and scintigraphy led to false-positive findings of bone metastases in 2 patients and in 1 patient, respectively. The sensitivity of PET/MRI and MRI alone was significantly better compared with CT ($p < 0.01$, difference 43.9%) and bone scintigraphy ($p < 0.01$, difference 63.4%).

Conclusion [¹⁸F]FDG PET/MRI and MRI are significantly better than CT or bone scintigraphy for the detection of bone metastases in patients with newly diagnosed breast cancer. Both CT and bone scintigraphy show a substantially limited sensitivity in detection of bone metastases.

Key Points

- [¹⁸F]FDG PET/MRI and MRI alone are significantly superior to CT and bone scintigraphy for the detection of bone metastases in patients with newly diagnosed breast cancer.
- Radiation-free whole-body MRI might serve as modality of choice in detection of bone metastases in breast cancer patients.

Nils Martin Bruckmann and Julian Kirchner contributed equally to this work.

Nils Martin Bruckmann
nils-m.bruckmann@web.de

¹ Department of Diagnostic and Interventional Radiology, Medical Faculty, University Dusseldorf, Moorenstrasse 5, D-40225 Dusseldorf, Germany

² Department of Diagnostic and Interventional Radiology and Neuroradiology, University Hospital Essen, University of Duisburg-Essen, D-45147 Essen, Germany

³ Department of Nuclear Medicine, University Hospital Essen, University of Duisburg-Essen, D-45147 Essen, Germany

⁴ Department Gynecology and Obstetrics, University Hospital Essen, University of Duisburg-Essen, D-45147 Essen, Germany

⁵ Department of Gynecology, Medical Faculty, University Dusseldorf, D-40225 Dusseldorf, Germany

⁶ Department of Nuclear Medicine, Medical Faculty, University Dusseldorf, 40225 Dusseldorf, Germany

⁷ Institute of Pathology, University Duisburg-Essen and the German Cancer Consortium (DKTK), University Hospital Essen, West German Cancer Center, Essen, Germany

⁸ Institute of Medical Informatics, Biometry and Epidemiology, University Hospital of Essen, Essen, Germany

Keywords Multimodal imaging · Positron emission tomography · Tomography, X-ray · Radionuclide imaging · Breast neoplasms

Abbreviations

AC	Attenuation correction
ADC	Apparent diffusion coefficient
CI	Confidence interval
CT	Computed tomography
DWI	Diffusion-weighted imaging
EPI	Echo-planar imaging
ESMO	European Society For Medical Oncology
FDG	Fluorodeoxyglucose
FOV	Field of view
FWHM	Full-width at half maximum
HASTE	Half Fourier acquisition single shot turbo spin echo
HDP	Hydroxydiphosphonate
HER2	Human epidermal growth factor receptor 2
MRI	Magnetic resonance imaging
OSEM	Ordered-subset expectation maximization
PET	Positron emission tomography
RF	Radiofrequency
VIBE	Volume interpolated breath-hold examination
WHO	World Health Organization

Introduction

Breast cancer is by far the most common solid neoplasm in women worldwide and with 15% the leading cause of tumor-related deaths in women every year [1]. Once the diagnosis is confirmed, the prognosis of disease depends largely on the stage of its spread and choice of an adequate therapy. Additionally to the assessment of the extent of the primary tumor in the breast and locoregional lymph node involvement, the detection of distant metastases is crucial, since this can result in an extension of the irradiation field or an adjustment of chemotherapy and eventually in a change to a palliative therapy concept [2]. Therefore, imaging-based whole-body staging plays a pivotal role in the primary diagnostics of breast cancer patients with a high risk for the presence of distant metastases.

Despite the advances in the treatment of breast cancer, up to 30% of patients still develop distant metastases over the course of the disease [3]. Herein, the skeleton is the most frequent site of distant metastases in breast cancer patients, accounting for 50–70% of all metastases [3–7]. The affection of the bone can cause various complications such as pain, pathological fractures, spinal cord compression, and hypercalcemia, which often have a major impact on patients' morbidity and mortality [8–10]. Early detection can help to better control the disease, minimize complications, and, as a result, achieve a better quality of life [9].

As the initial staging has become increasingly important in recent years, the diagnostic algorithm was adapted and a thoraco-abdominal CT as well as bone scintigraphy was implemented [11]. If available, a PET/CT examination can also be used in primary staging, but has been rarely applied so far due to its low availability and higher costs. Therefore, bone scintigraphy in combination with CT are widely considered to be the gold standard for the detection of bone metastases, and are also recommended as the methods of choice in current guidelines [12–14]. However, previous studies have suggested that MRI provides advantages in the detection of bone lesions when compared to bone scan and might top CT as most beneficial whole-body staging examination [9, 15]. Accordingly, MRI has been discussed as an alternative staging tool for breast cancer patients and has already been added as a method of choice in patients with neurological symptoms and signs which suggest the possibility of spinal cord compression in the latest 2018 and 2020 European Society For Medical Oncology (ESMO) guidelines [12, 14], but is rarely used in everyday clinical routine [16].

The application of hybrid imaging techniques has proven to be of additional benefit in this context [17–20]. However, the impact of a [¹⁸F]FDG PET/MRI examination for the detection of bone metastases in primary breast cancer patients has been scarcely investigated so far [21–23], and to the best of our knowledge, there is only a small cohort study investigating its role in comparison to conventional imaging for the detection of bone metastases in the initial staging of breast cancer [23].

Thus, the purpose of this study was to investigate and compare the diagnostic value of [¹⁸F]FDG PET/MRI, MRI alone, CT, and bone scintigraphy for the detection of bone metastases in the initial staging of primary breast cancer patients.

Material and methods

Patients

This prospective study was approved by the institutional review board of the University of Duisburg-Essen (study number 17-7396-BO) and Düsseldorf (study number 6040R) and performed in conformance with the Declaration of Helsinki and its later amendments. Written informed consent form was obtained from all patients. The present study is a sub-analysis of a prospective, super-ordinate, main study (BU3075/2-1), and the research question of the present sub-analysis is markedly different from the main study. Inclusion criteria were defined as follows: (1) newly diagnosed, treatment-naïve T2 tumor or higher T-stage, or (2) newly diagnosed, treatment-

Table 1 Histopathological data

		<i>N</i>
Total patients		154
Menopause status	Pre	63
	Peri	11
	Post	80
Family risk profile	Positive	42
	Negative	112
BRCA-1	Positive	4
	Negative	25
	Unknown	125
BRCA-2	Positive	2
	Negative	26
	Unknown	126
Ki 67	Positive (> 14%)	141
	Negative (< 14%)	13
PR status	Positive	107
	Negative	47
ER status	Positive	115
	Negative	39
HER2-neu expression	0	55
	1+	50
	2+	23
	3+	26
Subtype	Luminal A	7
	Luminal B	116
	HER2-enriched	3
	Basal-like	28
Tumor grade	G1	6
	G2	82
	G3	66
Histology	Ductal invasive/NST	136
	Lobular invasive	13
	Mucinous invasive	1
	Mixed type	1

naive triple-negative tumor of every size, or (3) newly diagnosed, treatment-naive tumor with molecular high risk (T1c, Ki67 > 14%, HER2-new over-expression, G3). Exclusion criteria were contraindications to MRI or MRI contrast agents, missing imaging of a modality, pregnancy or breast-feeding, and former malignancies in the last 5 years. Inclusion criteria were chosen according to clinical ESMO guidelines to set elevated pre-test probability for distant metastases [12, 14]. Between March 2018 and March 2020, a total of 177 consecutive breast cancer patients underwent a [¹⁸F]FDG PET/MRI whole-body examination prior to therapy. Twenty-three patients had to be excluded from this study, because a comparable CT examination was missing in 7 patients and a bone

scintigraphy in 17 patients, mainly due to patients not attending the examination appointment or the examination was performed in other medical institutions and were not available for evaluation. This resulted in a study cohort of 154 women (mean age 53.8 ± 11.9, range 30–82 years) (Fig. 1, Table 1).

PET/MRI

All patients underwent a [¹⁸F]FDG PET/MRI examination on an integrated 3.0-Tesla Biograph mMR scanner (Siemens Healthineers) with a mean delay of 64 ± 17 min after [¹⁸F]FDG application. Prior to intravenous injection of a body weight-adapted dosage of [¹⁸F]FDG (4 MBq/kg body weight, mean activity: 254.4 ± 43.6 MBq), blood samples were obtained to ensure blood glucose levels below 150 mg/dl. All patients received a whole-body [¹⁸F]FDG PET/MRI from head to the mid-thigh in headfirst supine position.

PET images were obtained simultaneously with the MRI data with an acquisition time of 3 min per bed position in four or five positions (axial FOV: 25.8 cm; matrix size: 344 × 344; pixel size 2.09 × 2.09 mm). An iterative 3D ordinary Poisson ordered-subset expectation maximization (3D OP-OSEM) algorithm was conducted for reconstruction of PET images utilizing 3 iterations and 21 subsets, a Gaussian filter FWHM 4.0 mm, and a scatter correction. Depending on the patient's height, up to 6-channel flex body coils, a dedicated 16-channel head-and-neck radiofrequency (RF) coil, and a 24-channel spine array RF coil were applied for MR imaging.

For tissue attenuation correction (AC) and scatter correction, a two-point (fat, water) transaxial acquired high-resolution CAIPIRINHA (CAIPI)-accelerated T1-weighted three-dimensional (3D) Dixon-VIBE (volume interpolated breath hold examination) sequence was acquired to generate a coronal four-compartment model attenuation map (umap, background air, lungs, fat, muscle). In addition, a bone atlas correction and a truncation correction as proposed by Blumhagen et al [24] was applied. Please see Table 2 for MRI protocol parameters. The PET/MRI scanner used was not time-of-flight (TOF) capable.

Computed tomography

Two CT scanners (Definition Edge and Definition Flash, Siemens Healthineers) were used for thoraco-abdominal multi-slice contrast-enhanced CT using automated tube current modulation and tube voltage selection (CareDose 4D and CareKV, Siemens Healthineers). CTs were acquired in portal venous phase after intravenous application of a body weight-adapted dosage of non-ionic contrast agent (Table 2). The arms of the patients were placed upwards. Accordingly, only parts of the limbs that were pictured in the FOV of all modalities were included in the evaluation.

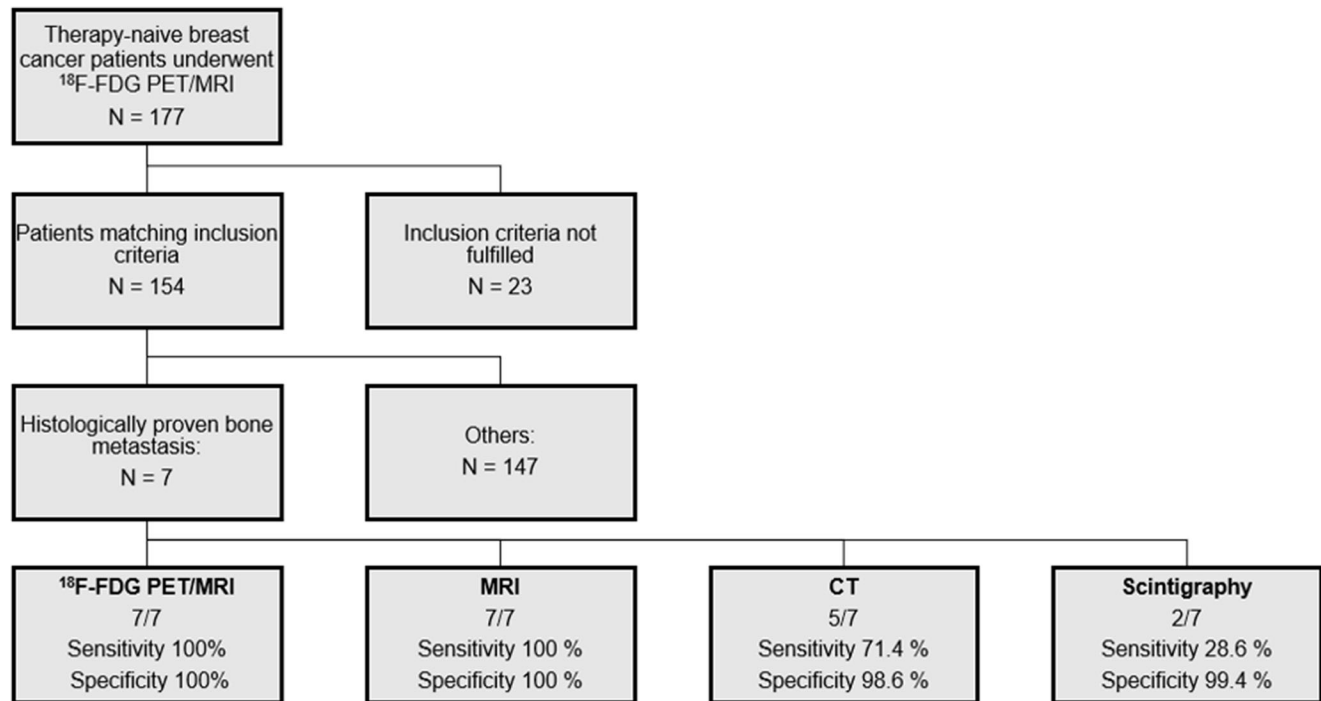


Fig. 1 Flow-chart showing process of inclusion and patient-based specificity and sensitivity of each modality. of non-fulfilment of inclusion criteria are described in the text

Bone scintigraphy

Bone scintigraphy was performed according to a clinical routine protocol with planar whole-body scans using a dual-headed gamma camera equipped with low-energy high-resolution collimator (Symbia S, Siemens Healthineers). Three hours after intravenous injection of an average amount of 700 MBq of [^{99m}Tc]-labeled polyphosphonate (HDP), anterior and posterior view scans were acquired with an acquisition time of 20 to 35 min. In all cases of uncertain radionuclide accumulations on bone scan, additional target images were taken or SPECT/CT images were acquired.

Image analysis

In each patient, all examinations were performed over a 3-week period and prior to any oncologic therapy. The CT and

PET/MRI datasets were analyzed separately and in random order by two radiologists experienced in hybrid and conventional imaging with a reading gap of 4 weeks to avoid recognition bias. Additionally, PET/MRI datasets and bone scintigraphy were also examined by a nuclear medicine physician. Discrepant findings were resolved by consensus decision-making in a separate session between the readers. For the evaluation of the MRI, images were separated from PET datasets. A picture archiving and communication system (Centricity; General Electric Medical Systems) and a dedicated image processing software OsiriX (Version 9.0.2, Pixmeo SARL) were used for image analysis. The readers were aware of the diagnosis but blinded to results of prior imaging.

The following criteria were applied to determine the presence of a bone metastasis in CT: a focal cortical destruction or increase of bone density, a focal bone expansion, periosteal

Table 2 Sequence parameters for the diagnostic MR-sequences and CT in staging of primary breast cancer patients

CT	Region	Contrast agent	Orientation	mAs	kV	Speed (s per rotation)	Silence thickness (mm)	FOV (mm)
Attenuation correction	Whole-body	No	Axial	80	120	0.75	4.0	600
Diagnostic CT	Thoraco-abdominal	Yes	Axial	210	120	0.75	4.0	350×459
MR sequence	Region	Contrast agent	Orientation	TR (ms)	TE (ms)	Matrix size	Slice thickness (mm)	FOV (mm)
EPI-DWI	Whole-body	No	Axial	11,900	86	192×144	5.0	380×285
T2w HASTE	Whole-body	No	Axial	1500	117	320×259	7.0	450×366
T1w fs VIBE	Whole-body	Yes	Axial	4.08	1.51	512×307	3.5	400×300

reaction, pathological fractures, and contrast enhancement. In MRI signal intensity typical of metastasis in conventional MRI sequences, pathological contrast enhancement, diffusion restriction, pathological fractures, and bone edema were signs of malignancy. In [¹⁸F]FDG PET/MRI and on bone scan, a visually detectable focal uptake above background signal was considered a sign of malignancy. Besides lesion count, localization, and characterization (benign or malignant), the diagnostic confidence of every lesion in terms of its characterization as benign or malignant (5-point ordinal scale, 1 = very low confidence, 2 = low confidence, 3 = indeterminate confidence, 4 = high confidence, 5 = very high confidence) was assessed with each modality. The body volumes examined were chosen identically for each modality and covered the body from the thorax to mid-thighs.

Reference standard

In all 154 women, diagnosis of primary breast cancer was confirmed histopathologically. Furthermore, in all patients with suspected osseous metastasis in any of the imaging modalities, at least one osseous lesion was histologically sampled. Due to clinical and ethical standards, a histological confirmation of some malignant lesions was not available, and a surrogate reference standard was applied taking into account all follow-up imaging. In all patients with suspected metastases, CT or MRI was performed as follow-up examination (mean delay 3.8 ± 1.3 month). In total, follow-up examinations were performed in 60 women, comprising 33 thoraco-abdominal CT, 22 whole-body MRI, and 5 patients receiving both examinations (mean delay 7.4 ± 5.1 month). The remaining patients, who did not undergo follow-up imaging, have been showing no clinical signs of bone metastases. Any increase of size or a decrease of size of suspicious lesions after therapy or newly occurred cortical destruction were regarded as signs of malignancy.

Statistical analysis

Statistical analysis was performed using SPSS 24™ (IBM). Descriptive analysis was performed, and all data are presented as mean \pm standard deviation including confidence intervals (CIs). To avoid statistical errors caused by clustered data (i.e., multiple observations within the same patient), all data were analyzed calculating sensitivity and specificity on a per-patient and a per-lesion basis. In addition, CIs have been adjusted using a ratio estimator, as described by Gender et al [25]. The lesion-based analysis was performed because knowledge of the exact number and localization of metastases can have large therapeutic impact, as solitary or oligometastases can be treated selectively with radiotherapy or surgery. For the comparison of sensitivity and specificity between the modalities, a McNemar χ^2 test was performed.

To assess the differences regarding the diagnostic confidence, a Wilcoxon signed rank test was applied. A p value < 0.05 was considered to indicate statistical significance.

Results

Patient-based analysis

According to the reference standard, bone metastases were present in 7/154 patients of the study cohort (4.5%). Both [¹⁸F]FDG PET/MRI and MRI alone were able to detect all of these patients. No false-positive patients were described by these two modalities. This resulted in a sensitivity of 100% (95% CI: 59.0–100.0) and a specificity of 100% (CI: 97.6–100.0). CT detected 5 of the 7 patients. In one patient with a single osteolytic metastasis, this was not visible on CT and in the other patient a small osteoblastic metastasis was misinterpreted as bone marrow island. Moreover, CT revealed false-positive findings in 2 non-metastasized patients, misinterpreting degenerative or posttraumatic lesions as malignant. This resulted in a sensitivity of 71.4% (CI: 35.9–91.8) and a specificity of 98.6% (CI: 95.2–99.6). Bone scintigraphy identified 2 of the 7 patients with bone metastases and showed a false-positive finding in a non-metastasized patient, resulting in a sensitivity of 28.6% (CI: 8.2–64.1) and a specificity of 99.4% (CI: 96.4–99.9). The McNemar χ^2 test yielded a not significant difference in favor of [¹⁸F]FDG PET/MRI and MRI in comparison to CT in detecting true-positive patients (100% vs. 71.4%, $p = 0.094$) and in specificity (100% vs. 98.6%, $p = 0.15$) and a significant difference in sensitivity comparing [¹⁸F]FDG PET/MRI and MRI to bone scan (100% vs. 28.6%, $p < 0.001$). The difference between CT and bone scan yielded no statistical significance (71.4% vs. 28.6%, $p = 0.076$).

Lesion-based analysis

A total of 45 bone lesions in 7 patients were included in the final evaluation, comprising 41 (91.1%) bone metastases and 4 (8.9%) benign bone lesions. One of the patients showed a diffuse infiltration of the entire axial skeleton, which was counted as 1 lesion. Twenty-three of the 41 metastases were classified as lytic, and 18 as sclerotic. Table 3 shows the localizations of all bone metastases. At least one lesion was confirmed by histopathological sampling in each patient; the remaining bone metastases were confirmed by follow-up imaging, according to the reference standard.

[¹⁸F]FDG PET/MRI did not miss any of the 41 malignant lesions (sensitivity 100%, CI: 79.0–100.0). All metastases showed a focal [¹⁸F]FDG uptake. There were no false-positive findings by [¹⁸F]FDG PET/MRI. MRI alone was also able to correctly identify all 41 metastases (sensitivity 100%,

Table 3 Locations of all 41 bone metastases and number of detected lesions in each modality in comparison to the reference standard (in brackets). Most metastases affected the vertebrae and the pelvic bones. Mainly osteolytic metastases were missed/misinterpreted by CT and bone

scan. Note that in CT arms were positioned upward and in PET/MRI besides the body. Only parts of the limbs that are pictured in the FOV of all modalities were evaluated

	PET/MRI and MRI		CT		Bone scan		Reference standard		
	Lytic	Sclerotic	Lytic	Sclerotic	Lytic	Sclerotic	Histology	CT	MRI
Vertebrae	9(9)	8(8)	4(9)	8(8)	1(9)	4(8)	1	12	4
Pelvic bones	6(6)	4(4)	2(6)	4(4)	3(6)	3(4)	5	3	2
Ribs	4(4)	1(1)	1(4)	0(1)	1(4)	0(1)	1	3	1
Limbs	4(4)	5(5)	1(4)	3(5)	2(4)	1(5)	1	5	3
Total	23(23)	18(18)	8(23)	15(18)	7(23)	8(18)	8	23	10

CI: 79.0–100.0), but misinterpreted one degenerative benign lesion as malignant. On MRI alone, the correct identification of 5 metastases was only possible through DWI, as they did not show a clear correlate on conventional morphologic MRI

sequences (see Fig. 2). In comparison to that, CT detected 23 of 41 malignant bone lesions (sensitivity 56.1%, CI: 43.7–68.5; 8 lytic, 15 sclerotic). Fifteen malignant lesions were missed by CT and 3 sclerotic metastases were misinterpreted

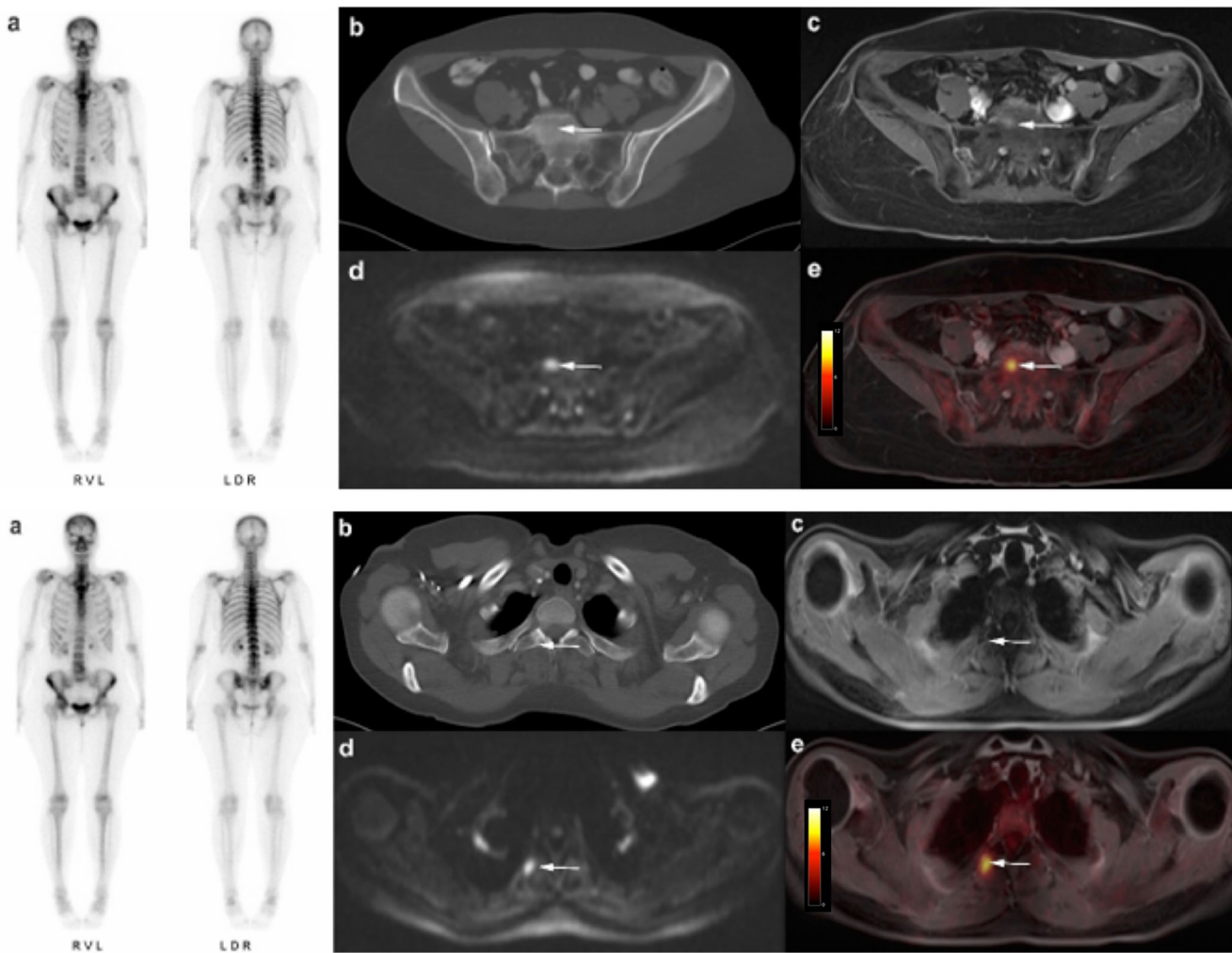


Fig. 2 Fifty-eight-year-old woman with breast cancer and histologically proven bone metastases in the os sacrum and the second right rib. Clear evidence of metastatic infestation in fused [¹⁸F]FDG PET/MRI (e) and in

DWI-sequences (d). In T1 fs Vibe the lesions are hard to detect (c). No signs of malignancy were seen in CT and bone scintigraphy (a, b)

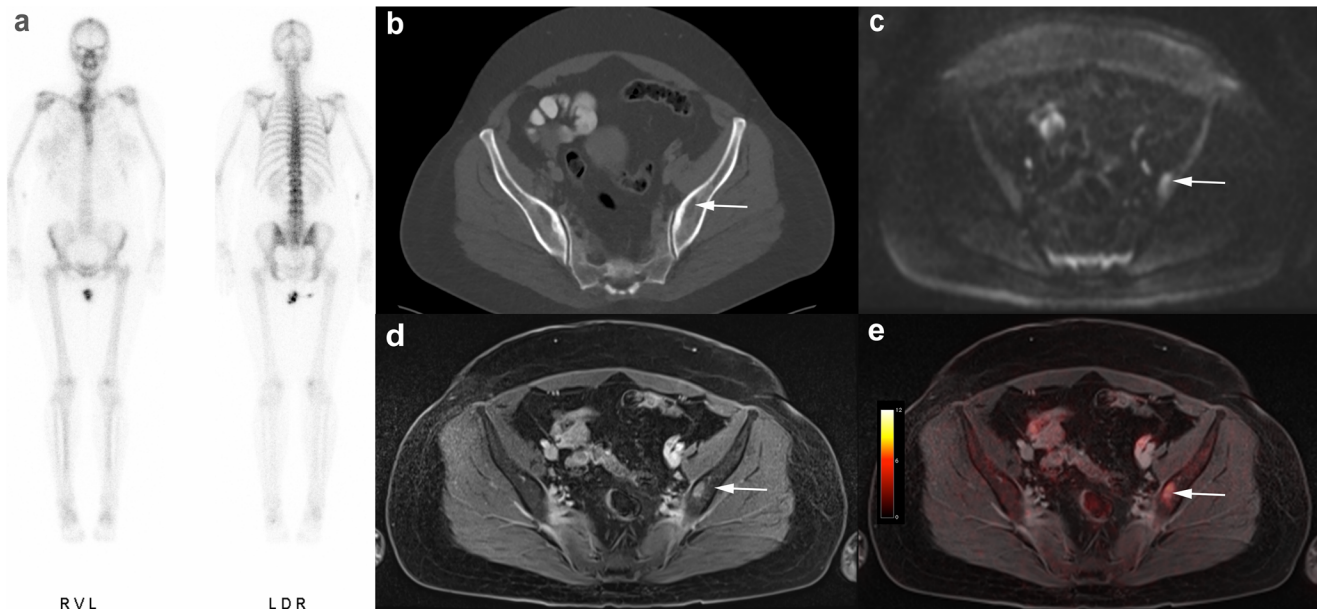


Fig. 3 Forty-eight-year-old woman with breast cancer and a single histologically confirmed osteolytic metastasis in the left iliac bone. In the absence of cortical destruction, CT and bone scintigraphy yielded

as bone islands. Especially osteolytic lesions of the bone marrow showing no signs of a tumor infestation such as cortical thinning or destruction were difficult to detect and often remained unrecognized on CT (Figs. 2, 3, and 4). Furthermore, there were 4 false-positive findings in CT, as 3 lesions in the axial skeleton and 1 lesion in a rib turned out to be degenerative or posttraumatic in histology and follow-up examination. Bone scintigraphy detected 15/41 bone metastases (sensitivity 36.6%, CI: 22.1–51.1; 7 lytic, 8 sclerotic)

false-negative results (a, b). Clear identification of metastasis in MRI alone (c, d) and in fused [^{18}F]FDG PET/MRI (e)

(Figs. 2, 3, and 4). Two of the lytic metastases detected with bone scintigraphy in one patient were not visible on CT. In addition, two posttraumatic lesions in the sternum and distal humerus in one patient were considered metastases in bone scintigraphy due to increased bone metabolism.

The McNemar χ^2 test yielded statistical significance when comparing sensitivities in lesion detection of [^{18}F]FDG PET/MRI with CT ($p < 0.01$, difference 43.9%, CI: 30.7–57.1) and MRI alone with CT ($p < 0.01$, difference 43.9%, CI: 30.7–

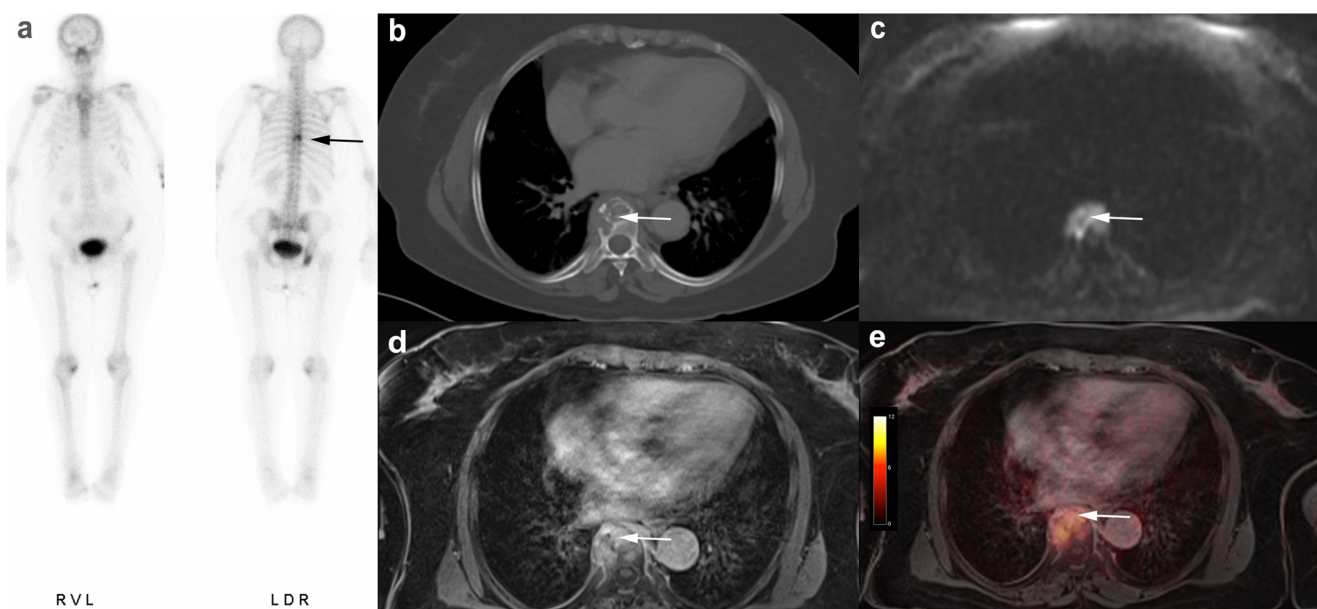


Fig. 4 Seventy-five-year-old woman with breast cancer and histologically confirmed osteolytic bone infestation in thoracic vertebral body T8. All modalities show clear evidence of metastasis: focal

accumulation in bone scintigraphy (a), cortical destruction and osteolysis in CT (b), diffusion restriction and contrast enhancement in MRI (c, d), and tracer uptake in fused [^{18}F]FDG PET/MRI (e)

57.1) as well as comparing [¹⁸F]FDG PET/MRI and MRI alone with bone scintigraphy ($p < 0.01$, difference 63.4%, CI: 40.7–76.1). The CT showed a statistically significant superiority in comparison to bone scintigraphy ($p = 0.039$, difference 19.5%, CI: 0.01–0.38).

Diagnostic confidence

[¹⁸F]FDG PET/MRI showed a significantly higher overall diagnostic confidence in lesion nature ratings compared to MRI alone (4.16 ± 0.71 vs. 3.3 ± 0.65 , $p < 0.0001$), CT (4.16 ± 0.71 vs. 3.04 ± 0.85 , $p < 0.0001$), and bone scintigraphy (4.16 ± 0.71 vs. 3.93 ± 0.26 , $p = 0.0003$). The difference of diagnostic confidence of MRI alone in comparison to CT did not reach statistical significance (3.3 ± 0.65 vs. 3.04 ± 0.85 , $p = 0.058$).

Discussion

In our study, [¹⁸F]FDG PET/MRI and MRI alone both outperform CT and bone scintigraphy when assessing bone metastases in the initial staging of patients with newly diagnosed breast cancer. On a lesion-based analysis, these modalities reveal a considerable advantage especially in the detection of osteolytic metastases. [¹⁸F]FDG PET/MRI shows no differences to MRI alone in sensitivity but offers a higher diagnostic confidence in correctly rating bone metastases. Bone scintigraphy achieved significantly worse results than CT in the detection of bone metastases.

Although the spectrum of available therapeutic options for breast cancer has significantly improved in recent years, distant metastases are still detectable in approximately one-third of patients during the course of the disease [3]. Bone metastases are by far the most frequent localization, accounting for 50–70% of distant metastases in the early phase of the disease [3–5]. Hence, a reliable initial staging has become increasingly important, as this allows for an individualized therapy regimen and early detection of patients with bone metastases to reduce skeletal morbidity by adjustment of chemotherapy, use of bisphosphonates, or targeted irradiation. Accordingly, the initial staging examination has recently been amended in guidelines, now including a thoraco-abdominal CT scan and a bone scintigraphy [12, 13]. Bone scintigraphy is still widely considered to be the gold standard in the detection of bone metastases, although a large number of studies in recent years have shown advantages of MRI as well as of hybrid imaging techniques [9, 15, 19, 20].

The results of our study raise the questions, whether a default bone scintigraphy is actually necessary in the primary staging of breast cancer patients when a CT is already performed and whether these two examinations should even remain the first choice considering the preeminent performance of PET/MRI or MRI alone. There have been various studies

indicating that CT is superior to bone scintigraphy in detection of breast cancer metastases [21, 26, 27], and according to the results of a study by Bristow et al [27] comparing CT and bone scintigraphy in 44 patients with bone metastases from breast cancer, the routine bone scan may not be required. One advantage of our study is the relatively large, prospectively enrolled patient cohort undergoing initial staging based on current ESMO guidelines, hence reflecting clinical routine. Our results show that only 4% of patients have bone metastases in the initial breast cancer staging, which further questions the importance of bone scintigraphy in addition to thoraco-abdominal CT, also because breast cancer patients tend to be rather young and radiation dose should be considered. Nevertheless, in a clinical setting, review of both examinations is advisable in any case, especially since CT can facilitate the differentiation of benign and malignant radionuclide accumulations detected on bone scans [26].

Several studies have reported a superiority of whole-body MRI over CT and bone scintigraphy in bone lesions [15, 28], although it is rarely used for initial staging examinations of breast cancer in current clinical routine [16]. A major advantage of MRI is the possibility to directly visualize metastatic tissue in the bone marrow. Consequently, especially osteolytic metastases could be detected earlier than with CT and usually before cortical bone destruction has occurred [29, 30]. Furthermore, the early detection of a solitary bone metastasis might offer the opportunity of a curative approach by application of a local radiation therapy. According to our results, the visualization of osteolytic bone metastases with sole medullary involvement is highly limited both with CT and bone scintigraphy. Depending on the location, osteolytic metastases are detectable by bone scintigraphy only when approximately 50% of the bone marrow is already destroyed [21, 31]. This also has an influence on the therapy decisions. The earlier the metastases are discovered, the better they can be treated. As a result, this might prevent tumor-related osteolysis or fractures and reduce pain or other comorbidities [30]. MRI offers further advantages, such as the lack of ionizing radiation, or the higher soft tissue contrast, which might be beneficial for the detection of non-osseous lesions. In our study, diffusion-weighted MR imaging (DWI) revealed multiple metastases that would otherwise have been missed; hence, it should be considered part of the imaging protocol.

The ability of hybrid imaging to detect bone metastases in different tumor entities has been investigated extensively in recent years. PET/CT has already proven to be advantageous in cancer staging in comparison to CT and bone scintigraphy [20, 32–35].

The comparison of PET/CT and MRI has yielded conflicting results so far [36, 37]. In a study by Jambor et al with 26 high risk breast cancer patients, both modalities are described to be equally suitable for the detection of bone metastases with sensitivities of 93% and 91% [37]. The introduction of fully

integrated PET/MRI in 2011 has enabled simultaneous acquisition of PET and high soft-tissue contrast morphological and functional MRI. In this study, the high sensitivity in detection of bone metastases is primarily caused by the [¹⁸F]FDG PET, but the combination with MRI offers the advantage of a high anatomical resolution and functional imaging. When comparing PET/CT and PET/MRI, available data is inconsistent. While Löfgren et al [38] did not see clear advantages of either one modality in the evaluation of bone metastases, studies of Sawicki et al [35] and Catalano et al [22] postulated a superiority of PET/MRI in recurrent breast cancer attributed to the higher soft tissue contrast and added information from functional imaging such as DWI.

Additionally to the mere detection of lesions, a high diagnostic confidence, allowing for a reliable differentiation between benign and malignant lesion nature, is relevant in daily routine. Although PET/MRI and MRI alone were able to detect all malignant bone lesions, our study emphasizes the level of diagnostic confidence achieved by hybrid imaging based on the ability to visualize pathologically increased glucose metabolism of malignant lesions [39].

This study has limitations. Despite the rather large study population with primary breast cancer, the number of patients with bone metastases was small. Second, in most cases, just one biopsy site has been chosen to histologically secure bone metastasis, since a histological sampling of all detected metastases is usually not required for determining the oncologic treatment concept. Therefore, the reference standard was also based on follow-up examinations using CT and MRI. Third, an adequate determination of a lesion-based specificity was not possible, since not all initially detected benign lesions were followed up with imaging. Fourth, up to 10% of osseous metastases in patients with breast cancer are located in the distal limbs and skull [40]. In this study, only lesions that could be detected by all modalities were included in the analysis. The thoracoabdominal CT had a slightly smaller FOV than the PET/MRI as the arms were raised above the head and were partly outside the FOV, while in PET/MRI the arms were lowered beside the body. So potential areas of metastasis may be excluded in this analysis, because of the limited FOV. Regardless, an additional separate evaluation of the complete FOV of each modality was performed but no additional metastases were found.

In conclusion, both [¹⁸F]FDG PET/MRI and MRI alone have shown to be significantly superior to CT and bone scintigraphy for the detection of bone metastases in patients with newly diagnosed breast cancer in our lesion-based analysis. MRI alone and [¹⁸F]FDG PET/MRI identified equivalent numbers of bone metastases. Considering the relatively low prevalence of bone metastases at initial diagnosis, the high number of patients at a relatively young age undergoing the clinical staging algorithm, and the therapeutic impact of bone metastases, radiation-free whole-body MRI might serve as modality of choice. In contrast, the use of currently

recommended CT and bone scintigraphy for the detection of bone metastases seems questionable.

Funding Open Access funding enabled and organized by Projekt DEAL. The study is funded by Deutsche Forschungsgemeinschaft (DFG), the German Research Foundation (BU3075/2-1). The funding foundation was not involved in trial design, patient recruitment, data collection, analysis, interpretation or presentation, writing or editing of the reports, or the decision to submit for publication. The corresponding author had full access to all data in the study and had all responsibility for the decision to submit for publication. We want to thank Deutsche Forschungsgemeinschaft (DFG) for financially promoting this research project.

Declarations

Guarantor The scientific guarantor of this publication is Nils-Martin Bruckmann, MD.

Conflict of interest The authors of this manuscript declare no relationships with any companies, whose products or services may be related to the subject matter of the article.

Statistics and biometry Institute of Medical Informatics, Biometry and Epidemiology, University Hospital of Essen, Germany; Prof. Andreas Stang, head of the department.

Informed consent Informed consent was obtained from all individual participants included in the study.

Ethical approval All procedures performed were in accordance with the ethical standards of the institutional research committee of the University Duisburg-Essen (study number 17-7396-BO) and Düsseldorf (study number 6040R) and with the principles of the 1964 Declaration of Helsinki and its later amendments.

Methodology

- prospective
- diagnostic or prognostic study
- performed at two institutions

Open Access This article is licensed under a Creative Commons Attribution 4.0 International License, which permits use, sharing, adaptation, distribution and reproduction in any medium or format, as long as you give appropriate credit to the original author(s) and the source, provide a link to the Creative Commons licence, and indicate if changes were made. The images or other third party material in this article are included in the article's Creative Commons licence, unless indicated otherwise in a credit line to the material. If material is not included in the article's Creative Commons licence and your intended use is not permitted by statutory regulation or exceeds the permitted use, you will need to obtain permission directly from the copyright holder. To view a copy of this licence, visit <http://creativecommons.org/licenses/by/4.0/>.

References

1. The Global Cancer Observatory G (2018) Breast cancer. Source: Globocan 2018. World Health Organ 876:2018–2019

2. Wockel A, Festl J, Stuber T et al (2018) Interdisciplinary screening, diagnosis, therapy and follow-up of breast cancer. Guideline of the DGGG and the DKG (S3-level, AWMF registry number 032/045OL, December 2017) - part 2 with recommendations for the therapy of primary, recurrent and advanced breast cancer. *Geburtshilfe Frauenheilkd* 78:1056–1088. <https://doi.org/10.1055/a-0646-4630>
3. Parkes A, Clifton K, Al-Awadhi A et al (2018) Characterization of bone only metastasis patients with respect to tumor subtypes. *NPJ Breast Cancer* 4:2. <https://doi.org/10.1038/s41523-018-0054-x>
4. Coleman RE, Rubens RD (1987) The clinical course of bone metastases from breast cancer. *Br J Cancer* 55:61–66. <https://doi.org/10.1038/bjc.1987.13>
5. Liede A, Jerzak KJ, Hernandez RK, Wade SW, Sun P, Narod SA (2016) The incidence of bone metastasis after early-stage breast cancer in Canada. *Breast Cancer Res Treat* 156:587–595. <https://doi.org/10.1007/s10549-016-3782-3>
6. Brockton NT, Gill SJ, Laborge SL et al (2015) The breast cancer to bone (B2B) metastases research program: a multi-disciplinary investigation of bone metastases from breast cancer. *BMC Cancer* 15:512. <https://doi.org/10.1186/s12885-015-1528-y>
7. Jung SY, Rosenzweig M, Sereika SM, Linkov F, Brufsky A, Weissfeld JL (2012) Factors associated with mortality after breast cancer metastasis. *Cancer Causes Control* 23:103–112. <https://doi.org/10.1007/s10552-011-9859-8>
8. Hortobagyi GN, Theriault RL, Lipton A et al (1998) Long-term prevention of skeletal complications of metastatic breast cancer with pamidronate. *J Clin Oncol* 16:2038–2044. <https://doi.org/10.1200/JCO.1998.16.6.2038>
9. Liu T, Cheng T, Xu W, Yan W-L, Liu J, Yang H-L (2011) A meta-analysis of 18FDG-PET, MRI and bone scintigraphy for diagnosis of bone metastases in patients with breast cancer. *Skeletal Radiol* 40:523–531. <https://doi.org/10.1007/s00256-010-0963-8>
10. Rossi L, Longhitano C, Kola F, Del Grande M (2020) State of art and advances on the treatment of bone metastases from breast cancer: a concise review. *Chin Clin Oncol* 9:18. <https://doi.org/10.21037/cco.2020.01.07>
11. Senkus E, Kyriakides S, Ohno S et al (2015) Primary breast cancer: ESMO clinical practice guidelines for diagnosis, treatment and follow-up. *Ann Oncol* 26(Suppl 5):v8–v30. <https://doi.org/10.1093/annonc/mdv298>
12. Cardoso F, Senkus E, Costa A et al (2018) 4th ESO-ESMO International Consensus Guidelines for Advanced Breast Cancer (ABC 4)dagger. *Ann Oncol* 29:1634–1657. <https://doi.org/10.1093/annonc/mdy192>
13. Gradishar WJ, Anderson BO, Balassanian R et al (2018) Breast cancer, version 4.2017, NCCN clinical practice guidelines in oncology. *J Natl Compr Canc Netw* 16:310–320. <https://doi.org/10.6004/jnccn.2018.0012>
14. Cardoso F, Paluch-Shimon S, Senkus E et al (2020) 5th ESO-ESMO international consensus guidelines for advanced breast cancer (ABC 5). *Ann Oncol* 31:1623–1649. <https://doi.org/10.1016/j.annonc.2020.09.010>
15. Ohlmann-Knafo S, Pickuth D, Kirschbaum M, Fenzl G (2009) Diagnostic value of whole-body MRI and bone scintigraphy in the detection of osseous metastases in patients with breast cancer - a prospective double-blinded study at two hospital centers. *RoFo* 181:255–263. <https://doi.org/10.1055/s-0028-1109104>
16. Hausmann D, Kern C, Schröder M et al (2011) Whole-body MRI in preoperative diagnostics of breast cancer-a comparison with [corrected] staging methods according to the S 3 guidelines. *RoFo* 183:1130–1137
17. Hildebrandt MG, Gerke O, Baun C et al (2016) [18F] fluorodeoxyglucose (FDG)-positron emission tomography (PET)/computed tomography (CT) in suspected recurrent breast cancer: a prospective comparative study of dual-time-point FDG-PET/CT, contrast-enhanced CT, and bone scintigraphy. *J Clin Oncol* 34:1889–1897. <https://doi.org/10.1200/JCO.2015.63.5185>
18. Bitencourt AGV, Andrade WP, da Cunha RR et al (2017) Detection of distant metastases in patients with locally advanced breast cancer: role of 18F-fluorodeoxyglucose positron emission tomography/computed tomography and conventional imaging with computed tomography scans. *Radiol Bras* 50:211–215. <https://doi.org/10.1590/0100-3984.2015-0232>
19. Park S, Yoon J-K, Lee SJ, Kang SY, Yim H, An Y-S (2017) Prognostic utility of FDG PET/CT and bone scintigraphy in breast cancer patients with bone-only metastasis. *Medicine (United States)* 96:e8985. <https://doi.org/10.1097/MD.0000000000000895>
20. Hahn S, Heusner T, Kümmel S et al (2011) Comparison of FDG-PET/CT and bone scintigraphy for detection of bone metastases in breast cancer. *Acta Radiol* 52:1009–1014. <https://doi.org/10.1258/ar.2011.100507>
21. Heindel W, Gübitz R, Vieth V et al (2014) The diagnostic imaging of bone metastases. *Dtsch Arztebl Int* 111:741–747. <https://doi.org/10.3238/arztebl.2014.0741>
22. Catalano OA, Nicolai E, Rosen BR et al (2015) Comparison of CE-FDG-PET/CT with CE-FDG-PET/MR in the evaluation of osseous metastases in breast cancer patients. *Br J Cancer* 112:1452–1460. <https://doi.org/10.1038/bjc.2015.112>
23. Sonni I, Minamimoto R, Baratto L et al (2020) Simultaneous PET/MRI in the evaluation of breast and prostate cancer using combined $[^{18}\text{F}]$ F and $[^{18}\text{F}]$ FDG: a focus on skeletal lesions. *Mol Imaging Biol* 22:397–406. <https://doi.org/10.1007/s11307-019-01392-9>
24. Blumhagen JO, Ladebeck R, Fenchel M, Scheffler K (2013) MR-based field-of-view extension in MR/PET: B0 homogenization using gradient enhancement (HUGE). *Magn Reson Med* 70:1047–1057. <https://doi.org/10.1002/mrm.24555>
25. Genders TSS, Spronk S, Stijnen T, Steyerberg EW, Lesaffre E, Hunink MGM (2012) Methods for calculating sensitivity and specificity of clustered data: a tutorial. *Radiology* 265:910–916. <https://doi.org/10.1148/radiol.12120509>
26. Muindi J, Coombes RC, Powles GSTJ, Khan O, Husband J (1983) The role of computed tomography in the detection of bone metastases in breast cancer patients. *Br J Radiol* 56:233–236. <https://doi.org/10.1259/0007-1285-56-664-233>
27. Bristow AR, Agrawal A, Evans AJ et al (2008) Can computerised tomography replace bone scintigraphy in detecting bone metastases from breast cancer? A prospective study. *Breast* 17:98–103. <https://doi.org/10.1016/j.breast.2007.07.042>
28. Engelhard K, Hollenbach HP, Wohlfart K et al (2004) Comparison of whole-body MRI with automatic moving table technique and bone scintigraphy for screening for bone metastases in patients with breast cancer. *Eur Radiol* 14:99–105. <https://doi.org/10.1007/s00330-003-1968-7>
29. Avrahami E, Tadmor R, Dally O, Hadar H (1989) Early MR demonstration of spinal metastases in patients with normal radiographs and CT and radionuclide bone scans. *J Comput Assist Tomogr* 13:598–602. <https://doi.org/10.1097/00004728-198907000-00008>
30. Steinborn M, Tiling R, Heuck A et al (2000) Diagnosis of bone marrow metastases with MRI. *Diagnostik der Metastasierung im knochenmark mittels MRT*. *Radiologe* 40:826–834. <https://doi.org/10.1007/s001170050830>
31. Rybak LD, Rosenthal DI (2001) Radiological imaging for the diagnosis of bone metastases. *Q J Nucl Med* 45:53–64
32. Hildebrandt M, Falch K, Baun C et al (2015) Imaging of bone metastases in suspected recurrent breast cancer. *J Nucl Med* 56:560
33. Mavriopoulou E, Zampakis P, Smilirli E et al (2018) Whole body bone SPET/CT can successfully replace the conventional bone scan in breast cancer patients. A prospective study of 257 patients. *Hell J Nucl Med* 21:125–133
34. Morris PG, Lynch C, Feeney JN et al (2010) Integrated positron emission tomography/computed tomography may render bone

- scintigraphy unnecessary to investigate suspected metastatic breast cancer. *J Clin Oncol* 28:3154–3159. <https://doi.org/10.1200/JCO.2009.27.5743>
35. Sawicki LM, Grueneisen J, Schaarschmidt BM et al (2016) Evaluation of ¹⁸F-FDG PET/MRI, ¹⁸F-FDG PET/CT, MRI, and CT in whole-body staging of recurrent breast cancer. *Eur J Radiol* 85:459–465. <https://doi.org/10.1016/j.ejrad.2015.12.010>
 36. Heusner T, Göltz P, Hamami M et al (2011) “One-stop-shop” staging: should we prefer FDG-PET/CT or MRI for the detection of bone metastases? *Eur J Radiol* 78:430–435. <https://doi.org/10.1016/j.ejrad.2009.10.031>
 37. Jambor I, Kuksma A, Ramadan S et al (2016) Prospective evaluation of planar bone scintigraphy, SPECT, SPECT/CT, ¹⁸F-NaF PET/CT and whole body 1.5T MRI, including DWI, for the detection of bone metastases in high risk breast and prostate cancer patients: SKELETA clinical trial. *Acta Oncol (Madr)* 55:59–67. <https://doi.org/10.3109/0284186X.2015.1027411>
 38. Löfgren J, Mortensen J, Rasmussen SH et al (2017) A prospective study comparing ^{99m}Tc-hydroxyethylene-diphosphonate planar bone scintigraphy and whole-body SPECT/CT with ¹⁸F-fluoride PET/CT and ¹⁸F-fluoride PET/MRI for diagnosing bone metastases. *J Nucl Med* 58:1778–1785. <https://doi.org/10.2967/jnumed.116.189183>
 39. Sawicki LM, Kirchner J, Umutlu L et al (2017) Comparison of ¹⁸F-FDG PET/MRI and MRI alone for whole-body staging and potential impact on therapeutic management of women with suspected recurrent pelvic cancer: a follow-up study. *Eur J Nucl Med Mol Imaging* 45:622–629. <https://doi.org/10.1007/s00259-017-3881-3>
 40. Kakhki VRD, Anvari K, Sadeghi R et al (2013) Pattern and distribution of bone metastases in common malignant tumors. *Nucl Med Rev* 16:66–69. <https://doi.org/10.5603/NMR.2013.0037>

Publisher's note Springer Nature remains neutral with regard to jurisdictional claims in published maps and institutional affiliations.

ORIGINAL RESEARCH

Open Access



Free-breathing 3D Stack of Stars GRE (StarVIBE) sequence for detecting pulmonary nodules in ¹⁸F-FDG PET/MRI

Nils Martin Bruckmann¹, Julian Kirchner^{1*} , Janna Morawitz¹, Lale Umutlu², Wolfgang P. Fendler³, Ken Herrmann³, Ann-Kathrin Bittner⁴, Oliver Hoffmann⁴, Tanja Fehm⁵, Maike E. Lindemann⁶, Christian Buchbender¹, Gerald Antoch¹ and Lino M. Sawicki¹

*Correspondence:
Julian.Kirchner@med.uni-duesseldorf.de
¹ Department of Diagnostic and Interventional Radiology, Medical Faculty, University Dusseldorf, Moorenstrasse 5, 40225 Düsseldorf, Germany
Full list of author information is available at the end of the article

Abstract

Background: The free-breathing T1-weighted 3D Stack of Stars GRE (StarVIBE) MR sequence potentially reduces artifacts in chest MRI. The purpose of this study was to evaluate StarVIBE for the detection of pulmonary nodules in ¹⁸F-FDG PET/MRI.

Material and methods: In this retrospective analysis, conducted on a prospective clinical trial cohort, 88 consecutive women with newly diagnosed breast cancer underwent both contrast-enhanced whole-body ¹⁸F-FDG PET/MRI and computed tomography (CT). Patients' chests were examined on CT as well as on StarVIBE and conventional T1-weighted VIBE and T2-weighted HASTE MR sequences, with CT serving as the reference standard. Presence, size, and location of all detectable lung nodules were assessed. Wilcoxon test was applied to compare nodule features and Pearson's, and Spearman's correlation coefficients were calculated.

Results: Out of 65 lung nodules detected in 36 patients with CT (3.7 ± 1.4 mm), StarVIBE was able to detect 31 (47.7%), VIBE 26 (40%) and HASTE 11 (16.8%), respectively. Overall, CT showed a significantly higher detectability than all MRI sequences combined (65 vs. 36, difference 44.6%, $p < 0.001$). The VIBE showed a significantly better detection rate than the HASTE (23.1%, $p = 0.001$). Detection rates between StarVIBE and VIBE did not significantly differ (7.7%, $p = 0.27$), but the StarVIBE showed a significant advantage detecting centrally located pulmonary nodules (66.7% vs. 16.7%, $p = 0.031$). There was a strong correlation in nodule size between CT and MRI sequences (HASTE: $p = 0.80$, $p = 0.003$; VIBE: $p = 0.77$, $p < 0.001$; StarVIBE: $p = 0.78$, $p < 0.001$). Mean image quality was rated as good to excellent for CT and MRI sequences.

Conclusion: The overall lung nodule detection rate of StarVIBE was slightly, but not significantly, higher than conventional T1w VIBE and significantly higher than T2w HASTE. Detectability of centrally located nodules is better with StarVIBE than with VIBE. Nevertheless, all MRI analyses demonstrated considerably lower detection rates for small lung nodules, when compared to CT.

Keywords: Lung nodule detection, PET/MRI, Breast cancer, Computed tomography

Background

Magnetic resonance imaging (MRI) has made tremendous progress over the last decades, driven by new developments in sequence technique, reducing the overall examination time and improving image quality.

In oncological imaging, whole-body MRI (WB-MRI) has gained growing importance as a method for cancer staging and follow-up and is nowadays recommended in international guidelines of various tumor entities (e.g. multiple myeloma, prostate cancer, breast cancer) [1–3]. As MRI is a radiation-free imaging method, it is a valuable alternative to computed tomography (CT), especially in younger patients. One major limitation is its susceptibility to respiratory and cardiac motion resulting in a markedly reduced assessability of the lung parenchyma and limited detectability of potentially metastatic lung nodules compared with chest CT. Performing conventional MR imaging under breath-holding conditions is currently the common way to ensure a good image quality [4]. A strict immobility and compliance to breathing instructions is therefore required, which can sometimes be difficult in everyday clinical routine, especially when scanning children or multi-morbid older patients. The application of navigated schemes has been proposed, but is also prone to failure and leads to an extension of examination time [5]. Additionally, the use of fast MR sequences is required, which are associated with a loss of spatial image resolution [6].

The high susceptibility of conventional MR images to motion results from the line-by-line acquisition (Cartesian sampling) of the data space (*k*-space). Even small movements during the examination create disturbances in the phase encoding scheme and yield to phase offsets to the direction of the motion causing inconsistent phases in the *k*-space. This results in artifacts in the phase encoding direction [7, 8] in conventional MR sequences like T2-weighted HASTE (Half Fourier Acquisition Single shot Turbo spin Echo) and T1-weighted fat saturated post-contrast VIBE (Volume Interpolated Breath-Hold Examination) sequence, which are the most common sequences for lung nodule detection in MRI. These sequences are used for thoracic imaging, since they are fast and can be acquired slice-by-slice between breaths. The speed results from an incomplete filling or scanning of the *k*-space, which makes these sequences very susceptible for motion artifacts [9]. A possible solution to reduce the influence of motion is to change the way of *k*-space acquisition. A more recent example is the free-breathing radially acquired Stack of Stars T1-weighted gradient-echo (GRE) 3D VIBE sequence (StarVIBE) [6, 10]. In the StarVIBE sequence, data are acquired along individual radial spokes (Fig. 5). Due to the overlapping of the spokes in the center, phase errors can be reduced by averaging low frequency components. This overlap has a motion-averaging effect and consequently, images can be acquired during free-breathing, which not only reduces artifacts but also offers the advantage of a higher spatial resolution, since acquisition time is not limited to the duration of a breath hold [9].

The reduced influence of motion in chest MRI is particularly interesting in the assessment of lung cancer and pulmonary metastases, because MRI still has major disadvantages compared to CT for the reasons mentioned above. Whether this technology offers advantages in lung nodule detection compared to conventional MRI sequences has, to the best of our knowledge, not yet been investigated.

Thus, the purpose of our study was to compare the diagnostic potential of the StarVIBE sequence to the conventional T1-weighted fat saturated post-contrast VIBE sequence, the T2-weighted fat-suppressed HASTE sequence and to the reference standard CT for detection of pulmonary nodules in contrast-enhanced whole-body ^{18}F -FDG PET/MRI.

Material and methods

Patients and inclusion criteria

The institutional review boards of the University Duisburg-Essen, Germany (study number 17–7396-BO) and Düsseldorf, Germany (study number 6040R) approved this study and it was performed in conformance with the Declaration of Helsinki [11]. After written informed consent was provided, a total of 88 women (mean age 52.5 ± 11.5 years, age range 28–82 years) with newly diagnosed therapy-naïve breast cancer were prospectively enrolled in this study between April 2019 and April 2020. For cancer staging, all patients underwent a whole-body ^{18}F -FDG PET/MRI as well as chest, abdomen and bone imaging recommended by current breast cancer guidelines, including thoraco-abdominal computed tomography, with a maximum of two weeks apart.

In accordance with the latest 2018 European Society For Medical Oncology (ESMO) guidelines for breast cancer [12], the following inclusion criteria had to be fulfilled to be eligible for whole-body staging: (1) newly diagnosed, treatment-naïve T2-tumor or higher T-stage or (2) newly diagnosed, treatment-naïve triple-negative tumor of every size or (3) newly diagnosed, treatment-naïve tumor with molecular high risk (T1c, Ki67 > 14%, HER2-new over-expression, G3). Exclusion criteria were age < 18 years, medical contraindications to MRI or CT or contrast agents as well as former malignancies in the last 5 years, pregnancy, or breast-feeding.

PET/MRI examination

All patients were instructed to fast for at least 6 h before the examination, and blood glucose levels were verified to be below 150 mg/dl. All patients underwent contrast-enhanced (Dotarem, Guerbet GmbH) ^{18}F -FDG PET/MRI on an integrated 3.0-Tesla PET/MR system (Biograph mMR, Siemens Healthcare GmbH, Erlangen, Germany) with a mean delay of 76.6 ± 17.3 min after intravenous injection of a body weight adapted dosage of ^{18}F -FDG (4 MBq/kg body-weight, mean activity: 240.9 ± 38.7 MBq). The scan volume covered head to the mid-thigh in supine position.

PET images were generated in four to five bed positions with a median of 3 min per bed position. PET data reconstruction was performed using an iterative 3D ordinary Poisson ordered-subset expectation maximization algorithm (3D OP-OSEM), 3 iterations and 21 subsets, a Gaussian filter with 4 mm Full Width at Half Maximum (FWHM) and a matrix dimension of $344 \times 344 \times 127$ with an axial field of view (FOV) of 25.8 cm and a reconstructed image resolution of $2.09 \times 2.09 \times 2.03$ mm.

For MR-based tissue attenuation correction (AC) and scatter correction the *syngo* MR E11P platform was used. A transaxial acquired high-resolution CAIPIRINHA (Controlled aliasing in parallel imaging results in higher spatial acceleration) T1-weighted three-dimensional (3D) Dixon-VIBE sequence was acquired, providing two sets of images (in- and opposed phase fat and water images) to generate a four-compartment

(background air, lungs, fat, soft tissue) attenuation correction map (μ map) in coronal orientation. A bone atlas and truncation correction as proposed by Blumhagen et al. [13] were additionally applied [14–16]. MRI data were acquired simultaneously using a 16-channel head-and-neck radiofrequency (RF) coil, a 24-channel spine array RF coil, and 5 or 6-channel flex body coils, depending on patients' height. Thoracic bed position was acquired with an acquisition time ranged from 6 to 8 min and with expiratory breath-hold, except for the duration of the 3D Stack of Stars GRE (StarVIBE) sequence, which was generated under free-breathing. Table 1 shows the scan parameters of the thoracic sequences.

Computed tomography

In addition to the ^{18}F -FDG PET/MRI all 88 patients underwent a thoraco-abdominal multi-slice contrast-enhanced (Ultravist 300TM, Bayer Schering Pharma AG, Berlin, Germany) CT examination from skull base to the mid-thigh (Definition Edge or Definition Flash, Siemens Healthcare GmbH, Erlangen, Germany). The mean time between PET/MRI and CT scans were 3.1 ± 3.6 days (range 1–14 days). An automatic tube current modulation and automatic tube voltage selection was applied (CareDose 4D and CareKV, Siemens Healthcare GmbH, Erlangen). All scans were acquired in portal venous phase after intravenous application of a body-weight adapted dosage of non-ionic contrast agent. Thoracic images were reconstructed in lung window setting, using a sharp kernel (B70s) and a slice thickness of 2 mm.

Image interpretation

The imaging datasets of CT (chest CT) and ^{18}F -FDG PET/MRI (HASTE, VIBE, StarVIBE sequence and PET alone) were analyzed on a dedicated OsiriX workstation (Pixmeo, SARL, Bernex, Switzerland) and evaluated by 4 readers, two board-certified radiologists with 7 and 8 years of experience in hybrid imaging and two residents with 3 and 4 years of experience in hybrid imaging since graduating from medical school. CT and MRI datasets were assessed in random order and in separate sessions with at least two weeks apart to avoid recognition bias. Both readers were informed regarding the primary diagnosis of the patients but remained blinded to results of prior and follow-up imaging and to the patients' history.

The quality of all thoracic imaging datasets was evaluated on a four-point Likert-scale (1=very poor image quality: major artifacts; 2=poor image quality: moderate artifacts; 3=good image quality: minor artifacts; 4=excellent image quality: no artifacts) and the

Table 1 Scan parameters of the considered thoracic MRI sequences

Sequence	Orientation	Contrast agent	TA (s)	TE/TR (ms)	Slice thickness (mm)	Matrix size	FOV (mm ²)
T2w HASTE	Axial	No	66	99/1.500	7.0	320 × 240	430 × 322
T1w fs VIBE	Axial	Yes	18	1.5/3.6	3	512 × 250	430 × 349
StarVIBE	Axial	Yes	220	1.5/3.2	1.1	520 × 204	360 × 360

T2w HASTE, T2-weighted half Fourier acquisition single shot turbo spin echo; T1w fs VIBE, T1-weighted fat-suppressed volume-interpolated breath-hold examination; StarVIBE, free-breathing 3D Stack of Stars GRE VIBE; TA, acquisition time; TR, repetition time; TE, echo time; FOV, field of view

presence and type of artifacts was documented. Lungs were systematically assessed in the same order, starting from the right upper lobe and continuing to the left lower lobe. Lung nodule number and location was noted, dividing the lungs into 4 quadrants (right upper, right lower, left upper, left lower) and subdividing lung sections into the regions pleural (lesions adjacent to the pleura), subpleural (within 1 cm of the pleura but not adjacent to it), and central (remaining lung tissue). Nodule size was measured (long-axis, short-axis and mean diameter) in millimeters. Furthermore, nodule contrast (1=very low contrast; 2=low contrast; 3=moderate contrast; 4=high contrast), nodule density (1=solid; 2=part-solid; 3=pure ground glass) and nodule shape (1=round; 2=oval; 3=ellipsoidal; 4=lobular; 5=notched; 6=irregular) were documented. PET data in fused PET/MRI were evaluated noting presence of focal tracer uptake above background level (normal lung tissue), and for quantitative assessment SUVmax was measured by placing a polygonal volume of interest over each nodule.

Statistical analysis

SPSS 24 (IBM, Armonk, NY, USA) was used for statistical analysis and all data are presented as mean \pm standard deviation and median \pm IQR. A *p* value < 0.05 was considered to indicate statistical significance. The Wilcoxon test was used to assess differences in nodule size, contrast, and image quality. For correlation analysis of nodule size, the Pearson's correlation coefficient was applied. Because contrast is a categorical variable, the Spearman's correlation coefficient was preferred.

Results

Nodule detection

According to the reference standard CT, there were 65 lung nodules in 36 of the 88 (40.9%) patients with a mean size of 3.7 ± 1.4 mm (range 2–8 mm, lung nodules per patient: 1–5, mean number 1.8 ± 1.6). In the remaining 52 (59.1%) patients, no lung nodules were present. Table 2 shows the distribution of lung nodules per patient. The HASTE sequence was able to detect 11 of 65 nodules (16.9%; 95% CI 8.8–28.3, mean size 4.1 ± 0.8 mm), while the post-contrast VIBE and the StarVIBE sequence detected 26 and 31 lung nodules (mean size 4.3 ± 1.4 mm and 3.9 ± 1.5 mm), respectively, resulting in detection rates of 40% (CI 28.0–52.9) and 47.7% (CI: 35.1–60.5) (Fig. 1). Detection rates between VIBE and StarVIBE did not differ significantly (difference 7.7%,

Table 2 Overview over the distribution of lung nodules among the patient collective

Number of patients	88
Patients with lung nodules	36
Patients without lung nodules	52
Lung nodules in total	65
Number of lung nodules per patient	
1	19
2	9
3	5
4	2
5	1

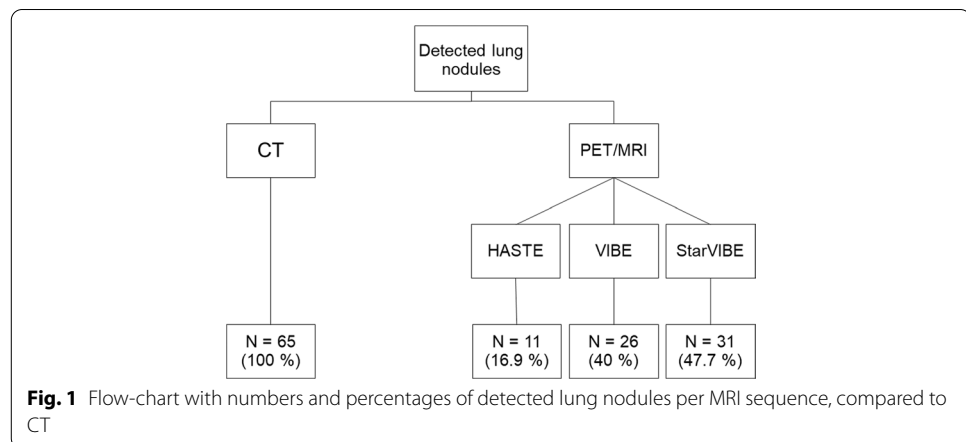


Table 3 Comparison of the performance of CT with the individual MRI sequences and combined MRI for lung nodule detection

	Detected nodules	Relative difference (%)	95% confidence interval	p value
CT vs. HASTE	65 vs. 11	83.1	0.71 to 0.9	<0.001
CT vs. VIBE	65 vs. 26	60	0.46 to 0.71	<0.001
CT vs. StarVIBE	65 vs. 31	52.3	0.39 to 0.64	<0.001
HASTE vs. VIBE	11 vs. 26	23.1	0.08 to 0.37	0.001
HASTE vs. StarVIBE	11 vs. 31	30.8	0.15 to 0.45	<0.001
VIBE vs. StarVIBE	26 vs. 31	7.7	-0.09 to 0.25	0.27
CT vs. MRI (combined)	65 vs. 36	44.6	0.31 to 0.57	<0.001

The StarVIBE sequence was able to increase the overall lung nodule detection of MRI, but CT still showed a significantly better performance

95% CI – 0.09 to 0.25, $p=0.27$). There were no false positive results on MRI. Further results concerning detection rates between CT and the individual MRI sequences can be found in Table 3. The number of lung nodules was correctly identified by HASTE in 3 of 36 patients (8.3%), by VIBE in 10 of 36 patients (27.8%) and by the StarVIBE in 13 of 36 patients (36.1%). Compared to the VIBE, StarVIBE missed 4 subpleural nodules in 2 patients (mean size in CT 4.5 ± 0.58 mm), but detected additional 9 (3 subpleural, 6 central) primarily small nodules in 6 patients (mean size in CT 3.2 ± 0.97 mm) (Fig. 2). The HASTE sequence was able to detect one nodule that was not detected with VIBE or StarVIBE. This nodule was a calcified granuloma on CT. None of the morphologically visible and not-visible nodules showed an ^{18}F -FDG uptake above the surrounding background level (mean SUVmax of all nodule detected with MRI sequences: 0.9 ± 0.5).

Comparison of nodule size and nodule contrast

The mean size of all lung nodules detected by CT was 3.7 ± 1.4 mm (range 2–8 mm, median 4.0 ± 1.5), compared to 4.1 ± 0.8 mm (range 2–5 mm, median 4.0 ± 1.0) by HASTE, 4.3 ± 1.4 mm (range 2–8 mm, median 4.0 ± 1.5) by VIBE, and 3.9 ± 1.5 mm (range 2–7 mm, median 4.0 ± 1.0) by StarVIBE. Analysis of size of corresponding nodule did not significantly differ between CT and MRI and between the MR sequences. Lung

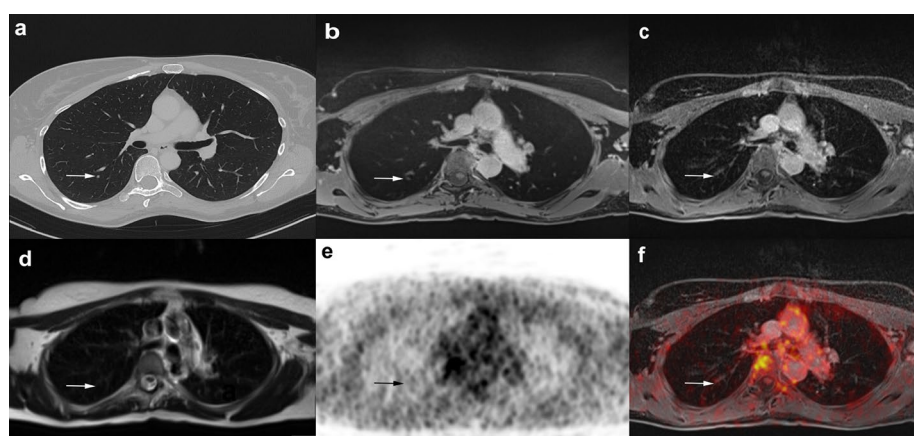


Fig. 2 A 49-year-old female patient with histologically proven breast cancer. Four-millimeter centrally located lung nodule in the right lower lobe, which is clearly visible with CT (a) and the StarVIBE sequence (b). Caused by motion artifacts and lower resolution, the lung nodule was missed with the VIBE (c) and HASTE (d) sequence. No focal ^{18}F -FDG uptake was seen on PET and fused ^{18}F -FDG PET/MRI images (e, f)

Table 4 Distribution of detected and missed nodules according to their location in the lung for each sequence

	CT	HASTE		VIBE		StarVIBE	
	Detected	Detected	Missed	Detected	Missed	Detected	Missed
Adjacent to pleura	7	2 (29.6%)	5 (71.4%)	6 (85.7%)	1 (14.3%)	6 (85.7%)	1 (14.3%)
Subpleural	46	8 (17.4%)	38 (82.6%)	18 (39.1%)	28 (60.9%)	17 (37.0%)	29 (63.0%)
Central	12	1 (8.3%)	11 (91.7%)	2 (16.7%)	10 (83.3%)	8 (66.7%)	4 (33.3%)

nodules missed by MRI were rather small, averaging 3.2 ± 1.3 mm on VIBE, 3.4 ± 1.4 mm on StarVIBE, and 3.6 ± 1.4 mm on HASTE, respectively (Fig. 2). A strong correlation in nodule size between CT and HASTE ($r=0.80, p=0.003$), VIBE ($r=0.77, p<0.001$), and StarVIBE ($r=0.78, p<0.001$) as well as between StarVIBE and VIBE ($r=0.94, p<0.001$) and StarVIBE and HASTE ($r=0.81, p<0.02$) could be observed. Nodule contrast differed significantly between CT and MRI in corresponding nodules, rated as moderate in CT with a mean of 2.91 ± 0.79 (median 3.0 ± 1.0), poor in StarVIBE (mean 2.07 ± 0.98 , median $2.0 \pm 2.0, p=0.001$) and VIBE (mean 2.00 ± 0.75 , median $2.0 \pm 0.25, p<0.001$), and very poor in the HASTE sequence (mean 1.45 ± 0.52 , median $1.0 \pm 1.0, p=0.004$). There was no statistically significant correlation between CT and MRI in nodule contrast (HASTE: $\rho=0.15, p=0.67$; VIBE: $\rho=0.17, p=0.42$; StarVIBE: $\rho=0.18, p=0.34$).

Localization

Forty-two of the 65 (64.6%) detected lung nodules were located in the lower parts of the lungs and 23 (36.4%) in the upper parts. Seven lung nodules were located adjacent to the pleura, while 46 were positioned subpleurally and 12 centrally in the lungs. The local distribution of missed lung nodules showed significant differences between VIBE and StarVIBE particularly in the detection of centrally located nodules (Table 4, 16.7% vs 66.7%, difference 50.0%, 95% CI 10.8–75.4, $p=0.031$) (Figs. 2, 3).

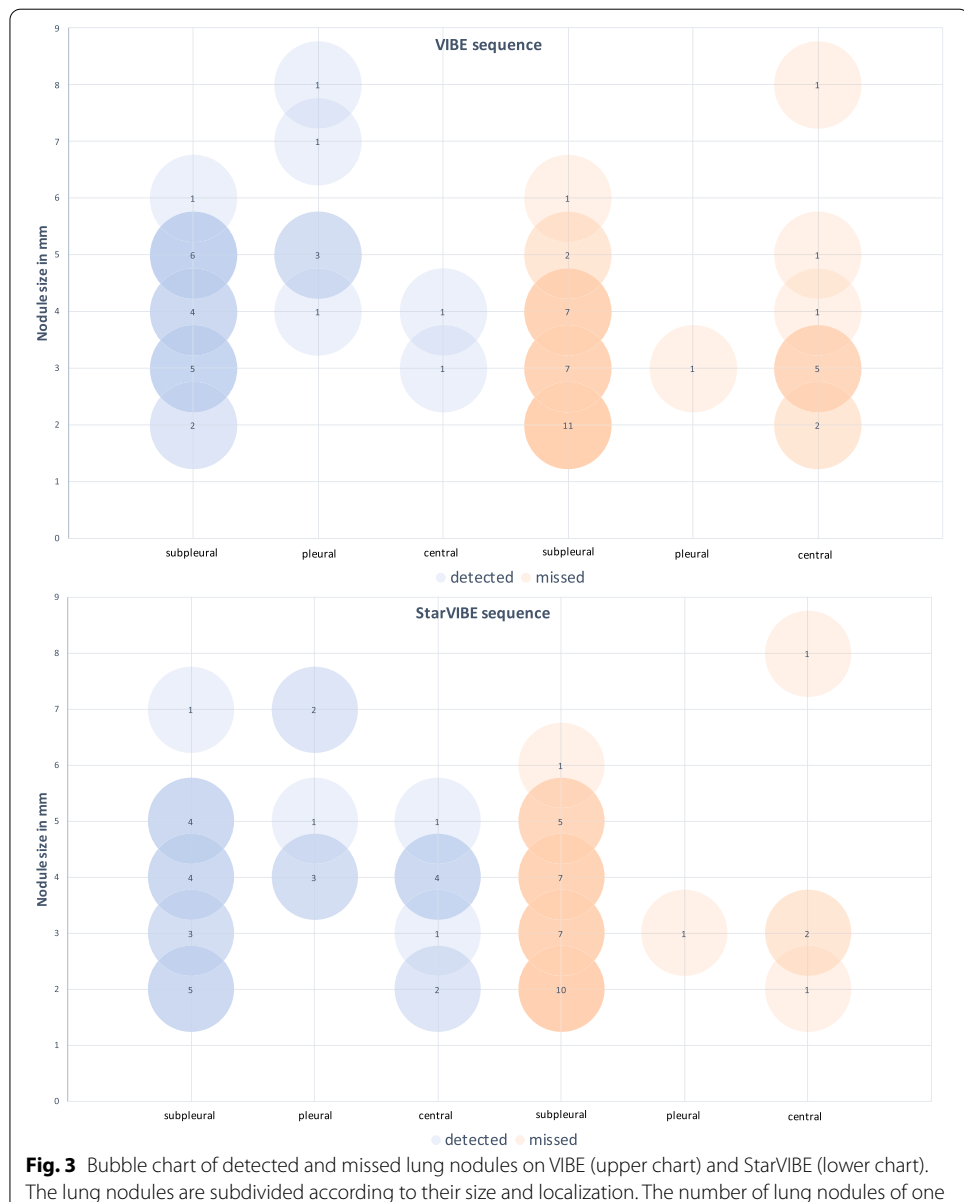


Image quality

The mean image quality was rated as good to excellent for both CT and all MRI sequences. Nevertheless, the statistical analysis yielded differences between CT (mean 3.99 ± 0.09 , median 4.0 ± 0.0) and MRI (HASTE: mean 3.91 ± 0.29 , median 4.0 ± 0.0 , $p < 0.001$; VIBE: mean 3.60 ± 0.68 , median 4.0 ± 1.0 , $p < 0.01$; StarVIBE: mean 3.91 ± 0.35 , median 4.0 ± 0.0 , $p < 0.001$). The difference between VIBE and StarVIBE also yielded a statistical significance with a better performance of the StarVIBE sequence ($p < 0.01$). Almost no artifacts were documented in CT imaging, while in 30 of 88 patients (34.0%) artifacts were documented in VIBE images, especially due to respiratory and cardiac

Table 5 Number of documented artifacts in CT and the individual MRI sequences

	CT	HASTE	VIBE	StarVIBE
Respiratory/cardiac motion	2	12	23	
Aliasing		2	7	
Ghosting			3	
Streak artifacts				14

The VIBE sequence in particular proved to be susceptible to breathing and heart motion artifacts, while the StarVIBE was only influenced by streak artifacts, which had only a minor impact on the image quality. CT was only hardly influenced by artifacts

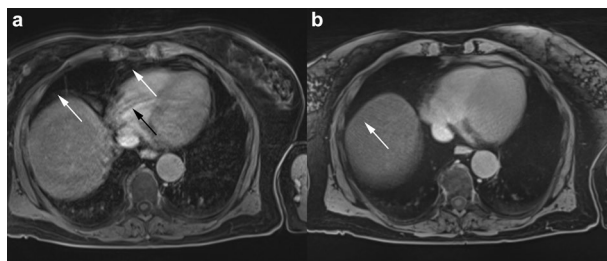


Fig. 4 Comparison of VIBE (a) and StarVIBE (b) sequence in a 70-year-old female patient with histologically proven breast cancer. Lower lung section with parts of the diaphragm and heart. Limited image quality of the VIBE sequence due to respiratory artifacts, heart motion (a white arrows) and ghosting (a black arrow). In the StarVIBE sequence minimal streak artifacts are visible (b white arrow), which have only a mild effect on image quality

motion and less also aliasing and ghosting. The StarVibe images were only affected by streak artifacts (14/88, 15.9%), which hardly influenced the assessability of lung nodules (Table 5, Fig. 4).

Discussion

In this study, we investigated the potential of the free-breathing Stack of Stars GRE StarVIBE sequence for the detection of lung nodules in breast cancer patients and compared it with the performance of CT and other common MRI sequences using ¹⁸F-FDG PET/MRI. Accurate and reliable detection of lung nodules is an important aspect of image-based cancer staging, since the identification of a metastatic spread has a considerable influence on treatment and ultimately on patient's survival, regardless of the cancer entity [17–19]. CT is still the gold standard, because of its clear superiority in the detection of even very small pulmonary nodules [20, 21]. While MRI has been shown to be equivalent for the detection of nodules > 10 mm, the capability of detecting smaller lung nodules is limited [22–24]. Even though most small nodules < 10 mm in oncologic patients are known to be benign (i.e. post-infectious, indurative etc.), about 20% of those lung nodules represent early metastases, with a high chance to be missed by chest MRI, even when using state-of-the-art T1-weighted breath hold GRE, pulse sequences or Propeller/Blade sequences (Periodically Rotated Overlapping Parallel Lines with Enhanced Reconstruction) [23, 25, 26]. Main reasons are a low tissue density in the lungs, rapid signal loss at the transition from lung to soft tissue, and artifacts caused by cardiac and respiratory motion [7]. Currently, T1-weighted gradient echo or pulse

sequences such as VIBE with a short echo time offer a reasonable result and are therefore recommended for MR-based lung nodule detection [27–29]. However, more sensitive MRI sequences have to be developed to increase the acceptance of MRI as a valuable thoracic staging examination [27].

One way to improve the detection of lung nodules by MRI is to change the way of k-space acquisition. In radial sampling, the k-space data are acquired along radial spokes. This was already used in the past for example in the Propeller/Blade sequences. The basic idea here is to use a set of radially directed strips or "blades", which are rotating around the k-space center. Each blade is composed of multiple parallel phase-encoded lines that can be collected using fast spin echo or gradient echo methods.

3D Stack of Stars approach represents the actual radial sampling, means applying the recently developed motion robust free-breathing radial T1-weighted gradient-echo 3D VIBE sequence for the acquisition of the in-plane dimension ($k_x - k_y$) along individual radial lines without rotation, while in slice direction the conventional sampling is applied, resulting in a cylindrical coverage [7, 9, 30] (Fig. 5). This allows a further reduction of motion artifacts even with free breathing and a consistent high spatial resolution. Consequently, the reduction of motion-related artifacts may improve the assessment of motion-prone organs, especially the lung.

Most studies dealing with this topic differentiate between sensitivity rates for MRI concerning nodules less or more than 10 mm in size. For nodules greater than 10 mm, various studies have shown that MRI sequences have a similar detection rate to CT and, as a combined PET/MRI examination, can also provide information on nodule dignity [23, 24, 27, 30–32]. In concordance with the results of prior studies for smaller lung nodules [20, 21, 27, 30, 32], CT outperformed the currently used MRI sequences in our study, which offered detection rates of 40% (VIBE) and 16.9% (HASTE). The StarVIBE sequence was even able to detect 47.7%, but also remained clearly inferior to CT. In a study by Sawicki et al. [27], comparing lung nodule detection of ^{18}F -FDG PET/MRI and ^{18}F -FDG PET/CT in 121 oncologic patients, nodules smaller than 5 mm were found with

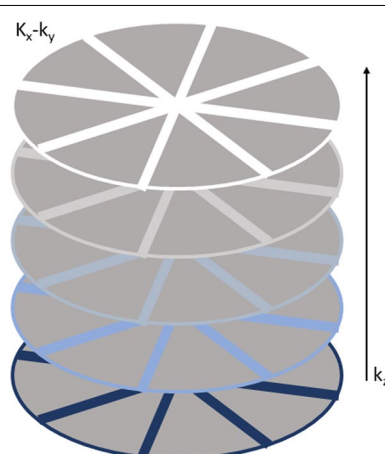


Fig. 5 "Stack of Stars" approach. Acquisition of the in-plane dimension ($k_x - k_y$) along radial spokes, while in slice direction (k_z) the conventional Cartesian sampling is applied, resulting in a cylindrical coverage. Inspired by [9]

the VIBE sequence in 43.1%. Furthermore, Rauscher et al. [32] described significantly lower detection rates for nodules < 10 mm when comparing PET/CT and PET/MRI in the detection of 40 lung nodules with a detection rate of 45.5% for the VIBE sequence. Chandarana et al. [30] compared ^{18}F -FDG PET/MRI and ^{18}F -FDG PET/CT in the detection of lung nodules using a radially acquired VIBE sequence, a preclinical prototype of the StarVIBE sequence. In their study, the radial VIBE received a sensitivity rate of 62.3% of all lung nodules (43/69), but only 28% (7/25) of the nodules < 5 mm were detected [30]. In keeping with their results, the mean size of missed lung nodules was 3.23 ± 1.31 mm and 3.41 ± 1.42 for VIBE and StarVIBE, so especially small nodules < 4 mm were missed (Fig. 2). The rather good results of the StarVIBE sequence result primarily from the fact, that images can be acquired in free-breathing, which is particularly important for elderly people with comorbidities or children, who are often staged using MRI, trying to keep the radiation burden as low as possible. Even though the acquisition of individual StarVIBE slices takes longer than of conventional MR sequences, a major advantage of performing exams during free-breathing is continuous data acquisition, resulting in sharper images and improved resolution (here, 1.1 mm isotropic). Although StarVIBE has the smallest voxel volume compared to the others, it still missed slightly larger nodules than VIBE did (3.42 mm vs. 3.23 mm). This could be, because radial imaging tends to have image blurring when motion or magnetic susceptibility differences are present. Additionally, because StarVIBE acquires the k-space lines in z direction rectilinearly, it may still have small aliasing artifacts in this direction.

When comparing the localization of detected and missed lung nodules in the VIBE and StarVIBE sequence, no relevant differences between pleural and subpleural nodules were found. However, the StarVIBE sequence detected significantly more centrally located lung nodules. Presumably, the detection of central, perihilar nodules is particularly hampered by heart motion and breathing and the lower susceptibility to artifacts of the StarVIBE sequence has a direct effect on the detection rate of pulmonary nodules.

In our study, none of the lung nodules presented a focal tracer uptake on the PET component. Yet, in various studies [33–35], it has been shown that PET negativity is not suitable to exclude malignancy, especially in lung nodules smaller than 10 mm, since there is a high proportion of false-negative PET diagnoses caused by motion- and breathing artifact and the limited spatial resolution of the PET component, which can lead to an underestimation of the true FDG avidity [26, 36, 37].

CT provided a significantly better contrast of lung nodules than MRI sequences. This was primarily due to the high number of granulomas, which were mostly small in size and frequently showing partial calcification. While CT offers a strong contrast between such high-density structures and aerated lungs, many lung nodules remain invisible in MRI due to low-proton density and susceptibility artifacts of the calcified parts.

This study is not without limitations. Only women with newly diagnosed breast cancer were enrolled, who were generally younger and physically better constituted than most other people suffering from cancer. Commonly, older, multi-morbid patients tend to have problems holding their breath and lying still, hence, the benefits of StarVIBE might be more significant in such cohorts. Furthermore, there might have been an influence of the different slice thicknesses in CT and MRI sequences and the additional evaluation of coronal and sagittal CT reconstructions for lung nodule

detection. However, the slice thicknesses and plane directions used in this study were clinical standard and thus our results should be valid to represent the performance of CT and MRI for lung nodule detection in everyday clinical routine. Moreover, the mean time between PET/MRI and CT scans were 3 days (range 1–14 days), hence interim intra-individual changes in size or number of lung nodules, while not likely, cannot totally be excluded. Overall, it is a relatively small cohort of patients, even though it is one of the largest studies of its kind. Further research in this field with larger cohorts is needed in the future.

In conclusion, this study has demonstrated that lung nodule detection with the free-breathing T1-weighted 3D Stack of Stars GRE (StarVIBE) MR sequence as part of a whole-body ¹⁸F-FDG PET/MRI cancer staging protocol was not significantly higher than with conventional breath-hold T1-weighted VIBE and significantly higher than with T2-weighted HASTE. The StarVIBE sequence seems to be especially advantageous in detecting centrally located lung nodules. However, PET/MRI still has a substantially limited sensitivity in lung nodule detection compared to CT and thus bears the risk of missing small lung metastases in oncologic patients. Further research towards more sensitive MRI sequences is necessary.

Acknowledgements

Not applicable.

Authors' contributions

NMB: Data curation, Writing—Original draft preparation, Investigation, Visualization, Validation, Formal analysis. JK: Conceptualization, Methodology, Investigation, Writing—Review and Editing, Supervision. JM: Data curation, Validation, Writing—Reviewing and Editing. WPF, AKB, OH, TF, MEL: Data Curation. KH, LU, CB, GA, LMS: Writing—Reviewing and Editing, Supervision, Resources. All authors read and approved the final manuscript.

Funding

Open Access funding enabled and organized by Projekt DEAL. The study is funded by Deutsche Forschungsgemeinschaft (DFG), the German Research Foundation (BU3075/2-1). The funding foundation was not involved in trial design, patient recruitment, data collection, analysis, interpretation or presentation, writing or editing of the reports, or the decision to submit for publication. The corresponding author had full access to all data in the study and had all responsibility for the decision to submit for publication. Gratitude to Deutsche Forschungsgemeinschaft (DFG) for financially promoting this research project.

Availability of data and materials

The datasets used and/or analysed during the current study are available from the corresponding author on reasonable request.

Declarations

Ethics approval and consent to participate

All procedures performed were in accordance with the ethical standards of the institutional research committee of the University Duisburg-Essen (study number 17-7396-BO) and Düsseldorf (study number 6040R) and with the principles of the 1964 Declaration of Helsinki and its later amendments. Informed consent was obtained from all individual participants included in the study.

Consent for publication

Not applicable.

Competing interests

The authors declare that they have no competing interests.

Author details

¹Department of Diagnostic and Interventional Radiology, Medical Faculty, University Düsseldorf, Moorenstrasse 5, 40225 Düsseldorf, Germany. ²Department of Diagnostic and Interventional Radiology and Neuroradiology, University Hospital Essen, University of Duisburg-Essen, 45147 Essen, Germany. ³Department of Nuclear Medicine, University Hospital Essen, University of Duisburg-Essen and German Cancer Consortium (DKTK), Essen, Germany. ⁴Department of Gynecology and Obstetrics, University Hospital Essen, University of Duisburg-Essen, 45147 Essen, Germany. ⁵Department of Gynecology, Medical Faculty, University Düsseldorf, 40225 Düsseldorf, Germany. ⁶High-Field and Hybrid MR Imaging, University Hospital Essen, University of Duisburg-Essen, 45147 Essen, Germany.

Received: 27 August 2021 Accepted: 24 January 2022

Published online: 07 February 2022

References

- Gradishar WJ, Anderson BO, Balassanian R, Blair SL, Burstein HJ, Cyr A, et al. Breast cancer, Version 4.2017, NCCN clinical practice guidelines in oncology. *J Natl Compr Cancer Netw.* 2018;16(3):310–20.
- Kumar SK, Callander NS, Hillengass J, Liedtke M, Baljevic M, Campagnaro E, et al. NCCN guidelines insights: multiple myeloma, Version 1.2020. *J Natl Compr Cancer Netw.* 2019;17(10):1154–65.
- Mottet N, Bellmunt J, Bolla M, Briers E, Cumberbatch MG, De Santis M, et al. EAU-ESTRO-SIOG guidelines on prostate cancer. Part 1: screening, diagnosis, and local treatment with curative intent. *Eur Urol.* 2017;71(4):618–29.
- Schafer JF, Vollmar J, Schick F, Seemann MD, Kamm P, Erdtmann B, et al. Detection of pulmonary nodules with breath-hold magnetic resonance imaging in comparison with computed tomography. *Rofo.* 2005;177(1):41–9.
- Bruegel M, Gaa J, Woertler K, Ganter C, Waldt S, Hillerer C, et al. MRI of the lung: value of different turbo spin-echo, single-shot turbo spin-echo, and 3D gradient-echo pulse sequences for the detection of pulmonary metastases. *J Magn Reson Imaging.* 2007;25(1):73–81.
- Block KT, Chandarana H, Milla S, Bruno M, Mulholland T, Fatterpekar G, et al. Towards routine clinical use of radial stack-of-stars 3D gradient-echo sequences for reducing motion Sensitivity. *J Korean Soc Magn Reson Med.* 2014;18(2):87.
- Kumar S, Rai R, Stemmer A, Josan S, Holloway L, Vinod S, et al. Feasibility of free breathing Lung MRI for radiotherapy using non-Cartesian k-space acquisition schemes. *Br J Radiol.* 2017;90(1080):20170037.
- McRobbie DW, Moore EA, Graves MJ, Prince MR. MRI from picture to proton. 3rd ed. Cambridge: Cambridge University Press; 2017.
- Block KT, Chandarana H, Fatterpekar G, Hagiwara M, Milla S, Mulholland T, et al. Improving the robustness of clinical T1-weighted MRI using radial VIBE. *Magnetom Flash.* 2013;5:6–11.
- Azevedo RM, De Campos ROP, Ramalho M, Herédia V, Dale BM, Semelka RC. Free-breathing 3D T1-weighted gradient-echo sequence with radial data sampling in abdominal MRI: preliminary observations. *Am J Roentgenol.* 2011;197(3):650–7.
- World Medical Association Declaration of Helsinki. ethical principles for medical research involving human subjects. *JAMA.* 2013;310(20):2191–4.
- Cardoso F, Senkus E, Costa A, Papadopoulos E, Aapro M, Andre F, et al. 4th ESO-ESMO international consensus guidelines for advanced breast cancer (ABC 4)dagger. *Ann Oncol Off J Eur Soc Med Oncol.* 2018;29(8):1634–57.
- Blumhagen JO, Ladebeck R, Fenchel M, Scheffler K. MR-based field-of-view extension in MR/PET: B0 homogenization using gradient enhancement (HUGE). *Magn Reson Med.* 2013;70(4):1047–57.
- Paulus DH, Quick HH, Geppert C, Fenchel M, Zhan Y, Hermosillo G, et al. Whole-body PET/MR imaging: quantitative evaluation of a novel model-based MR attenuation correction method including bone. *J Nucl Med.* 2015;56(7):1061–6.
- Lindemann ME, Oehmigen M, Blumhagen JO, Gratz M, Quick HH. MR-based truncation and attenuation correction in integrated PET/MR hybrid imaging using HUGE with continuous table motion. *Med Phys.* 2017;44(9):4559–72.
- Oehmigen M, Lindemann ME, Gratz M, Kirchner J, Ruhlmann V, Umutlu L, et al. Impact of improved attenuation correction featuring a bone atlas and truncation correction on PET quantification in whole-body PET/MR. *Eur J Nucl Med Mol Imaging.* 2018;45(4):642–53.
- Barth A, Wanek LA, Morton DL. Prognostic factors in 1,521 melanoma patients with distant metastases. *J Am Coll Surg.* 1995;181(3):193–201.
- Biederer J, Beer M, Hirsch W, Wild J, Fabel M, Puderbach M, et al. MRI of the lung (2/3). Why... when ... how? *Insights Imaging.* 2012;3(4):355–71.
- AJCC Cancer Staging Manual. AJCC cancer staging manual. 8th ed. New York: Springer; 2017.
- Sommer G, Koenigkam-Santos M, Biederer J, Puderbach M. Role of MRI for detection and characterization of pulmonary nodules. *Radiologe.* 2014;54(5):470–7.
- Biederer J, Hintze C, Fabel M. MRI of pulmonary nodules: technique and diagnostic value. *Cancer Imaging.* 2008;8(1):125–30.
- Sawicki LM, Grueneisen J, Schaarschmidt BM, Buchbender C, Nagarajah J, Umutlu L, et al. Evaluation of 18F-FDG PET/MRI, 18F-FDG PET/CT, MRI, and CT in whole-body staging of recurrent breast cancer. *Eur J Radiol.* 2016;85(2):459–65.
- de Galiza BF, Geismar JH, Delso G, Messerli M, Huellner M, Stolzmann P, et al. Pulmonary nodule detection in oncological patients—value of respiratory-triggered, periodically rotated overlapping parallel T2-weighted imaging evaluated with PET/CT-MR. *Eur J Radiol.* 2018;98:165–70.
- Biondetti P, Vangel MG, Lahoud RM, Furtado FS, Rosen BR, Groshar D, et al. PET/MRI assessment of lung nodules in primary abdominal malignancies: sensitivity and outcome analysis. *Eur J Nucl Med Mol Imaging.* 2021;48(6):1976–86.
- Benjamin MS, Drucker EA, McLoud TC, Shepard JAO. Small pulmonary nodules: detection at chest CT and outcome. *Radiology.* 2003;226:489–93.
- Sawicki LM, Grueneisen J, Buchbender C, Schaarschmidt BM, Gomez B, Ruhlmann V, et al. Evaluation of the outcome of lung nodules missed on 18F-FDG PET/MRI compared with 18F-FDG PET/CT in patients with known malignancies. *J Nucl Med.* 2016;57(1):15–20.
- Sawicki LM, Grueneisen J, Buchbender C, Schaarschmidt BM, Gomez B, Ruhlmann V, et al. Comparative performance of 18F-FDG PET/MRI and 18F-FDG PET/CT in detection and characterization of pulmonary lesions in 121 oncologic patients. *J Nucl Med.* 2016;57(4):582–6.

28. Regier M, Kandel S, Kaul MG, Hoffmann B, Ittrich H, Bansmann PM, et al. Detection of small pulmonary nodules in high-field MR at 3 T: evaluation of different pulse sequences using porcine lung explants. *Eur Radiol.* 2007;17:1341–51.
29. Schäfer JF, Vollmar J, Schick F, Seemann MD, Kamm P, Erdtmann B, et al. Detection of pulmonary nodules with breath-hold magnetic resonance imaging in comparison with computed tomography. *Rofo.* 2005;177(1):41–9.
30. Chandarana H, Heacock L, Rakheja R, DeMello LR, Bonavita J, Block TK, et al. Pulmonary nodules in patients with primary malignancy: comparison of hybrid PET/MR and PET/CT imaging. *Radiology.* 2013;268(3):874–81.
31. Dewes P, Frelesen C, Al-Butmeh F, Albrecht MH, Scholtz JE, Metzger SC, et al. Comparative evaluation of non-contrast CAIPIRINHA-VIBE 3T-MRI and multidetector CT for detection of pulmonary nodules: in vivo evaluation of diagnostic accuracy and image quality. *Eur J Radiol.* 2016;85(1):193–8.
32. Rauscher I, Eiber M, Fürst S, Souvatzoglou M, Nekolla SG, Ziegler SI, et al. PET/MR imaging in the detection and characterization of pulmonary lesions: technical and diagnostic evaluation in comparison to PET/CT. *J Nucl Med.* 2014;55(5):724–9.
33. Yilmaz F, Tastekin G. Sensitivity of (18)F-FDG PET in evaluation of solitary pulmonary nodules. *Int J Clin Exp Med.* 2015;8(1):45–51.
34. Khalaf M, Abdel-Nabi H, Baker J, Shao Y, Lamonica D, Gona J. Relation between nodule size and 18F-FDG-PET SUV for malignant and benign pulmonary nodules. *J Hematol Oncol.* 2008;1:13.
35. Farid K, Poullias X, Alifano M, Regnard J-F, Servois V, Caillat-Vigneron N, et al. Respiratory-gated imaging in metabolic evaluation of small solitary pulmonary nodules: 18F-FDG PET/CT and correlation with histology. *Nucl Med Commun.* 2015;36(7):722–7.
36. Bar-Shalom R, Valdivia AY, Blaufox MD. PET imaging in oncology. *Semin Nucl Med.* 2000;30:150–85.
37. Cruickshank A, Stieler G, Ameer F. Evaluation of the solitary pulmonary nodule. *Intern Med J.* 2019;49(3):306–15.

Publisher's Note

Springer Nature remains neutral with regard to jurisdictional claims in published maps and institutional affiliations.

Submit your manuscript to a SpringerOpen® journal and benefit from:

- Convenient online submission
- Rigorous peer review
- Open access: articles freely available online
- High visibility within the field
- Retaining the copyright to your article

Submit your next manuscript at ► springeropen.com



Correlation of the apparent diffusion coefficient (ADC) and standardized uptake values (SUV) with overall survival in patients with primary non-small cell lung cancer (NSCLC) using ^{18}F -FDG PET/MRI



Nils Martin Bruckmann^{a,b,*}, Julian Kirchner^b, Johannes Grueneisen^a, Yan Li^a, Angela McCutcheon^d, Clemens Aigner^e, Christoph Rischpler^c, Lino M. Sawicki^b, Ken Herrmann^c, Lale Umutlu^a, Benedikt Michael Schaarschmidt^a

^a Department of Diagnostic and Interventional Radiology and Neuroradiology, University Hospital Essen, University of Duisburg-Essen, D-45147 Essen, Germany

^b University Dusseldorf, Medical Faculty, Department of Diagnostic and Interventional Radiology, D-40225 Dusseldorf, Germany

^c Department of Nuclear Medicine, University Hospital Essen, University of Duisburg-Essen, D-45147 Essen, Germany

^d Department of Medical Oncology, West German Cancer Center, University Hospital of Essen, D-45147 Essen, Germany

^e Department of Thoracic Surgery, Ruhrlandklinik, University Duisburg-Essen, D-45239 Essen, Germany

ARTICLE INFO

Keywords:

Non-small cell lung cancer
PET/MRI
Prognostic markers

ABSTRACT

Objectives: To investigate if the combined analysis of the apparent diffusion coefficient (ADC) and standardized uptake values (SUV) measured in ^{18}F -fluoro-deoxy-glucose-positron emission tomography/magnetic resonance imaging (^{18}F -FDG PET/MRI) examinations correlates with overall survival in non-small cell lung cancer (NSCLC).

Material and methods: A total of 92 patients with newly diagnosed, histopathologically proven NSCLC (44 women and 48 men, mean age 63.1 ± 9.9 years) underwent a dedicated thoracic ^{18}F -FDG PET/MRI examination. A manually drawn polygonal region of interest (ROI), encompassing the entire primary tumor mass, was placed over the primary tumor on fused PET/MR images to determine the maximum and mean standardized uptake values (SUV_{max} ; SUV_{mean}) as well as on the ADC maps to quantify the mean and minimum ADC values (ADC_{mean} , ADC_{min}). The impact of these parameters to predict patient's overall survival was tested using hazard ratios (HR). Pearson's correlation coefficients were calculated to assess dependencies between the different values. A p-value < 0.05 indicated statistical significance.

Results: In all 92 patients (n = 59 dead at time of retrospective data collection, mean time till death: 19 ± 16 month, n = 33 alive, mean time to last follow-up: 56 ± 22 month) the Hazard ratios (HR) as independent predictors for overall survival (OS) of SUV_{max} were 2.37 (95 % CI: 1.23–4.59, p = 0.008) and for SUV_{mean} 1.85 (95 % CI: 1.05–3.26, p = 0.03) while ADC_{min} showed a HR of 0.95 (95 % CI: 0.57–1.59, p = 0.842) and ADC_{mean} a HR of 2.01 (95 % CI: 1.2–3.38, p = 0.007). Furthermore, a combined analysis for $\text{SUV}_{\text{max}}/\text{ADC}_{\text{mean}}$, $\text{SUV}_{\text{max}} / \text{ADC}_{\text{min}}$ and $\text{SUV}_{\text{mean}}/\text{ADC}_{\text{mean}}$ revealed a HR of 2.01 (95 % CI: 1.10–3.67, p = 0.02), 1.75 (95 % CI: 0.97–3.15, p = 0.058) and 1.78 (95 % CI: 1.02–3.10, p = 0.04).

Conclusion: SUV_{max} and SUV_{mean} of the primary tumor are predictors for OS in therapy-naïve NSCLC patients, whereas the combined analysis of SUV and ADC values does not improve these results. Therefore, ADC values do not further enhance the diagnostic value of SUV as a prognostic biomarker in NSCLC.

1. Introduction

Lung cancer is the most frequently diagnosed cancer entity worldwide and with approximately 18 % the leading cause of cancer related death by far [1]. Non-small cell lung cancer (NSCLC) accounts for more

than 83 % of total lung cancer cases [2,3]. Effective tumor treatment heavily depends on exact initial clinical staging. Therefore, diagnostic imaging plays a pivotal role in the diagnostic work-up. ^{18}F -fluoro-deoxy-glucose-positron emission tomography/computed tomography (^{18}F -FDG PET/CT) has already proven to be an indispensable tool

* Corresponding author at: University Dusseldorf, Medical Faculty, Department of Diagnostic and Interventional Radiology, Moorenstraße 5, D-40225 Dusseldorf, Germany.

E-mail address: Nils-Martin.Bruckmann@med.uni-duesseldorf.de (N.M. Bruckmann).

for initial tumor staging and the detection of recurrent disease, in particular due to its high accuracy for detection of primary tumor mass as well as locoregional and distant metastases [4–7]. Therefore, hybrid imaging has been implemented in all major guidelines for primary lung cancer staging [3,8].

The recent introduction of ¹⁸F-FDG PET/MRI into clinical practice has provided new possibilities to both nuclear medicine physicians and radiologists. Combining the advantages of a higher soft-tissue contrast and benefits of functional imaging techniques, PET/MRI provides a comparable diagnostic accuracy in lung cancer staging in comparison to PET/CT [9–12]. Furthermore, diffusion weighted imaging (DWI) can supplement the metabolic information obtained by PET-imaging with additional information regarding tumor cellularity in NSCLC patients [13–16], assessing the degree to which diffusion of water molecules is restricted in the extracellular space [17].

The role of preoperative SUV_{max} as a useful prognostic factor for the overall survival has been well examined in many different cancer entities, for example in colorectal and breast cancer. Especially high SUV_{max} of the primary tumor correlate with an increased risk of cancer recurrence and are associated with a poor prognosis [18–22]. Several studies already evaluated the predictive value of SUV_{max} in early-stage NSCLC with conflicting results [23–27]. In some studies, SUV_{max} seems to be a significant independent prognostic marker for progression-free survival in NSCLC patients suffering from early stage disease [23–25], while no correlation was observed in other studies [26, 27].

A positive correlation between the apparent diffusion coefficient (ADC), which can be derived from DWI as a quantitative biomarker, and prognostic factors has already been described in other cancer entities, e.g. in prostate cancer [28]. But to the best of our knowledge, the ADC has not been examined as a prognostic factor in lung cancer patients so far. Still, some studies indicate the potential of ADC values in the prediction of tumor response in comparison to PET/CT [29,30]. For example Weiss et al. observed a significant increase of ADC values in a cohort of ten NSCLC patients over the course of their radiochemotherapy [30]. Therefore, DWI with ADC value measurement might represent a further prognostic marker for the overall survival in NSCLC.

A potential correlation between tissue metabolism, quantified with SUV, and tissue cellularity, quantified with ADC values has already been investigated in various studies [13,15,16,31,32]. The consensus appears to be a rather weak inverse correlation between different tumor entities. For example Schaarschmidt et al. [16] showed a weak inverse correlation in lymph node metastases of 36 NSCLC patients (SUV_{max} and ADC_{mean}: r = -0.30).

Therefore, SUV and ADC values may offer complementary

information and especially the combined analysis of SUV and ADC in simultaneous PET/MRI examinations might increase the diagnostic value of hybrid imaging in the pretherapeutic assessment by potentially predicting overall survival.

Thus, the aim of our study was to correlate ADC and SUV with overall survival in order to investigate an independent or combined marker for long-term outcome of patients with advanced NSCLC undergoing PET/MRI examinations.

2. Material and methods

2.1. Patients & inclusion criteria

A total of 92 patients (44 women and 48 men, mean age at time of examination 63.1 ± 9.9 y) with histopathologically proven and untreated NSCLC that underwent a whole-body ¹⁸F-FDG PET/CT and a subsequent dedicated thoracic ¹⁸F-FDG PET/MRI examination between August 2012 and November 2018 were enrolled in this retrospective study (Fig. 1). The results from ¹⁸F-FDG PET/CT data were not considered in this study. Two patients had to be excluded, because of severe artefacts of the ADC map and an invisible tumor on the b0-images of DWI. Histopathological results were obtained from the clinical reports, samples were acquired by endobronchial ultrasound-guided transbronchial needle aspiration (EBUS-TBNA) or biopsy. In all patients, tumor staging was assessed according to the eighth edition of the American Joint Committee on Cancer staging manual [33]. Current diagnostic criteria of the WHO/IARC were applied [34]. TNM stages which were determined with older versions have been adjusted to the current manual using all clinical, imaging and histopathological data available. Survival data from all patients were obtained from the corresponding resident registration office. The study was approved by the institutional review board (IRB) and written informed consent was waived by the IRB.

2.2. PET/MR imaging

Thoracic ¹⁸F-FDG PET/MRI scans were performed using an integrated 3.0-Tesla Biograph mMR (Siemens Healthineers, Erlangen, Germany) subsequently after a clinically indicated PET/CT scan, with a mean delay of 139.4 ± 30.4 min after radiotracer injection. Prior to the injection of a body-weight adapted activity of ¹⁸F-FDG (4 M Bq/kg bodyweight, mean activity 270 ± 46 MBq), blood glucose levels were measured to ensure values below 150 mg/dl. In PET/MRI, thoracic ¹⁸F-FDG PET data were acquired in one position for 20 min and were reconstructed using the 3D-iterative OSEM-algorithm (ordered-subset

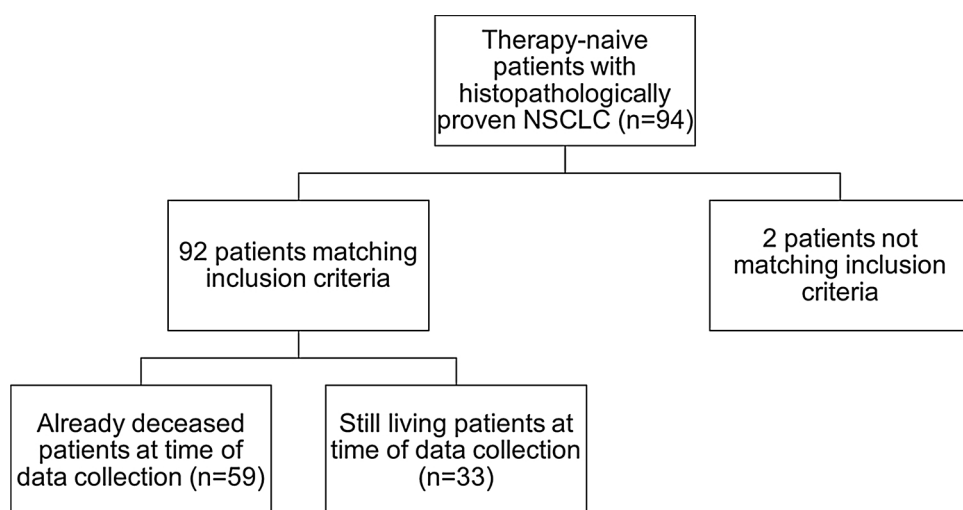


Fig. 1. Flow-chart showing process of inclusion and survival data.

expectation maximization), 3 iterations and 21 subsets, a Gaussian filter with 4-mm full width at half maximum (FWHM) as well as a 344×344 image matrix. No respiratory gating was applied.

For MR-based attenuation correction of the patient tissues a two-point (fat, water) coronal T1-weighted 3D-Dixon-VIBE sequence was acquired to generate a four-compartment attenuation map (background air, lungs, fat, muscle).

The thoracic MRI protocol was performed according to current imaging guidelines for lung cancer [35,36]. The dedicated MRI protocol comprised the following sequences, which were acquired during PET acquisition (**Table 1**):

- 1 A transversal diffusion-weighted (DWI) echo-planar imaging (EPI) sequence (TR 17,900 ms, TE 78 ms, slice thickness 5 mm, field of view (FOV) 450 mm, matrix size 160×120 mm, b values: 0, 100, 500, 1000 and 2000s/mm^2) in free breathing.
- 2 A transversal T2-weighted (T2w) BLADE sequence in free breathing (TR 4360 ms, TE 160 ms; matrix size 384; slice thickness 5 mm, FOV 400 mm).
- 3 A coronal T2 steady-state free-precession (TrueFISP) sequence in deep inspiration breath hold (TR 3.75 ms; TE 1.64 ms; matrix size 384; slice thickness 6 mm; FOV 330 mm).
- 4 A coronal T2 half-Fourier acquired single-shot turbo spin echo (HASTE) sequence in deep inspiration breath hold (TR 649 ms; TE 51 ms; matrix size 320; slice thickness 6 mm FOV 330 mm).
- 5 A non-enhanced transversal T1-weighted (T1w) fast low-angle shot (FLASH) sequence in deep inspiration breath hold (TR 1510 ms; TE 2.15 ms; inversion time (TI) 1200 ms; matrix size 320; slice thickness 5 mm; FOV 400 mm).
- 6 A transversal T1w FLASH after intravenous administration of gadolinium (TR 1700 ms; TE 3.33; TI 1200 ms; matrix size 256; slice thickness 7.5 mm; FOV 450 mm).

After image acquisition, monoexponential ADC-Maps were calculated using the preinstalled software supplied by the vendor (Siemens Healthineers, Erlangen, Germany) on the associated PET/MRI console.

2.3. Image analysis

All images were analyzed using the dedicated image processing software OsiriX (Version 9.0.2, Pixmeo SARL, Bernex, Switzerland). In a first step, ^{18}F -FDG PET data and the ADC-Map were coregistered and the PET images were reformatted to the voxel size of the ADC-Map. Then, the primary NSCLC tumor mass was identified. If the tumor was visible on PET image and DWI, a freehand polygonal region of interest (ROI) was created encompassing the tumor mass on the T2-BLADE sequence and on b0-image and copied to the corresponding PET image and ADC-Map, respectively. Afterwards, the ROI was adapted manually to avoid pixel void. SUV_{max} and SUV_{mean} in PET as well as ADC_{mean} and ADC_{min} in DWI were automatically calculated using OsiriX. To estimate values for partly included pixels automated subpixel interpolation was used by the software. Standard uptake values (SUV_{max}, SUV_{mean}) as well as ADC values (ADC_{mean}, ADC_{min}) were recorded for the primary tumor mass in every patient [16].

2.4. Statistical analysis

In order to examine the correlation of SUV and ADC values with the overall survival, an optimal cut-off value was determined for each measurement using a Cox regression and a log-rank test, dividing the patients into two groups, each containing at least 25 % of the patients. For the combined analysis a ratio between SUV and ADC values was calculated, as recommended by Rakheja et al. [15]. The bragg approach [37] with 1000 subsets was employed to reduce overfitting of the data. The median of all cut-off values was then used to divide all patients into a low-risk and a high-risk group. Kaplan-Meier curves were estimated and the hazard ratio as well as the statistical significance based on a log-rank test were computed. Unadjusted p-values were reported, where $p < 0.05$ was considered to be significant. All computations were performed using R version 3.4 and the Cutoff Finder package [38].

3. Results

At time of retrospective data collection, 59 of all 92 patients had already died (time till death: 19 ± 16 months, range: 2–70 months). For the remaining 33 patients, the average time to last follow-up was 56 ± 22 months (range: 16–80 months) (**Fig. 1**, **Table 2**). A total of 52 patients suffered from adenocarcinoma, 22 from squamous-cell carcinoma (SCC), 2 from adenosquamous carcinoma (ASC), 7 from large cell neuroendocrine carcinoma (LCNEC) and 9 patients suffered from other tumor entities. The analyzed cohort consisted of 16 patients with UICC (Union for International Cancer Control) stage I, 10 patients with stage II, 35 patients with stage III and 31 patients with a stage IV disease (**Table 2**), respectively. The mean measured tumor size was 4.9 ± 2.5 cm (range: 1.0–12.3 cm) and all tumors had a solid morphology, so that ADC values could be assessed appropriately.

For all patients in total, the mean SUV_{max} in PET/MRI was 13.6 ± 8.1 , the mean SUV_{mean} was 6.7 ± 4.3 , the mean ADC_{min} $428.4 \pm 189.8 \times 10^{-5} \text{ mm}^2/\text{s}$ and the mean ADC_{mean} was

Table 2
Patients demographics and tumor characteristics of all 92 patients.

	Dead	Alive	Both
Men	33	15	48
Women	26	18	44
Mean Age (at time of data collection in years)	64.6 ± 10.8	68.3 ± 9.4	66.0 ± 10.4
Histological subtype			
Adenocarcinoma	34	18	52
Squamous-cell carcinoma (SCC)	14	8	22
Adenosquamous carcinoma (ASC)	2	0	2
Large cell neuroendocrine carcinoma (LCNEC)	4	3	7
Not further classified	5	4	9
Tumor stage			
I	6	10	16
II	5	5	10
III	25	10	35
IV	23	8	31
Tumor size (largest diameter in cm)	4.1 ± 1.8	3.9 ± 2.1	4.0 ± 1.9

Table 1
MR-sequence parameters.

Name	Region	Orientation	TR (ms)	TE (ms)	Time (min)	Matrix size	Slice thickness (mm)	FOV (mm)
EPI-DWI	thorax	transverse	17,900	78	3:01	160×120	5	450×330
T2 BLADE TSE (breath hold)	thorax	transverse	4360	160	2:29	384×384	5	400×400
T2 TrueFISP	thorax	coronal	3.75	1.64	1:20	320×330	6	330×330
T2 HASTE	thorax	coronal	649	51	0:48	320×288	6	330×330
T1 FLASH	thorax	transverse	1510	2.15	1:20	320×256	5	400×325
T1 FLASH (after contrast injection, T1 = 1200)	thorax	transverse	1700	3.33	1:20	256×205	7.5	450×366

$942.3 \pm 209.0 \times 10^{-5}$ mm²/s. Unadjusted analysis of SUV_{max} and SUV_{mean} as independent predictors for the OS revealed a HR of 2.37 (95 % CI: 1.23–4.59, p = 0.008) and 1.85 (95 % CI: 1.05–3.26, p = 0.03) while ADC_{min} and ADC_{mean} obtained a HR of 0.95 (95 % CI: 0.57–1.59, p = 0.842) and 2.01 (95 % CI: 1.2–3.38, p = 0.007) (Table 3, Fig. 4).

The combined analysis of tracer uptake and DWI by creating the ratio of SUV_{max} / ADC_{min} resulted in a not significant correlation with the overall survival with a HR of 1.75 (95 % CI: 0.97–3.15, p = 0.058), while SUV_{max} / ADC_{mean} and SUV_{mean} / ADC_{mean} yielded statistical significant results with a HR of 2.01 (95 % CI: 1.10–3.67, p = 0.02) and 1.78 (95 % CI: 1.02–3.10, p = 0.04), but worse compared to SUV_{max} alone (Table 3, Figs. 2–4). A subgroup analysis for different tumor entities and tumor stages was not performed due to the small size of the individual subcohorts.

4. Discussion

NSCLC is by far the leading cause of cancer related death every year [1]. To decrease these numbers, it is essential to identify patients who are at risk for an unfavourable course of the disease as early as possible and modifying treatment accordingly. Therefore, prognostic factors are necessary to indicate the cases who will attain the most benefit from an optimized treatment regime.

SUV_{max} is an established parameter in hybrid imaging diagnosis, mainly due to its high reproducibility and availability. Especially the prognostic value of SUV_{max} has widely been investigated, showing a correlation between a high SUV_{max} and increased cancer recurrence and poor prognosis in several cancer entities [18,20,21]. In early stage NSCLC the SUV_{max} as a predictor for the OS revealed conflicting results so far [24–27].

With the introduction of PET/MRI, simultaneous PET- and DWI-measurements are possible, enhancing PET with additional information derived from functional MRI. According to prior studies, an inverse correlation between SUV and ADC in therapy-naïve NSCLC can be expected, because the increased cellular density in malignant lesions leads to a restriction of water diffusion in the interstitial space, resulting in lower ADC values than in scar tissue or necrosis [13,14,16,39,40]. Still, ADC values as further prognostic factor for OS in therapy-naïve NSCLC patients have not been examined so far.

The results of our study underline the importance of SUV_{max} and SUV_{mean} as a possible prognostic marker for OS in therapy-naïve NSCLC, showing a significant correlation between high SUV values and a poor prognosis, regardless of the histological subtype and the tumor stage. The results are consistent with previous studies: In a meta-analysis by Dong et al. SUV values were considered to be good prognostic markers in early stage NSCLC in patients undergoing ¹⁸F-FDG PET/CT [23]. The study of Horne et al. supports this thesis: According to their data SUV_{max} served as a reliable prognostic factor for progression-free survival in stage I NSCLC in ¹⁸F-FDG PET/CT examinations [24].

In this context, however, it is important to note that PET/MRI requires a different attenuation correction than PET/CT. In combined PET/CT, the CT provides useful data about tissue density, which can directly be easily transformed to be used for CT-based attenuation correction (CTAC) while the MR-signal is not related to radiodensity of

the examined tissue. The most frequently used MR-based attenuation correction (MRAC) relies on a tissue classification by using a Dixon-based two-point (fat, water) sequence to generate a four-compartment attenuation map (μ -map, background air, lungs, fat, muscle). Hence, the discrepancy in MRAC and CTAC may result in differences of SUV measurements. However, former studies already proved a good correlation between SUV measurements between PET/CT and PET/MRI examinations, confirming that SUV values derived from PET/MRI can be considered as reliable in clinical routine [13,41–43]. Therefore, it is not surprising that the inverse correlations between SUV_{max} and SUV_{mean} with OS initially described in PET/CT can also be observed in PET/MRI.

In our cohort, however, we did neither observe an additional value of ADC_{min} nor ADC_{mean} measurements in the prediction of OS. ADC_{mean} even showed an unexpected negative correlation with the OS. In our opinion, this finding is caused by the overrepresentation of patients suffering from stage III or IV lung cancer. As postulated in a previous study, it is probable that tumor necrosis is more frequent in more advanced tumor lesions, thus increasing ADC values [16]. A morphological correlation for the necrosis does not necessarily have to be visible, since changes take place on a cellular level. On the other hand the glucose metabolism of adjacent vital tumor cells might remain high leading to barely unaltered high SUV values [16].

Accordingly, the combined analysis of tracer uptake and tumor cellularity by investigating ratios of SUV_{max}, SUV_{mean} and ADC_{min}, ADC_{mean} did not detect a ratio that is suitable for the usage as a predictive value in NSCLC patients. Here, only the ratio of SUV_{max} and ADC_{mean} resulted in a statistically significant correlation, however, in comparison to SUV_{max} alone, without any added benefit.

Especially in the lung, MRI imaging has to cope with several problems: ADC values are measured in free-breathing, leading to cardiac and respiratory motion, further deteriorated by aortic pulsation and esophageal peristalsis. Furthermore the commonly employed echo-planar sequences are prone to geometric distortions from magnetic susceptibility effects of the air-filled lung parenchyma, aggravating the application of DWI-MRI for evaluating lung tumors [44–46]. Furthermore, it must be taken into account, that DWI still suffer from a lack of standardization. Here, several studies already show that intrapatient and interscanner repeatability in DWI in different vendors and different field strengths is still problematic, thus necessitating further standardization [16,44,47,48].

This study has some limitations. First of all, all patients received a whole-body ¹⁸F-FDG-PET/CT and subsequently a dedicated ¹⁸F-FDG PET/MRI. The long waiting time after tracer injection for the PET/MRI examination may have an impact on SUV values due to tracer decay and a different tracer distribution, as described by Cheng et al. [49]. Furthermore, conventional diffusion-weighted imaging was performed in this study using a single-shot echo-planar sequence (EPI). To improve the image quality and reduce spatial blurring and susceptibility artefacts, new DWI-sequences like readout-segmented DWI (rs-DWI, RESOLVE) and radially sampled FSE methods have recently been developed at expense of increased acquisition time. It is possible, that ADC measurements will become more reliable with these methods, here, further research is necessary. Moreover, the results in this study have only been tested for internal validity. An external validation has not been done. Despite the size of our cohort compared to previously published studies, a valid subgroup analysis, especially differentiating the tumor stages, histological subtypes or treatment responses is still not possible. With increasing use of PET/MRI in clinical routine, the realization of appropriate subgroup analyses becomes feasible and useful in future. However, in accordance with the literature, SUV values seem to be useful as reliable parameters for OS in NSCLC subgroups [23,25]. In accordance with our study, additional benefits from ADC are not yet described.

In conclusion, this study underlines the value of SUV_{max} and SUV_{mean} as an independent prognostic marker for overall survival in NSCLC patients. ADC as a further independent prognostic marker, however, has to

Table 3

P-values and hazard ratios of all measurements.

Name	p-value	HR	HR 95 % CI
SUV _{max}	0.008	2.37	1.23 - 4.59
SUV _{mean}	0.03	1.85	1.05 - 3.26
ADC _{mean}	0.007	2.01	1.20 - 3.38
ADC _{min}	0.842	0.95	0.57 - 1.59
SUV _{max} _ADC _{mean}	0.02	2.01	1.10 - 3.67
SUV _{max} _ADC _{min}	0.058	1.75	0.97 - 3.15
SUV _{mean} _ADC _{mean}	0.04	1.78	1.02 - 3.10
SUV _{mean} _ADC _{min}	0.105	1.58	0.90 - 2.75

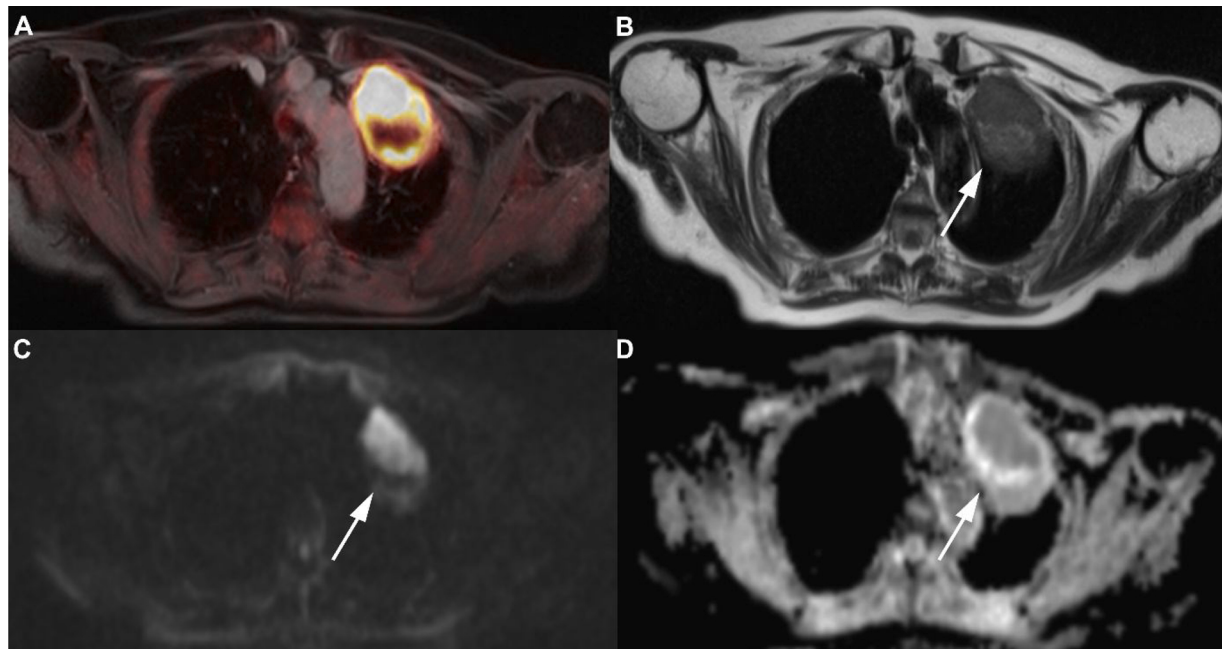


Fig. 2. Images of a 70-year-old female patient with a histological proven NSCLC in the left upper lobe with tumor stage III (cT4cN1cM0). The tumor manifestation reveals a strong metabolic activity on fused ^{18}F -FDG PET/MR images (A), shows infiltration of the thoracic wall (B, T2w Haste image) as well as restricted diffusivity (C, DWI b-1000; D, ADC-Map, see arrow).

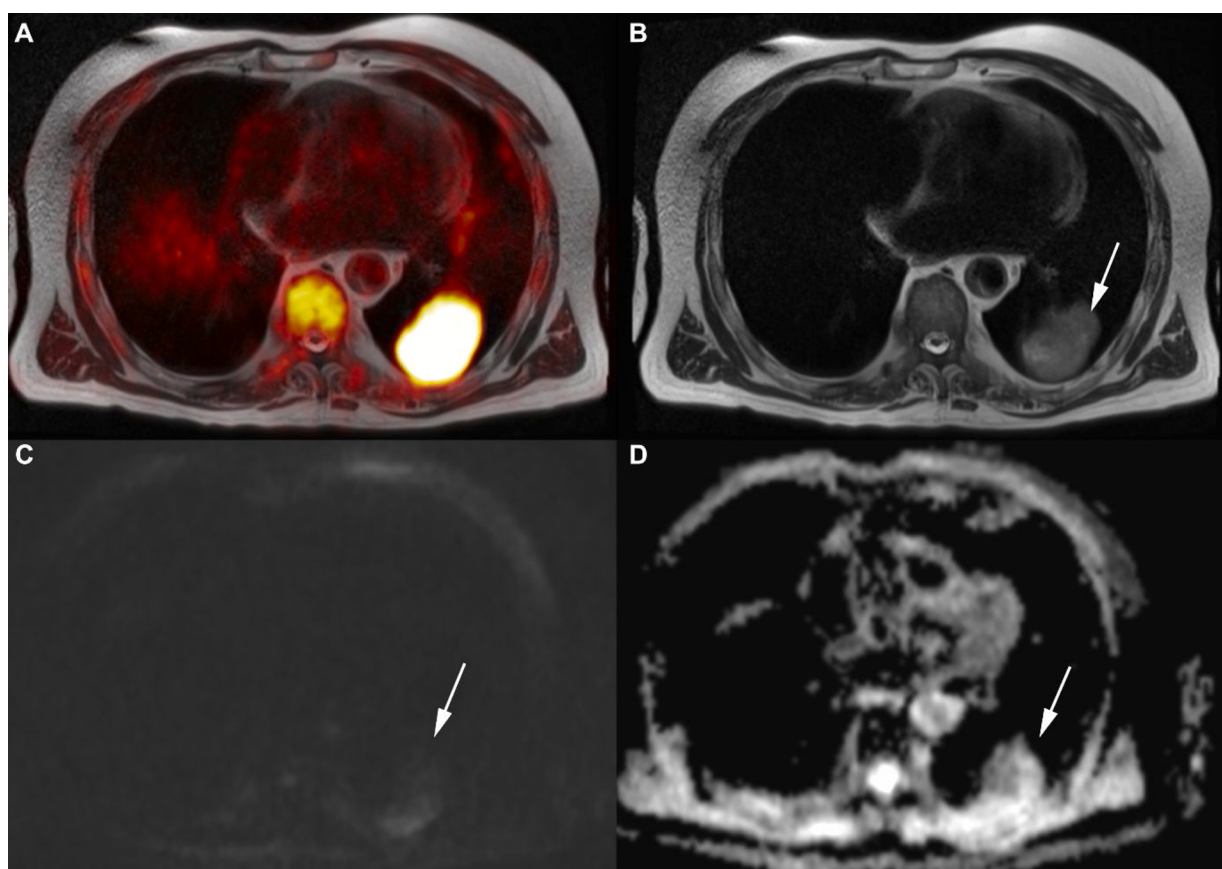


Fig. 3. Images of a 76-year-old male patient with a histological proven NSCLC in the left upper lobe (tumor stage IV, cT3cN3cM1a) The tumor manifestation reveals a strong metabolic activity on fused ^{18}F -FDG PET/MR images (A), but just a slight diffusion restriction (C, DWI b-1000; D, ADC-Map, see arrow).

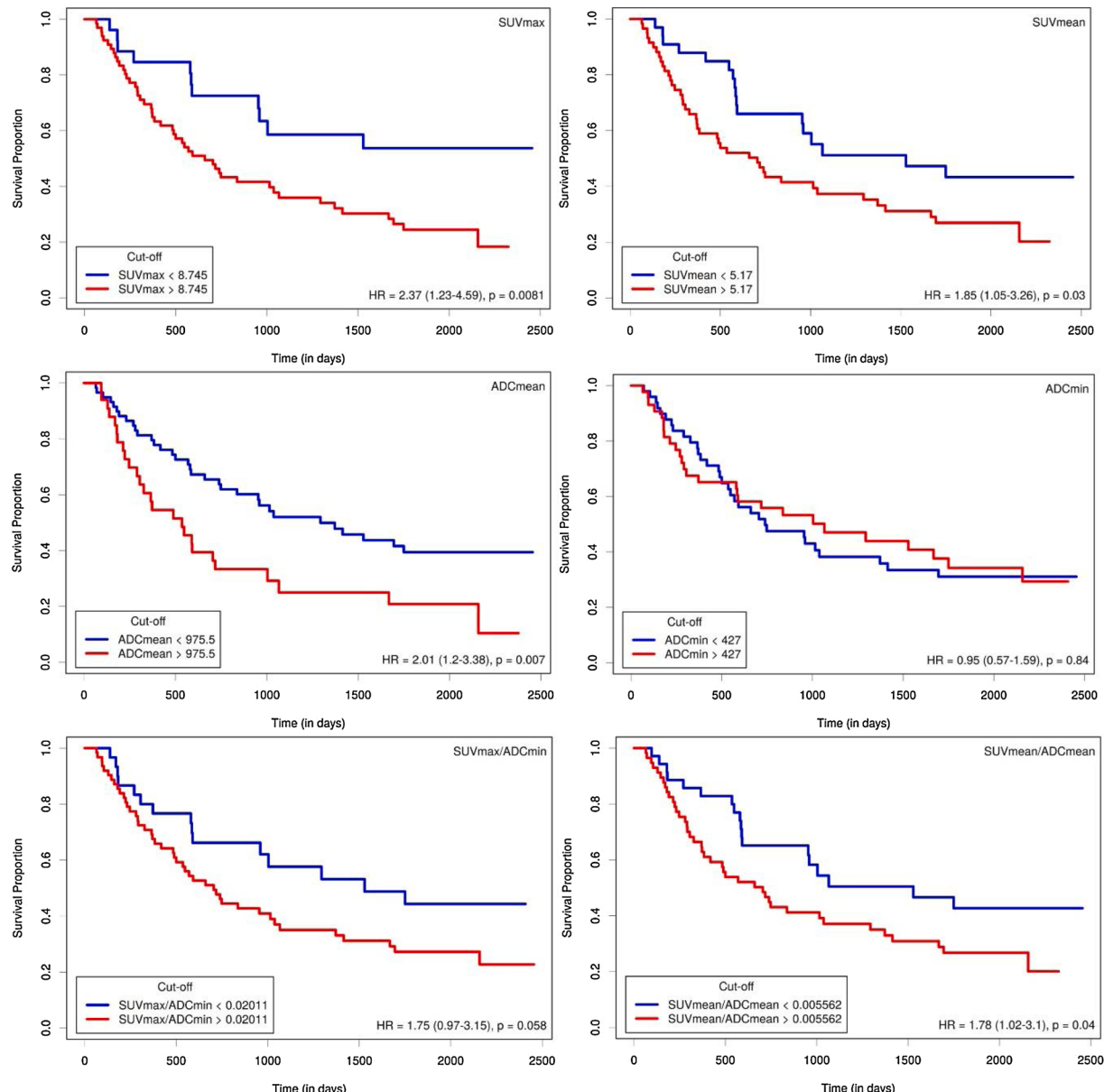


Fig. 4. Kaplan-Meier Curves of SUV and ADC values and for ADC/SUV ratios. Survival proportion against time in days are plotted in each diagram. The study cohort is divided into a low risk (blue) and a high risk (red) group. Cut off values are presented in the lower left corner.

be considered as inferior to SUV_{max} . A combined analysis of glucose metabolism and tumor cellularity by creating ratios between SUV_{max} , SUV_{mean} and ADC_{min} , ADC_{mean} did not lead to further improvements in predicting overall survival compared to SUV_{max} . Hence, we have to conclude that the multiparametric evaluation of NSCLC patients in ^{18}F -FDG PET/MRI by a combined analysis of SUV and ADC is not superior to sole SUV_{max} measurements in the prediction of overall survival.

Ethical approval

All procedures performed were in accordance with the ethical standards of the institutional research committee and with the principles of the 1964 Declaration of Helsinki and its later amendments.

Informed consent

Informed consent was obtained from all individual participants included in the study.

CRediT authorship contribution statement

Nils Martin Bruckmann: Data curation, Writing - original draft, Investigation, Visualization, Validation, Formal analysis. **Julian Kirchner:** Writing - review & editing. **Johannes Grueneisen:** Writing - review & editing. **Yan Li:** Writing - review & editing. **Angela McCutcheon:** Data curation. **Clemens Aigner:** Data curation. **Christoph Rischpler:** Data curation, Writing - review & editing. **Lino M. Sawicki:** Data curation, Writing - review & editing. **Ken Herrmann:** Supervision, Resources. **Lale Umutlu:** Supervision, Resources. **Benedikt Michael Schaarschmidt:** Conceptualization, Methodology, Investigation, Writing - review & editing, Supervision.

Declaration of Competing Interest

None.

References

- [1] The global cancer observatory G. Breast cancer. source: globocan 2018, World Heal Organ. 876 (2018), 2018–9.
- [2] L.A. Torre, R.L. Siegel, A. Jemal, Lung cancer statistics, *Adv. Exp. Med. Biol.* 893 (2016) 1–19.
- [3] D.S. Ettinger, D.L. Aisner, D.E. Wood, W. Akerley, J. Bauman, J.Y. Chang, et al., NCCN guidelines insights: non-small cell lung Cancer, version 5.2018, *J Natl Compr Cancer Netw.* 16 (7) (2018) 807–821.
- [4] T. Bunyaviroch, R.E. Coleman, PET evaluation of lung cancer, *J. Nucl. Med.* 47 (3) (2006) 451–469.
- [5] G. Antoch, F.M. Vogt, L.S. Freudenberg, F. Nazaradeh, S.C. Goehde, J. Barkhausen, et al., Whole-body dual-modality PET/CT and whole-body MRI for tumor staging in oncology, *J. Am. Med. Assoc.* 290 (24) (2003) 3199–3206.
- [6] G. Goekenjan, H. Sitter, M. Thomas, D. Branscheid, M. Flentje, F. Griesinger, et al., Prevention, diagnosis, therapy, and follow-up of lung cancer: interdisciplinary guideline of the German respiratory society and the German cancer society, *Pneumologie* 65 (8) (2011) e51–75.
- [7] S.H. Choi, Y.T. Kim, S.K. Kim, K.W. Kang, J.M. Goo, C.H. Kang, et al., Positron emission tomography-computed tomography for postoperative surveillance in non-small cell lung cancer, *Ann. Thorac. Surg.* 92 (5) (2011) 1826–1832.
- [8] P.E. Postmus, K.M. Kerr, M. Oudkerk, S. Senan, D.A. Waller, J. Vansteenkiste, et al., Early and locally advanced non-small-cell lung cancer (NSCLC): ESMO Clinical Practice Guidelines for diagnosis, treatment and follow-up, *Ann. Oncol.* 28 (suppl. 4) (2017) iv1–iv21.
- [9] P. Heusch, C. Buchbender, J. Köhler, F. Nensa, T. Gauler, B. Gomez, et al., Thoracic staging in lung cancer: prospective comparison of 18F-FDG PET/MR imaging and 18F-FDG PET/CT, *J. Nucl. Med.* 55 (3) (2014) 373–378.
- [10] B.M. Schaarschmidt, J. Grueisenen, M. Metzenmacher, B. Gomez, T. Gauler, C. Roesel, et al., Thoracic staging with (18)F-FDG PET/MR in non-small cell lung cancer - does it change therapeutic decisions in comparison to (18)F-FDG PET/CT? *Eur. Radiol.* 27 (2 February) (2017) 681–688.
- [11] J. Kirchner, L.M. Sawicki, F. Nensa, B.M. Schaarschmidt, H. Reis, M. Ingenwerth, et al., Prospective comparison of 18 F-FDG PET/MRI and 18 F-FDG PET/CT for thoracic staging of non-small cell lung cancer, *Eur. J. Nucl. Med. Mol. Imaging* 46 (2) (2019) 437–445.
- [12] O. Martin, B.M. Schaarschmidt, J. Kirchner, S. Suntharalingam, J. Grueisenen, A. Demircioğlu, et al., PET/MRI versus PET/CT in whole-body staging: results from a unicenter observational study in 1003 subsequent examinations, *J. Nucl. Med.* (December) (2019) jnumed.119.
- [13] P. Heusch, C. Buchbender, J. Köhler, F. Nensa, K. Beiderwellen, H. Kühl, et al., Correlation of the apparent diffusion coefficient (ADC) with the standardized uptake value (SUV) in hybrid 18F-FDG PET/MRI in non-small cell lung cancer (NSCLC) lesions: initial results, *RoFo Fortschritte auf dem Gebiet der Röntgenstrahlen und der Bildgeb Verfahren.* 185 (11) (2013) 1056–1062.
- [14] M. Regier, T. Derlin, D. Schwarz, A. Laqmani, F.O. Henes, M. Groth, et al., Diffusion weighted MRI and 18F-FDG PET/CT in non-small cell lung cancer (NSCLC): Does the apparent diffusion coefficient (ADC) correlate with tracer uptake (SUV)? *Eur. J. Radiol.* 81 (10) (2012) 2913–2918.
- [15] R. Rakheja, H. Chandarana, L. DeMello, K. Jackson, C. Geppert, D. Faul, et al., Correlation between standardized uptake value and apparent diffusion coefficient of neoplastic lesions evaluated with whole-body simultaneous hybrid PET/MRI, *Am J Roentgenol.* 201 (5) (2013) 1115–1119.
- [16] B.M. Schaarschmidt, C. Buchbender, F. Nensa, J. Grueisenen, B. Gomez, J. Köhler, et al., Correlation of the apparent diffusion coefficient (ADC) with the standardized uptake value (SUV) in lymph node metastases of non-small cell lung cancer (NSCLC) patients using hybrid 8F-FDG PET/MRI, *PLoS One* 10 (1) (2015) 1–14.
- [17] J. Zhong, J.C. Gore, Studies of restricted diffusion in heterogeneous media containing variations in susceptibility, *Magn. Reson. Med.* 19 (2) (1991) 276–284.
- [18] J.P. Hwang, I. Lim, B.H. Byun, B. Kim II, C.W. Choi, S.M. Lim, Prognostic value of SUVmax measured by pretreatment 18F-FDG PET/CT in patients with primary gastric lymphoma, *Nucl. Med. Commun.* 37 (12) (2016) 1267–1272.
- [19] Shi D., Cai G., Peng J., Li D., Li X., Xu Y., et al. The preoperative SUVmax for 18 F-FDG uptake predicts survival in patients with colorectal cancer. *BMC Cancer.* 15: 991.
- [20] Song B. II, H.W. Kim, K.S. Won, S.W. Ryu, S.S. Sohn, Y.N. Kang, Preoperative standardized uptake value of metastatic lymph nodes measured by 18F-FDG PET/CT improves the prediction of prognosis in gastric cancer, *Med (United States)*. 94 (26) (2015) e1037.
- [21] W. Diao, F. Tian, Z. Jia, The prognostic value of SUVmax measuring on primary lesion and ALN by 18F-FDG PET or PET/CT in patients with breast cancer, *Eur. J. Radiol.* 105 (2018) 1–7.
- [22] K. Kitajima, T. Yamano, Y. Miyoshi, T. Katsuura, T. Enoki, K. Yamakado, Prognostic value of 18 F-FDG PET/CT prior to breast cancer treatment. Comparison with magnetic resonance spectroscopy and diffusion weighted imaging, *Hell. J. Nucl. Med.* 22 (1) (2019) 25–35.
- [23] M. Dong, J. Liu, X. Sun, L. Xing, Prognostic significance of SUVmax on pretreatment 18F-FDG PET/CT in early-stage non-small cell lung cancer treated with stereotactic body radiotherapy: a meta-analysis, *J. Med. Imaging Radiat. Oncol.* (2017).
- [24] Z.D. Horne, D.A. Clump, J.A. Vargo, S. Shah, S. Beriwal, S.A. Burton, et al., Pretreatment SUVmax predicts progression-free survival in early-stage non-small cell lung cancer treated with stereotactic body radiation therapy, *Radiat. Oncol.* 9 (2014) 41.
- [25] J. Liu, M. Dong, X. Sun, W. Li, L. Xing, J. Yu, Prognostic value of 18F-FDG PET/CT in surgical non-small cell lung cancer: a meta-analysis, *PLoS One* 11 (1) (2016) e0146195.
- [26] A. Sharma, A. Mohan, A.S. Bhalla, M.C. Sharma, S. Vishnubhatla, C.J. Das, et al., Role of various metabolic parameters derived from baseline 18 F-FDG PET/CT as prognostic markers in non-small cell lung Cancer patients undergoing platinum-based chemotherapy, *Clin. Nucl. Med.* 43 (1) (2018) e8–17.
- [27] M.J. Burdick, K.L. Stephans, C.A. Reddy, T. Djemil, S.M. Srinivas, G.M.M. Videtic, Maximum standardized uptake value from staging FDG-PET/CT does not predict treatment outcome for early-stage non-small-cell lung cancer treated with stereotactic body radiotherapy, *Int. J. Radiat. Oncol. Biol. Phys.* 78 (4) (2010) 1033–1039.
- [28] M.P. Chung, D. Margolis, S. Mesko, J. Wang, P. Kupelian, M. Kamrava, Correlation of quantitative diffusion-weighted and dynamic contrast-enhanced MRI parameters with prognostic factors in prostate cancer, *J. Med. Imaging Radiat. Oncol.* 58 (5) (2014) 588–594.
- [29] Y. Ohno, H. Koyama, T. Yoshikawa, K. Matsumoto, N. Aoyama, Y. Onishi, et al., Diffusion-weighted MRI versus 18F-FDG PET/CT: Performance as predictors of tumor treatment response and patient survival in patients with non-small cell lung cancer receiving chemoradiotherapy, *Am J Roentgenol.* 198 (1) (2012) 75–82.
- [30] E. Weiss, J.C. Ford, K.M. Olsen, K. Karki, S. Saraiya, R. Groves, et al., Apparent diffusion coefficient (ADC) change on repeated diffusion-weighted magnetic resonance imaging during radiochemotherapy for non-small cell lung cancer: a pilot study, *Lung Cancer [Internet].* 96 (2016) 113–119, <https://doi.org/10.1016/j.lungcan.2016.04.001>. Available from:
- [31] J. Grueisenen, K. Beiderwellen, P. Heusch, P. Buderath, B. Aktas, M. Gratz, et al., Correlation of standardized uptake value and apparent diffusion coefficient in integrated whole-body PET/MRI of primary and recurrent cervical cancer, *PLoS One* (2014).
- [32] K. Nakamura, I. Joja, J. Kodama, A. Hongo, Y. Hiramatsu, Measurement of SUVmax plus ADCmin of the primary tumour is a predictor of prognosis in patients with cervical cancer, *Eur. J. Nucl. Med. Mol. Imaging* (2012).
- [33] S.S. Badve, P.D. Beitsch, S. Bose, D.R. Byrd, V.W. Chen, J.A. Mayer, et al., 8th AJCC Breast Cancer Staging [Internet], 2017. Available from: <https://cancerstaging.org/references-tools/deskreferences/Documents/AJCC%20Breast%20Cancer%20Staging%20System.pdf>.
- [34] W.D. Travis, E. Brambilla, A.G. Nicholson, Y. Yatabe, J.H.M. Austin, M.B. Beasley, et al., WHO classification of tumours of the lung, pleura, Thymus and heart, *J. Thorac. Oncol.* 10 (9) (2015) 1240–1242.
- [35] H.S. Kim, K.S. Lee, Y. Ohno, E.J.R. Van Beek, J. Biederer, PET/CT versus MRI for diagnosis, staging, and follow-up of lung cancer, *J. Magn. Reson. Imaging* 42 (2) (2015) 247–260.
- [36] J. Biederer, M. Beer, W. Hirsch, J. Wild, M. Fabel, M. Puderbach, et al., MRI of the lung (2/3), Why... when ... how? *Insights Imaging.* 3 (4) (2012) 355–371.
- [37] P. Bühlmann, Bagging, Subbagging and Bragging for Improving Some Prediction Algorithms. Bühlmann, Zürich, 2003.
- [38] J. Budczies, F. Klauschen, B.V. Sinn, B. Györffy, W.D. Schmitt, S. Darb-Esfahani, et al., Cutoff finder: a comprehensive and straightforward web application enabling rapid biomarker cutoff optimization. Van Diest P, editor, *PLoS One* (2012) [Internet]. Dec 14 [cited 2019 Oct 21];7(12):e51862. Available from: <https://doi.org/10.1371/journal.pone.0051862>.
- [39] P. Heusch, J. Köhler, H.J. Wittsack, T.A. Heusner, C. Buchbender, T.D. Poepel, et al., Hybrid [18F]-FDG PET/MRI including non-Gaussian diffusion-weighted imaging (DWI): preliminary results in non-small cell lung cancer (NSCLC), *Eur. J. Radiol.* 82 (11) (2013) 2055–2060.
- [40] H. Schmidt, C. Brendle, C. Schraml, P. Martirosian, I. Bezrukova, J. Hetzel, et al., Correlation of simultaneously acquired diffusion-weighted imaging and 2-deoxy-[18F] fluoro-2-D-glucose positron emission tomography of pulmonary lesions in a dedicated whole-body magnetic resonance/positron emission tomography system, *Invest. Radiol.* 48 (5) (2013) 247–255.
- [41] P. Heusch, C. Buchbender, K. Beiderwellen, F. Nensa, V. Hartung-Knemeyer, T. C. Lauenstein, et al., Standardized uptake values for [18F] FDG in normal organ tissues: comparison of whole-body PET/CT and PET/MRI, *Eur. J. Radiol.* 82 (5) (2013) 870–876.
- [42] F. Seith, S. Gatidis, H. Schmidt, I. Bezrukova, C. La Fougerie, K. Nikolaou, et al., Comparison of positron emission tomography quantification using magnetic resonance- and computed tomography-based attenuation correction in physiological tissues and lesions, *Invest. Radiol.* 51 (1) (2016) 66–71.
- [43] H.H. Quick, Integrated PET/MR, *J. Magn. Reson. Imaging* 39 (2) (2014) 243–258.
- [44] L. Bernardin, N.H.M. Douglas, D.J. Collins, S.L. Giles, E.A.M. O'Flynn, M. Orton, et al., Diffusion-weighted magnetic resonance imaging for assessment of lung lesions: repeatability of the apparent diffusion coefficient measurement, *Eur. Radiol.* 24 (2) (2014) 502–511.
- [45] H. Liu, Y. Liu, T. Yu, N. Ye, Usefulness of diffusion-weighted MR imaging in the evaluation of pulmonary lesions, *Eur. Radiol.* 20 (2010) 807–815.
- [46] S. Satoh, Y. Kitazume, S. Ohdama, Y. Kimura, S. Taura, Y. Endo, Can malignant and benign pulmonary nodules be differentiated with diffusion-weighted MRI? *Am J Roentgenol.* 191 (2) (2008) 464–470.

- [47] O.F. Donati, D. Chong, D. Nanz, A. Boss, J.M. Froehlich, E. Andres, et al., Diffusion-weighted MR imaging of upper abdominal organs: field strength and intervendor variability of apparent diffusion coefficients, *Radiology*. 270 (2) (2014) 454–463.
- [48] D. Malyarenko, C.J. Galbán, F.J. Lonyd, C.R. Meyer, T.D. Johnson, A. Rehemtulla, et al., Multi-system repeatability and reproducibility of apparent diffusion coefficient measurement using an ice-water phantom, *J. Magn. Reson. Imaging* 37 (5) (2013) 1238–1246.
- [49] G. Cheng, A. Alavi, E. Lim, T.J. Werner, C.V. Del Bello, S.R. Akers, Dynamic changes of FDG uptake and clearance in normal tissues, *Mol. Imaging Biol.* 15 (3) (2013) 345–352.



Research article

Correlation between contrast enhancement, standardized uptake value (SUV), and diffusion restriction (ADC) with tumor grading in patients with therapy-naïve neuroendocrine neoplasms using hybrid ^{68}Ga -DOTATOC PET/MRI



Nils Martin Bruckmann ^{a,1}, Christoph Rischpler ^{b,1}, Julian Kirchner ^{a,*}, Lale Umutlu ^b, Ken Herrmann ^c, Marc Ingenwerth ^d, Sarah Theurer ^d, Harald Lahner ^e, Gerald Antoch ^a, Lino M. Sawicki ^a

^a University Düsseldorf, Medical Faculty, Department of Diagnostic and Interventional Radiology, D-40225 Düsseldorf, Germany

^b Department of Diagnostic and Interventional Radiology and Neuroradiology, University Hospital Essen, University of Duisburg-Essen, D-45147 Essen, Germany

^c Department of Nuclear Medicine, University Hospital Essen, University of Duisburg-Essen, D-45147 Essen, Germany

^d Institute of Pathology, University Hospital Essen, West German Cancer Center, University Duisburg-Essen and the German Cancer Consortium (DKTK) Essen, Germany

^e Department of Endocrinology and Metabolism, Division of Laboratory Research, University Hospital Essen, University Duisburg-Essen, D-45247 Essen, Germany

ARTICLE INFO

Keywords:

PET/MRI

Neuroendocrine neoplasms

Imaging parameters

Tumor grading

ABSTRACT

Objectives: To investigate a correlation between ^{68}Ga -DOTATOC PET/MR imaging parameters such as arterial and venous contrast enhancement, diffusion restriction, and maximum standardized uptake value (SUVmax) with histopathological tumor grading in patients with neuroendocrine neoplasms (NEN).

Material and methods: A total of 26 patients with newly diagnosed, therapy-naïve neuroendocrine neoplasms (NEN) were enrolled in this prospective study and underwent ^{68}Ga -DOTATOC PET/MRI. Images were evaluated regarding NEN lesion number and location, predominant tumor signal intensity on precontrast T1w and T2w images and on postcontrast arterial and portal venous phase T1w images, apparent diffusion coefficient (ADC) and SUVmax. Histopathological tumor grading was assessed and related to PET/MRI features using Pearson's correlation coefficient and Fisher's exact *t*-test. A binary logistic regression analysis was performed to evaluate a potential relation with an aggressive tumor biology and odds ratios (OR) were calculated.

Results: There was a moderate negative correlation between arterial contrast enhancement and tumor grading ($r=-0.35$, $p=0.005$), while portal venous enhancement showed a weak positive correlation with the Ki-67 index ($r=0.28$, $p=0.008$) and a non-significant positive correlation with tumor grading ($r=0.19$, $p=0.063$). Features that were significantly associated with an aggressive tumor biology were the presence of liver metastases (OR 2.6, $p=0.042$), T1w hyperintensity in comparison to muscle (OR 12.7, $p=0.0001$), arterial phase hyperenhancement (OR 1.4, $p=0.001$), diffusion restriction (OR 2.8, $p=0.02$) and SUVmax above the hepatic level (OR 7.0, $p=0.001$).

Conclusion: The study reveals that PET/MRI features might be useful for prediction of NEN grading and thus provide a preliminary assessment of tumor aggressiveness.

Abbreviations: ADC, apparent diffusion coefficient; CT, computed tomography; CUP, cancers of unknown primary; DOTA, 1,4,7,10-tetraazacyclododecane-1,4,7,10-tetraacetic acid; DOTATOC, DOTA-Phel-Tyr3-octreotide; DWI, diffusion-weighted imaging; EPI, echo-planar imaging; EUS-FNA, endoscopic ultrasound-guided fine-needle aspiration; FWHM, full-width at half maximum; HASTE, half fourier acquisition single shot turbo spin echo; MRI, magnetic resonance imaging; NEC, neuroendocrine carcinoma; NEN, neuroendocrine neoplasms; NET, neuroendocrine tumors; OR, odds ratio; OSEM, ordered-subset expectation maximization; PET, positron emission tomography; ROI, region of interest; SSTR, somatostatin receptor; SUV, standardized uptake value; VIBE, volume interpolated breath-hold examination; VOI, volume of interest; WHO, World Health Organization.

* Corresponding author.

E-mail address: JulianKirchner@gmx.de (J. Kirchner).

¹ Authors contributed equally to this study.

1. Introduction

Neuroendocrine neoplasms (NEN) are considered to be rare, causing about 1 % of all neoplasms worldwide with an incidence of approximately 7/100,000 [1]. However, due to new detection possibilities, the incidence has increased considerably over the last decades [2]. NENs are a heterogeneous group of tumors that arise from the endocrine system throughout the body with a large range of histological appearance, hormonal activity, molecular signature and in degree of aggressiveness [3]. Due to this heterogeneity, both treatment and treatment response as well as prognosis can vary drastically depending on the type of NEN [4]. The most common NEN manifestation in Western populations is the small bowel, while rectal NEN are predominant in Asia. Other common locations of NEN are the pancreas, lungs, and stomach [2,4,5]. According to the current World Health Organization (WHO) classification of 2017 NEN can be histopathologically divided into well and poorly differentiated types. The well differentiated neuroendocrine tumors (NET) can additionally be subcategorized as low-grade (G1, Ki-67 < 3 %), intermediate-grade (G2, Ki-67 3–20 %), or high-grade (G3, Ki-67 > 20 %), based on the mitotic rate and the Ki-67 index [4,6,7]. Poorly differentiated neoplasms with a large-cell or small-cell type are designated neuroendocrine carcinomas (NECs) and also categorized as grade 3 [4].

By means of highly somatostatin receptor (SSTR) avid ^{68}Ga -labelled 1,4,7,10-tetraazacyclododecane-1,4,7,10-tetraacetic acid (DOTA) peptides, such as ^{68}Ga -DOTA-Phel-Tyr3-octreotide (DOTATOC) for positron emission tomography (PET) in combination with computed tomography (CT) or magnetic resonance imaging (MRI) in hybrid imaging, the detection rate of even very small lesions has significantly improved in the last few years. For this reason, ^{68}Ga -DOTA peptide-based PET/CT or PET/MR imaging has lately become the imaging gold standard for NEN. Due to the higher soft tissue contrast of MRI and functional imaging sequences such as diffusion-weighted imaging (DWI), PET/MRI was recently found to offer better detectability and visibility of NEN lesions compared to PET/CT [8–12]. In addition to the benefits of an improved NEN detection, results from several studies have suggested that ^{68}Ga -DOTATOC PET/MRI might be the most useful imaging method to predict the tumor grade and aggressiveness of NEN [13–19], especially since it allows a truly simultaneous acquisition of morphological and functional MR sequences and PET images. For instance, as DWI from MRI is a surrogate parameter for tumor cell density, which can be quantified by the apparent diffusion coefficient (ADC) [13], a correlation analysis between ADC and tumor grading could show an association between these features and allows a non-invasive assessment of tumor aggressiveness [13–15]. Furthermore, it has been found that an increasing dedifferentiation of NENs leads to a decrease in SSTR expression and thus in SUV on DOTATOC PET imaging. Imaging features of NENs on contrast enhanced MRI or CT scans include an intense arterial and venous enhancement [17]. However, recent studies show that a large proportion of tumors can also show less perfusion, especially for G2/G3 tumors [18,19]. Since the right treatment heavily depends on the grade of the tumor, image-based characterization of NEN histopathology and selection of suitable biopsy sites is highly desirable [16]. Few studies have investigated a correlation between NEN contrast-enhancement and tumor grading in MRI so far [6,20], yet, to our best knowledge, this is the first study to use various, simultaneously acquired ^{68}Ga -DOTATOC PET/MRI data for this purpose.

Therefore, the aim of this study was to correlate the extent of contrast enhancement, diffusion restriction and SUV in hybrid ^{68}Ga -DOTATOC PET/MRI with tumor grading in therapy-naive NEN patients.

2. Material and methods

2.1. Patients

This study was performed in conformance with the Declaration of

Helsinki [21] and approved by the local ethics committee. All patients had signed a written informed consent form prior to enrolment. Between January 2013 and August 2019, a total of 26 patients (mean age 61.7 ± 14.1 years; range 24–85 years, 11 women, 15 men) with histopathologically confirmed, treatment-naïve NENs were included in this prospective study. All patients underwent a diagnostic ^{68}Ga -DOTATOC PET/MRI scan. The scans were performed in accordance with the EANM guidelines on DOTATOC PET imaging [22]. Exclusion criteria were any sort of systemic oncologic therapy before histological sampling, second malignancy, age < 18 years, and contraindications for PET/MRI.

2.2. PET/MRI

The ^{68}Ga -DOTATOC PET/MRI scans were performed on an integrated 3-Tesla PET/MRI device (Biograph mMR, Siemens Healthineers, Erlangen, Germany) with an average delay of 78.4 ± 38.2 min after intravenous injection of a mean dosage of 72.5 ± 11.2 MBq ^{68}Ga -DOTATOC. Adapted to the respective question, 18 patients received a whole-body examination (head to mid-thigh), while 8 patients underwent an abdominal examination only. A gadolinium-based contrast agent (0.2 mmol/kg body weight, Dotarem, Guerbet GmbH, Germany) was administered in all patients.

PET images were performed simultaneously with the MRI data acquisition and an acquisition time of 4 min per bed position. PET datasets were reconstructed utilizing an iterative ordered-subset expectation maximization (OSEM) algorithm, three iterations and 21 subsets, and a Gaussian filter with 4-mm full-width at half maximum (FWHM) and a 344×344 image matrix.

A two-point (fat, water) transaxial high-resolution CAIPIRINHA (CAIPI)-accelerated 3D-Dixon-VIBE (Volume Interpolated Breath-hold Examination) sequence was acquired for MR-based PET attenuation correction and scatter correction, generating a coronal four-compartment model (background, lungs, fat, muscle) [23]. In addition, a bone atlas correction and a truncation correction as proposed by Blumhagen et al. was applied. The dedicated ^{68}Ga -DOTATOC PET/MRI protocol consisted in most patients of the following sequences (Table 1):

- 1 A whole-body transverse T2-weighted (T2w) fat-suppressed half Fourier acquisition single shot turbo spin echo (HASTE) sequence in respiratory medium position and a slice thickness of 7 mm.
- 2 A whole-body axial T1-weighted (T1w) fat-suppressed (fs) (VIBE) sequence in respiratory medium position and a slice thickness of 3.5 mm.
- 3 A whole-body transverse non-motion corrected diffusion-weighted echo-planar imaging (EPI DWI) sequence (b values 0, 500, 1000) in respiratory medium position with a slice thickness of 5 mm.
- 4 Repeated axial sequences (T1w, fs, VIBE) of the upper abdomen for dynamic liver imaging (arterial phase, portal venous phase, delayed phase) following intravenous administration of a gadolinium-based contrast agent.
- 5 A whole-body transversal T1-weighted (T1w, fs, VIBE) sequence after intravenous injection of a gadolinium-based contrast agent (0.2 mmol/kg body weight, Dotarem, Guerbet GmbH, Germany) with a slice thickness of 3 mm.

In 8 patients who underwent only an abdominal examination, dynamic liver imaging was not performed or with coronary sequences instead of axial pictures. For better comparability, arterial enhancement was not considered in these patients. The further protocol remained unchanged.

2.3. Image analysis

The datasets of the ^{68}Ga -DOTATOC PET/MRI examination were analysed in two separate reading sessions by two independent radiologists with 2 and 5 years of experience in hybrid imaging at least two

weeks apart to avoid recognition bias. Analysis was performed on a dedicated Osirix Workstation (Pixmeo SARL, Bernex, Switzerland). Among other imaging features, diffusion restriction and visually increased ^{68}Ga -DOTATOC uptake above the surrounding background level were regarded as suspicious for NET. Up to five largest lesions per organ were evaluated per patient.

Following imaging parameters were obtained for all lesions: (i) NEN lesion number, (ii) location, (iii) predominant signal intensity on pre-contrast T1w and T2w images, (iv) predominant signal intensity on postcontrast arterial and portal venous phase T1w sequences, (v) diffusion restriction (ADC) and (vi) SUVmax. As previously described by Canellas et al. [6] lesions were characterized as having hypo-intense/isointense or hyperintense signal intensity relative to the surrounding tissue. Accordingly, on the postcontrast arterial and venous phase T1-weighted fat-saturated MR images NEN lesions were characterized as hypoenhancing, isoenhancing or hyperenhancing in relation to the surrounding tissue and to the autochthonous back muscles on the same slide. For DWI quantification, an ADC map was generated utilizing a dedicated hybrid imaging system software (syngo VB18 P, Siemens Healthineers GmbH, Germany). A high signal intensity in DWI and a corresponding low signal in the ADC map was regarded as diffusion restriction. The lowest ADC value per tumor (ADCmin) was measured by placing a manually drawn polygonal region of interest (ROI) exactly around the tumor mass. Additionally, we measured the maximum standardized uptake value (SUVmax) of each lesion. Therefore, a free-hand isocontour volume of interest (VOI) was drawn over the tumor mass on attenuation-corrected PET images. In order to obtain consistent results, visible necrosis was not measured if possible. In conformity with previous studies [12] lesion shape, signal intensity and contrast behaviour were taken into account of lesion characterization.

2.4. Reference standard

Histopathology served as reference standard in all 26 patients. In 16 patients histological data were obtained from the resectate of the primary tumor in order to receive the most accurate histological sampling. In 9 of 16 patients further metastases were already present at time of resection. In 5 patients resection was performed due to potential resectable liver metastases and in 4 patients to prevent complications (small bowel and colon/rectum). In 7 patients histology was confirmed by liver biopsy, for example in cancers of unknown primary (CUP), and in 3 patients by endoscopic ultrasound-guided fine-needle aspiration biopsy (EUS-FNA) of the pancreas. Based on the 2017 WHO classification [4], the NENs were divided into well- and poorly differentiated categories. The well-differentiated neuroendocrine tumors (NETs) were further subdivided utilizing the mitosis rate and Ki-67, which is a marker for the growth rate of tumors, as low-grade (G1, Ki-67 < 3 %), intermediate-grade (G2, Ki-67 3–20 %), and high-grade (G3, Ki-67 > 20 %). The poorly differentiated large-cell or small-cell neuroendocrine carcinomas (NECs) were assigned to high-grade G3, Ki-67 > 20 %. The exact Ki-67 values were available in 23 of 26 patients (missing in 1 patient with grade 3, 1 patient with grade 2, and 1 patient with grade 1).

2.5. Statistical analysis

SPSS Statistics version 24 (IBM, Armonk, NY, USA) was used for

statistical analysis. All data are presented as mean \pm standard deviation. A p value < 0.05 was considered to indicate statistical significance. For correlation analysis of aforementioned parameters and Ki-67 index, the Pearson's correlation coefficient was applied. In conformity with the classification by Cohen [24], the correlation coefficient was subdivided into the three groups, (i) weak correlation ($r \leq 0.3$), (ii) moderate correlation ($r = 0.3 - 0.5$), and (iii) strong correlation ($r > 0.5$). According to the literature, the likelihood of all estimated PET and MRI features to predict a more aggressive tumor biology (G2/G3) was independently examined using binary logistic regressions and odds ratios were computed. To investigate statistically significant differences Fisher's exact test was applied.

3. Results

A total of 26 therapy-naive NEN patients with 101 NEN lesions were included in this study, for primary tumor location and grade see Table 2. The number of tumors, divided according to tumor grading, does not allow any conclusions about the severity of disease, since a maximum of 5 lesions was measured per organ and the liver in particular presented often more metastases. In total, there was only one patient with G1 and at least 5 liver metastases, while 8 patients in stage G2/G3 had at least 5 liver metastases.

In the correlation analysis a moderate negative correlation was found between an arterial contrast enhancement and tumor grading ($r = -0.35$, $p = 0.005$, Fig. 1). There was a non-significant, weak correlation between arterial contrast enhancement and Ki-67 index ($r = -0.18$, $p = 0.19$). Also, we found a positive weak correlation of portal venous contrast enhancement with the Ki-67 index ($r = 0.28$, $p = 0.008$, Fig. 2) and with tumor grading ($r = 0.19$, $p = 0.063$). A non-significant negative weak correlation between the SUVmax and tumor grading ($r = -0.11$, $p = 0.27$) and between ADCmin and tumor grading ($r = -0.15$, $p = 0.37$) was observed.

Table 3 shows PET and MRI features in all lesions according to tumor grade. Of note are the following features, in which an association with an aggressive tumor biology (G2/G3) has been discovered: [1] presence

Table 2
Patient demographics.

Demographics	Number	Percentage
Gender (M:W)	15:11	57.7:43.3
Age (year \pm SD)	61.7 \pm 14.1	
Primary tumor location		
Small bowel	4	15.4
Stomach	2	7.7
Adrenal gland	1	3.8
Pancreas	10	38.5
Colon/Rectum	3	11.6
Lung	1	3.8
Cervix	1	3.8
CUP	4	15.4
WHO Grade		
Grade 1	10	38.5
Grade 2	11	42.3
Grade 3	5	19.2
NET	4	15.4
NEC	1	3.8
median Ki-67 index (range)		5 (1–50)

Table 1
Sequence parameters of the diagnostic MRI sequences.

Sequence	Orientation	Contrast agent	TA (s)	TE/TR (ms)	Slice thickness (mm)	Matrix size	FOV (mm)
T2w HASTE	Axial	No	66	117/1500	7.0	320 \times 259	450 \times 366
T1w fs VIBE	Axial	No	18	1.5/4.1	3.5	512 \times 317	400 \times 300
EPI DWI	Axial	No	369	86/11,900	5	192 \times 144	380 \times 285
T1w fs VIBE (dynamic)	Axial	Yes	18	1.5/4.1	3.5	512 \times 307	400 \times 300
T1w fs VIBE	Axial	Yes	18	1.5/4.1	3.5	512 \times 307	400 \times 300

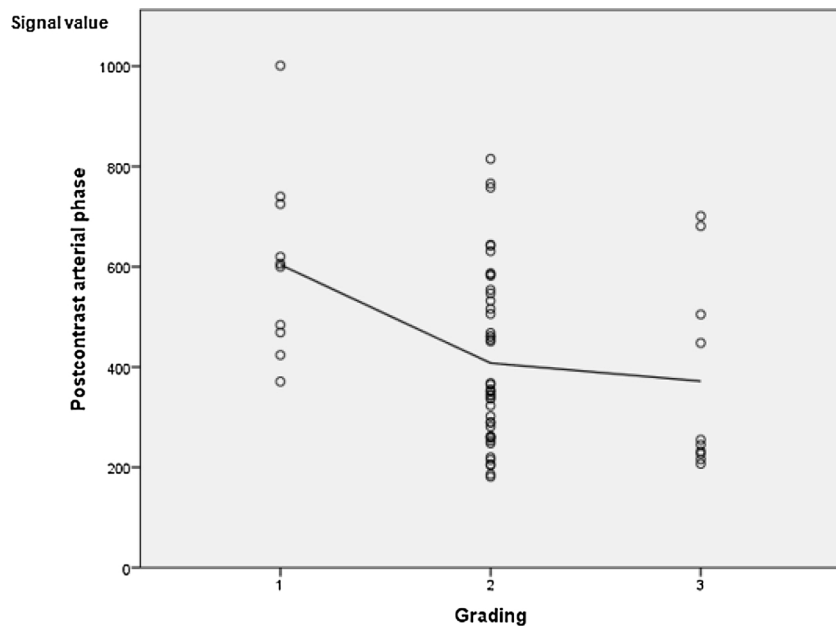


Fig. 1. Contrast-enhancement in arterial phase in comparison with WHO tumor grading in NETs.

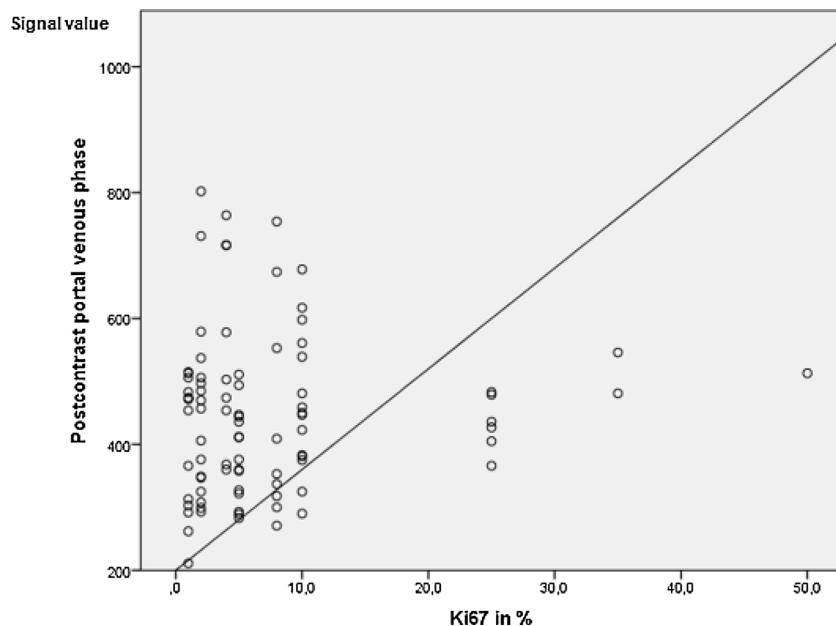


Fig. 2. Contrast-enhancement in portal venous phase in comparison with WHO tumor grading in NETs.

of liver metastases (19/35 vs. 50/66, OR = 2.6, $p = 0.042$) [2]; hyperintensity in precontrast T1-weighted images compared to muscle (4/35 vs. 41/66, OR = 12.7, $p = 0.0001$); and [3] hyperenhancing in arterial phase compared to the surrounding tissue (OR = 1.4, $p = 0.001$). The latter appeared counter-intuitive as all of the G1-lesions (10/10) but only 25/55 (45.5 %) of G2/G3 had an arterial hyperenhancement; however it might be a statistical effect due to the higher absolute number of G2/3 lesions in the study cohort. [4] Diffusion restriction (10/35 vs. 35/66, OR = 2.8, $p = 0.02$) and [5] SUVmax value above liver level (21/33 vs. 61/66, OR = 7, $p = 0.001$) (Fig. 3, Fig. 4).

4. Discussion

The present study shows that simultaneously acquired ^{68}Ga -DOTATOC PET/MRI features such as arterial and portal venous enhancement

as well as diffusion restriction and SUVmax values correlate with tumor grading/Ki-67 index in therapy-naïve NEN patients, suggesting a role for ^{68}Ga -DOTATOC PET/MRI to potentially indicate an aggressive tumor histopathology.

Tumor grading has been discovered to be a helpful predictor of clinical outcome of NEN patients [25]. Therefore, an early and accurate tumor grading prior to therapy plays a decisive role in the treatment decision of NEN patients. While in localized stages well-differentiated G1 and G2 tumors are treated with curative intent, G3 tumors or NEC are primarily addressed by systemic approaches. Furthermore, tumor grading determines intervals in diagnostic aftercare [26]. Currently, primary NEN histology is often obtained by EUS-FNA and liver biopsy. However, these procedures have limitations, since only a small piece of tissue is assessed and the tumor hotspot might not be included in the sample. As a result, misclassification of tumors can occur [27,28].

Table 3

Distribution of PET and MRI features in comparison to WHO tumor grade in neuroendocrine tumors.

	G1	G2	G3	Odds ratio G1 vs. G2/G3	P value G1 vs. G2/G3
Patient number	10	11	5		
Lesion number	35	54	12		
Tumor location					
Small bowel	2	2	0		
Liver	19	45	5	2.6	0.042
Lymph node	2	1	1		
Stomach	2	0	0		
Adrenal gland	0	0	2		
Osseous	3	1	0		
Pancreas	4	3	3		
Colon/Rectum	2	1	0		
Lung	1	0	0		
Cervix	0	0	1		
Tumor pattern					
T1-weighted image					
Hyperintense to organ	0 (0 %)	2 (3.7 %)	0 (0 %)	1.5	0.54
Isointense/hypointense to organ	35 (100 %)	52 (96.3 %)	12 (100 %)		
Hyperintense to muscle	4 (11.4 %)	33 (61.1 %)	8 (66.6 %)	12.7	0.0001
Isointense/hypointense to muscle	31 (88.6 %)	21 (38.9 %)	4 (33.4 %)		
T2-weighted image					
Hyperintense to organ	27 (77.1 %)	52 (96.3 %)	7 (58.3 %)	2.5	0.14
Isointense/hypointense to organ	8 (22.9 %)	2 (3.7 %)	5 (41.7 %)		
Hyperintense to muscle	35 (100 %)	54 (100 %)	12 (100 %)		
Isointense/hypointense to muscle	0 (0 %)	0 (0 %)	0 (0 %)		
Arterial phase					
Hyperenhancing to organ	10 (100 %)	23 (51.1 %)	2 (20 %)	1.4	0.001
Iso-/hypoenhancing to organ	0 (0 %)	22 (48.9 %)	8 (80 %)		
Hyperenhancing to muscle	9 (90 %)	45 (100 %)	9 (90 %)	6	0.286
Iso-/hypoenhancing to muscle	1 (10 %)	0 (0 %)	1 (10 %)		
Portal venous phase					
Hyperenhancing to organ	10 (28.6 %)	4 (7.4 %)	6 (50 %)	0.45	0.12
Iso-/hypoenhancing to organ	25 (71.4 %)	50 (92.6 %)	6 (50 %)		
Hyperenhancing to muscle	35 (100 %)	54 (100 %)	12 (100 %)		
Iso-/hypoenhancing to muscle	0 (0 %)	0 (0 %)	0 (0 %)		
Diffusion restriction (ADC)	10 (28.6 %)	26 (48.1 %)	9 (75.5 %)	2.8	0.02
SUVmax lesions > SUVmax Liver	21 (60 %)	50 (92.6 %)	11 (91.7 %)	7.0	0.001

Therefore, other non-invasive methods, such as oncologic imaging should serve as a helpful alternative to predict tumor grading as accurately as possible, prior to a potentially extensive abdominal surgery.

In addition to established imaging criteria like local invasion or the presence of metastases, Jang et al. discovered that NEN lesion hyperenhancement in the arterial phase occurs more frequently in pancreatic G1 tumors compared to G2/G3 tumors in MRI [20,29]. This is supported by our results showing that 100 % of G1 tumors had arterial hyperenhancement compared to only 45.5 % of G2/G3 tumors. Furthermore, we found that the Ki-67 index had a significantly positive correlation with NEN lesion enhancement in the portal venous phase, meaning that higher proliferative NEN lesions had a stronger venous enhancement. As a possible explanation, this might have been due to incipient necrosis and increasing heterogeneity by the high proliferative tumors, so that the perfusion is delayed and hyperenhancement is seen rather in portal venous phase. This is consistent with the fact that necrosis is generally more frequently observed in advanced tumor lesions [30]. Although it has been avoided to measure necrotic tumor areas, a morphological correlation for necrosis is not necessarily visible, since changes might only occur on a cellular level [30].

Pancreatic NEN grading by means of DW-MRI has already been examined in studies [14,31,32]. Even though a significant negative correlation between ADC values and tumor grade, as for example described by Kim et al. [31] and Pereira et al. [14], could not be found in our study, diffusion restriction was 2.8 times more frequent in aggressive tumor grades ($p = 0.02$), supporting previous results by De Robertis et al. [33] and Canellas et al. [6].

When comparing PET parameters like SUVmax with tumor grading or the Ki-67 index, very similar results could be observed: SUVmax values above liver level were seven times more frequent in aggressive tumor grades ($p = 0.001$). The study of Kayani et al. supports these results in a study with 38 patients with neuroendocrine tumors using ^{68}Ga -DOTATATE and ^{18}F -FDG in combined PET/CT and was even able to determine a significant correlation with tumor grading [34].

Our study has some limitations. First, the study cohort of 26 patients was rather small. However, NENs are rare tumors and primary staging is seldom performed on PET/MRI. Second, this study did not exclusively examine entero-pancreatic NEN, but all types of NEN were included. Ki-67 index was missing in three patients. Also, in some lesions the cystic and necrotic areas might not have been completely excluded from measurement which could to some minor extent have affected the results, for example increase ADC values of aggressive tumors. Finally, different types of biopsies were included as described above and therefore, an undergrading of some tumors due to limited sampling is possible. However, in cases with surgically resected NEN, histopathology from the whole specimen was obtained.

In conclusion, the present study indicates that ^{68}Ga -DOTATOC PET/MRI features like arterial and portal venous enhancement, diffusion restriction and SUVmax are associated with tumor grading and might be used to predict NEN grade and aggressiveness in a non-invasive one-stop-shop examination.

Ethical approval

All procedures performed were in accordance with the ethical standards of the institutional research committee and with the principles of the 1964 Declaration of Helsinki and its later amendments.

Informed consent

The study was approved by the institutional review board (IRB) and written informed consent was waived by the IRB. Informed consent was obtained from all individual participants included in the study.

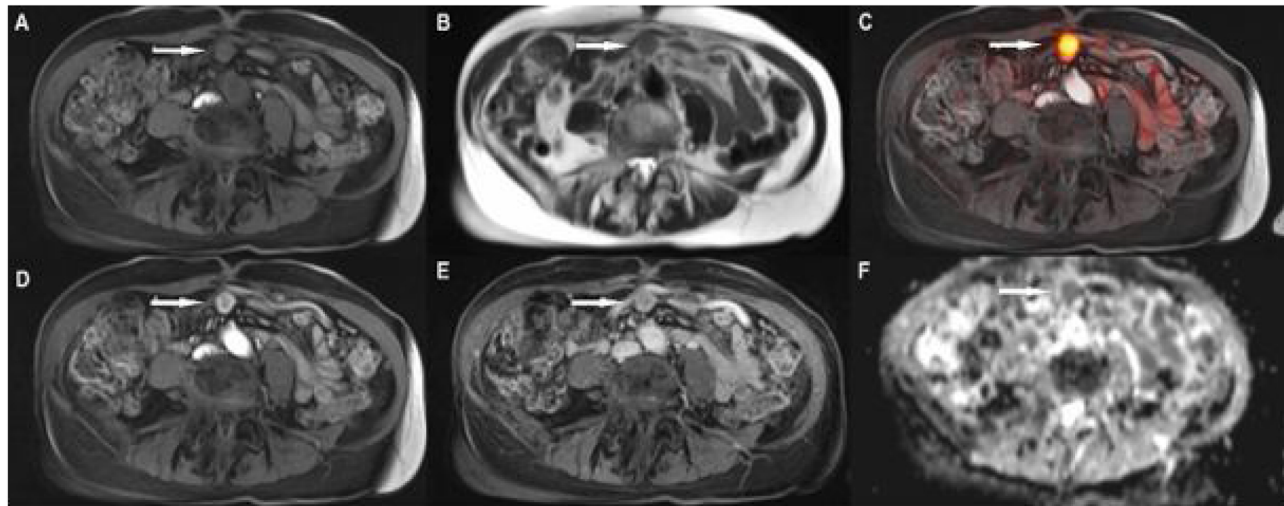


Fig. 3. PET/MR images of a 69-year-old woman with a mesenteric lymph node metastasis of a pancreatic neuroendocrine tumor grade I. Precontrast T1- (A) and T2- (B) weighted images show a rather iso-/hypointensity. After contrast media application the node shows a hyperenhancement in arterial (D) and a rather iso-enhancement in portal venous phase (E). A strong ^{68}Ga -DOTATOC uptake (C) and diffusion restriction on the ADC map (F) is visible.

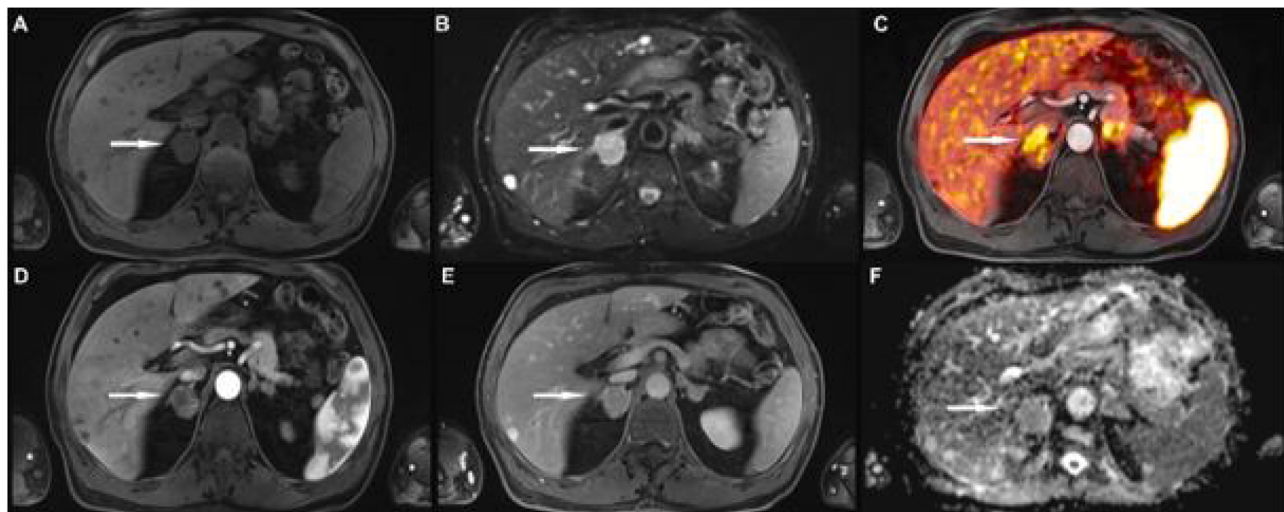


Fig. 4. PET/MR images of a 70-year-old man with a neuroendocrine tumor in the right adrenal gland grade III. The tumor shows a hypointensity in precontrast T1- (A) and a hyperintensity in T2- (B) weighted images. After contrast media application the tumor shows an isoenhancement in arterial (D) and a slight hyperenhancement in portal venous (E) phase. Note the pathologically increased ^{68}Ga -DOTATOC uptake (C) and diffusion restriction on the ADC map (F).

Declaration of Competing Interest

None.

CRediT authorship contribution statement

Nils Martin Bruckmann: Data curation, Formal analysis, Investigation, Validation, Visualization, Writing - original draft. **Christoph Rischpler:** Formal analysis, Validation, Writing - original draft. **Julian Kirchner:** Conceptualization, Investigation, Methodology, Supervision, Writing - review & editing. **Lale Umutlu:** Supervision, Resources. **Ken Herrmann:** Supervision, Resources. **Marc Ingenwerth:** Investigation, Resources, Writing - review & editing. **Sarah Theurer:** Investigation, Resources, Writing - review & editing. **Harald Lahner:** Supervision, Resources. **Gerald Antoch:** Supervision, Resources. **Lino M. Sawicki:** Conceptualization, Investigation, Methodology, Supervision, Writing - review & editing.

References

- [1] B.G. Taal, O. Visser, Epidemiology of neuroendocrine tumours, *Neuroendocrinology* 80 (Suppl 1) (2004) 3–7.
- [2] J.C. Yao, M. Hassan, A. Phan, C. Dagleish, C. Leary, J.E. Mares, et al., One hundred years after “carcinoid”: epidemiology of and prognostic factors for neuroendocrine tumors in 35,825 cases in the United States, *J. Clin. Oncol.* 26 (18) (2008) 3063–3072.
- [3] D.S. Klimstra, H. Beltran, R. Lilienbaum, E. Bergsland, The Spectrum of neuroendocrine tumors: histologic classification, unique features and areas of overlap, *Am. Soc. Clin. Oncol. Educ. Book* (2015) 92–103.
- [4] S.M. Chai, I.S. Brown, M.P. Kumarasinghe, Gastroenteropancreatic neuroendocrine neoplasms: selected pathology review and molecular updates, *Histopathology* 72 (1) (2018) 153–167.
- [5] P.L. Kunz, Carcinoid and neuroendocrine tumors: building on success, *J. Clin. Oncol.* 33 (16) (2015) 1855–1863.
- [6] R. Canellas, G. Lo, S. Bhowmik, C. Ferrone, D. Sahani, Pancreatic neuroendocrine tumor: Correlations between MRI features, tumor biology, and clinical outcome after surgery, *J. Magn. Reson. Imaging* 47 (2) (2018) 425–432.
- [7] A.D. Singh, D.S. Klimstra, Well-differentiated pancreatic neuroendocrine tumours (PanNETs) and poorly differentiated pancreatic neuroendocrine carcinomas (PanNECs): concepts, issues and a practical diagnostic approach to high-grade (G3) cases, *Histopathology* 72 (1) (2018) 168–177.

- [8] M.S. Hofman, W.F. Eddie Lau, R.J. Hicks, Somatostatin receptor imaging with ⁶⁸Ga-DOTATATE PET/CT: clinical utility, normal patterns, pearls, and pitfalls in interpretation, *Radiographics*. 35 (2) (2015) 500–516.
- [9] T.A. Hope, M.H. Pampaloni, E. Nakakura, H. VanBroeklin, J. Slater, S. Jivan, et al., Simultaneous ⁶⁸Ga-DOTA-TOC PET/MRI with gadoxetate disodium in patients with neuroendocrine tumor, *Abdom. Imaging* 40 (6) (2015) 1432–1440.
- [10] G. Treglia, P. Castaldi, G. Rindi, A. Giordano, V. Rufini, Diagnostic performance of Gallium-68 somatostatin receptor PET and PET/CT in patients with thoracic and gastroenteropancreatic neuroendocrine tumours: a meta-analysis, *Endocrine*. 42 (1) (2012) 80–87.
- [11] K.J. Beiderwellen, T.D. Poepel, V. Hartung-Knemeyer, C. Buchbender, H. Kuehl, A. Bockisch, et al., Simultaneous ⁶⁸Ga-DOTATOC PET/MRI in patients with gastroenteropancreatic neuroendocrine tumors: initial results, *Invest. Radiol.* 48 (5) (2013) 273–279.
- [12] L.M. Sawicki, C. Deuschl, K. Beiderwellen, V. Ruhlmann, T.D. Poepel, P. Heusch, et al., Evaluation of ⁶⁸Ga-DOTATOC PET/MRI for whole-body staging of neuroendocrine tumours in comparison with ⁶⁸Ga-DOTATOC PET/CT, *Eur. Radiol.* 27 (10) (2017) 4091–4099.
- [13] C. Schmid-Tannwald, A. Oto, M.F. Reiser, C.J. Zech, Diffusion-weighted MRI of the abdomen: current value in clinical routine, *J. Magn. Reson. Imaging* 37 (1) (2013) 35–37.
- [14] J.A.S. Pereira, E. Rosado, M. Bali, T. Metens, S.L. Chao, Pancreatic neuroendocrine tumors: correlation between histogram analysis of apparent diffusion coefficient maps and tumor grade, *Abdom. Imaging* 40 (8) (2015) 3122–3128.
- [15] E. Lotfali zadeh, M. Ronot, M. Wagner, J. Cros, A. Couvelard, M.P. Vullierme, et al., Prediction of pancreatic neuroendocrine tumour grade with MR imaging features: added value of diffusion-weighted imaging, *Eur. Radiol.* 27 (4) (2017) 1448–1459.
- [16] M.Ö. Öksüz, L. Winter, C. Pfannenberg, G. Reischl, K. Müssig, R. Bares, et al., Peptide receptor radionuclide therapy of neuroendocrine tumors with ⁹⁰Y-DOTATOC: Is treatment response predictable by pre-therapeutic uptake of ⁶⁸Ga-DOTATOC? *Diagn. Interv. Imaging* (2014) jnumed.119.
- [17] S.E. Rha, S.E. Jung, K.H. Lee, Y.M. Ku, J.Y. Byun, J.M. Lee, CT and MR imaging findings of endocrine tumor of the pancreas according to WHO classification, *Eur. J. Radiol.* 62 (3) (2007) 371–377.
- [18] P.E. Humphrey, F. Alessandrino, A.M. Bellizzi, K.J. Morte, Non-hyperfunctioning pancreatic endocrine tumors: multimodality imaging features with histopathological correlation, *Abdom. Imaging* 40 (7) (2015) 2398–4010.
- [19] R. Manfredi, M. Bonatti, W. Mantovani, R. Grazianni, D. Segala, P. Capelli, et al., Non-hyperfunctioning neuroendocrine tumours of the pancreas: MR imaging appearance and correlation with their biological behaviour, *Eur. Radiol.* 23 (11) (2013) 3029–3039.
- [20] C. Guo, X. Chen, W. Xiao, Q. Wang, K. Sun, Z. Wang, Pancreatic neuroendocrine neoplasms at magnetic resonance imaging: comparison between grade 3 and grade 1/2 tumors, *Onco. Ther.* 10 (2017) 1465–1474.
- [21] World Medical Association Declaration of Helsinki: ethical principles for medical research involving human subjects, *JAMA* 310 (November 20) (2013) 2191–2194.
- [22] I. Virgolini, V. Ambrosini, J.B. Bomanji, R.P. Baum, S. Fanti, M. Gabriel, et al., Procedure guidelines for PET/CT tumour imaging with ⁶⁸Ga-DOTA- conjugated peptides: ⁶⁸Ga-DOTA-TOC, ⁶⁸Ga-DOTA-NOC, ⁶⁸Ga-DOTA-TATE, *Eur. J. Nucl. Med. Mol. Imaging* 37 (10) (2010) 2004–2010.
- [23] H.H. Quick, Integrated PET/MR, *J. Magn. Reson. Imaging* 39 (2) (2014) 243–258.
- [24] J. Cohen, Statistical Power Analysis for the Behavioural Sciences, NJ Lawrence Earlbauim Assoc., Hillside, 1988.
- [25] E. Martin-Perez, J. Capdevila, D. Castellano, P. Jimenez-Fonseca, R. Salazar, A. Beguiristain-Gomez, et al., Prognostic factors and long-term outcome of pancreatic neuroendocrine neoplasms: Ki-67 index shows a greater impact on survival than disease stage. The large experience of the spanish national tumor registry (RGETNE), *Neuroendocrinology*. 98 (2) (2013) 156–168.
- [26] S. Faiss, C. Fottner, B. Gebauer, P. Goretzki, P.L. Jansen, G. Pöpperl, et al., S2k-Leitlinie Neuroendokrine Tumore Practice Guideline Neuroendocrine Tumors., 2018, pp. 583–681.
- [27] V.L. Weiss, C. Kiernan, J. Wright, N.B. Merchant, A.C. Coogan, C. Shi, Fine-needle aspiration-based grading of pancreatic neuroendocrine neoplasms using Ki-67: is accurate WHO grading possible on cytologic material? *J. Am. Soc. Cytopathol.* 7 (3) (2018) 154–159.
- [28] L. Fuccio, A. Larghi Dr, Endoscopic ultrasound-guided fine needle aspiration: how to obtain a core biopsy? *Endosc. Ultrasound* 3 (2) (2014) 71–81.
- [29] K.M. Jang, S.H. Kim, S.J. Lee, D. Choi, The value of gadoxetic acid-enhanced and diffusion-weighted MRI for prediction of grading of pancreatic neuroendocrine tumors, *Acta radiol.* 55 (2) (2014) 140–148.
- [30] B.M. Schaarschmidt, C. Buchbender, F. Nensa, J. Grueneien, B. Gomez, J. Köhler, et al., Correlation of the apparent diffusion coefficient (ADC) with the standardized uptake value (SUV) in lymph node metastases of non-small cell lung cancer (NSCLC) patients using hybrid ⁸⁹FDG PET/MRI, *PLoS One* 10 (1) (2015) 1–14.
- [31] M. Kim, T.W. Kang, Y.K. Kim, S.H. Kim, W. Kwon, S.Y. Ha, et al., Pancreatic neuroendocrine tumour: correlation of apparent diffusion coefficient or WHO classification with recurrence-free survival, *Eur. J. Radiol.* 85 (3) (2016) 680–687.
- [32] Y. Wang, Z.E. Chen, V. Yaghmai, P. Nikolaidis, R.J. McCarthy, L. Merrick, et al., Diffusion-weighted MR imaging in pancreatic endocrine tumors correlated with histopathologic characteristics, *J. Magn. Reson. Imaging* 33 (5) (2011) 1071–1079.
- [33] R. De Robertis, S. Cingarlini, P.T. Martini, S. Ortolani, G. Butturini, L. Landoni, et al., Pancreatic neuroendocrine neoplasms: magnetic resonance imaging features according to grade and stage, *World J. Gastroenterol.* 23 (2) (2017) 275–285.
- [34] I. Kayani, J.B. Bomanji, A. Groves, G. Conway, S. Gacinovic, T. Win, et al., Functional imaging of neuroendocrine tumors with combined PET/CT using ⁶⁸Ga-DOTATATE (Dota-DPhe1, Tyr3-octreotide) and ¹⁸F-FDG, *Cancer*. 112 (11) (2008) 2447–2455.



Research article

Comparison of pre- and post-contrast-enhanced attenuation correction using a CAIPI-accelerated T1-weighted Dixon 3D-VIBE sequence in ^{68}Ga -DOTATOC PET/MRI



Nils Martin Bruckmann ^{a,*}, Maike E. Lindemann ^b, Johannes Grueneisen ^c, Hong Grafe ^{b,d}, Yan Li ^c, Lino M. Sawicki ^a, Christoph Rischpler ^d, Ken Herrmann ^d, Lale Umutlu ^c, Harald H. Quick ^b, Benedikt Michael Schaarschmidt ^c

^a Department of Diagnostic and Interventional Radiology, University Dusseldorf, Medical Faculty, Dusseldorf, D-40225, Germany

^b High-Field and Hybrid MR Imaging, University Hospital Essen, University of Duisburg-Essen, Essen, D-45147, Germany

^c Department of Diagnostic and Interventional Radiology and Neuroradiology, University Hospital Essen, University of Duisburg-Essen, Essen, D-45147, Germany

^d Department of Nuclear Medicine, University Hospital Essen, University of Duisburg-Essen, Essen, D-45147, Germany

ARTICLE INFO

Keywords:
PET/MRI
Attenuation correction
Contrast agent

ABSTRACT

Objectives: To investigate the influence of contrast agent administration on attenuation correction (AC) based on a CAIPIRINHA (CAIPI)-accelerated T1-weighted Dixon 3D-VIBE sequence in ^{68}Ga -DOTATOC PET/MRI.

Material and methods: Fifty-one patients with neuroendocrine tumors underwent whole-body ^{68}Ga -DOTATOC PET/MRI for tumor staging. Two PET reconstructions were performed using AC-maps that were created using a high-resolution CAIPI-accelerated Dixon-VIBE sequence with an additional bone atlas and truncation correction using the HUGE (B0 homogenization using gradient enhancement) method before and after application of Gadolinium (Gd)-based contrast agent. Standardized uptake values (SUVs) of 21 volumes of interest (VOIs) were compared between in both PET data sets per patient. A student's *t*-test for paired samples was performed to test for potential differences between both AC-maps and both reconstructed PET data sets. Bonferroni correction was performed to prevent α -error accumulation, $p < 0.0024$ was considered to indicate statistical significance.

Results: Significant quantitative differences between SUVmax were found in the perirenal fat ($19.65 \pm 48.03\%$, $p < 0.0001$), in the axillary fat ($17.46 \pm 63.67\%$, $p < 0.0001$) and in the dorsal subcutaneous fat on level of lumbar vertebral body L4 ($10.26 \pm 25.29\%$, $p < 0.0001$). Significant differences were also evident in the lungs apical ($5.80 \pm 10.53\%$, $p < 0.0001$), dorsal at the level of the pulmonary trunk ($15.04 \pm 19.09\%$, $p < 0.0001$) and dorsal in the basal lung ($51.27 \pm 147.61\%$, $p < 0.0001$).

Conclusion: The administration of (Gd)-contrast agents in this study has shown a considerable influence on the AC-maps in PET/MRI and, consequently impacted quantification in the reconstructed PET data. Therefore, dedicated PET/MRI staging protocols have to be adjusted so that AC-map acquisition is performed prior to contrast agent administration.

1. Introduction

Due to successful combination of magnetic resonance imaging (MRI) and positron emission tomography (PET) into one single hybrid PET/MRI system, diagnostic imaging profits from synergistic effects of both modalities [1–4]. While MRI offers an excellent soft tissue contrast and provides functional imaging aspects like diffusion weighted imaging

(DWI), the evaluation of radiotracer metabolism using PET provides high sensitivity. The combined analysis of these data increases the diagnostic confidence and might change clinical management in oncologic applications [5–7]. Furthermore, especially younger patients might benefit from the clinically relevant dose reduction in comparison to PET/CT [8].

During PET data acquisition, photons are attenuated by surrounding

* Corresponding author at: University Dusseldorf, Medical Faculty, Department of Diagnostic and Interventional Radiology, Moorenstrasse 5, Dusseldorf, D-40225, Germany.

E-mail address: Nils-Martin.Bruckmann@med.uni-duesseldorf.de (N.M. Bruckmann).

body tissues and hardware components before they reach the PET detector [3]. This photon attenuation leads to a systematic bias in PET-based tracer quantification, and, consequently, PET data reconstruction requires accurate means for attenuation correction (AC) in order to provide correct quantitative results.

In PET/CT, CT imaging provides useful information about the electron density of individual tissues and about the geometric representation of photon-attenuating tissues within the body. These data can directly be transformed by converting the measured CT-based Hounsfield Units (HU) of each tissue to linear attenuation coefficients (LACs) at the PET emission energy level of 511 keV. Thus, CT data can be used for CT-based attenuation correction (CTAC), which is a well-established method in PET/CT [3,9,10].

In PET/MRI, attenuation correction is inherently challenging. The MR signal is not related to the electron density of examined tissues and cannot directly be used for MR attenuation correction (MRAC) [11]. In clinical application of PET/MRI the most commonly used method for MRAC today is a segmentation approach based on a MR Dixon-VIBE (volumetric interpolated breath-hold examination) sequence [11,12]. MR images are segmented into four tissue classes (air, lung, fat, soft tissue) and a predefined LAC is assigned to each segmented tissue class to generate a four-compartment attenuation map, the so-called μ map [3, 11,13]. In recent years such MRAC methods have been further refined and initial limitations compared to CTAC have been reduced by adding bone models as further tissue class and by adding truncation correction to the μ map such as the fully MR-based HUGE (B0 homogenization using gradient enhancement) method proposed by Blumhagen et al. [14,15]. In addition, a CAIPIRINHA-accelerated (Controlled aliasing in parallel imaging results in higher acceleration) Dixon 3D-VIBE (MRAC_{caipi}) has recently been introduced to further improve the spatial resolution of the resulting μ maps compared to the initial Dixon-VIBE sequences [16,17].

In general, the manufacturers of PET/MRI systems recommend acquisition of a non-contrast enhanced Dixon MRAC sequence for μ map reconstruction to ensure an optimal tissue classification [18]. Accordingly, the Dixon MRAC sequence has to be performed at the beginning of the whole-body PET/MRI examination and, thus, before potential administration of intravenous contrast agent. In a clinical setting, however, PET/MRI protocols for ⁶⁸Ga-tracer based examinations often consist of two steps: first, whole-body imaging providing an overview and second, a dedicated imaging of individual organs, such as in ⁶⁸Ga-PSMA for prostate or ⁶⁸Ga-DOTATOC for gastrointestinal cancer imaging. In such protocol setting, the administration of contrast agent during the acquisition of whole-body sequences might lead to μ map reconstruction with contrast enhanced Dixon MRAC sequences for dedicated organ imaging or vice versa. Since Gd-based contrast agents lead to a reduction in T1-relaxation of blood and tissue, tissue segmentation in the post-contrast μ map may be influenced and, consequently, falsify PET tracer quantification in whole-body PET/MRI, as has been shown in previous studies for an older version of the Dixon MRAC sequence [19].

According to these practical requirements of the clinical workflow in selected PET/MR applications, the purpose of this retrospective study was to evaluate a potential influence of (Gd)-contrast agent administration on MR-based attenuation correction using a state of the art CAIPI-accelerated Dixon-based sequence with high spatial resolution, bone atlas and MR-based truncation correction in ⁶⁸Ga-DOTATOC PET/MRI. The overarching aim of this study is to test, whether the latest version of the Dixon MRAC sequence and its segmentation algorithm provides identical results before and after contrast agent administration in a clinical setting, since this would provide a higher flexibility for the planning of complex clinical PET/MRI protocols.

2. Material and methods

2.1. Patients

A total of 51 patients (30 female, 21 male; mean age 55 ± 17 years, mean body mass index (BMI) 24.9 ± 4.4 kg/m²) with histopathologically proven diagnosis of a neuroendocrine tumor were enrolled in this retrospective study. In all patients, a whole-body ⁶⁸Ga-DOTATOC PET/MRI examination and further single-organ PET/MRI examinations were performed between August 2018 and January 2020. This study was approved by the institutional review board (application number: 20-9219-BO) and performed in accordance with the regulations of the Declaration of Helsinki [20].

2.2. PET/MR imaging

All PET/MRI examinations were performed using an integrated 3.0-Tesla PET/MRI system Biograph mMR (Siemens Healthcare GmbH, Erlangen, Germany; Version: syngo MR E11). PET/MRI exams were started with an average delay of 48 ± 24 min after injection of a body-weight adapted dosage of ⁶⁸Ga-DOTATOC with a mean activity of 79 ± 13 MBq. The field of view (FOV) included the body volume from head to the mid-thigh. PET images were acquired simultaneously to MRI data acquisition with an acquisition time of 3 min per bed position. Reconstruction of PET datasets was conducted using an iterative 3D ordinary Poisson ordered-subset expectation maximization (3D OP-OSEM) algorithm, 3 iterations and 21 subsets, Gaussian filter: Full Width at Half Maximum (FWHM) 4.0 mm, scatter correction and a 344 × 344 image matrix with a voxel size of 2.09 × 2.09 × 2.03 mm. Depending on the patient's height, up to four flexible radiofrequency (RF) body array coils were applied together with the spine array and head/neck array coils for MR imaging.

2.3. Attenuation correction

Tissue AC and scatter correction were performed using the syngo MR E11 P software platform (Siemens Healthcare GmbH, Erlangen, Germany). A transaxial acquired high-resolution CAIPIRINHA (CAIPI)-accelerated T1-weighted three-dimensional (3D) Dixon-VIBE sequence [16], providing four sets of MR images (T1-weighted in- and opposed-phase, fat and water images) was applied. This MR image information serves an in-line image segmentation algorithm to generate a five-compartment attenuation μ map (background air, lungs, fat, muscle and bone) [21,22] and assigns specific linear LACs to each segmented compartment: soft tissue (0.1 cm⁻¹), fat (0.0854 cm⁻¹), lung (0.0224 cm⁻¹), air (0.0 cm⁻¹) and continuous LACs for bone (0.1 cm⁻¹ up to 0.2485 cm⁻¹). The generation of MR-based μ maps for AC and scatter correction was performed in coronal orientation. Following scan parameters were used for the Dixon-VIBE soft-tissue AC sequence: parallel imaging acceleration factor R = 5; matrix 390 × 240 with 1.3 × 1.3 mm² in-plane pixel size, 136 slices each 3.0 mm, flip angle 10°, TR 3.8 ms, TE1/TE2 1.2/2.4 ms, TA 10.6 s per bed position. To prevent the truncation of external body parts, mainly the arms, due to the limited transaxial FOV in MR imaging, the HUGE-technique (B0 homogenization using gradient enhancement) proposed by Blumhagen et al. [14] in its latest product implementation [15] was applied.

2.4. MRI protocol

The MRI protocol in this study comprised the following sequences (Fig. 1). MRI contrast-enhancement was achieved with intravenous injection of a gadolinium-based contrast agent (0.2 mmol/kg body weight, Dotarem, Guerbet GmbH, Germany).

Pre-contrast acquisition:

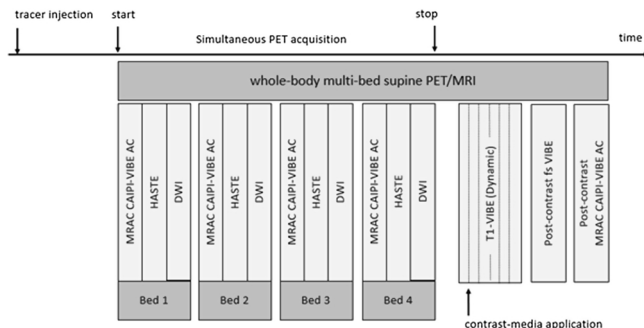


Fig. 1. PET/MRI protocol for gastrointestinal tumor imaging. MRAC (CAIPI-accelerated T1-weighted 3D Dixon-VIBE) was acquired twice in this protocol: first, at the beginning of the examination with simultaneous PET acquisition and, second, at the end of the protocol following contrast-media application.

- 1 MRAC: A whole-body axial high-resolution CAIPIRINHA-accelerated T1-weighted (T1w) three-dimensional (3D) Dixon-VIBE soft-tissue AC sequence with a slice thickness of 3 mm.
- 2 HASTE: A whole-body axial T2-weighted (T2w) fat-suppressed (fs) half Fourier acquisition single shot turbo spin echo (HASTE) sequence in respiratory medium position and a slice thickness of 7 mm.
- 3 DWI: A whole-body transverse diffusion-weighted echo-planar imaging (EPI DWI) sequence (*b*-values 0, 500, 1000) in respiratory medium position with a slice thickness of 5 mm.

Post-contrast acquisition:

- 4 T1-VIBE (dynamic): Repeated axial sequences (T1w, fs, VIBE) of the upper abdomen for dynamic liver imaging (arterial phase, portal venous phase, delayed phase)
- 5 T1-VIBE: A whole-body axial T1-weighted (T1w, fs, VIBE) sequence with a slice thickness of 3 mm.
- 6 MRAC: A whole-body axial high-resolution CAIPI-accelerated T1-weighted 3D Dixon-VIBE soft-tissue AC sequence with a slice thickness of 3 mm.

The acquisition times of AC-maps before and after the administration of contrast media were separated by about 15 min in this study.

2.5. Data processing

The PET data for each patient was reconstructed twice: 1. using the native pre-contrast μ map, and 2. using the post-contrast μ map. Both reconstructed PET data sets were then also processed to form PET difference maps for each patient. These PET difference maps allowed a quantitative evaluation of relative differences (SUV) in all PET data as described in the following.

2.6. Image analysis

All PET images were analyzed with the dedicated image processing software OsiriX (Version 9.0.2, Pixmeo SARL, Bernex, Switzerland). The two pre- and post-contrast MRAC data (μ maps) for each patient were compared slice by slice and MRAC difference maps for each patient were reconstructed to visualize relative qualitative differences in resulting μ maps as an indicator for potential changes in the μ maps due to contrast-agent administration. All resulting μ maps were evaluated for potential artifacts.

Based on the method described by Heusch et al. [23], a total of 21 subsequent volume of interests (VOIs) were manually drawn for each patient data set in the T2-HASTE sequence: a 3.0 cm^3 VOI in physiological liver tissue (unremarkable appearance on MR and PET) in the

right liver lobe (Segment VII). If this was not possible, e.g. due to tumor infiltration or resection, liver segment II was chosen; 1.0 cm^3 VOIs were placed in physiological tissue of the left ventricular myocardium (apical left ventricular wall), the lung (7 VOIs: right lung apical above aortic arch; right ventral, dorsal and medial on level of the pulmonary trunk and in the basal lung), mediastinal blood pool (right atrium), perirenal and perirectal fat, subcutaneous fat (5 VOIs: axillary right, right ventral and dorsal on level of lumbar vertebral body L4, right ventral and dorsal on level of the femoral head), urinary bladder, psoas muscle and bone marrow (on level of L4 vertebral body) (Fig. 2). Afterwards, the ^{68}Ga -DOTATOC PET images, reconstructed using both μ maps acquired before and after administration of contrast medium, were fused with the HASTE-sequence, so that the 21 VOIs per patient in each of the two PET datasets were measured in exactly the same position. A potential minimal deviation due to patient movement between the acquisitions of both μ maps was neglected. In the 21 VOIs SUVmax, SUVmean and SUVpeak were assessed for every organ site. Relative difference images between pre- and post-contrast agent μ maps and reconstructed PET data were calculated using Matlab (MATrixLABoratory, Mathworks, Natick, USA).

2.7. Statistics

Statistical analysis was performed using SPSS 24™ (IBM, Armonk, NY, USA). All data are presented as mean \pm standard deviation. A Student's *t*-test for paired samples was performed to test for potential differences of the mean values of SUVmax, SUVmean and SUVpeak. A Bonferroni correction was applied to prevent α -error accumulation. A *p* value < 0.0024 was considered to indicate statistical significance.

3. Results

^{68}Ga -DOTATOC PET/MRI acquisition was completed successfully in all 51 patients. Due to prior resection, SUV values of liver segment VII and II could not be measured in one (1/51) patient, respectively. For each patient, two μ maps (pre- and post-contrast) were successfully acquired and two PET data sets per patient were reconstructed, serving as basis for further quantitative evaluation.

The mean time between acquisition of the first non-contrast μ map and the second post-contrast μ map was separated by about 15 min in this study and the time between Gd-contrast application and acquisition of the post-contrast μ map after acquisition of the dynamic VIBE sequences was about 5 min (Fig. 1).

The visual evaluation of the μ maps showed marked differences in relative attenuation in post-contrast AC-maps especially in the lungs of (90.2 % of the patients (46/51) with proof of additional perihilar soft tissue segmentation and in the fatty tissue of all patients (Table 1, Fig. 3). In the post-contrast μ maps it was observed that fatty tissue was partially segmented with an additional compartment in all patients. This second compartment within fatty tissue was automatically assigned with a LAC of 0.0927 cm^{-1} , which is between the LAC of soft tissue (0.1 cm^{-1}) and fat (0.0854 cm^{-1}). In 27.5 % (14/51 patients), additional soft tissue in the bone marrow could also be detected.

Furthermore, in 3.9 % (2/51) of the patients there was a lack of signal from the skull base and a lack of signal from parts of the axial skeleton in the post-contrast AC-map, respectively. In 5.9 % (3/51) a small offset of the axial skeleton was detectable. Consequently, LAC of bone in these three cases was set equal to the LAC of soft tissue. This resulted in a slight systematic underestimation of PET data in these bone regions. However, this did not directly affect any of the chosen volumes of interest (Fig. 3). In one patient (1/51), a complete misclassification of the internal organs and a "swap" of fat and soft tissue could be observed (Fig. 4). The HUGE-technique for truncation correction provided correct results in all patients (51/51).

When comparing the mean values in PET images before and after the administration of contrast agents, significant quantitative differences between SUVmax measurements were found in the perirenal fat

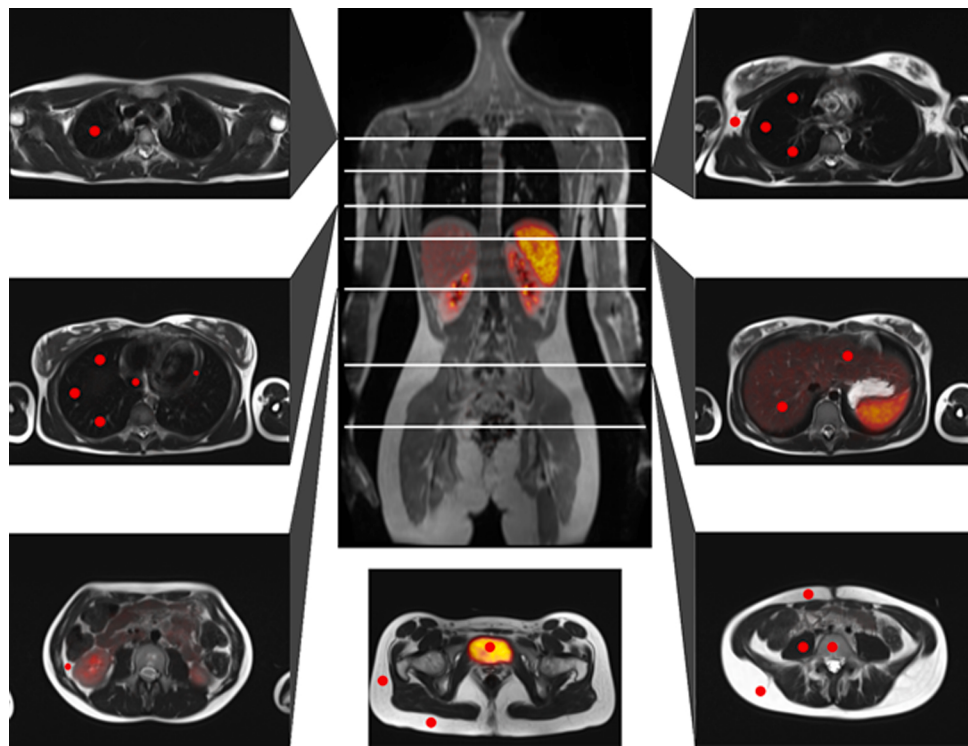


Fig. 2. Schematic overview of the 21 selected VOIs in each patient (missing: VOI in the perirectal fat).

Table 1

Listing of absolute patient numbers and according percentage of visual differences between pre- and post-contrast AC-maps in all 51 patients.

Findings	Absolute	Percentage (%)
Segmentation of additional soft tissue		
- Perirenal and subcutaneous fat	51/51	100
- Lung	46/51	90.2
- Bone marrow	14/51	27.5
Missegmentation of bone		
- Offset of axial skeleton	3/51	5.9
- Lack of signal from skull base	2/51	3.9
- Lack of signal of axial skeleton	2/51	3.9
Fat/water signal swap	1/51	2.0
Presence of truncation artifacts after the implementation of HUGE	0/51	0

($19.65 \pm 48.03\%$, $p < 0.0001$), in the axillary fat ($17.46 \pm 63.67\%$, $p < 0.0001$) and in the dorsal subcutaneous fat on level of lumbar vertebral body L4 ($10.26 \pm 25.29\%$, $p < 0.0001$) (SUVmean and SUVpeak results are attached in the supplements). In addition, further significant differences were evident in the lungs apical ($5.80 \pm 10.53\%$, $p < 0.0001$), dorsal on level of the pulmonary trunk ($15.04 \pm 19.09\%$, $p < 0.0001$) and dorsal in the basal lung ($51.27 \pm 147.61\%$, $p < 0.0001$) (see Table 2, Figs. 2 and 3). For the remaining VOIs, the comparison of the mean values did not show any statistical significance. However, large standard deviations were also found in the psoas muscle ($8.38 \pm 51.24\%$), in the bone marrow ($1.99 \pm 23.82\%$), myocardium ($3.64 \pm 22.86\%$) and the liver ($5.62 \pm 21.45\%$) (Table 2).

4. Discussion

In order to achieve a valid quantification of tracer distribution activity in clinical routine, appropriate attenuation correction and scatter correction of PET data is essential. Even small changes in measured SUVs can be crucial for the assessment of a therapy-response in follow-

up examinations [24]. In hybrid PET/CT systems, the CT data already contain useful information about tissue density, which can directly be used for attenuation correction after conversion to LACs at PET emission energy. In PET/MRI, however, μ maps used for AC must be created using MR information, such as proton density or relaxation properties. Thus, attenuation correction in PET/MRI is challenging [25].

Most clinical MRI examinations and PET/MRI protocols depend on the administration of small volumes of Gadolinium-containing contrast agents. The primary effect of Gd-contrast medium in MRI is to shorten the relaxation times of nuclei within body tissues. Depending on the specific tissue and vascularity, this leads to contrast enhancement in T1-weighted MRI sequences. In a clinical PET/MRI setting this may lead to signal variation in the T1-weighted Dixon sequences that today are widely used for MR-based AC in PET/MRI. As a consequence, the subsequent algorithms for tissue segmentation from T1-weighted Dixon images may assign faulty tissue classes and attenuation coefficients to selected tissues in the resulting μ maps. A direct outcome of tissue misclassification in MR-based μ maps is a potential quantitative impact on PET tracer quantification in PET/MRI.

Several previous studies have investigated the impact of artifacts and the specific impact of Gd-contrast administration in Dixon-based μ maps on PET quantification in PET/MRI. Keller et al. [26] evaluated the impact of motion, metal artifacts and tissue misclassification on the Dixon μ maps and the associated impact on AC PET data [26]. Brendle et al. [27] investigated the segmentation-based μ maps of 100 patients and found a high number of different artifacts (altogether 276 artifacts). These artifacts had visible impact on tissue segmentation in the μ maps, however, the authors did not find any change of diagnosis in PET/MRI due to any of the observed artifacts. Ladefoged et al. [28] observed frequent (in 23/283 patients) fat/water tissue inversions (fat/water swaps) in Dixon sequences in head/neck imaging [28]. Ruhlmann et al. in a whole-body PET/MRI study found that the administration of Gd-contrast before acquisition of the Dixon-based AC maps frequently (in 12/30 patients) triggered a fat/water swap in the brain bed position only [19]. All these previous studies [19,26–28] have in common that they were based on an older version of the Dixon-based AC sequence and

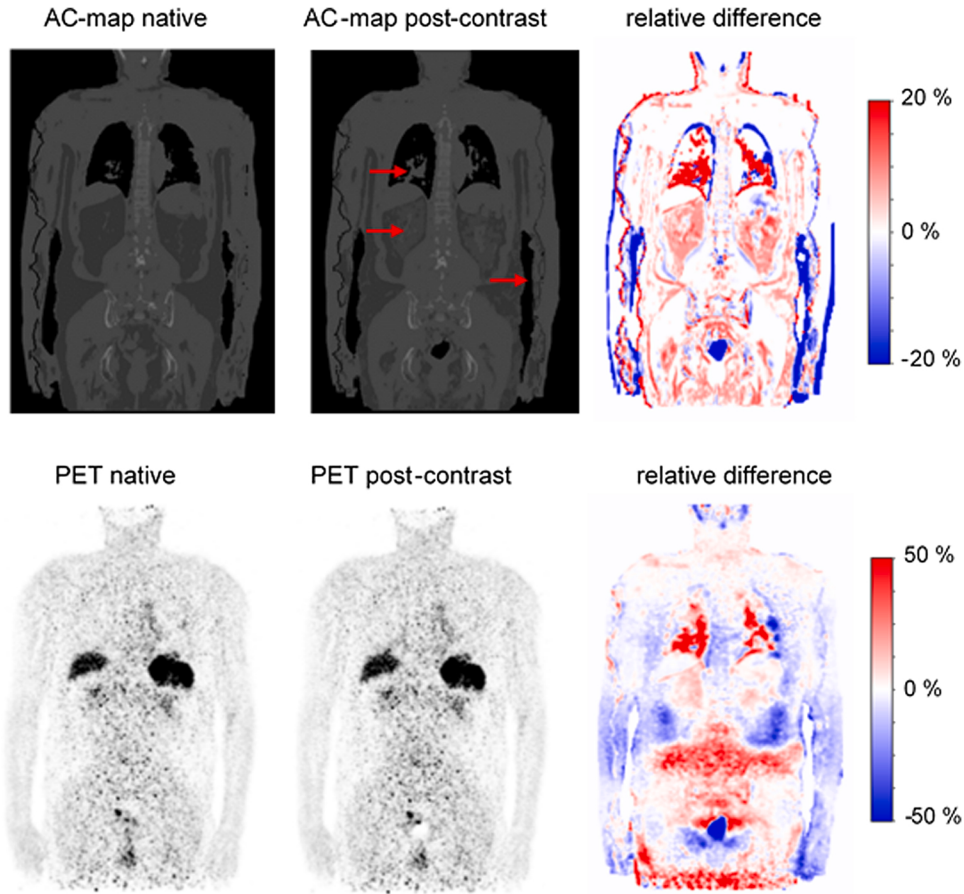


Fig. 3. Patient example showing relative differences in the AC-maps (native and post-contrast, upper row) and in the reconstructed PET-images (lower row). The native AC-maps (upper row, left) serves as reference standard. For matching the two AC-maps, landmark-based registration was used. The resulting AC difference map (upper row, right) visualizes and quantifies relative differences in attenuation factors. Red colour indicates higher relative attenuation (post-contrast), blue colour indicates lower relative attenuation (post-contrast). The blue and red contours indicate slight patient motion between acquisitions of both AC-maps. Red arrows from top to bottom: (1) additional soft tissue segmented in the lungs, (2) significant differences in the perirenal fatty tissue, (3) motion artefacts. The two PET images (lower row) show only faint visible differences. The PET difference map (lower row, right) reveals the resulting relative differences due to PET data reconstruction with the two AC-maps.

associated tissue segmentation algorithm. In the present study, however, the most recent version of a high spatial-resolution CAIPIRINHA-accelerated Dixon sequence and associated tissue segmentation algorithm was investigated. More specifically, the potential impact of Gd-contrast administration on μ map generation was systematically investigated in this study, as this may be a requirement in more complex clinical PET/MRI studies.

The results of our study show both visual differences in the resulting MR-based μ maps due to changes in tissue segmentation as well as significant quantitative influences on SUV measurements in attenuation corrected PET data, following Gd-contrast agent administration. Most differences in this study were observed in the lungs and in fatty tissue. In addition, larger differences were also measured in the psoas muscle, bone marrow and partly in the liver.

Since the acquisition times of the AC-maps before and after administration of contrast agent were about 15 min apart, an additional influence by patient movement is generally conceivable. However, the defined volumes of interest in our study are exclusively body regions that can only be influenced slightly by movement. Furthermore, the influence of respiratory motion on the PET emission data has already been investigated previously [19,26]. In these previous studies, differences due to respiratory motion were mainly visible in organs adjacent to the diaphragm [26]. In the present study differences after contrast agent administration are particularly evident in lung regions with a high vascular density. Here, respiratory motion is not the primary course. Rather, the administration of Gd-contrast has led to an increase of signal in the central pulmonary vessels and subsequent tissue segmentation has assigned larger portions of surrounding lung tissue as soft tissue that is characterized with a higher attenuation factor (LAC) (see Fig. 3). This results in higher relative changes in the μ map difference maps (Figs. 3 and 4) and also in the PET difference maps (Figs. 3 and 4). Largest

discrepancies were found in the dorsal lung sections (Table 2).

Another finding of this study is the frequent observation that fatty tissues across the whole-body μ maps following Gd-contrast administration have been assigned not only with the LAC of fat (0.0854 cm^{-1}), but also have been assigned with a second LAC with higher attenuation value (0.0927 cm^{-1}). This resulted in visible differences in the μ map difference maps and also in measurable differences in the PET difference maps (Figs. 3 and 4). In particular, larger volumes of subcutaneous and visceral fat showed a homogeneous assignment with a second, higher LAC value in the post-contrast μ maps (Figs. 3 and 4).

As discussed above, the study by Ruhlmann et al. [19] showed that the presence of Gd-contrast agents exerted a potential influence on fat/water separation and led to frequent (in 12/30 patients) fat/water swaps in the μ maps of the brain using ^{18}F -FDG PET/MRI. In our study a misclassification of the internal organs due to a characteristic fat/water swap was found in only one patient (1/51) following contrast agent administration. The fact that only one fat/water swap was detected in our study can be explained by the significantly improved MRAC reconstruction using a CAIPI-accelerated Dixon-VIBE with improved spatial resolution and a more robust tissue segmentation algorithm. In this context, the addition of bone as a further tissue class was impacted in 5/51 patient cases following Gd-contrast administration (Table 1). In these five cases only single bones were e.g. misclassified as soft tissue. Truncation correction with the MR-based HUGE method worked robust in all 51/51 cases and did not show any differences in μ maps acquired before and after contrast administration (Table 1).

A potential direct attenuating effect of Gadolinium contrast agent on PET photons has already been examined recently by Lois et al. [29]. Due to the typically small amounts of Gd-contrast agent applied during an examination (only few to 20 ml), the direct attenuation effect was found to be negligible in previous studies [19,29].

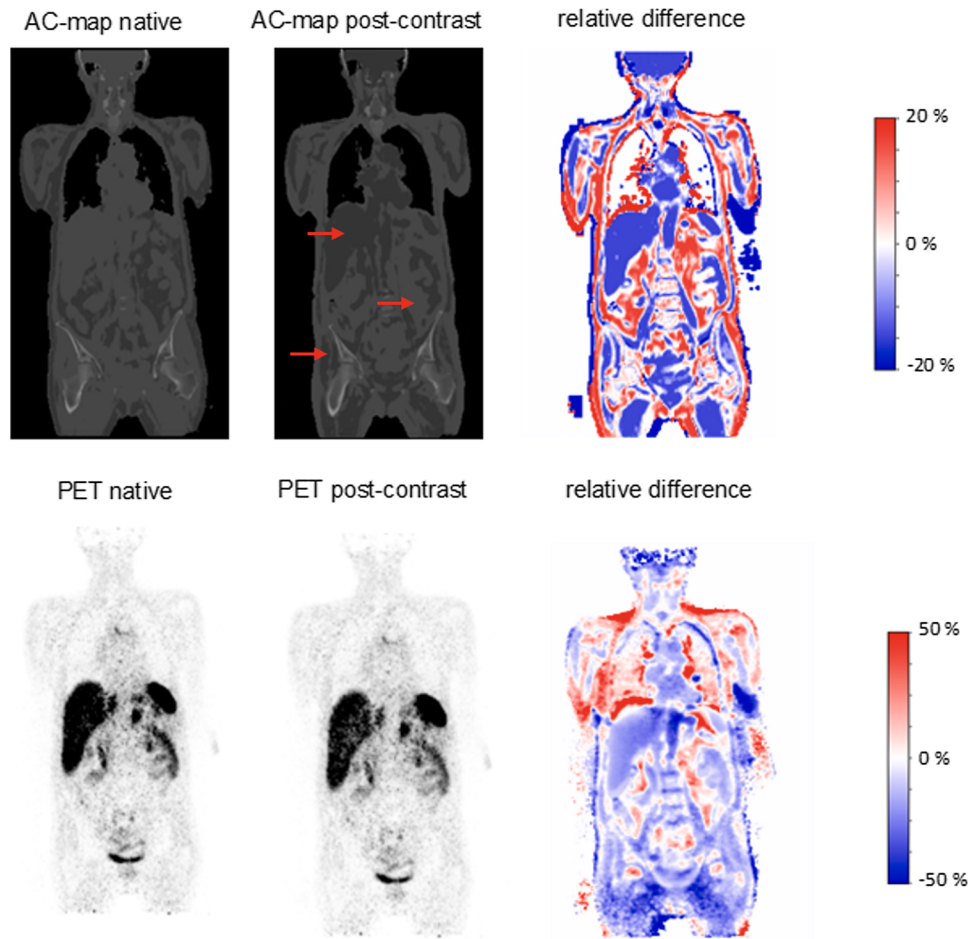


Fig. 4. The single patient example with complete misclassification of tissue classes due to a fat/water swap in the T1-weighted Dixon 3D-VIBE sequence post-contrast. Arrows point at multiple locations where the LAC values for soft-tissue and fat have been swapped. Expectedly, the AC difference map (upper row, right) shows strong differences across the entire body. Consequently, this also results in visible differences in the two PET reconstructions (lower row) and in the resulting PET difference image (lower row, right).

Table 2

Mean SUV_{max} values with standard deviation in all 21 VOIs measured in all 51 patients. Relative differences in SUV_{max} and statistical significance are given. Largest differences were found for the lungs, perirenal and subcutaneous tissue.

Organ/Tissue	SUV _{max} native	SUV _{max} with contrast	Difference in %	P value
Liver Segment VII	10.44 ± 3.30 (5.08–18.45)	10.57 ± 3.40 (5.11–19.13)	1.39 ± 8.63	0.29
Liver Segment II	10.28 ± 3.33 (2.29–18.75)	10.80 ± 3.72 (2.28–20.7)	5.62 ± 21.45	0.06
Perirenal fat	2.21 ± 1.37 (0.40–6.06)	2.55 ± 1.54 (0.39–6.92)	19.65 ± 48.03	<0.0001
Lung apikal	1.25 ± 0.56 (0.5–3.03)	1.33 ± 0.6 (0.5–3.26)	5.80 ± 10.53	<0.0001
Lung central ventral	0.81 ± 0.31 (0.32–1.67)	0.87 ± 0.36 (0.38–1.96)	6.82 ± 22.72	0.03
Lung central medial	0.78 ± 0.42 (0.06–2.28)	0.81 ± 0.41 (0.06–2.06)	4.74 ± 18.03	0.28
Lung central dorsal	0.96 ± 0.38 (0.45–2.59)	1.09 ± 0.41 (0.47–2.26)	15.04 ± 19.09	<0.0001
Lung basal ventral	0.71 ± 0.40 (0.14–2.06)	0.74 ± 0.39 (0.09–2.08)	6.06 ± 15.32	0.24
Lung basal medial	0.93 ± 0.73 (0.15–3.70)	0.92 ± 0.73 (0.06–4.20)	1.16 ± 32.36	0.71
Lung basal dorsal	0.99 ± 0.56 (0.10–2.81)	1.27 ± 0.70 (0.48–3.86)	51.27 ± 147.61	<0.0001
Myocardium	1.42 ± 0.65 (0.39–3.56)	1.45 ± 0.67 (0.27–1.42)	3.64 ± 22.86	0.38
Bloodpool	1.62 ± 0.97 (0.18–6.46)	1.66 ± 0.93 (0.19–5.89)	3.09 ± 12.68	0.21
Axillary fat	1.12 ± 0.54 (0.22–3.09)	1.23 ± 0.55 (0.26–3.23)	17.46 ± 63.67	<0.0001
Subcutaneous fat	0.88 ± 0.40 (0.27–1.82)	0.86 ± 0.37 (0.26–1.79)	-0.75 ± 13.91	0.20
L4 ventral				
Subcutaneous fat	1.08 ± 0.39 (0.33–2.19)	1.16 ± 0.40 (0.49–2.36)	10.26 ± 25.29	<0.0001
L4 dorsal				
Subcutaneous fat femoral lateral	0.66 ± 0.21 (0.09–1.04)	0.71 ± 0.29 (0.10–1.76)	8.23 ± 42.65	0.19
Subcutaneous fat femoral dorsal	0.80 ± 0.36 (0.30–1.96)	0.85 ± 0.41 (0.38–2.08)	8.75 ± 33.98	0.08
Psoas muscle	1.87 ± 0.87 (0.34–3.79)	1.98 ± 1.07 (0.28–5.5)	8.38 ± 51.24	0.21
Bone marrow	2.23 ± 1.03 (0.62–5.1)	2.27 ± 1.19 (0.35–5.51)	1.99 ± 23.82	0.65
Perirectal fat	1.14 ± 1.14 (0.0–7.90)	1.18 ± 1.19 (0.0–8.04)	-1.57 ± 36.47	0.25
Urinary bladder	90.83 ± 100.26 (8.32–516.07)	92.08 ± 101.38 (8.24–528.91)	1.26 ± 4.11	0.008

In general, the manufacturers of PET/MRI systems do not advise creating a MR-based AC-map after administration of Gd-contrast agents. However, in more extensive clinical imaging protocols, a whole-body examination is often combined with a dedicated organ examination to

obtain the most diagnostic benefit. In this scenario, the administration of Gd-contrast medium during the whole-body examination may require the use of a contrast-agent-supported μ map for the dedicated protocol. The radiopharmaceutical Gallium-68 is mostly used with very specific

tracers like DOTATOC in neuroendocrine tumors or Prostate-Specific Membrane Antigen (PSMA) in prostate cancer, and, therefore, dedicated organ protocols are common. The results may be relevant for various tumor entities, e.g. due to the partially considerable deviations in the liver (SD 21.45 %, Table 2), the detection of liver metastases in neuroendocrine tumors may be limited. Furthermore, in the staging examination of prostate cancer patients with dedicated prostate sequences, the inter-individual deviations of the perirectal fat tissue (SD 36.47 %, Table 2) may influence the detection of affected locoregional lymph nodes. Consequently, PET/MRI specific protocol adjustments should be made if feasible, e.g. creating native whole-body sequences first. Generally, when post-KM μ maps are applied in more extensive protocols, the reporting nuclear medicine physician/radiologist must be aware of the possibility of large inter-individual differences and interpret quantitative data with caution. In addition, the MR-based AC data should be included in the reading routine to avoid diagnostic errors.

The following two points may be considered as limitations of this study. First, as described before, the radiopharmaceutical Gallium-68 was used, and results may not be directly transferrable to the frequently used fluorine-18 or other tracers. We decided to focus on this isotope (^{68}Ga), as it is the basis for generator based radiotracers such as ^{68}Ga -PSMA or ^{68}Ga -DOTATOC, which are frequently used in PET/MRI examinations that demand the combined acquisition of a dedicated as well as a whole-body examinations in one single PET/MRI scan. Two examples for such setting are a whole-body examination followed by a dedicated liver examination such as in neuroendocrine tumors examined with ^{68}Ga -DOTATOC, or a dedicated prostate examination followed by a whole-body examination such as in prostate cancer examined with ^{68}Ga -PSMA. Due to the fact that mainly the impact of Gd-contrast agent on MRAC was investigated here, which is completely independent of the radiotracer applied, we believe that our findings are transferrable also to different clinical PET/MRI settings and tracers. Secondly, the acquisition times of pre- and post-KM AC-maps in this study are about 15 min apart (Fig. 1), so certain patient motion artefacts are possible. However, the figures show that this mainly affects the outer body contours and has no relevant influence on the selected measurement points (VOIs).

5. Conclusion

The results of our study suggest that the administration of (Gd)-contrast agent may have a potential influence on MR-based attenuation correction in certain tissue compartments like fat and lung and may cause substantial inter-individual variations in several organs, specifically when using a CAIPI-accelerated Dixon-based sequence in ^{68}Ga -DOTATOC PET/MRI. Therefore, acquisition of MR-based attenuation correction in PET/MRI should be performed prior to contrast agent administration. Complex hybrid imaging protocols, that include whole-body as well as dedicated examinations of specific organs such as prostate or gastrointestinal tumor imaging, should be adapted accordingly.

Ethical approval

All procedures performed were in accordance with the ethical standards of the institutional research committee of the University Duisburg-Essen and with the principles of the 1964 Declaration of Helsinki and its later amendments.

Informed consent

Informed consent was waived by the institutional review board due to the retrospective nature of this study.

CRediT authorship contribution statement

Nils Martin Bruckmann: Data curation, Writing - original draft,

Investigation, Visualization, Validation, Formal analysis. **Maike E. Lindemann:** Data curation, Visualization, Writing - review & editing. **Johannes Grueneisen:** Writing - review & editing. **Hong Grawe:** Data curation, Writing - review & editing. **Yan Li:** Writing - review & editing. **Lino M. Sawicki:** Writing - review & editing. **Christoph Rischpler:** Writing - review & editing. **Ken Herrmann:** Supervision, Resources. **Lale Umutlu:** Supervision, Resources. **Harald H. Quick:** Supervision, Data curation, Writing - review & editing. **Benedikt Michael Schaarschmidt:** Conceptualization, Methodology, Investigation, Writing - review & editing, Supervision.

Declaration of Competing Interest

None.

Appendix A. Supplementary data

Supplementary material related to this article can be found, in the online version, at doi:<https://doi.org/10.1016/j.ejrad.2021.109691>.

References

- [1] G. Delso, S. Fürst, B. Jakoby, et al., Performance measurements of the siemens mMR integrated whole-body PET/MR scanner, *J. Nucl. Med.* 52 (2011) 1914–1922.
- [2] H. Zaidi, N. Ojha, M. Morich, et al., Design and performance evaluation of a whole-body Ingenuity TF PET-MRI system, *Phys. Med. Biol.* 56 (2011) 3091–3106.
- [3] H.H. Quick, Integrated PET/MR, *J. Magn. Reson. Imaging* 39 (2014) 243–258.
- [4] A.M. Grant, T.W. Deller, M.M. Khalighi, et al., NEMA NU 2-2012 performance studies for the SiPM-based ToF-PET component of the GE SIGNA PET/MR system, *Med. Phys.* 43 (2016) 2334.
- [5] C. Buchbender, T.A. Heusner, T.C. Lauenstein, et al., Oncologic PET/MRI, part 1: tumors of the brain, head and neck, chest, abdomen, and pelvis, *J. Nucl. Med.* 53 (2012) 928–938.
- [6] C. Buchbender, T.A. Heusner, T.C. Lauenstein, et al., Oncologic PET/MRI, part 2: bone tumors, soft-tissue tumors, melanoma, and lymphoma, *J. Nucl. Med.* 53 (2012) 1244–1252.
- [7] M. Mayerhofer, H. Prosch, L. Beer, et al., PET/MRI versus PET/CT in oncology: a prospective single-center study of 330 examinations focusing on implications for patient management and cost considerations, *Eur. J. Nucl. Med. Mol. Imaging* 47 (2020) 51–60.
- [8] O. Martin, B.M. Schaarschmidt, J. Kirchner, et al., PET/MRI versus PET/CT in whole-body staging: results from a unicenter observational study in 1003 subsequent examinations, *J Nucl Med. United States* (2019) jnumed.119.
- [9] J.P.J. Carney, D.W. Townsend, V. Rapoport, et al., Method for transforming CT images for attenuation correction in PET/CT imaging, *Med. Phys.* 38 (2006) 2948–2956.
- [10] D. Visvikis, D.C. Costa, I. Croasdale, et al., CT-based attenuation correction in the calculation of semi-quantitative indices of [^{18}F]FDG uptake in PET, *Eur. J. Nucl. Med. Mol. Imaging* 30 (2003) 344–353.
- [11] A. Martinez-Moller, M. Souvatzoglou, G. Delso, et al., Tissue classification as a potential approach for attenuation correction in whole-body PET/MRI: evaluation with PET/CT data, *J. Nucl. Med.* 50 (2009) 520–526.
- [12] T. Beyer, M.L. Lassen, R. Boellaard, et al., Investigating the state-of-the-art in whole-body MR-based attenuation correction: an intra-individual, inter-system, inventory study on three clinical PET/MR systems, *Magn Reson Mater Physics, Biol Med.* 29 (2016) 75–87.
- [13] F. Seith, S. Gatidis, H. Schmidt, et al., Comparison of positron emission tomography quantification using magnetic resonance- and computed tomography-based attenuation correction in physiological tissues and lesions, *Invest. Radiol.* 51 (2016) 66–71.
- [14] J.O. Blumhagen, R. Ladebeck, M. Fenchel, et al., MR-based field-of-view extension in MR/PET: BO homogenization using gradient enhancement (HUGE), *Magn. Reson. Med.* 70 (2013) 1047–1057.
- [15] M.E. Lindemann, M. Oehmigen, J.O. Blumhagen, et al., MR-based truncation and attenuation correction in integrated PET/MR hybrid imaging using HUGE with continuous table motion, *Med. Phys.* 44 (2017) 4559–4572.
- [16] F.A. Breuer, M. Blaimer, R.M. Heidemann, et al., Controlled aliasing in parallel imaging results in higher acceleration (CAIPRINHA) for multi-slice imaging, *Magn. Reson. Med.* 53 (2005) 684–691.
- [17] M.T. Freitag, M. Fenchel, P. Bäumer, et al., Improved clinical workflow for simultaneous whole-body PET/MRI using high-resolution CAIPRINHA-accelerated MR-based attenuation correction, *Eur. J. Radiol.* 96 (2017) 12–20.
- [18] H.H. Quick, C. Von Gall, M. Zeilinger, et al., Integrated whole-body PET/MR hybrid imaging: clinical experience, *Invest. Radiol.* 48 (2013) 280–289.
- [19] V. Ruhlmann, P. Heusch, H. Kühl, et al., Potential influence of Gadolinium contrast on image segmentation in MR-based attenuation correction with Dixon sequences in whole-body ^{18}F -FDG PET/MR, *Magn. Reson. Mater. Phys. Biol.* 29 (2016) 301–308.

- [20] World Medical Association Declaration of Helsinki: ethical principles for medical research involving human subjects, JAMA. United States 310 (2013) 2191–2194.
- [21] D.H. Paulus, H.H. Quick, C. Geppert, et al., Whole-body PET/MR imaging: quantitative evaluation of a novel model-based MR attenuation correction method including bone, *J. Nucl. Med.* 56 (2015) 1061–1066.
- [22] M. Oehmigen, M.E. Lindemann, M. Gratz, et al., Impact of improved attenuation correction featuring a bone atlas and truncation correction on PET quantification in whole-body PET/MR, *Eur. J. Nucl. Med. Mol. Imaging* 45 (2018) 642–653.
- [23] P. Heusch, C. Buchbender, K. Beiderwellen, et al., Standardized uptake values for [¹⁸F] FDG in normal organ tissues: Comparison of whole-body PET/CT and PET/MRI, *Eur. J. Radiol.* 82 (2013) 870–876.
- [24] M. Eiber, A. Martinez-Möller, M. Souvatzoglou, et al., Value of a Dixon-based MR/PET attenuation correction sequence for the localization and evaluation of PET-positive lesions, *Eur. J. Nucl. Med. Mol. Imaging* 38 (2011) 1691–1701.
- [25] G. Wagenknecht, H.J. Kaiser, F.M. Mottaghy, et al., MRI for attenuation correction in PET: methods and challenges, *Magn Reson Mater Physics, Biol Med.* 26 (2013) 99–113.
- [26] S.H. Keller, S. Holm, A.E. Hansen, et al., Image artifacts from MR-based attenuation correction in clinical, whole-body PET/MRI, *Magn Reson Mater Physics, Biol Med.* 26 (2013) 173–181.
- [27] C. Brendle, H. Schmidt, A. Oergel, et al., Segmentation-based attenuation correction in positron emission tomography/magnetic resonance: erroneous tissue identification and its impact on positron emission tomography interpretation, *Invest Radiol. United States* 50 (2015) 339–346.
- [28] C.N. Ladefoged, A.E. Hansen, S.H. Keller, et al., Impact of incorrect tissue classification in Dixon-based MR-AC: fat-water tissue inversion, *EJNMMI Phys.* 1 (2014) 101.
- [29] C. Lois, I. Bezrukova, H. Schmidt, et al., Effect of MR contrast agents on quantitative accuracy of PET in combined whole-body PET/MR imaging, *Eur. J. Nucl. Med. Mol. Imaging* 39 (2012) 1756–1766.

Effects of Anti-Tumor Necrosis Factor Therapy on Osteoblastic Activity at Sites of Inflammatory and Structural Lesions in Radiographic Axial Spondyloarthritis: A Prospective Proof-of-Concept Study Using Positron Emission Tomography/Magnetic Resonance Imaging of the Sacroiliac Joints and Spine

Nils Martin Bruckmann,¹  Christoph Rischpler,² Styliani Tsiami,³ Julian Kirchner,¹ Daniel B. Abrar,¹ Timo Bartel,² Jens Theysohn,¹ Lale Umutlu,¹ Ken Herrmann,² Wolfgang P. Fendler,² Christian Buchbender,¹ Gerald Antoch,¹ Lino M. Sawicki,¹ Athanasios Tsobanelis,³ Juergen Braun,³ and Xenofon Baraliakos³ 

Objective. Proof-of-concept trial to determine the effects of tumor necrosis factor inhibitor (TNFi) therapy on osteoblastic activity at sites of inflammatory and structural lesions in patients with radiographic axial spondyloarthritis (SpA), using fluorine 18-labeled NaF (¹⁸F-NaF) positron emission tomography/magnetic resonance imaging (PET/MRI).

Methods. Sixteen patients with clinically active radiographic axial SpA were prospectively enrolled to receive TNFi treatment and undergo ¹⁸F-NaF PET/MRI of the sacroiliac (SI) joints and spine at baseline and at a follow-up visit 3–6 months after treatment initiation. Three readers (1 for PET/MRI and 2 for conventional MRI) evaluated all images, blinded to time point. Bone marrow edema, structural lesions (i.e., fat lesions, sclerosis, erosions, and ankylosis), and ¹⁸F-NaF uptake at SI joint quadrants and vertebral corners (VCs) were recorded.

Results. Overall, 11 male and 5 female patients (mean age \pm SD 38.6 \pm 12.0 years) were followed up for a mean duration of 4.6 months (range 3–6). ¹⁸F-NaF PET/MRI was conducted on SI joints for 16 patients and the spine for 10; 128 SI joint quadrants and 920 VCs were analyzed at each time point. At baseline, ¹⁸F-NaF uptake was demonstrated in 96.0% of SI joint quadrants with bone marrow edema, 94.2% with sclerosis, and 88.3% with fat lesions. At follow-up, 65.3% of SI joint quadrants with bone marrow edema ($P < 0.001$), 33.8% with sclerosis ($P = 0.23$), and 24.5% with fat lesions ($P = 0.01$) had less ¹⁸F-NaF uptake, compared with baseline. For VCs, ¹⁸F-NaF uptake at baseline was found in 81.5% of edges with sclerosis, 41.9% with fat lesions, and 33.7% with bone marrow edema. At follow-up, 73.5% of VCs with bone marrow edema ($P = 0.01$), 53.3% with fat lesions ($P = 0.03$), and 55.6% with sclerosis ($P = 0.16$) showed less ¹⁸F-NaF uptake, compared with baseline.

Conclusion. Anti-TNF antibody treatment led to a significant decrease in osteoblastic activity within 3–6 months, especially, but not solely, at sites of inflammation. Larger data sets are needed for confirmation of the antiosteoblastic effects of TNFi for the prevention of radiographic progression in axial SpA.

INTRODUCTION

Radiographic axial spondyloarthritis (SpA), also known as ankylosing spondylitis (AS) (1), is a chronic inflammatory rheumatic disease, representing the most advanced form of axial

SpA (2). In its early phase, the disease is characterized by chronic inflammation in the lower back and inflammation in the sacroiliac (SI) joints (3). As the disease progresses, inflammation may extend to the spine, potentially resulting in complete stiffness of the axial skeleton and postural deformation, which are associated

Drs. Bruckmann and Rischpler contributed equally to this study.

Supported by an unrestricted research grant from MSD Germany.

¹Nils Martin Bruckmann, MD, Julian Kirchner, MD, Daniel B. Abrar, MD, Jens Theysohn, MD, Lale Umutlu, MD, Christian Buchbender, MD, Gerald Antoch, MD, Lino M. Sawicki, MD: University Dusseldorf, Dusseldorf, Germany; ²Christoph Rischpler, MD, Timo Bartel, Ken Herrmann, MD, Wolfgang P. Fendler, MD: University of Duisburg-Essen, Essen, Germany; ³Styliani Tsiami, Athanasios Tsobanelis, Juergen Braun, MD, Xenofon Baraliakos, MD: Rheumazentrum Ruhrgebiet, Herne, and Ruhr-University Bochum, Bochum, Germany.

Author disclosures are available at [https://onlinelibrary.wiley.com/action/downloadSupplement?doi=10.1002%20art.42149&file=art42149-sup-0001-Disclosureform.pdf](https://onlinelibrary.wiley.com/action/downloadSupplement?doi=10.1002/art.42149&file=art42149-sup-0001-Disclosureform.pdf).

Address correspondence to Xenofon Baraliakos, MD, Rheumazentrum Ruhrgebiet, Ruhr-University Bochum, Claudiusstrasse 45, 44649 Herne, Germany. Email: xenofon.baraliakos@elisabethgruppe.de.

Submitted for publication December 5, 2021; accepted in revised form April 19, 2022.

with severe physical disability and reduced quality of life (4,5). Treatment comprises nonpharmacologic and pharmacologic interventions, with the latter involving nonsteroidal antiinflammatory drugs (NSAIDs) as a first step. Among patients who do not respond to NSAID treatment, biologic disease-modifying anti-rheumatic drugs (bDMARDs), such as antibodies inhibiting tumour necrosis factor (TNFi) or interleukin-17, are efficacious (6).

Imaging plays an essential role in the diagnosis and management of axial SpA and may also be used for assessment of treatment responses, especially in clinical trials (7,8). The current gold standard imaging technique in axial SpA is magnetic resonance imaging (MRI), since it can assess changes in inflammation, such as bone marrow edema, as well as structural damage, such as fat lesions, erosion, sclerosis, and ankylosis (7,9,10). The introduction of hybrid imaging techniques such as positron emission tomography/computed tomography (PET/CT) and PET/MRI has provided additional insights into the pathogenesis and metabolic activity of radiographic axial SpA (11). Therefore, use of the osteoblast-specific radiotracer fluorine 18-labeled NaF (^{18}F -NaF) to visualize local osteoblastic activity in inflammatory and structural lesions due to radiographic axial SpA has recently increased (11–13). These studies confirmed that the level of osteoblastic activity was especially high at sites where bone marrow edema and fat lesions had been detected by MRI and that bone marrow edema and fat lesions are associated with the development of syndesmophytes and new bone formation (14). This is consistent with findings of recent biopsy studies involving patients with radiographic axial SpA (15).

Treatment with TNFi continuously for ≥ 4 years has been shown to result in lower rates of radiographic progression than treatment with non-bDMARDs (7,16–18). This is very likely due to the beneficial effect of bDMARDs on early spinal inflammation as compared to their minimal impact on more advanced disease. However, a direct effect of bDMARDs on osteoblastic activity has not been proven to date. In this prospective, observational, proof-of-concept study, we used ^{18}F -NaF PET/MRI to analyze the effect of TNFi on osteoblastic activity in disease-specific lesions detected by MRI in the SI joints and the spine of patients with active radiographic axial SpA.

PATIENTS AND METHODS

Patients and treatment. This observational proof-of-concept study was approved by the institutional research committee of the University Duisburg-Essen (protocol 17-7709-BO) and accorded with the principles of the 1964 Declaration of Helsinki and its later amendments. Written informed consent was obtained from all individual participants prior to their enrollment in the study.

The main inclusion criteria were 1) diagnosis of radiographic axial SpA by the treating rheumatologist, based on the presence of advanced radiographic changes in the SI joints according to

the modified New York criteria for AS (19), 2) evidence of active disease, based on a Bath AS Disease Activity Index (BASDAI) score of ≥ 4 despite treatment with a full dose of at least 2 NSAIDs for ≥ 4 weeks prior to imaging (20), and 3) presence of at least 1 inflammatory lesion on MRI of the SI joints or spine. Pretreatment with bDMARDs was not allowed. If a decision was made to treat a patient with a compound other than TNFi, the patient was not eligible for study participation. According to the study protocol, treatment had to be initiated within 1 week after the baseline (i.e., initial) MRI. Follow-up imaging was performed at least 3–6 months after treatment initiation, based on the availability of the patient.

Specifications of conventional MRI and PET/MRI. All ^{18}F -NaF PET/MRI examinations were performed on an integrated 3.0T PET/MRI system (Biograph mMR, Siemens Healthineers) in a caudocranial direction. Scanning was performed during the mineralization phase, 40 minutes after intravenous injection of a mean \pm SD ^{18}F -NaF dose of 161 ± 8 MBq. Images were prepared as described by Buchbender et al (11). An attenuation-correction map (μmap) in coronal orientation was generated using a transaxial acquired high-resolution CAIPIRINHA (controlled aliasing in parallel imaging results in higher spatial acceleration), T1-weighted, 3-dimensional Dixon-VIBE (volumetric interpolated breath-hold examination) sequence. In addition, a bone atlas and a truncation correction proposed by Blumhagen et al (21) were used (22–24). The scanning parameters for the sequences used in this study are shown in Table 1.

Analysis of MRI and PET scans. Three experienced readers (1 nuclear medicine specialist [for PET data] and 2 radiologists [for conventional MRI data]) blinded to time point (i.e., baseline versus follow-up) and patient demographic characteristics independently evaluated all MRI and PET scans in paired order.

SI joints. The iliac and sacral parts of each SI joint were subdivided into an upper part (including the first sacral foramen) and a lower part (including the second and third foramen), resulting in 4 SI joint quadrants per side. All SI joint quadrants were evaluated in a binary way for the presence or absence of inflammatory activity (i.e., bone marrow edema, based on the STIR sequence, and chronic structural changes to bone, such as fat lesions, erosion, sclerosis, and ankylosis, based on the T1-weighted turbo spin-echo sequence). Each SI joint quadrant was also assessed for the presence or absence of ^{18}F -NaF uptake.

Spine. All vertebral bodies were divided into 4 vertebral corners (VCs; superior anterior, superior posterior, inferior posterior, and inferior anterior). Similar to the evaluation of SI joints, the presence or absence of bone marrow edema was assessed on the basis of the STIR sequence, and the presence or absence of

Table 1. Scanning parameters of the fluorine 18-labeled NaF positron emission tomography/magnetic resonance imaging sequences used to determine the effect of tumor necrosis factor inhibitor therapy on osteoblastic activity in patients with radiographic axial spondyloarthritis*

Sequence	Orientation(s)	TE/TR, msec	Slice thickness, mm	Matrix size, pixels	Field of view, mm ²
T1-weighted 3D Dixon-VIBE with fat suppression	Semicoronal	2.46/3.97	3.12	192 × 158	492 × 450
T1-weighted TSE	Sagittal for VCs, semicoronal for SI joints	12/650	3.6	448 × 224	715 × 322
T2-weighted STIR with fat suppression	Sagittal for VCs, semicoronal for SI joints	57/6,180	3.0	384 × 230	250 × 250
T1-weighted STIR with fluid suppression	Semicoronal for SI joints	11/2,840	3.0	448 × 314	250 × 250

* TE = echo time; TR = repetition time; 3D = 3-dimensional; VIBE = volumetric interpolated breath-hold examination; TSE = turbo spin-echo; VCs = vertebral corners; SI = sacroiliac.

structural lesions such as fat lesions and sclerosis was assessed using the T1-weighted turbo spin-echo sequence. Each VC was also assessed for the presence or absence of ¹⁸F-NaF uptake on mineralization phase PET (11,14).

Osteoblastic activity. For semiquantitative analysis of osteoblastic activity, maximum standardized uptake values (SUV_{max}) were measured using a volume of interest covering the entire individual lesion at each SI joint quadrant or VC. Focal ¹⁸F-NaF uptake was defined as a visually detectable uptake of ¹⁸F-NaF that was greater than the level in adjacent bone marrow.

Statistical analysis. Only lesions that were identified by the 2 readers of MRIs at each imaging time point were used for analyses. Data are presented as the mean ± SD, the mean (range), or percentage (95% confidence interval [95% CI]). Proportions of SI joint quadrants showing bone marrow edema, fat lesions, erosions, sclerosis, or ankylosis, or any combination of these findings and focal ¹⁸F-NaF uptake were calculated to investigate the relation between MRI-based changes in inflammation before and after initiation of TNFi therapy and local osteoblastic activity visualized by PET/MRI. McNemar's test was performed to compare results between baseline and follow-up examinations. A *P* value of less than 0.05 was considered to indicate statistical significance. Wilcoxon's signed rank test was used to assess differences between SUV_{max} before and SUV_{max} after treatment initiation. Statistical analysis was performed using SPSS, version 24 (IBM).

Data availability. The data sets used and/or analyzed during the current study are available from the corresponding author on reasonable request.

RESULTS

Demographic characteristics and image availability.

Sixteen patients were included. All patients had complete data sets of SI joint images, and 10 had complete data sets of spinal images,

permitting analysis of 128 SI joint quadrants and 920 VCs. The mean ± SD age at baseline was 38.3 ± 12.0 years, 11 patients (68.8%) were male (including 7 of 10 [70%] with spinal images), and 13 patients (81.3%) were HLA-B27 positive. Mean ± SD clinical values at baseline were 6.1 ± 1.6 (range 4.1–7.9) for the BASDAI, 3.4 ± 0.7 (range 2.1–4.9) for the Ankylosing Spondylitis Disease Activity Score (ASDAS) (25), and 1.0 ± 1.3 mg/dl (range 0.0–4.4) for the C-reactive protein level (Table 2). The mean follow-up period was 4.6 months (range 3–6 months).

Analysis of follow-up data showed that all patients improved during treatment. The mean ± SD BASDAI score decreased to 4.1 ± 1.5 (range 2.1–7.4), although 5 patients (31.3%) still reported a BASDAI score of >4, which is indicative of advanced disease on the 10-point index. The mean ± SD ASDAS decreased to 2.1 ± 0.5 (range 1.6–3.2) during treatment, with all 5 patients exhibiting a BASDAI score of >4 also having an ASDAS of >2.1. Finally, the mean ± SD C-reactive protein level decreased to 0.1 ± 0.2 mg/dl (range 0.0–0.5) (Table 2).

Evaluation and quantification of pathologic lesions in SI joints.

Of the 128 SI joint quadrants, 75 (58.6 %) showed bone marrow edema, 120 (93.8%) showed fat lesions, 69 (53.9%) showed sclerosis, 99 (77.3%) showed erosions, and 16 (12.5%) showed ankylosis at baseline; focal ¹⁸F-NaF uptake was visible in 111 (86.7%), with a mean ± SD SUV_{max} of 14.637 ± 4.687. Increased ¹⁸F-NaF uptake in SI joint quadrants was most frequently associated with bone marrow edema (72 [96%] of 75 quadrants), but uptake was also in a high percentage of quadrants showing sclerosis (65 [94.2%] of 69), fat lesions (106 [88.3%] of 120), erosions (86 [86.9%] of 99), and ankylosis (14 [87.5%] of 16; all 14 were associated with 5 patients). All SI joint quadrants showing ¹⁸F-NaF uptake also had at least 1 type of lesion detected on conventional MRI at baseline.

At follow-up, 37 SI joint quadrants showed bone marrow edema (including 3 that did not show bone marrow edema at baseline), for a net reduction of 50.7% (95% CI 38.9–62.4;

Table 2. Demographic characteristics, clinical characteristics at baseline and follow-up, and changes between the 2 time points among patients with radiographic axial spondyloarthritis who underwent fluorine 18-labeled NaF (^{18}F -NaF) positron emission tomography/magnetic resonance imaging to determine the effect of tumor necrosis factor inhibitor (TNFi) therapy on osteoblastic activity*

Patient, sex, age, imaging time point†	TNFi duration, week	BASDAI	ASDAS	CRP level, mg/dl	SUV_{\max}^{\pm}	
					SI joints	Spine
1, M, 26 years						
Baseline	0	6.4	3.5	0.1	16.254	–
Follow-up	16	5.0	3.0	0.0	11.203	–
Change	–	–1.4	–0.5	–0.1	–5.051	–
2, M, 52 years						
Baseline	0	5.6	3.2	0.5	15.979	–
Follow-up	24	3.6	1.7	0.2	11.696	–
Change	–	–2.0	–1.5	–0.3	–4.283	–
3						
Baseline	0	5.2	3.8	1.5	20.464	–
Follow-up	24	2.4	1.6	0.0	10.000	–
Change	–	–2.8	–2.2	–1.5	–10.464	–
4						
Baseline	0	6.0	3.0	0.3	7.534	–
Follow-up	24	3.8	1.9	0.0	5.354	–
Change	–	–2.2	–1.1	–0.3	–2.180	–
5						
Baseline	0	5.6	3.7	1.6	7.505	–
Follow-up	12	4.0	2.2	0.2	10.102	–
Change	–	–1.6	–1.5	–1.4	2.597	–
6						
Baseline	0	6.5	3.1	0.0	24.154	–
Follow-up	16	5.9	2.6	0.1	11.106	–
Change	–	–0.6	–0.5	0.1	–13.048	–
7						
Baseline	0	6.0	3.2	1.1	14.620	15.695
Follow-up	16	2.2	1.6	0.4	11.225	7.290
Change	–	–3.8	–1.6	–0.7	–3.395	–8.405
8						
Baseline	0	7.9	4.4	1.2	15.332	19.455
Follow-up	12	3.8	1.9	0.0	9.550	13.763
Change	–	–4.1	–2.5	–1.2	–5.782	–5.692
9						
Baseline	0	4.1	2.5	1.2	9.291	5.314
Follow-up	16	2.1	1.7	0.0	11.323	9.797
Change	–	–2.0	–0.8	–1.2	2.032	4.483
10						
Baseline	0	7.5	3.2	0.1	16.534	17.200
Follow-up	20	6.2	2.2	0.1	14.535	13.708
Change	–	–1.3	–1.0	0.0	–1.999	–3.492
11						
Baseline	0	6.9	4.9	4.4	8.312	19.965
Follow-up	20	2.3	2.0	0.2	10.426	10.256
Change	–	–4.6	–2.9	–4.2	2.114	–9.709
12						
Baseline	0	6.4	3.2	0.1	15.662	0.000
Follow-up	16	5.1	2.7	0.3	11.950	0.000
Change	–	–1.3	–0.5	0.2	–3.712	0.000
13						
Baseline	0	4.9	3.8	3.6	16.453	25.159
Follow-up	24	3.6	1.8	0.2	13.375	17.343
Change	–	–1.3	–2.0	–3.4	–3.078	–7.816
14						
Baseline	0	7.5	3.6	0.3	11.930	0.000
Follow-up	20	7.4	3.2	0.5	14.805	0.000
Change	–	–0.1	–0.4	0.2	2.875	0.000

(Continued)

Table 2. (Cont'd)

Patient, sex, age, imaging time point ^t	TNFi duration, week	BASDAI	ASDAS	CRP level, mg/dl	SUV _{max} [‡]	
					SI joints	Spine
15						
Baseline	0	7.6	3.4	0.5	15.858	15.950
Follow-up	12	3.7	1.7	0.1	15.573	0.000
Change	-	-3.9	-1.7	-0.4	-0.285	-15.950
16						
Baseline	0	4.1	2.1	0.1	18.313	0.000
Follow-up	12	3.8	1.9	0.0	11.227	0.000
Change	-	-0.3	-0.2	-0.1	-7.086	0.000

* BASDAI = Bath Ankylosing Spondylitis Disease Activity Index; ASDAS = Ankylosing Spondylitis Disease Activity Score; CRP = C-reactive protein; SI = sacroiliac.

† Imaging was performed before initiation (baseline) and after the specified duration (follow-up) of TNFi therapy.

‡ For semiquantitative analysis of osteoblastic activity, the maximum standardized uptake value (SUV_{max}) for ¹⁸F-NaF in SI joint quadrants and spinal vertebral corners was determined. For patients 1–6, imaging of the spine was not performed.

$P < 0.01$). No significant changes between baseline and follow-up were observed for chronic lesions (Figures 1 and 2).

An improvement in ¹⁸F-NaF uptake was observed for all lesion types. The largest effect was observed for lesions associated with bone marrow edema, with 47 (65.3% [95% CI 53.1–76.1]) fewer SI joint quadrants showing ¹⁸F-NaF uptake at follow-up ($P < 0.01$) (Figures 1 and 2). Of the 3 SI joint quadrants with new onset of bone marrow edema at follow-up, 2 did not show ¹⁸F-NaF uptake at baseline or follow-up, whereas 1 had uptake at baseline and follow-up.

Quantification of osteoblastic activity demonstrated that the mean SUV_{max} for all SI joint quadrants decreased significantly during the study, from 14.637 at baseline to 11.466 at follow-up (change, -3.171 [range -13.050, 2.875]; $P < 0.01$). Four patients had a very minor increase in mean SUV_{max} (range 2.031–2.875) without worsening clinical scores. No relation

between changes in mean SUV_{max} and clinical scores was observed (Table 2).

Evaluation and quantification of pathologic lesions in the spine. Of the 920 VCs, 101 (11.0%) showed bone marrow edema, 62 (6.7%) showed fat lesions, and 11 (1.2%) showed sclerosis at baseline; increased ¹⁸F-NaF uptake was found in 77 VCs (8.4%), with a mean \pm SD SUV_{max} of 11.873 ± 9.140 . Increased ¹⁸F-NaF uptake was most frequently associated with sclerosis (9 [81.8%] of 11 VCs) and less commonly associated with fat lesions (26 [41.9%] of 62 VCs) or bone marrow edema (34 [33.7%] of 101 VCs).

At follow-up, bone marrow edema was still found in 34 VCs (including 6 that did not show bone marrow edema at baseline), for a net reduction of 66.3% (95% CI 57.1–75.6; $P < 0.01$), whereas fat lesions were found in 15 VCs, for a net reduction of

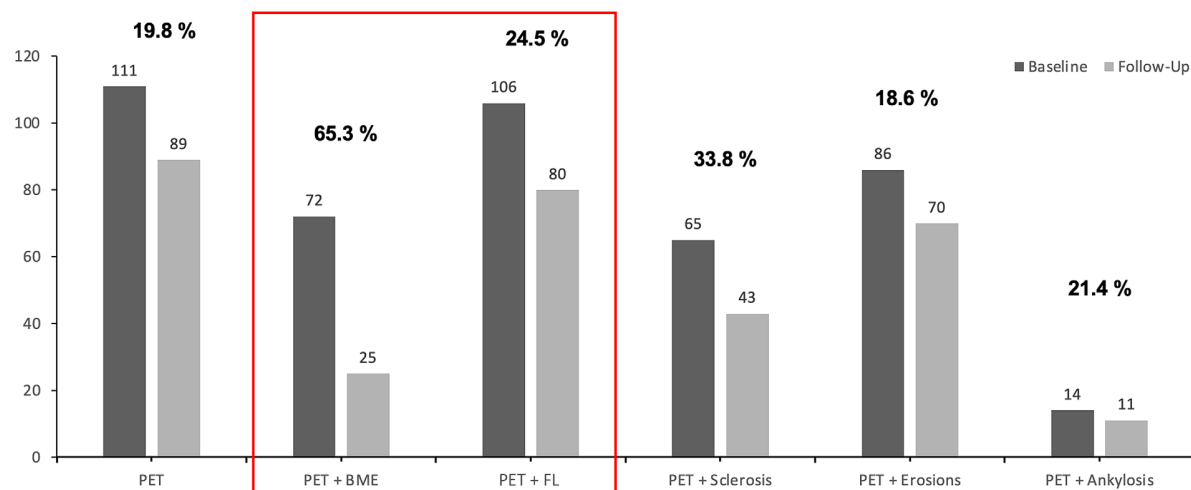


Figure 1. Number of sacroiliac joint quadrants showing lesions on conventional magnetic resonance imaging (MRI) and those showing uptake of fluorine 18-labeled NaF on positron emission tomography (PET)/MRI at baseline (dark gray) and after 4 months of treatment with tumor necrosis factor inhibitors (light gray) among patients with radiographic axial spondyloarthritis. The bold numbers show the percentage decrease between baseline and follow-up. Statistically significant differences are indicated by the red box. BME = bone marrow edema; FL = fat lesions.

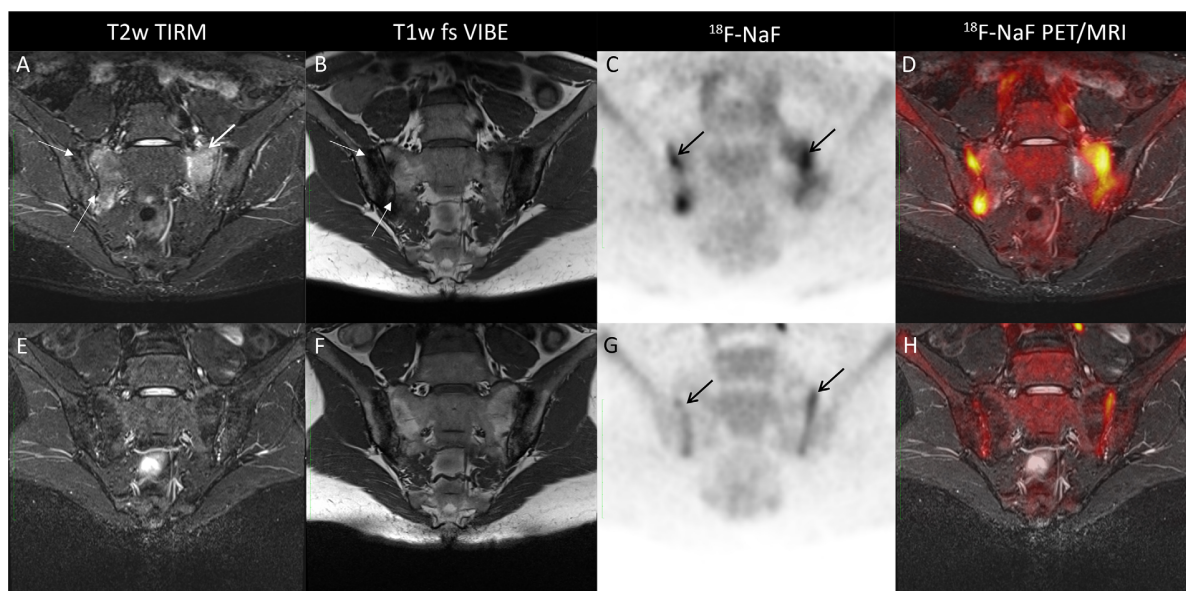


Figure 2. Findings of sacroiliac joint imaging at baseline (A–D) and follow-up (E–H) for a 34-year-old patient with clinically active radiographic axial spondyloarthritis. Shown are areas of sclerosis and erosions (thin white arrows) and extensive surrounding bone marrow edema and fatty degeneration (thick white arrow) on scans obtained by a T2-weighted turbo inversion recovery magnitude (T2w TIRM) sequence (A) and T1-weighted volumetric interpolated breath-hold examination with fat suppression (T1w fs VIBE) (B), as well as evidence of osteoblastic activity based on increased signal on fluorine 18-labeled NaF ($^{18}\text{F-NaF}$) PET/MRI (C and D; black arrows). Follow-up imaging after 4 months of tumor necrosis factor inhibitor treatment showed significant decrease in osteoblastic activity (black arrows). See Figure 1 for other definitions.

75.8% (95% CI 62.8–84.8; $P < 0.01$). Sclerosis was found in 43 VCs, which was significantly greater than the number at baseline (Figures 3 and 4).

Similar to the analysis of SI joints, the largest reduction in $^{18}\text{F-NaF}$ uptake was found in lesions associated with bone marrow edema, with 25 (73.5% [95% CI 43.3–71.6]) fewer VCs showing uptake at follow-up ($P = 0.01$). In comparison, 18 (69.2%) fewer VCs associated with fat lesions ($P = 0.03$) and

5 (55.6%) fewer VCs associated with sclerosis ($P = 0.16$) showed $^{18}\text{F-NaF}$ uptake at follow-up (Figures 3 and 4).

Quantification of osteoblastic activity showed that the mean SUV_{\max} for all VCs decreased significantly, from 11.873 at baseline to 7.215 at follow-up (change, -4.658 [range -15.950 , 4.483]; $P < 0.025$). Only 1 patient had a slight increase in her mean SUV_{\max} . Similar to findings for SI joints, no relation between changes in SUV_{\max} and clinical outcomes was observed (Table 2).

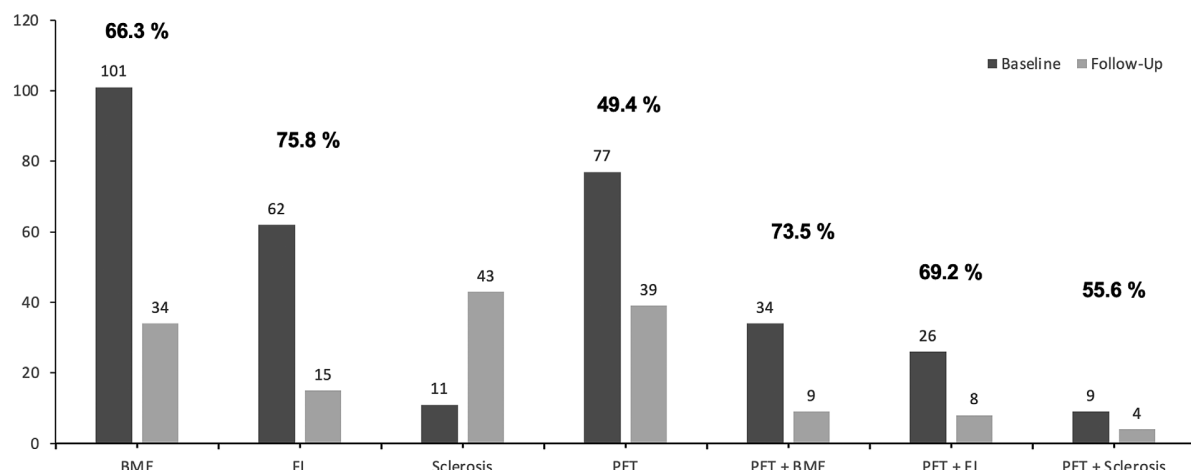


Figure 3. Number of vertebral corners showing lesions on conventional MRI and those showing uptake of fluorine 18-labeled NaF on PET/MRI at baseline (dark gray) and after 4 months of treatment with tumor necrosis factor inhibitors (light gray) among patients with radiographic axial spondyloarthritis. The bold numbers show the percentage decrease between baseline and follow-up. See Figure 1 for definitions.

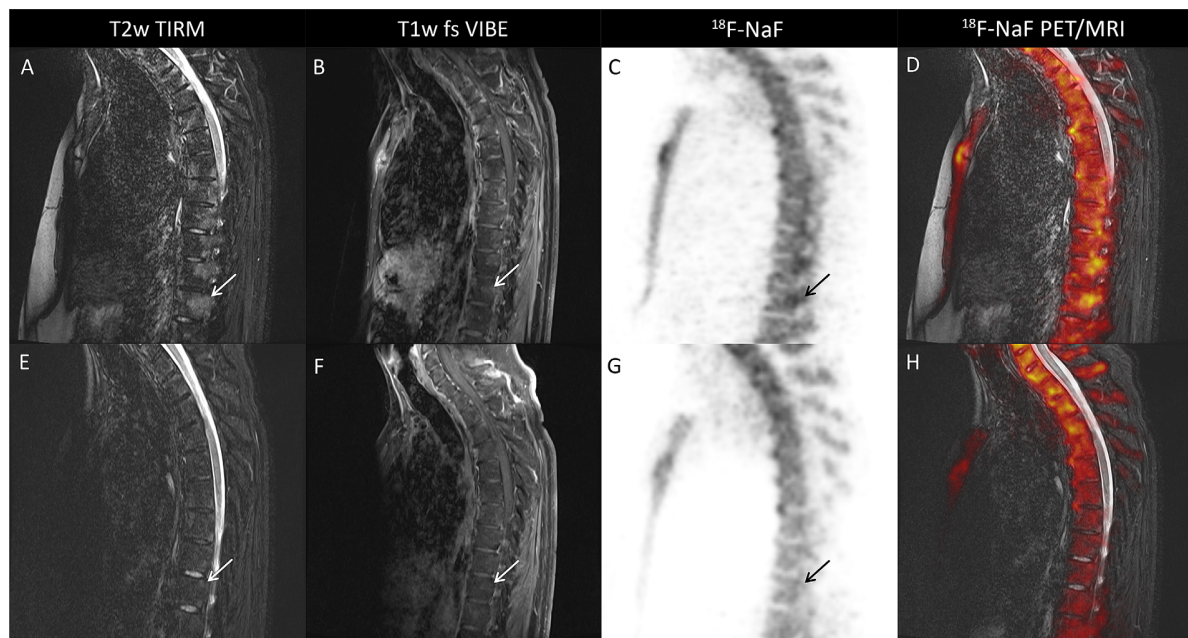


Figure 4. Findings of thoracic spine imaging at baseline (A–D) and follow-up (E–H) for a 40-year-old patient with clinically active radiographic axial spondyloarthritis. At baseline, signs of extensive bone edema are evident in the thoracal vertebral bodies (A and B; white arrows) with evidence of osteoblastic activity based on increased signal on fluorine 18-labeled NaF ($^{18}\text{F-NaF}$) PET/MRI (C and D; black arrow). Follow-up imaging after 4 months of tumor necrosis factor inhibitor treatment (E–H) showed visible decrease of inflammation and osteoblastic activity (white arrows, black arrow). T2w TIRM = T2-weighted turbo inversion recovery magnitude; T1w fs VIBE = T1-weighted volumetric interpolated breath-hold examination with fat suppression (see Figure 1 for other definitions).

DISCUSSION

With this study, we are the first to show that TNFi therapy decreases osteoblastic activity in the SI joints and spine of patients with active radiographic axial SpA within a few months after treatment initiation. As expected, there was clinical improvement at the group level, as assessed by a decrease in BASDAI and ASDAS values, including a significant decrease in C-reactive protein levels. The effect of the treatment on bone metabolism was demonstrated on the basis of a detailed analysis of bone marrow edema, fat lesions, sclerosis, and ankylosis on MRI in comparison to the quantification of osteoblastic activity on PET. Overall, we found a significant reduction of bone marrow edema in both the SI joints and the spine, whereas the beneficial effect on osteoblastic lesions mostly involved those that were present in combination with bone marrow edema prior to treatment initiation. These findings were independent of the anti-TNF compound used (data not shown). In comparison, no changes were observed for chronic lesions of the SI joints, whereas a decrease in fat lesions and an increase in sclerotic lesions were observed in the analysis of spinal VCs at follow-up. Taking into account the short follow-up duration, these data are in line with earlier observations (26) that inflammation and new bone formation are not directly linked but instead represent a reparative process that occurs via erosive, sclerotic, and fat transformation (27) and ends in ankylosis.

Analysis of the lesion types with respect to changes in osteoblastic activity showed a reduction in $^{18}\text{F-NaF}$ uptake at follow-up in both the SI joints and the spine and for both active and chronic lesions. However, the difference in reduction in the SI joints as compared to that in the spine was not statistically significant. This might have been because axial SpA in all patients was in the more advanced, radiographic stage, when the SI joints had likely been affected by the disease for a longer period than the spine, which is generally affected later during the disease course.

On the other hand, no relation was found between the clinical response to TNFi treatment and changes in the quantification of osteoblastic activity as measured by the SUV_{\max} . Interestingly, overall and despite disease activity status at follow-up, as assessed by both the BASDAI and the ASDAS, all patients benefited from treatment, but not all of them achieved low disease activity. Still, quantification of osteoblastic activity demonstrated that the SUV_{\max} decreased, stayed similar, or, on rare occasion, showed only a minor increase. These data indicate that the magnitude of the treatment effect at the structural level, as assessed by imaging, may not necessarily reflect the magnitude of its effect on treatment outcomes, which might depend on the tool used to assess global disease activity or on the effect of comorbidities, such as concomitant fibromyalgia (28–31). Another explanation for this observation may be that, in some patients, treatment with TNFi but also with other

bDMARDs needs >6 months to reach its full potency with regard to clinical outcomes and structural changes (32,33). However, because the effects of treatment were most visible during the early course of disease, when inflammatory activity was present (i.e., at sites where tissue is just beginning to transform), and less apparent in terms of PET findings and chronic changes, these findings might also be applicable to patients with nonradiographic axial SpA (34).

Some limitations of this study need to be taken into account. Importantly, the sample size in our study was too small to yield strong conclusions about the effect of TNFi on bone metabolism. Furthermore, we did not include bDMARDs other than TNFi in our analysis. We therefore see these results as a proof of concept for future research to understand the expected “disease-modifying” effect of bDMARDs, including TNFi, in patients with radiographic axial SpA (16–18). In an era of broader use of such treatments due to the wide application of biosimilar agents, this information is of great importance for both physicians and patients. Furthermore, as mentioned above, the follow-up period may have been too short to demonstrate the full effect of treatment in all patients. Nevertheless, it is still impressive that, despite this relatively short follow-up period, a clear effect was seen in the imaging analyses. It would be interesting to study these effects over longer follow-up periods and to determine whether the benefit of TNFi therapy becomes even more pronounced. Finally, PET/MRI technology is only available in larger centers and is associated with a high level radiation exposure if performed often, making frequent use of the technology unfeasible.

Together, the results of this observational proof-of-concept study suggest that early initiation of antiinflammatory therapy with TNFi may have a beneficial, antosteoblastic effect that results in regression of radiographic progression in patients with active radiographic axial SpA. Further research involving larger patient collectives is needed to confirm these results. It will also be interesting to see whether treatment with other bDMARDs, such as interleukin-17 inhibitors, or with small molecules, such as JAK inhibitors, will have similar results.

ACKNOWLEDGMENT

Open Access funding enabled and organized by Projekt DEAL.

AUTHOR CONTRIBUTIONS

All authors were involved in drafting the article or revising it critically for important intellectual content, and all authors approved the final version to be published. Dr. Bruckmann had full access to all of the data in the study and takes responsibility for the integrity of the data and the accuracy of the data analysis.

Study conception and design. Rischpler, Kirchner, Umutlu, Herrmann, Fendler, Buchbender, Antoch, Sawicki, Tsobanelis, Braun, Baraliakos.

Acquisition of data. Bruckmann, Tsiami, Abrar, Bartel, Theysohn.

Analysis and interpretation of data. Bruckmann, Rischpler, Kirchner, Fendler, Baraliakos.

REFERENCES

- Boel A, Molto A, van der Heijde D, Ciurea A, Dougados M, Gensler LS, et al. Do patients with axial spondyloarthritis with radiographic sacroiliitis fulfil both the modified New York criteria and the ASAS axial spondyloarthritis criteria? Results from eight cohorts. *Ann Rheum Dis* 2019;78:1545–9.
- Rudwaleit M, van der Heijde D, Landewé R, Akkoc N, Brandt J, Chou CT, et al. The Assessment of SpondyloArthritis International Society classification criteria for peripheral spondyloarthritis and for spondyloarthritis in general. *Ann Rheum Dis* 2011;70:25–31.
- Sieper J, Rudwaleit M, Baraliakos X, Brandt J, Braun J, Burgos-Vargas R, et al. The Assessment of SpondyloArthritis International Society (ASAS) handbook: a guide to assess spondyloarthritis. *Ann Rheum Dis* 2009;68 Suppl 2:ii1–44.
- Kiltz U, Baraliakos X, Braun J. Ankylosing spondylitis. In: El Miedany Y, ed. Comorbidity in rheumatic diseases. Springer; 2017. p. 125–43.
- Kiltz U, Baraliakos X, Regel A, Bühring B, Braun J. Causes of pain in patients with axial spondyloarthritis [review]. *Clin Exp Rheumatol* 2017;35 Suppl 107:102–7.
- Van der Heijde D, Ramiro S, Landewé R, Baraliakos X, Van den Bosch F, Sepriano A, et al. 2016 update of the ASAS-EULAR management recommendations for axial spondyloarthritis. *Ann Rheum Dis* 2017;76:978–91.
- Baraliakos X, Listing J, Rudwaleit M, Sieper J, Braun J. The relationship between inflammation and new bone formation in patients with ankylosing spondylitis. *Arthritis Res Ther* 2008;10:R104.
- Baraliakos X, Fruth M, Kiltz U, Braun J. Inflammatory spinal diseases: axial spondyloarthritis: central importance of imaging. *Z Rheumatol* 2017;76:149–62. In German.
- Krohn M, Braum LS, Sieper J, Song IH, Weiß A, Callhoff J, et al. Erosions and fatty lesions of sacroiliac joints in patients with axial spondyloarthritis: evaluation of different MRI techniques and two scoring methods. *J Rheumatol* 2014;41:473–80.
- Maksymowych WP, Chiowchanwisawakit P, Clare T, Pedersen SJ, Østergaard M, Lambert RG. Inflammatory lesions of the spine on magnetic resonance imaging predict the development of new syndesmophytes in ankylosing spondylitis evidence of a relationship between inflammation and new bone formation. *Arthritis Rheum* 2009;60:93–102.
- Buchbender C, Ostendorf B, Ruhmann V, Heusch P, Miese F, Beiderwellen K, et al. Hybrid 18F-labeled fluoride positron emission tomography/magnetic resonance (MR) imaging of the sacroiliac joints and the spine in patients with axial spondyloarthritis: a pilot study exploring the link of MR bone pathologies and increased osteoblastic activity. *J Rheumatol* 2015;42:1631–7.
- Hawkins RA, Choi Y, Huang SC, Hoh CK, Dahlbom M, Schiepers C, et al. Evaluation of the skeletal kinetics of fluorine-18-fluoride ion with PET. *J Nucl Med* 1992;33:633–42.
- Fischer DR, Pfirrmann CW, Zubler V, Stumpf KD, Seifert B, Strobel K, et al. High bone turnover assessed by 18F-fluoride PET/CT in the spine and sacroiliac joints of patients with ankylosing spondylitis: comparison with inflammatory lesions detected by whole body MRI. *EJNMMI Res* 2012;2:38.
- Sawicki LM, Lütje S, Baraliakos X, Braun J, Kirchner J, Boos J, et al. Dual-phase hybrid 18F-fluoride positron emission tomography/MRI in ankylosing spondylitis: investigating the link between MRI bone changes, regional hyperaemia and increased osteoblastic activity. *J Med Imaging Radiat Oncol* 2018;62:313–9.
- Baraliakos X, Boehm H, Bahrami R, Samir A, Schett G, Luber M, et al. What constitutes the fat signal detected by MRI in the spine of patients with ankylosing spondylitis? A prospective study based on biopsies obtained during planned spinal osteotomy to correct hyperkyphosis or spinal stenosis. *Ann Rheum Dis* 2019;78:1220–5.

16. Baraliakos X, Haibel H, Listing J, Sieper J, Braun J. Continuous long-term anti-TNF therapy does not lead to an increase in the rate of new bone formation over 8 years in patients with ankylosing spondylitis. *Ann Rheum Dis* 2014;73:710–5.
17. Haroon N, Inman RD, Learch TJ, Weisman MH, Lee M, Rahbar MH, et al. The impact of tumor necrosis factor α inhibitors on radiographic progression in ankylosing spondylitis. *Arthritis Rheum* 2013;65:2645–4.
18. Molnar C, Scherer A, Baraliakos X, de Hooge M, Micheroli R, Exer P, et al. TNF blockers inhibit spinal radiographic progression in ankylosing spondylitis by reducing disease activity: results from the Swiss Clinical Quality Management cohort. *Ann Rheum Dis* 2018;77:63–9.
19. Van der Linden S, Valkenburg HA, Cats A. Evaluation of diagnostic criteria for ankylosing spondylitis: a proposal for modification of the New York criteria. *Arthritis Rheum* 1984;27:361–8.
20. Garrett S, Jenkinson T, Kennedy LG, Whitelock H, Gaisford P, Calin A. A new approach to defining disease status in ankylosing spondylitis: the Bath Ankylosing Spondylitis Disease Activity Index. *J Rheumatol* 1994;21:2286–91.
21. Blumhagen JO, Ladebeck R, Fenchel M, Scheffler K. MR-based field-of-view extension in MR/PET: B0 homogenization using gradient enhancement (HUGE). *Magn Reson Med* 2013;70:1047–57.
22. Paulus DH, Quick HH, Geppert C, Fenchel M, Zhan Y, Hermosillo G, et al. Whole-body PET/MR imaging: quantitative evaluation of a novel model-based MR attenuation correction method including bone. *J Nucl Med* 2015;56:1061–6.
23. Lindemann ME, Oehmigen M, Blumhagen JO, Gratz M, Quick HH. MR-based truncation and attenuation correction in integrated PET/MR hybrid imaging using HUGE with continuous table motion. *Med Phys* 2017;44:4559–72.
24. Oehmigen M, Lindemann ME, Gratz M, Kirchner J, Ruhlmann V, Umutlu L, et al. Impact of improved attenuation correction featuring a bone atlas and truncation correction on PET quantification in whole-body PET/MR. *Eur J Nucl Med Mol Imaging* 2018;45:642–53.
25. Lukas C, Landewé R, Sieper J, Dougados M, Davis J, Braun J, et al, for the Assessment of SpondyloArthritis international Society. Development of an ASAS-endorsed disease activity score (ASDAS) in patients with ankylosing spondylitis. *Ann Rheum Dis* 2009;68:18–24.
26. Appel H, Sieper J. Spondyloarthritis at the crossroads of imaging, pathology, and structural damage in the era of biologics [review]. *Curr Rheumatol Rep* 2008;10:356–63.
27. Baraliakos X, Heldmann F, Callhoff J, Listing J, Appelboom T, Brandt J, et al. Which spinal lesions are associated with new bone formation in patients with ankylosing spondylitis treated with anti-TNF agents? A long-term observational study using MRI and conventional radiography. *Ann Rheum Dis* 2014;73:1819–25.
28. López-Medina C, Ladehesa-Pineda L, Puche-Larrubia MÁ, Escudero-Contreras A, Font-Ugalde P, Collantes-Estevez E. Which factors explain the patient global assessment in patients with ankylosing spondylitis? A hierarchical cluster analysis on REGISPONER-AS. *Semin Arthritis Rheum* 2021;51:875–9.
29. Nam B, Koo BS, Lee TH, Shin JH, Kim JJ, Lee S, et al. Low BASDAI score alone is not a good predictor of anti-tumor necrosis factor treatment efficacy in ankylosing spondylitis: a retrospective cohort study. *BMC Musculoskelet Disord* 2021;22:140.
30. Kiltz U, Baraliakos X, Karakostas P, Igelmann M, Kalthoff L, Klink C, et al. The degree of spinal inflammation is similar in patients with axial spondyloarthritis who report high or low levels of disease activity: a cohort study. *Ann Rheum Dis* 2012;71:1207–11.
31. Moltó A, Etcheto A, Gossec L, Boudersa N, Claudepierre P, Roux N, et al. Evaluation of the impact of concomitant fibromyalgia on TNF α blockers' effectiveness in axial spondyloarthritis: results of a prospective, multicentre study. *Ann Rheum Dis* 2018;77:533–40.
32. Kim K, Son SM, Goh TS, Pak K, Kim IJ, Lee JS, et al. Prediction of response to tumor necrosis value- α blocker is suggested by 18F-NaF SUVmax but not by quantitative pharmacokinetic analysis in patients with ankylosing spondylitis. *Am J Roentgenol* 2020;214:1352–8.
33. Baraliakos X, van den Bosch F, Machado PM, Gensler LS, Marzo-Ortega H, Sherif B, et al. Achievement of remission endpoints with secukinumab over 3 years in active ankylosing spondylitis: pooled analysis of two phase 3 studies. *Rheumatol Ther* 2021;8:273–88.
34. Van der Heijde, Baraliakos X, Hermann KG, Landewé RB, Machado PM, Maksymowich WP, et al. Limited radiographic progression and sustained reductions in MRI inflammation in patients with axial spondyloarthritis: 4-year imaging outcomes from the RAPID-axSpA phase III randomised trial. *Ann Rheum Dis* 2018;77:699–705.